Internal Structures in the Sub-Neptune Regime

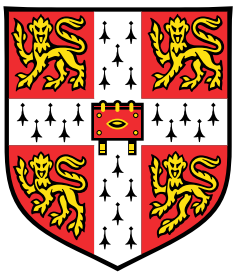

Frances Elizabeth Rigby

Supervisor: Professor Nikku Madhusudhan

Magdalene College
University of Cambridge

This thesis is submitted for the degree of
Doctor of Philosophy

August 2025

Declaration

This thesis is the result of my own work and includes nothing which is the outcome of work done in collaboration except as declared in the preface and specified in the text. It is not substantially the same as any work that has already been submitted, or, is being concurrently submitted, for any degree, diploma or other qualification at the University of Cambridge or any other University or similar institution except as declared in the preface and specified in the text. It does not exceed the prescribed word limit for the relevant Degree Committee.

The work in this thesis is based on the following published and submitted papers:

- **Chapter 2**: Published in *Monthly Notices of the Royal Astronomical Society* as **On the ocean conditions of Hycean worlds**, (Rigby and Madhusudhan, 2024). I developed the internal structure modelling code and performed the calculations in this study. I prepared the manuscript with comments from Nikku Madhusudhan.

- **Chapter 3 and Appendix A**: Published in *The Astrophysical Journal* as **Toward a Self-Consistent Evaluation of Gas Dwarf Scenarios for Temperate Sub-Neptunes**. F.E. Rigby, L. Pica-Ciamarra, N. Madhusudhan, M. Holmberg, S. Constantinou, J. Deng, K. Lee, L. Schaefer, J.I. Moses (Rigby et al., 2024). The work presented in this chapter is based on this lead-author publication. I performed the internal structure modelling, using equations of state I collected and implemented; the choices of equations of state were informed by discussions with Jie Deng and Kanani Lee. The atmospheric structure modelling was performed by Nikku Madhusudhan using the code GENESIS (Gandhi and Madhusudhan, 2017; Piette and Madhusudhan, 2020). The melt-atmosphere calculations were performed by Måns Holmberg, with discussions and model comparisons with Laura Schaefer. The solubility laws used in these calculations were compiled by Lorenzo Pica-Ciamarra. The photochemical calculations were performed by me and Savvas Constantinou, using the open-source code VULCAN (Tsai et al., 2021). Comparisons were made to photochemical calculations

performed by Julianne Moses. The spectral modelling was carried out by Savvas Constantinou using the VIRA framework from Constantinou and Madhusudhan (2024). The co-authors of this publication contributed to the preparation of the manuscript, including the relevant figures. The contents of this published paper were also adapted to form part of Chapter 5 of the thesis of Måns Lars Holmberg, submitted for the degree of Doctor of Philosophy at the University of Cambridge.

- **Chapter 4**: This chapter is based on a paper that has been submitted to the *Monthly Notices of the Royal Astronomical Society* as **The Surface and Interior Conditions of the Temperate Sub-Neptune TOI-270 d**, Rigby & Madhusudhan. I conducted the calculations and interpretation in this study with the exception of the atmospheric structure calculations which were performed by Nikku Madhusudhan using the GENESIS code (Gandhi and Madhusudhan, 2017; Piette and Madhusudhan, 2020). I prepared the manuscript with comments from Nikku Madhusudhan.

Some figures in Chapter 1 are from or have been adapted from other published works. These are specified and referenced in the captions for these figures.

The use of "we" rather than "I" throughout this thesis is a stylistic choice. This thesis contains fewer than 60,000 words including the abstract, appendices, footnotes and tables, but excluding the table of contents, diagrams, figure captions, list of figures/diagrams, bibliography and acknowledgements.

Frances Elizabeth Rigby
August 2025

Abstract

Sub-Neptune planets have been shown to be common among the exoplanet population. The sub-Neptune regime, spanning ∼1-4 Earth radii, encompasses a diverse possible range of planetary conditions, with no analogue in our solar system. The bulk properties of these planets give rise to compositional degeneracies, with a wide range of compositions able to explain each mass and radius. In this thesis, I explore the diversity of interiors possible for temperate sub-Neptune exoplanets. To do this, I developed an internal structure model specialised for sub-Neptunes. This model relates the bulk properties of a planet to the possible interior compositions, incorporating equations of state to describe the behaviour of different planetary materials, including hydrogen/helium, water, silicates, and iron.

I first use the model to conduct a theoretical exploration of the possible interiors and ocean depths of a new class of habitable sub-Neptune, known as hycean worlds. These planets are characterised by liquid water oceans at their surfaces beneath hydrogen-rich atmospheres. Hycean worlds have been the subject of recent investigations of habitability and the potential for biosignature detections, due to their being more conducive to atmospheric observations compared to Earth-like planets. I calculate the range of ocean depths possible for hycean worlds, dependent on the surface gravity and surface temperature. I then explore the range of possible interior compositions and ocean depths for five hycean candidates, placing constraints on the envelope and water mass fractions required for hycean conditions.

Secondly, I apply the internal structure model to the scenario of a gas dwarf sub-Neptune. A gas dwarf is defined by the presence of thick hydrogen-rich envelope atop a rocky interior, with the possibility of a solid or magma ocean surface. The interior model is coupled to atmospheric observations and atmospheric models to evaluate the feasibility of a temperate sub-Neptune hosting such conditions. In this way, the inferences made about the atmospheric properties and composition from atmospheric observations can begin to ease the interior compositional degeneracies. The model framework is used to consider the plausibility of a gas dwarf scenario for the

temperate sub-Neptune K2-18 b, which was recently observed with the James Webb Space Telescope (JWST).

Lastly, I use the internal structure model to conduct a detailed exploration of the possible interior and surface conditions of TOI-270 d, a temperate sub-Neptune recently observed with JWST. This investigation, informed by the findings of the recent observations, spans possible scenarios of a gas dwarf, a hycean world, and a mini-Neptune, with a water-rich interior but no distinct surface. In the modelling of mini-Neptune scenarios I consider the potential for hydrogen and water to be mixed, which has been shown to occur across a wide range of pressures and temperatures relevant to sub-Neptunes.

I conclude with a discussion of possible future directions for modelling the interiors of sub-Neptune exoplanets, and prospects for their characterisation. Potential directions include the incorporation of more complex treatments of planetary materials. I discuss the need for further experimental data to inform modelling efforts.

Acknowledgements

Firstly, I'd like to thank the UKRI STFC for the PhD studentship that has allowed me to pursue this research.

Secondly, I'd like to thank my supervisor Professor Nikku Madhusudhan for his enthusiastic guidance and support throughout the past four years. I'm incredibly grateful for the varied opportunities that have allowed me to gain invaluable experience across multiple exciting areas.

I'd also like to thank my examiners, Amy Bonsor and Lena Noack, for the interesting discussion and thoughtful comments and questions.

Thank you to the rest of the research group who I've been lucky to overlap with during my PhD. The PhD students who were senior to me: Connor Cheverall, Måns Holmberg, Savvas Constantinou, Matt Nixon and Adam Langeveld; the PhD students who joined after me: Edouard Barrier, Lorenzo Pica-Ciamarra, and Martin Binet; and the postdocs: Greg Cooke, Lalitha Sairam, and Sam Cabot; and our project co-ordinator Charles. Our research group has grown and changed throughout my time in it, but has remained unwaveringly unhinged and entertaining.

I have been lucky to have lovely office mates throughout my time at the IoA. I particularly want to thank Hannah Petrovic, my friend and officemate for three of my four years of PhD, without whom my time at the IoA would not have been the same. To my friends I started the PhD with, thank you for the excellent coffee time company and pub quiz wins (and losses): Adam, Elliot, Adam O and Matt. And Annabelle: your friendship has been an unexpected joy of my last year in the IoA!

The PhD has certainly not been a linear journey, especially thanks to a close cranial encounter with a stone mantle piece in my college accommodation. Therefore, I'd like to thank Debbie Peterson and Paul Hewett for their support before, during and on my return from medical intermission.

To decide which of two colleges to put as my first preference in my application, I left it up to fate: which won a particular round of University Challenge. Aside from the very solid fireplaces, I have felt lucky to be part of Magdalene College. To my wonderful friends from Magdalene MCR over the years: Hannah, Siobhán, Sam, Chris,

Hugh, Charles, Marius, Eleanor and Jo, but especially to the Blonde Women. Also to Daniel, thank you for your belief in me and your friendship. A huge thank you as well to the fellowship of Magdalene College, for the honour of being elected as a Bye-Fellow during my third-year.

Beyond Cambridge, I am forever grateful to my friends from school, Holly and Eilidh, who remain a constant source of love, support and inspiration. Holly, I couldn't imagine life without you, and I am thankful for you and your rambling voicenotes every day. And I give you full permission to stop reading now!

Last, and by no means least: to my parents, Sarah and David (affectionately referred to as Saz and Daz). I am immensely grateful to you, and know that I am extremely lucky to have both the means and the unwavering, enthusiastic support to pursue everything I have done so far. I could not ask for better parents, and I hope you guys are as proud of me as I most certainly am of you.

Table of contents

List of figures

List of tables

Chapter 1

Introduction

In the 30 years since the first discovery of an exoplanet around a main sequence star (Mayor and Queloz, 1995), the field of exoplanet study has shifted from detection to characterisation. This shift, largely thanks to spectroscopic observations of exoplanet atmospheres, has been cemented by the unprecedented capabilities of the James Webb Space Telescope (JWST). To be studying exoplanets in this era of characterisation is to be presented with a wealth of information never before available to humanity. The difficulty now lies in the robust interpretation of the precise spectroscopic data available and the translation of this to well-informed inferences about the nature of these planets.

Planets in the sub-Neptune regime, with sizes between 1-4 Earth radii, between that of Earth and Neptune, have emerged as the most abundant class of planet. This planetary regime spans a diverse range of densities and hence potential compositions unlike any seen in our own solar system. The characterisation of such planets provide a key avenue to improving our understanding of exoplanet formation and evolution, in addition to the potential for habitability on planets vastly different to our own. For such planets, their bulk properties – the mass, radius, and equilibrium temperature – permit a wide range of possible interior compositions. Determining the nature of planets in the sub-Neptune regime is at the forefront of exoplanet research, which requires a number of complementary observational and theoretical methods. In recent years, the first molecular detections have been made in the atmospheres of temperate sub-Neptunes (e.g. Madhusudhan et al., 2023b; Holmberg and Madhusudhan, 2024), allowing the first insight into their atmospheric composition. Understanding the nature of these planets requires connecting their observable atmospheres to the surface and interior composition, relying on theoretical models of the atmosphere and interior, and their interactions.

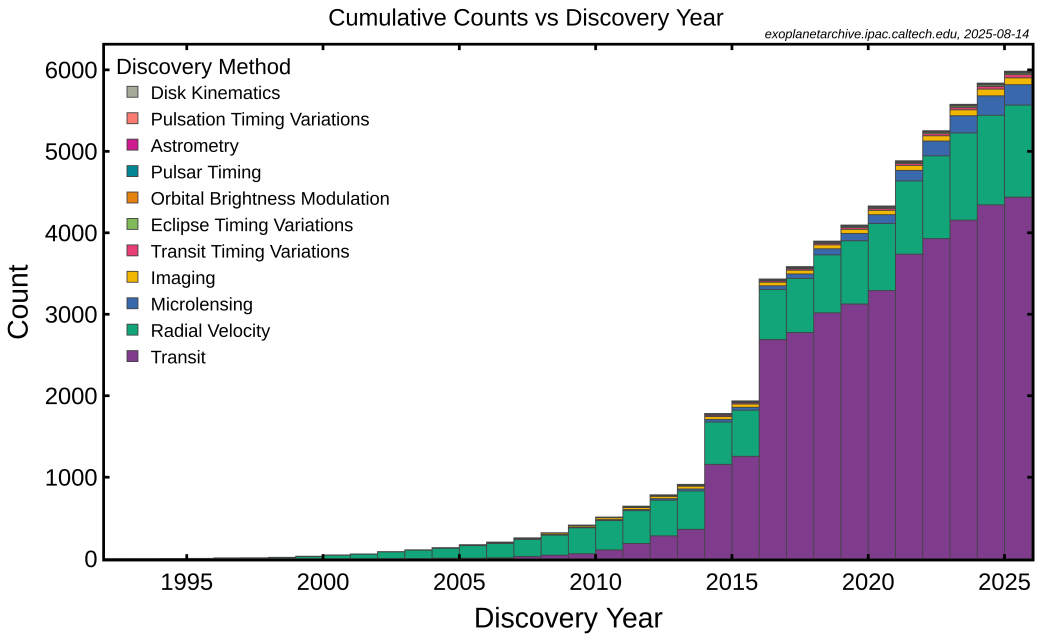

Fig. 1.1 Cumulative exoplanet detections across discovery years. This figure is from the NASA Exoplanet Archive, generated on 14/08/25.

In this thesis we explore the range of interiors possible across planets in the sub-Neptune regime, with a focus on temperate sub-Neptunes. We begin in this chapter with an introduction to the detection and observation of sub-Neptune exoplanets, the theoretical methods used in the study of their interiors and atmospheres, and the exciting importance of this planetary regime for learning about planet formation, evolution and habitability.

1.1 Exoplanet Detection

Figure 1.1 shows the cumulative exoplanet discoveries since 1995, colour-coded according to discovery method. To date, the method yielding the most detections has been the transit method, with 4437 confirmed exoplanets discovered via this method (NASA Exoplanet Archive, accessed 26/08/25). The second most productive discovery technique is the radial velocity method, which was the predominant method until the launch of the Kepler telescope in 2009. Other methods, including transit timing variations (TTVs) and direct imaging, have contributed smaller numbers of exoplanets. Due to their predominance and importance in determining the mass and radius of the majority of exoplanets, we will focus on the transit and radial velocity methods, before briefly outlining some other methods.

1.1.1 Radial Velocity Method

The first exoplanet to be discovered orbiting a main sequence star, 51 Pegasi b, was detected using the radial velocity method (Mayor and Queloz, 1995). The technique relies on the periodic Doppler shifting of absorption lines in the stellar spectrum due to the gravitational interaction between the orbiting planet and the host star.

The radial velocity semi-amplitude of the host star can be written

$$K_\star^3 = \frac{2\pi G}{P(1-e^2)^{3/2}} \frac{M_\mathrm{p}^3 \sin^3 i}{(M_\mathrm{p} + M_\star)^2} \tag{1.1}$$

where M_p and $M_\star$ are the planetary and stellar masses respectively, P and e are the period and eccentricity of the planetary orbit respectively, and i is the inclination of the orbit perpendicular to the line-of-sight. The true stellar orbital velocity will be greater than the measured value, which is only the component along the line-of-sight. There is therefore a degeneracy between the observed motion of the star and the inclination of the system, which can be resolved through additional observations via the transit method, if available.

In this way, the planetary mass can be estimated. In reality, due to the aforementioned degeneracy, the constraint derived from this method is a lower limit on the planetary mass, in the absence of additional information on the orbital inclination.

The radial velocity method is best suited to detecting large mass planets with short orbital periods, as this will result in a larger semi-amplitude, which is more easily detected repeatedly. With current facilities, the best velocity precision achievable is $\sim$0.1 ms^{-1} with ESPRESSO (Pepe et al., 2021) – approaching the precision that would be required to detect an Earth-like planet around a Sun-like star.

1.1.2 Transit Method

If a planetary system is favourably aligned to our line-of-sight, the planet will be seen to pass in front of its host star, in an event known as a transit. The fractional change in the apparent brightness in and out of transit is known as the transit depth. By assuming the planet is fully opaque and spherical, the transit depth can be related to the relative sizes of the planet and host star:

$$\Delta = \left(\frac{R_\mathrm{p}}{R_\star}\right)^2 \tag{1.2}$$

where R_p and $R_\star$ are the planetary and stellar radii respectively. Therefore, given a known stellar radius, a measurement of the transit depth allows a derivation of the

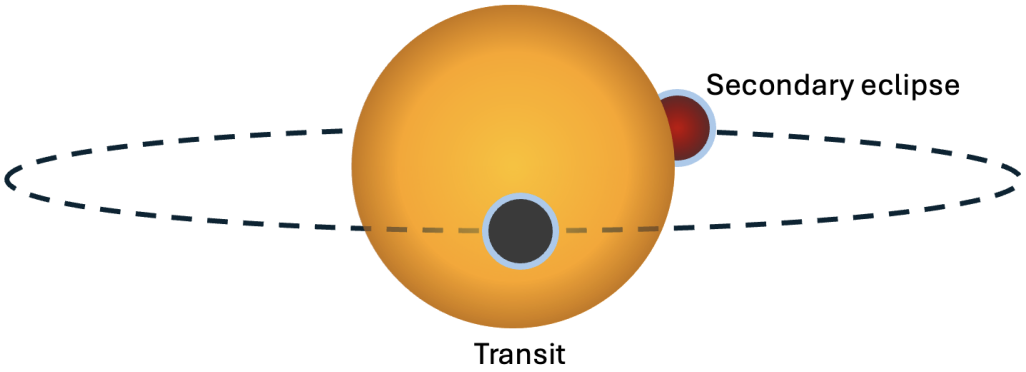

Fig. 1.2 Schematic of primary and secondary eclipse of an exoplanet.

planetary radius. Furthermore, Kepler's third law, which relates the planetary orbital period P to the semi-major axis a:

$$a^3 = GM_\star \left(\frac{P}{2\pi}\right)^2 \tag{1.3}$$

can be used to derive a value for a, given that P can be found from the time between successive transits. The transit method is most conducive to the detection of large planets, as the transit depth will be largest. To detect small planets, targeting small, cool stars such as M dwarfs results in a larger transit depth than for larger, hotter stars. Due to the frequency of observable transit events, shorter period planets are often discovered more readily via the transit method.

At the opposite end of the planetary orbit to the primary transit, the planet can be seen to pass behind the host star, in what is known as the secondary eclipse. Both primary transit and secondary eclipse are crucial configurations for spectroscopic observations of exoplanet atmospheres, which will be outlined in Section 1.4.1.

Measurement of a allows a calculation of the planetary equilibrium temperature, $T_{\rm eq}$. The equilibrium temperature assumes that the planet is in radiative equilibrium, such that it is heated only by its host star, with both the planet and star behaving as blackbodies.

Treating the star as a blackbody, its luminosity is written as $L_\star = 4\pi R_\star^2 \sigma T_\star^4$, where σ is the Stefan-Boltzmann constant, and $T_\star$ is the stellar effective temperature. The planet absorbs a fraction of the incident energy from the star, based on the distance to the star and the cross-sectional area of the planet. This absorbed energy will also be moderated by the Bond albedo, $A_{\rm B}$. In equilibrium, the energy absorbed and emitted by the planet are equal. If the planet radiates as a blackbody, assuming the absorbed energy is uniformly redistributed, we can therefore write

$$\frac{L_\star}{4\pi a^2}\ \pi R_{\rm p}^2(1-A_{\rm B}) = 4\pi R_{\rm p}^2 \sigma T_{\rm eq}^4 \tag{1.4}$$

Hence, using the expression for $L_\star$, $T_{\rm eq}$ can be written

$$T_{\rm eq} = T_\star \sqrt{\frac{R_\star}{2a}}(1-A_{\rm B})^{1/4} \tag{1.5}$$

The equilibrium temperature provides a theoretical estimate of the planetary temperature. In reality, the temperature at the planetary surface will be impacted by greenhouse warming due to the atmosphere, if present, and any internal energy sources, such as gravitational contraction or tidal heating.

1.1.3 Other Detection Methods

Transit timing variations can be used to detect additional planets in systems where a transit has already been observed (Agol et al., 2005). The secondary planet will gravitationally perturb the already detected planet, such that the transit events for this original planet will occur at a slightly different time to what is expected without a companion. These variations in transit time can be measured, allowing inference of the properties of the secondary planet, including its mass (e.g. Nesvorný and Morbidelli, 2008; Ford et al., 2012).

Direct imaging involves the measurement of a planet's flux, excluding the flux from the host star. This method is therefore only feasible for large orbital separations (e.g. Marois et al., 2008) and even then, a coronagraph is often used to block the starlight to allow the planetary flux to be effectively isolated. Nevertheless, a large planetary intrinsic flux is essential, hence directly imaged planets are typically young and hot (e.g. Chauvin et al., 2004).

Other detection methods with lower yields, as shown in Figure 1.1, include microlensing (e.g. Bond et al., 2004), pulsar timing (e.g. Wolszczan and Frail, 1992), and astrometry (e.g. Stefánsson et al., 2025).

1.2 Exoplanet Formation and Demographics

1.2.1 Exoplanet Diversity

In Figure 1.3 we show the radius-period distribution for the confirmed exoplanets to date (from NASA Exoplanet Archive, accessed 14/08/25), and the equivalent mass-period distribution in Figure 1.4. The solar system planets are also shown. Two

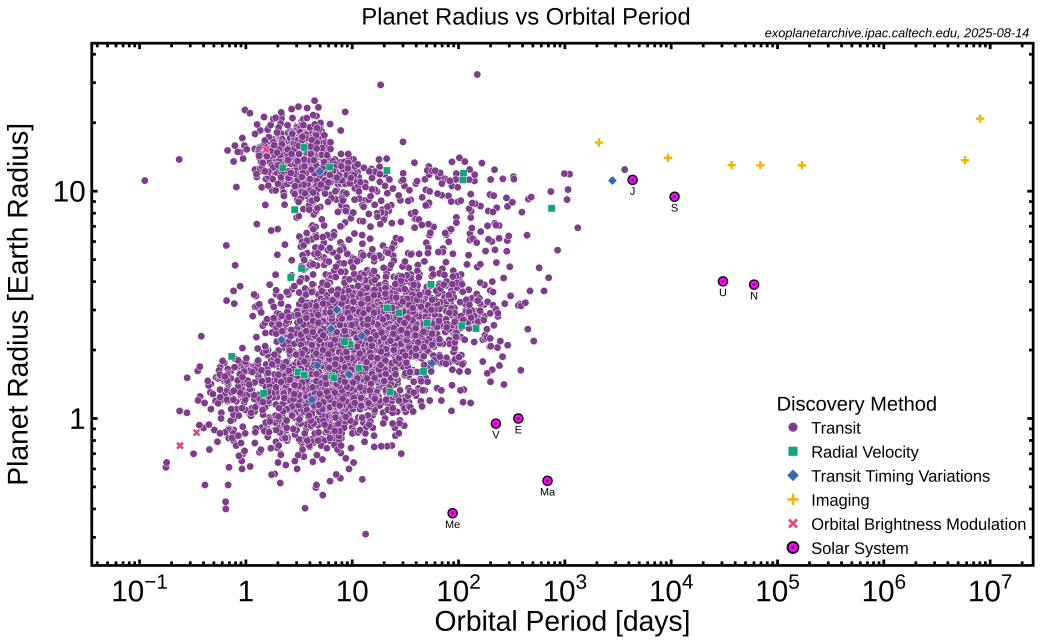

Fig. 1.3 Exoplanets detected according to their radius and orbital period. This figure is from the NASA Exoplanet Archive (generated on 14/08/25).

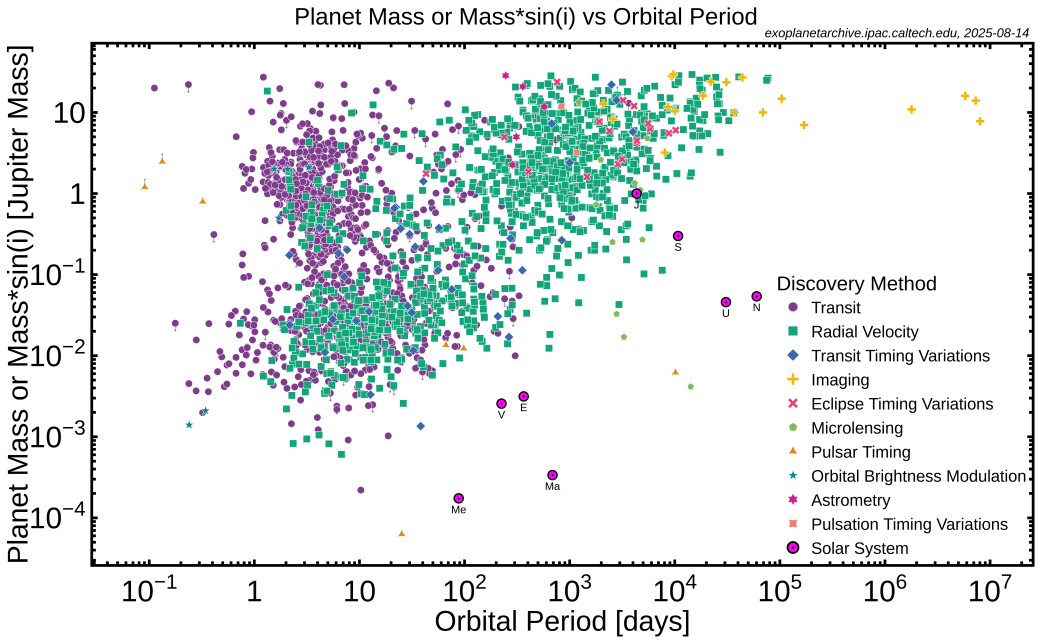

Fig. 1.4 Exoplanets detected according to their mass and orbital period. This figure is from the NASA Exoplanet Archive (generated on 14/08/25).

things are important to note from these plots. Firstly, there is a huge diversity of exoplanets, far beyond those seen in our own solar system. As shown in Figures 1.3 and 1.4, planets with radii > 7 times Jupiter's radius have been detected, and $\sim$10 times Jupiter mass. In Figure 1.3 it can be seen that there is an abundance of exoplanets with radii intermediate between Earth and Neptune. This population is known as the sub-Neptune regime, and will be the focus of this thesis. We discuss the sub-Neptune population further in Section 1.5.

Secondly, it is important to consider the biases and observational limits of the current detection surveys. As is clear from Figures 1.3 and 1.4, we are yet to push these limits to detect an Earth-analogue, with an Earth-like mass, radius and orbital period. As described in Section 1.1, the transit and radial velocity methods are more conducive to shorter period planets.

The exoplanet population can be broadly categorised based on the planetary bulk properties. Naturally, these categorisations follow from our understanding of our own solar system. Further sub-categorising exoplanets requires additional information, which can be done to first order using the equilibrium temperature.

Rocky Planets. These planets have similar masses and radii to the terrestrial planets in our solar system. Their bulk properties are consistent with largely rocky compositions, with only a small proportion of mass contained in volatile layers. Rocky planets on close-in orbits have the potential to be what is known as a lava world, with little to no atmosphere and a molten surface (e.g. Léger et al., 2011).

Sub-Neptunes. The sub-Neptune regime spans the radius range not seen in our own solar system, between the size of Earth and Neptune, $\sim$1-4 $R_\oplus$. This regime covers a diverse range of possible compositions, from the largely rocky super-Earths, to gas dwarfs with hydrogen-rich atmospheres, to planets with high water content, such as mini-Neptunes. Planets in the sub-Neptune regime are the focus of this thesis, and as such, we will discuss this population further in the following section. As is clear from Figures 1.3 and 1.4, the sub-Neptune population is the most abundant class of planet detected to date, particularly with short orbital periods $\lesssim$100 days (e.g. Fressin et al., 2013; Fulton and Petigura, 2018a).

Ice Giants. The ice giant planets have masses and radii similar to those in our solar system, Neptune and Uranus, which have masses of $\sim 17 M_\oplus$ and $\sim 14.5 M_\oplus$ respectively and radii of $\sim 4 R_\oplus$. As for the sub-Neptunes, the majority of the ice giants detected to date have orbital periods $\lesssim$100 days. Their interiors are thought to be primarily composed of ices, including water, ammonia and methane, in addition to some hydrogen and helium, and a rocky core.

Gas Giants. The largest class of planet in both mass and radius are the gas giants, which have comparable bulk properties to Jupiter and Saturn. However, depending on the level of instellation received from the host star, these planets can have inflated radii and high equilibrium temperatures – these close-in gas giants are typically known as hot Jupiters. As we saw in Section 1.1, hot Jupiters are very conducive to transit and radial velocity observations. The cold gas giants, like Jupiter and Saturn, are on much wider orbits.

In Figure 1.5 we show the masses and radii of confirmed exoplanets, shown against mass-radius (M-R) relations from Seager et al. (2007). The exoplanets shown, from the NASA Exoplanet Archive (accessed 17/07/25), are those with masses and radii measured to a precision of better than 20%. The M-R curves, as outlined in depth in Section 1.3.4, are for isothermal planets with compositions of pure H, H_2O, $MgSiO_3$ and Fe, and an Earth-like proportion of $MgSiO_3$ (67.5%) to Fe. These relations are a useful first estimate of a planet's bulk composition. The population of small Earth-like planets can be seen in the lower left corner, lying around the M-R curves for rocky compositions. The largest radius planets are the gas giants, shown to lie close to or above the pure hydrogen M-R curve. For intermediate density planets, including sub-Neptunes, those with masses and radii lying above the pure H_2O curve but below the pure H curve, require some proportion of hydrogen to explain their density. M-R relations and their underlying models are explained in detail in Section 1.3.4.

1.2.2 Planet Formation

The fields of planet formation and exoplanet characterisation are complementary: through understanding the present-day compositions of exoplanets we can shed some light on planet formation processes. Of course, up until the discovery of exoplanets, the only test case for planet formation models was the solar system. We now know that the diversity of extra-solar systems is vast, with alien configurations including the high abundance of sub-Neptune planets, and the existence of giant planets on close-in orbits. Now, planet formation models must explain these varied configurations. These modelling efforts are aided by today's technology, providing, for example, observations of protoplanetary disks and young planetary systems (e.g. Hardy et al., 2015; Banzatti et al., 2023).

Planet and indeed star formation begins with the collapse of a giant molecular cloud under its own gravity. This goes on, due to conservation of angular momentum, to form a protoplanetary disk around the central protostar. Any remaining material in the disk that is not used in planet formation will later be accreted onto the star, or is ejected

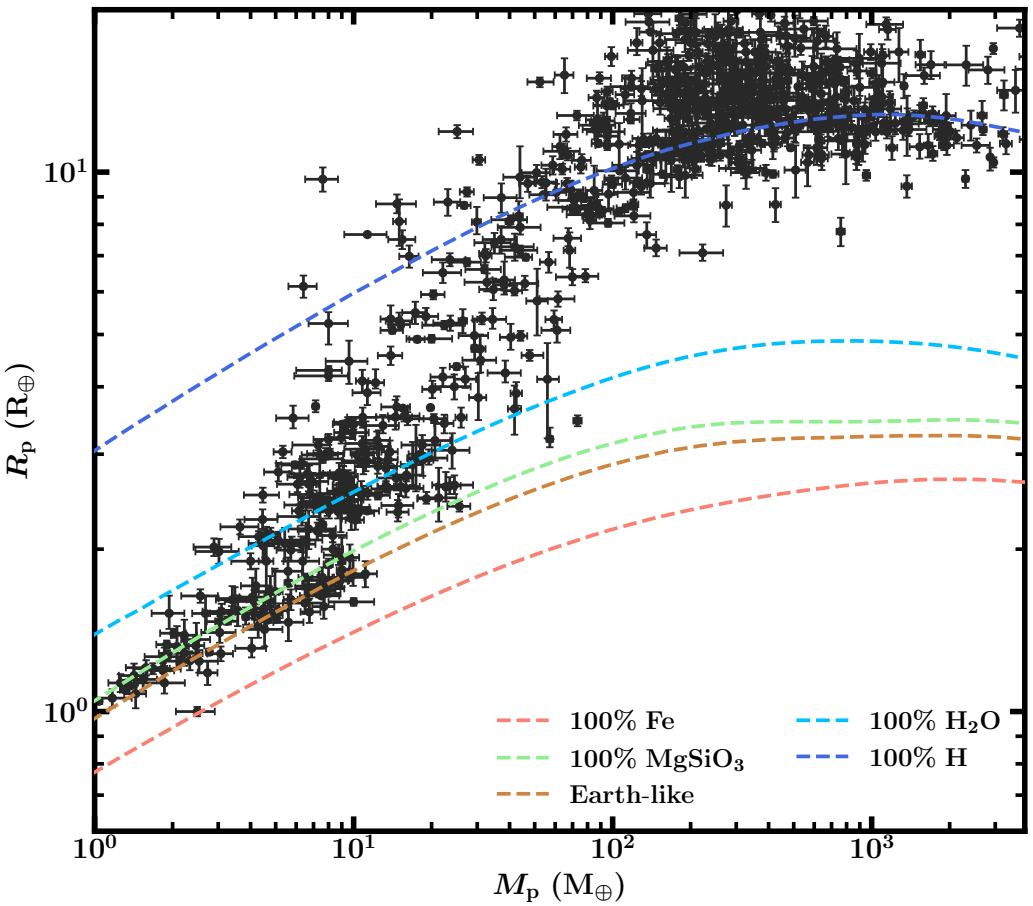

Fig. 1.5 Masses and radii of exoplanets with mass and radius measured to a precision of better than 20%. Exoplanet data is from the NASA Exoplanet Archive (accessed 17/07/25). Also shown are mass-radius curves of different compositions from Seager et al. (2007).

from the system. The precise process of planet formation from the protoplanetary disk stage is uncertain, with many open questions remaining. The standard model of this formation process is known as the core accretion model (e.g. Alibert et al., 2005; Bodenheimer and Pollack, 1986; Pollack et al., 1996; Helled et al., 2014). We will describe this in terms of three phases:

Phase 1. The planetary core/embryo is formed, consisting of heavy elements. This forms from the combination of, first, small pebbles and dust grains into planetesimals, and then of the planetesimals themselves (e.g. Pollack et al., 1996). The result is known as a planetary embryo if it goes on to form a terrestrial planet, or a planetary core if it is sufficiently massive to go on to form a giant planet.

Phase 2. If the mass of the planetary core is sufficiently large, $\gtrsim 2$ $M_\oplus$, hydrogen and helium can be accreted from the disk (e.g. Brouwers and Ormel, 2020). This relies on the formation of the core being sufficiently rapid, with the gaseous protoplanetary disk still present for gas to be accreted from. If the planet formation process terminates here, a Neptune or sub-Neptune planet would be formed.

Phase 3. Once sufficient gas has been accreted for the heavy element mass and the H/He mass to be comparable, the accretion enters a runaway phase. This leads to the formation of giant planets.

Figure 1.6, adapted from Helled and Morbidelli (2021), shows the planet formation process described above. The dependence of the evolutionary outcome on the core mass is shown, along with the variation in the proportion of envelope H/He and metallicity over time.

There remain, however, many open questions in planet formation. The core accretion model of planet formation cannot fully explain all aspects of the observed planetary populations. Orbital migration has been suggested to explain multiple aspects of the exoplanet population, including the existence of very short-period exoplanets (e.g. Terquem and Papaloizou, 2007; Cossou et al., 2014), and the observations of planetary systems with intermediate mass planets in orbital resonance (e.g. Mills et al., 2016; Tamayo et al., 2017). In-situ formation versus migration remains an active area of study for different planetary populations (Boley et al., 2016; Pan et al., 2022). Furthermore, the role of gravitational instability – the process where an overdense region of the protoplanetary disk undergoes gravitational collapse – in the formation of giant planets remains uncertain (e.g. Kratter and Lodato, 2016).

Understanding the formation for intermediate mass planets such as Neptunes and sub-Neptunes remains challenging (e.g. Helled and Bodenheimer, 2014). These planets are expected to form at larger orbital radii and migrate inwards (e.g. Bitsch et al., 2015; Venturini and Helled, 2017). If this is the case, they would be expected to contain large mass fractions of water due to their formation beyond the water ice line (e.g. Venturini et al., 2020; Bitsch et al., 2021). This could be altered by the formation of a giant planet beyond the ice line (e.g. Bitsch et al., 2021), blocking water-rich pebbles and causing the formation of a dry sub-Neptune. The sub-Neptune population has been observed to contain a bimodality in radius distribution, known as the radius valley (e.g. Fulton et al., 2017), which will be discussed further in Section 1.5.1. The role of formation and evolution processes in sculpting the sub-Neptune population remains an important area of study, and improved constraints on the composition of sub-Neptunes can help to shed light on such processes.

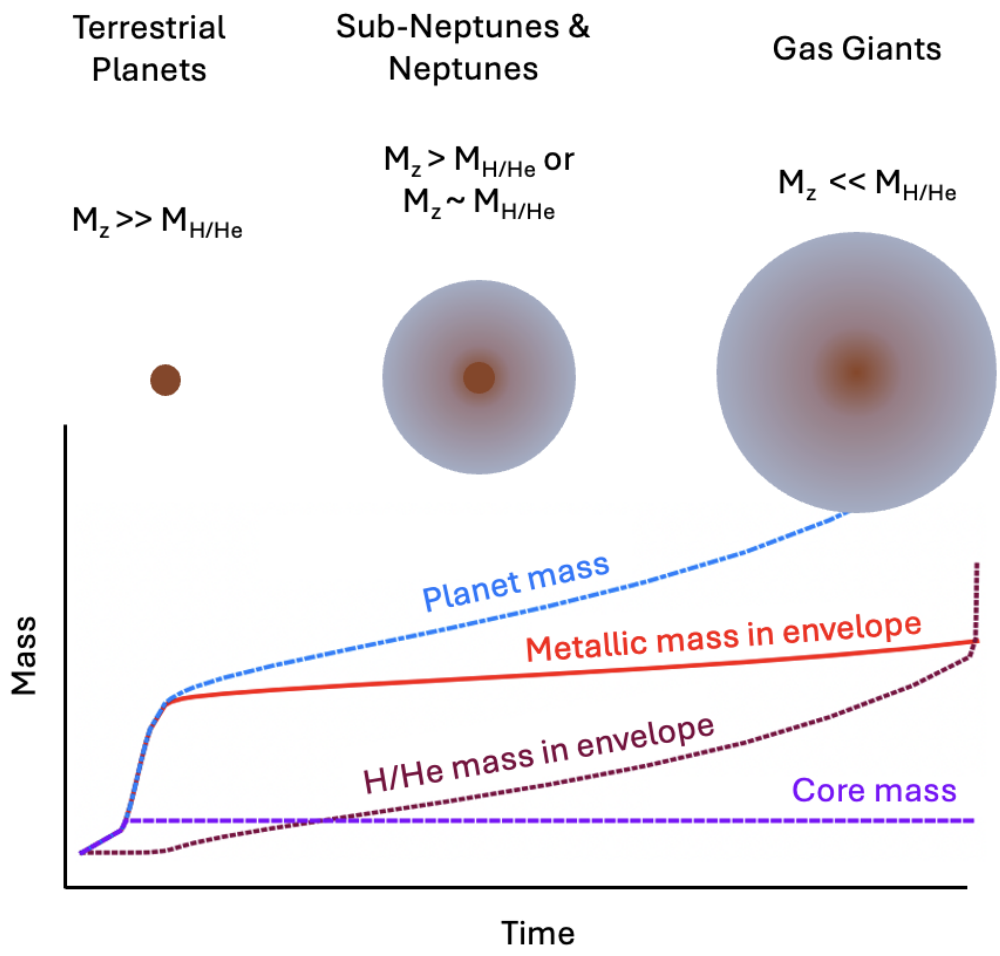

Fig. 1.6 Diagram showing planetary growth during core accretion, adapted from Helled and Morbidelli (2021).

1.3 Planetary Interiors

The interior of the Earth is the best understood planetary interior, primarily due to the availability of seismic data. The interiors of other solar system planets remain active areas of study, combining observational data with theoretical models. Our understanding of Jupiter's interior, for instance, comes from a combination of gravity and magnetic field measurements, largely thanks to the Juno mission (e.g. Wahl et al., 2017; Helled et al., 2022). This data, along with theoretical models, leads to the inference of a diffuse metal-enriched core, surrounded by metallic hydrogen, with a hydrogen and helium atmosphere (e.g. Wahl et al., 2017; Helled et al., 2022). In contrast, Uranus and Neptune have more limited data, which comes from the Voyager

2 spacecraft, hence limiting the constraints on their interior composition and structure (e.g. Guillot, 2005; Podolak and Helled, 2012; Helled and Fortney, 2020).

The amount of information available to help constrain the nature of exoplanet interiors is minimal. For the majority of exoplanets, to make inferences about their interior conditions, we rely on their bulk properties: the planetary mass $M_{\rm p}$, radius $R_{\rm p}$ and equilibrium temperature $T_{\rm eq}$. Internal structure models are used to relate these bulk properties to the planet's internal structure parameters, typically the mass fractions of different materials potentially present in the planet's interior. Determining the internal structure is an inherently degenerate problem, with a wide range of compositions able to explain the bulk density of a given planet. In the era of JWST, the introduction of atmospheric data can begin to ease the degeneracies in composition.

In this section, we give an overview of internal structure models in the context of exoplanets, with a focus on sub-Neptunes.

1.3.1 Internal Structure Modelling

The first internal structure models date to the 1960s (Zapolsky and Salpeter, 1969). In their seminal work, Zapolsky and Salpeter (1969) presented mass-radius (M-R) relations for zero-temperature spheres of various homogeneous compositions. Their method integrated the planetary structure equations under the assumption of spherical symmetry. These equations are for mass continuity:

$$\frac{dR}{dM} = \frac{1}{4\pi R^2 \rho} \tag{1.6}$$

and hydrostatic equilibrium:

$$\frac{dP}{dM} = -\frac{GM}{4\pi R^4} \tag{1.7}$$

where R is the radius of a spherical shell which encloses mass M, and ρ and P are the density and pressure at this R respectively. The density ρ is described by an equation of state (EOS), typically as a function of pressure and temperature, $\rho = \rho(P, T)$, with the pressure and temperature linked by a P-T profile, $T = T(P)$. In the case of Zapolsky and Salpeter (1969), they assumed zero-temperature spheres, hence adopting an isothermal EOS. For this, they used equations of state presented by Salpeter and Zapolsky (1967), which were derived using a zero-temperature Thomas-Fermi-Dirac (TFD) model – this will be discussed further below.

For static internal structure models, i.e. non-time evolving, the most significant differences in modelling procedure tend to arise from the assumptions about the

equations of state and pressure-temperature profiles. The TFD EOS used by Zapolsky and Salpeter (1969) is only accurate for extreme pressure conditions where quantum effects dominate. As we will see in the following sections, the choice of EOS can have significant impact on inferred internal structures and mass-radius relations.

1.3.2 Planetary Adiabats

There are many potential sources of energy in planetary interiors, including the primordial heat remaining from formation, gravitational contraction, differentiation, phase transitions, radioactive decay, and tidal heating. It is common for static internal structure models to assume a vigorously convective interior below some radiative-convective boundary (e.g. Sotin et al., 2007; Thomas and Madhusudhan, 2016). However, the validity of this assumption has been questioned based on studies of solar system ice giants (e.g. Nettelmann et al., 2011; Podolak et al., 2019; Scheibe et al., 2021), due to compositional gradients and material phase transitions potentially suppressing convection.

If a planet's interior is indeed assumed to be vigorously convective, the temperature structure can be considered adiabatic. The equation for the adiabatic gradient is written

$$\nabla_{\mathrm{ad}} = \left.\frac{\partial T}{\partial P}\right|_S = \frac{\alpha T}{\rho c_{\mathrm{p}}} \tag{1.8}$$

where c_{p} is the isobaric specific heat capacity, S is the specific entropy, and α is the volume expansion coefficient, defined as

$$\alpha = -\left.\frac{\partial \ln \rho}{\partial T}\right|_P \tag{1.9}$$

The variation of α, c_p and ρ (or specific volume, V) with P and T is material dependent – in addition to an EOS to relate $\rho = \rho(P, T)$, a prescription for α and c_p is required.

1.3.3 Equations of State and Phase Diagrams

The equations of state (EOS) for materials present in planetary interiors are a key element of internal structure modelling. For solids, the effect of temperature on the density is much less than for gases, hence many early studies of planetary interiors simplified the problem by considering only pressure-dependence in the EOS (e.g.

Zapolsky and Salpeter, 1969; Seager et al., 2007), i.e. considering $V = V(P)$ or $\rho = \rho(P)$. The simplest isothermal EOS is given directly from the definition of the bulk modulus, K (Poirier, 2000):

$$K = -\frac{dP}{d\ln(V)} = \frac{dP}{d\ln(\rho)} \tag{1.10}$$

If infinitesimal strains of hydrostatic pressure are applied to an unstressed solid, linear elasticity will apply, and hence we can assume a constant value of K. Therefore, we can set $K = K_0$ and obtain through integration the simple EOS:

$$V = V_0 \exp\left(-\frac{P}{K_0}\right) \tag{1.11}$$

This EOS neglects a key effect: the bulk modulus K will increase with pressure. To take this into account, more complex EOS treatments are used. We will briefly introduce some of these most common EOS parameterisations used in planetary internal structure models.

Birch-Murnaghan EOS:

The Birch-Murnaghan (BM) EOS (Birch, 1952) is commonly used for minerals with high-pressure compression data, often obtained using experiments such as shock compression or with a diamond anvil cell. This EOS prescription is temperature-independent, and is often used for solid materials under high pressures where the effect of pressure on the density dominates over temperature. The fourth-order BM EOS is written:

$$\begin{aligned} P = \frac{3}{2}K_0\left(\eta^{\frac{7}{3}} - \eta^{\frac{5}{3}}\right)\Bigg[1 + \frac{3}{4}\left(K_0^{'} - 4\right)\left(\eta^{\frac{2}{3}} - 1\right) + \\ \frac{3}{8}K_0\left(\eta^{\frac{2}{3}} - 1\right)^2\left[K_0K_0^{''} + K_0^{'}\left(K_0^{'} - 7\right) + \frac{143}{9}\right]\Bigg] \end{aligned} \tag{1.12}$$

where $\eta = \rho/\rho_0$ for ρ_0 the ambient density, $K_0^{'}$ is the pressure derivative of the isothermal bulk modulus, and $K_0^{''}$ the second pressure derivative.

Vinet EOS:

For very high pressures, the Vinet EOS (Vinet et al., 1989), derived directly from an empirical potential, is often used over a BM EOS. This EOS is given by

$$P = 3K_0\eta^{\frac{2}{3}}\left(1 - \eta^{-\frac{1}{3}}\right)\exp\left[\frac{3}{2}\left(K_0^{'} - 1\right)\left(1 - \eta^{-\frac{1}{3}}\right)\right] \tag{1.13}$$

where, again, $\eta = \rho/\rho_0$, for ρ_0 the ambient density. Since the Vinet EOS is derived by considering interatomic potentials, it more accurately captures the behaviour of materials under extreme pressure conditions than a BM EOS.

Mie-Grüneisen EOS:

The BM and Vinet EOSs are temperature-independent. To incorporate the additional effect of temperature a thermal pressure term is often used:

$$P_{\rm th} = \gamma \frac{E_{\rm vib}}{V} \tag{1.14}$$

where the proportionality factor γ is the macroscopic Grüneisen parameter, and $E_{\rm vib}$ is the vibrational energy. This term can be added to the "cold" EOS:

$$P(V,T) = P_{\rm cold}(V) + P_{\rm th}(V,T) \tag{1.15}$$

where the "cold" EOS could be, for instance, an isothermal Vinet or BM EOS.

The Mie-Grüneisen thermal pressure can be calculated directly from the vibrational energy of a solid, under a set of simplifying assumptions known as Debye's approximation. However, this cannot be easily determined via experiments. The alternative formulation using the empirical expression $P_{\rm th} = a + bT$ (Anderson, 1984) can be used. By expressing the thermal pressure along an isotherm, the physical meaning of a and b can be seen,

$$P_{\rm th} = -\int_0^{\Theta_D} \alpha K_{\rm T} dT + \alpha K_{\rm T}(T - \Theta_D) \tag{1.16}$$

where Θ_D is the Debye temperature. This is valid for $T > \Theta_D$ with αK_T being temperature-independent.

An example use of a Mie-Grüneisen thermal correction can be seen in Chapter 3, where we use a Mie-Grüneisen thermal correction to a third-order BM EOS (Thomas and Asimow, 2013) to describe peridotitic melt.

Thomas-Fermi-Dirac EOS:

The Thomas-Fermi-Dirac (TFD) EOS arises from a first-principles model of the behaviour of atoms under extreme pressure. In this situation, the material is assumed to consist of degenerate electron gas. In the Thomas-Fermi model, the pressure arises due to the electron kinetic energy and Coulomb interactions. The Dirac correction to this model incorporates the exchange energy due to the Pauli exclusion principle. The TFD EOS is only valid at extreme pressures, >1 TPa, deep in massive planetary cores, where any chemical bonding effects can be ignored. It is dependent only on the atomic number of the material considered.

Ab-Initio EOS:

Ab-initio, in this context, means "from first-principles". Ab-initio EOSs are derived from simulations using fundamental physical laws of molecular dynamics and quantum mechanics. This method avoids the need for experimentally-derived parameters, which are difficult to obtain at the high pressures and temperatures deep in planetary interiors. Electrons are commonly modelled using density functional theory (DFT), i.e. quantum mechanically treated, at finite temperature. DFT is often used to derive the parameters for the BM or Vinet EOS at extreme pressures that are difficult to create experimentally. This method allows the exploration of the exotic behaviour of planetary materials under extreme conditions, including their phase transitions and miscibility (e.g. Mookherjee et al., 2008; Santra et al., 2011; Kovačević et al., 2022; Grande et al., 2022; Gupta et al., 2025).

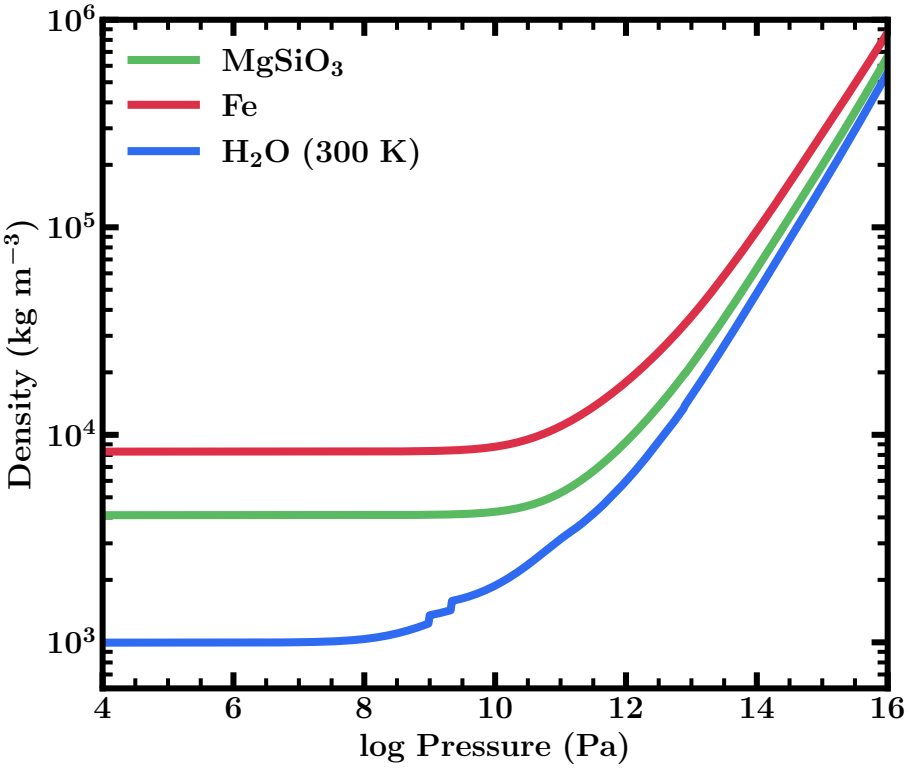

Fig. 1.7 Isothermal equations of state for H_2O, $MgSiO_3$ and Fe, plotted using the equations of state from Seager et al. (2007).

In Figure 1.7 we show some examples of isothermal EOSs from Seager et al. (2007), comprised of EOS parameterisations we have encountered above. These are composite EOSs: different EOS formulations most applicable to each pressure range are patched

together to best represent the pressure-dependent behaviour. For instance, for Fe this is in the form of a Vinet EOS, transitioning to a TFD EOS at high pressures.

Water Phase Diagram and Equation of State

Modelling the interiors of water-rich planets requires an accurate treatment of the complex phase diagram and associated EOS for water. The phase structure of any H_2O present in the planet's interior can vary significantly, depending on the temperature structure of the planetary atmosphere.

In Figure 1.8 we show the phase diagram for pure water, using the phase boundaries from Dunaeva et al. (2010). At Earth's atmospheric pressure and below ($\lesssim$ 1 bar), water can exist as low-pressure ice, liquid, or vapour. The critical point of water is at 647 K and 221 bar, beyond which it becomes a supercritical fluid. With increasing pressure, water forms different phases of high-pressure ice. The most relevant to the interiors of temperate sub-Neptunes are ice VII and ice X. The EOS for water has been determined across different pressure and temperature conditions experimentally (e.g. Fei et al., 1993; Knudson et al., 2012; Grande et al., 2022) and using quantum mechanical simulations (e.g. French et al., 2009). Internal structure models typically use a composite temperature-dependent EOS that combines different sources across pressure/temperature space (e.g. Mazevet et al., 2019; Haldemann et al., 2020; Nixon and Madhusudhan, 2021). The behaviour of water at high-pressures remains an active area of study (e.g. Grande et al., 2022), with an improved understanding and refined EOS expected to affect inferred internal structures (e.g. Huang et al., 2021).

Equations of State for Rocky Interiors

Typically, internal structure models of exoplanets assume a silicate composition based on Earth's mantle (e.g. Seager et al., 2007; Fortney et al., 2007; Wagner et al., 2012; Zeng and Sasselov, 2013; Valencia et al., 2013; Madhusudhan et al., 2020). Earth's upper mantle is predominantly peridotite, which is composed of multiple minerals, including enstatite ($MgSiO_3$) and olivine (also known as forsterite, Mg_2SiO_4) (e.g. Hirschmann, 2000). These component minerals typically undergo transitions with increasing mantle depth, forming minerals such as silicate perovskite $MgSiO_3$, also known as bridgmanite (e.g. Irifune, 1994). Perovskite undergoes a transition to post-perovskite with increasing pressure and temperature, in the deepest regions of Earth's mantle (e.g. Murakami et al., 2004).

Simple approaches are commonly seen in static internal structure models, for example, considering just one mineral such as silicate perovskite (Seager et al., 2007).

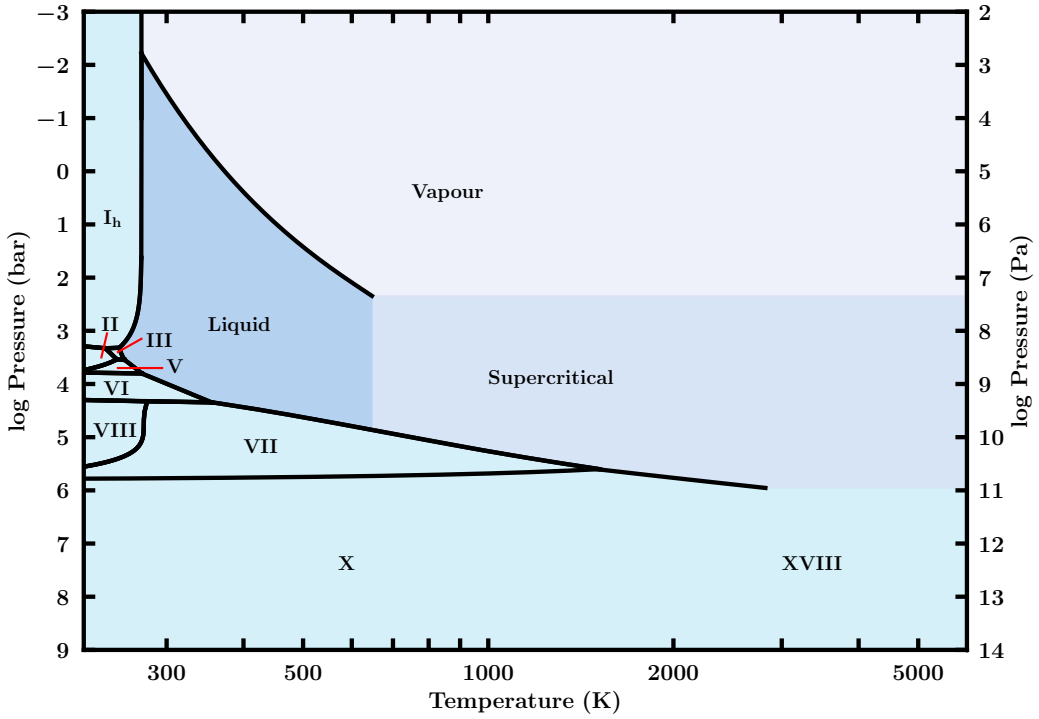

Fig. 1.8 Water phase diagram, with the solid, liquid, vapour and supercritical phases shaded and labelled. The phase boundaries used are from Dunaeva et al. (2010).

These EOSs are often isothermal, using experimentally derived parameters for Vinet and BM EOSs (e.g. Seager et al., 2007), and hence neglect the thermal effects for solid rock, which have been suggested to have only a small effect on the M-R relation (e.g. Howe et al., 2014). Other studies, including evolving models, choose to adopt a more complex approach, considering stable assemblages at each pressure and temperature (e.g. Stixrude and Lithgow-Bertelloni, 2011).

Encapsulating the possibility of a magma ocean requires an appropriate EOS incorporating temperature dependence, and a description of the phase transition. The simplest approach would be to adopt an EOS and melt curve for a single mineral. Alternatively, the solidus and liquidus of some assemblages, e.g. peridotite, have been used in some studies (Dorn et al., 2018). Between the solidus and liquidus curves there will be a region of partial melting, due to the differing melt temperatures of the composite minerals. The EOS and melt curves of silicates are often extrapolated to high-pressures relevant to super-Earths and sub-Neptunes, however experimental data is needed to increase the accuracy of such modelling (e.g. Fei et al., 2021).

Many internal structure models use a temperature-independent Vinet EOS for hexagonal close-packed iron (e.g. Seager et al., 2007; Zeng and Sasselov, 2013; Nixon

and Madhusudhan, 2021). Thermal behaviour is also incorporated by some models using a Mie-Grüneisen thermal correction (e.g. Valencia et al., 2007a; Hakim et al., 2018). Recent studies have also suggested that iron and silicates may be miscible in planetary interiors (Young et al., 2024), challenging the typical assumption of differentiated silicate and iron layers.

1.3.4 Internal Structure Models and Mass-Radius Relations

In the decade before the first detection of a sub-Neptune with the Kepler telescope (Borucki et al., 2011), a range of planets with properties and structures beyond those seen in our solar system were suggested. Léger et al. (2004) proposed the existence of ocean worlds, based on the assumption that planets similar to or less massive than Uranus and Neptune could have migrated sufficiently close to their host star to lie within the habitable zone. This study, considering planets with masses 1-8 $M_\oplus$, investigated the internal structures and ocean depths for water-rich interiors. Other studies around this time considered different potential compositions, producing M-R relations under various assumptions. For instance, Valencia et al. (2006) produced M-R relations for rocky super-Earths and super-Mercuries using an internal structure model that included thermal evolution. This model was then applied to explore the possible interior of the super-Earth GJ 876 d in Valencia et al. (2007b). In Figure 1.9 we show some examples of M-R relations for a range of different compositions – these relations were generated using our internal structure model, which will be described in Section 2.2.1.

Seager et al. (2007) conducted a broad investigation of planetary compositions, producing M-R relations across a wide mass range. This study built upon the work of Zapolsky and Salpeter (1969), using EOSs more accurate at lower pressures, $\leq$1000 GPa. They considered differentiated compositions more realistic to possible planetary interiors to produce isothermal M-R relations – some of their resulting M-R relations are shown in Figure 1.5. In addition to Earth-like and H_2O-incorporated compositions, they showed that the addition of a H/He envelope atop a rocky interior increases the planetary radius.

Sotin et al. (2007) produced M-R relations for water-rich planets, finding that a planet with 50% H_2O could have a radius 25% larger than for an Earth-like composition. Valencia et al. (2007a) investigated the degeneracy between rocky and icy compositions for planets with masses $1-10$ $M_\oplus$. They showed that planets with radius measurements with uncertainties better than 5% and mass measurements with uncertainties better than 10% would allow a distinction between these compositions. However, this study

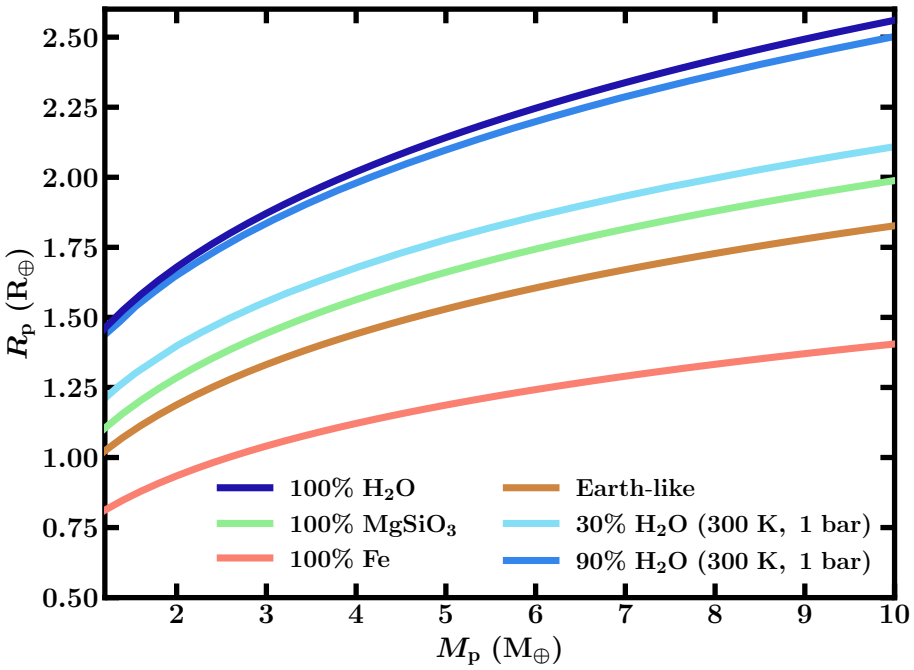

Fig. 1.9 Mass-radius (M-R) relations for different compositions, generated using our internal structure model. The model will be described further in Section 2.2.1. The Earth-like composition is comprised of 2/3 silicates and 1/3 iron. The 30% and 90% H_2O cases have an Earth-like core and an adiabatic temperature structure in the water layer, with the surface at 300 K and 1 bar.

did not consider H_2/He atmospheres. In their calculations, they found a larger radius for an Earth-like planet with 50% H_2O by mass compared to Sotin et al. (2007). Valencia et al. (2007a) suggested this was due to their use of a new silicate EOS following the discovery of the post-perovskite phase of $MgSiO_3$ in Earth's lower mantle (Murakami et al., 2004). This demonstrates an early example of the impact that EOS choice can have on the inferred internal structure, and the long-standing importance of choosing accurate and up-to-date EOSs motivated by experimental data where possible. We leave a detailed discussion of internal structure modelling for water-rich interiors to the following section.

H/He atmospheres were incorporated into internal structure models to investigate sub-Neptune and Neptune mass planets (e.g. Seager et al., 2007; Adams et al., 2008; Rogers et al., 2011). Using an evolving model, Fortney et al. (2007) calculated the radii of planets across a wide mass range, including for H/He-rich gas giants. Rogers et al. (2011) considered highly irradiated sub-Neptune to Neptune sized planets in an evolving model, using an analytic temperature profile for the H/He envelope. They found for a 4-layer differentiated interior that the radii of these planets increased with

increasing temperature, with the largest radius difference for smaller mass planets. Valencia et al. (2013) demonstrated using both static and evolving interior models of GJ 1214b that the radius was most sensitive to the H/He envelope, for which they found a mass fraction of at most 7%, whilst little could be inferred about the ratio of H_2O/rock.

As evident thus far, most internal structure models considered some combination of an iron-rich core, a silicate mantle, a water layer, and some atmosphere, often H_2/He. However, the existence of carbon-rich exoplanets was also suggested and explored by a range of theoretical studies (Lodders, 2004; Kuchner and Seager, 2005; Bond et al., 2010; Madhusudhan et al., 2011; Öberg et al., 2011; Madhusudhan et al., 2012). For example, the highly irradiated super-Earth 55 Cancri e was suggested to potentially have a carbon-rich interior (Madhusudhan et al., 2012), in contrast to previous studies which suggested the more standard interpretation of a silicate and iron interior with a supercritical water layer (Winn et al., 2011; Demory et al., 2011; Gillon et al., 2012; Demory et al., 2012). This was partially motivated by the host star being carbon-rich, with C/O=1.12 ± 0.19 (Delgado Mena et al., 2010), and metal-rich (Valenti and Fischer, 2005).

There is an inherent degeneracy in internal structure modelling, whereby planets of identical mass and radius can have vastly different compositions (e.g. Valencia et al., 2007a; Adams et al., 2008; Rogers and Seager, 2010a; Valencia et al., 2013; Otegi et al., 2020). This is exacerbated for planets with masses and radii lying above the pure water M-R curve, with the possible introduction of a H/He layer to explain the bulk density. One important strategy to eliminate possible compositions is the introduction of atmospheric data, as we will explore in this thesis. An alternate strategy used by some studies to attempt to alleviate degeneracies in interior composition uses the composition of the host star (Dorn et al., 2015, 2017; Brugger et al., 2017; Acuña et al., 2021; Leleu et al., 2021). Namely, these studies assume the bulk Fe/Si and Mg/Si ratios of the host star apply also to the planetary composition. Otegi et al. (2020) found that this does not always give improved constraints on the planetary internal structure, depending on the values for the stellar abundances. These methods tend to use Bayesian inference methods to give the relative likelihoods of different interior scenarios (e.g. Rogers and Seager, 2010a; Dorn et al., 2017). In recent years studies have additionally begun to explore the use of machine-learning to characterise exoplanet interiors faster than Bayesian methods (e.g. Baumeister et al., 2020; Haldemann et al., 2023; Zhao et al., 2023).

1.3.5 Water-Rich Interiors

As we saw in Section 1.3.3, modelling the interiors of water-rich planets will require an accurate treatment of the complex phase diagram for water. The work of Léger et al. (2004) was the first to present models of the interiors of water-rich planets, in particular with surface oceans. These models considered differentiated layers of an iron core, silicate mantle and pure water layer, as also adopted by many subsequent studies (e.g. Sotin et al., 2007; Valencia et al., 2007a; Noack et al., 2016; Thomas and Madhusudhan, 2016). In their model, H_2O ices were described by the EOS of Hemley et al. (1987), measured for ice VII, as similarly used by subsequent studies including Sotin et al. (2007) and Seager et al. (2007). Léger et al. (2004) performed calculations of ocean depths for a water-rich interior scenario, finding this varies with surface temperature for a fixed planetary mass and water mass fraction. The depths of oceans on water-rich exoplanets have been explored by a range of subsequent studies (e.g. Sotin et al., 2007; Alibert, 2014; Noack et al., 2016; Nixon and Madhusudhan, 2021). This will be discussed further in Chapter 2.

In the following decades, the accurate modelling of the complex behaviour of the water phase diagram and associated EOS was shown to be crucial in understanding the possible compositions of planets lying above the rocky M-R curves. This is in contrast to some earlier studies – for instance, Grasset et al. (2009) suggested thermal effects for water were unimportant, with the water mass fraction the more significant factor. However, this study assumed a liquid or icy surface, and the presence of water in the vapour or supercritical phases would have a substantial effect on the inferred radius for a given planetary mass and water mass fraction (e.g. Thomas and Madhusudhan, 2016; Nixon and Madhusudhan, 2021; Aguichine et al., 2021).

Thomas and Madhusudhan (2016) conducted a study into the internal structures of water-rich super-Earths – these would now more commonly referred to as sub-Neptunes, given a significant volatile fraction would be required to explain the planetary bulk density. In this study, they included an extensive treatment of the water phase diagram and EOS, using a composite EOS for those valid for different phases and/or regions of P-T space, to incorporate thermal effects. This approach to use a composite, temperature-dependent EOS for the treatment of water in planetary interiors has become the standard (e.g. Mazevet et al., 2019; Haldemann et al., 2020; Nixon and Madhusudhan, 2021). Accounting for the thermal behaviour of H_2O for water-rich sub-Neptunes was shown to have a significant effect on the resulting planetary radius. Varying the surface temperature between 300 K and 1000 K for a surface pressure of 100 bar, Thomas and Madhusudhan (2016) showed that this can cause a 25% difference

in radius, assuming 30% H_2O by mass above an Earth-like rocky core. The inclusion of vapour and supercritical layers, considering adiabatic temperature structures, has the largest impact on the planetary radius. Steam-dominated atmospheres, proposed some decades before (Kuchner, 2003), have been shown by other studies to inflate the radius of irradiated sub-Neptunes, suggesting that a H_2-rich envelope may not be necessary to explain the large radii of these sub-Neptunes (Mousis et al., 2020; Aguichine et al., 2021).

The wide diversity of water-rich sub-Neptune interiors was also subsequently explored by Nixon and Madhusudhan (2021). Building on the work of Thomas and Madhusudhan (2016), they additionally included the effect of an H_2/He atmosphere atop the water-rich interior, along with the potential for mixed H_2/H_2O envelopes. It has been shown that H_2O and H_2 are expected to be fully miscible across a wide pressure/temperature range, relevant to warm planetary atmospheres (e.g. Soubiran and Militzer, 2015; Gupta et al., 2025).

As discussed in Section 1.3.3 the H_2O EOS is not well known at high-pressures. Recently, studies have proposed the existence of a new phase of high-pressure ice, known as ice VIIt (Grande et al., 2022). Considering this new data, Huang et al. (2021) investigated the effect of H_2O EOS choice on the inferred planetary radius. Their results indicated that the radii of water-rich planets may be larger than previous models suggested. To verify this, further study is required into the properties of ice VIIt and its phase boundary with ice X, as currently the EOS for ice VIIt is only constrained at 300 K.

1.4 Exoplanet Atmospheres

Revealing information about exoplanet interiors requires a deep knowledge of the planet's atmosphere, through both observation and theory. Figure 1.10 from Madhusudhan (2019) summarises the atmospheric processes taking place and the regions probed by different wavelengths of atmospheric observation, in addition to some possible temperature structures. In the following, we will outline some key atmospheric processes and observational methods relevant to the study of sub-Neptune interiors.

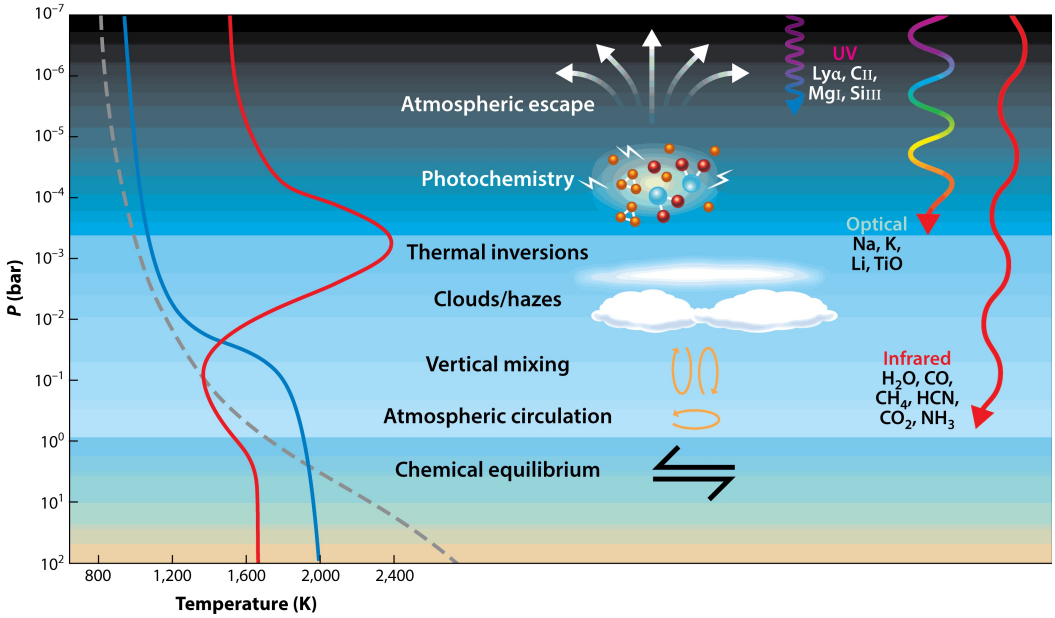

Fig. 1.10 Diagram from Madhusudhan (2019), showing an overview of the atmospheric processes, possible temperature structures, and chemical species in the atmospheres of exoplanets. The temperature structures show examples of a thermal inversion which could occur for a highly irradiated planet, the equivalent without a thermal inversion, and an example for a poorly irradiated planet. The regions of the atmosphere probed by different wavelengths are also shown, along with some chemical species that these observations would be sensitive to. JWST probes exoplanet atmospheres in the infrared.

1.4.1 Atmospheric Observation

Transmission Spectroscopy

In transmission spectroscopy, the exoplanet is observed during its primary eclipse, such that some light from the host star is able to pass through the planetary atmosphere. During primary transit, an annulus of planetary atmosphere is probed. For a tidally-locked planet with a permanent day and night side, transmission spectroscopy probes the region called the terminator, which is the boundary between the day and night sides. The wavelength dependence of light absorption by different chemical species in the planet's atmosphere results in a wavelength dependence to the light transmitted through the atmosphere. At wavelengths that are readily absorbed, the atmosphere appears more opaque, resulting in a larger transit depth. Therefore, at these wavelengths the transit depth, Δ, will now correspond to an apparent radius $R'_{\rm p} = R_{\rm p} + H(\lambda)$, for $H(\lambda)$ the effective height of the atmosphere at a given wavelength λ. If we now include an atmosphere in Equation 1.2, the transit depth can be written

$$\Delta(\lambda) \approx \left(\frac{R_\mathrm{p} + H(\lambda)}{R_\star}\right)^2 \approx \left(\frac{R_\mathrm{p}}{R_\star}\right)^2 + \frac{2H(\lambda)R_\mathrm{p}}{R_\star^2} \tag{1.17}$$

where $(H/R_\star)^2$ has been neglected since $H << R_p, R_\star$.

The effective atmospheric height H depends on the vertical extent of the atmosphere and the abundance of absorbing species in the atmosphere. The vertical extent can be described by the scale height, H_sc, which can be found by considering hydrostatic equilibrium in an isothermal atmosphere,

$$\frac{dP}{dz} = -\rho g \tag{1.18}$$

where P is the pressure, z is the height, ρ is the density and g is the surface gravity, assumed to be constant. The pressure can be expressed using the ideal gas law,

$$P = \frac{k_\mathrm{B}\rho T}{\mu} \tag{1.19}$$

where μ is the mean molecular weight and k_B is the Boltzmann constant. Combining these equations results in an expression for the scale height:

$$H_\mathrm{sc} = \frac{k_\mathrm{B}T}{\mu g} \tag{1.20}$$

Spectral features in a transmission spectrum are largest for low mean molecular weight atmospheres and low surface gravities, i.e. for large, hot planets, such as hot Jupiters. Large planets have historically been the focus for transmission spectroscopy studies, with the first transmission spectroscopy observations of the hot Jupiter HD 209458 b using HST (Charbonneau et al., 2002).

In this thesis, to inform our internal structure modelling we will be largely concerned with the findings from transmission spectra of sub-Neptunes. In Figure 1.11 we show an example of such a transmission spectrum for the hydrogen-dominated atmosphere of the temperate sub-Neptune K2-18 b from Madhusudhan et al. (2023b). This spectrum was obtained using two transits, one observed with each of JWST NIRISS SOSS and NIRSpec G395H, spanning 0.8-5.2 μm. A summary of sub-Neptune observations using JWST will be provided in Section 1.5.4.

Emission Spectroscopy

In emission spectroscopy, the planet is observed when it is close to secondary eclipse. In this configuration, the planet's dayside is visible to the observer, while during

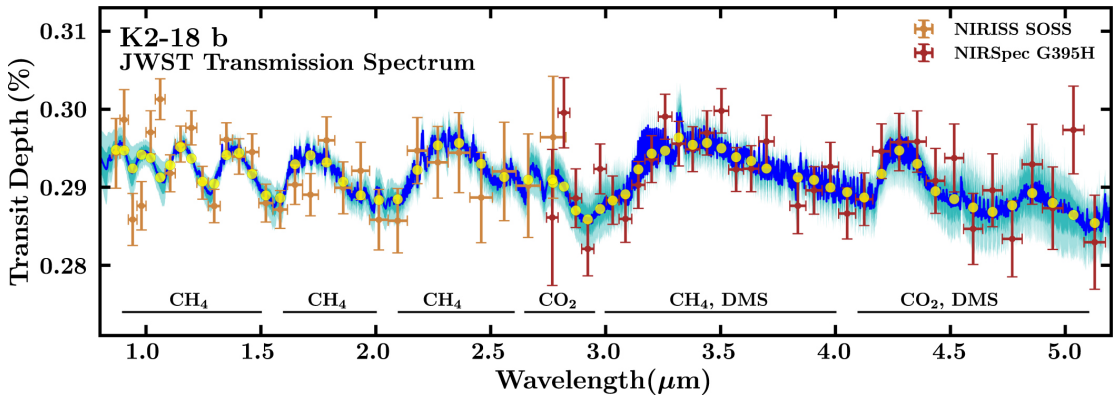

Fig. 1.11 Figure from Madhusudhan et al. (2023b), showing the transmission spectrum of the temperate sub-Neptune K2-18 b. The spectral data (binned for clarity) taken with NIRISS and NIRSpec G395H are shown alongside the retrieved model fit. The retrieved spectrum is shown in blue, and the contours show the 1σ and 2σ intervals.

secondary eclipse, only the stellar spectrum is visible. Therefore, by taking the ratio of the detected flux just before and during secondary eclipse, the emission spectrum of the planet can be obtained. The ratio of this flux can be expressed $f_\mathrm{p}/f_\star$, and can be approximated by assuming both stellar and planetary emission to be blackbodies:

$$\frac{f_\mathrm{p}}{f_\star} = \frac{R_\mathrm{p}^2}{R_\star^2}\frac{B_\lambda(T_\mathrm{p})}{B_\lambda(T_\star)} \tag{1.21}$$

where $T_\star$ is the effective stellar temperature, T_p is the effective temperature of the planet's dayside and $B_\lambda(T)$ is the Planck function:

$$B_\lambda(T) = \frac{2hc^2}{\lambda^5}\frac{1}{e^{(hc/\lambda k_B T)} - 1} \tag{1.22}$$

where h is the Planck constant and c is the speed of light. The Planck function describes the spectral radiance at a given wavelength λ for a blackbody with temperature T.

From Equation 1.21 it can be seen that the flux ratio will be greater for large, hot planets. It can also be inferred that the flux ratio will be larger at longer wavelengths, since $B_\lambda(T_\mathrm{p})$ peaks at a longer wavelengths than $B_\lambda(T_\star)$, owing to $T_\star > T_\mathrm{p}$. In the very long wavelength limit, the Rayleigh Jeans approximation can be used. In this case, $\lambda >> hc/k_\mathrm{B}T_\mathrm{p}$ such that the observed flux ratio is well approximated by

$$\frac{f_\mathrm{p}}{f_\star} \rightarrow \frac{R_\mathrm{p}^2 T_\mathrm{p}}{R_\star^2 T_\star} \tag{1.23}$$

i.e. a constant value.

Approximating the star and planet as blackbodies is, however, not a perfect assumption. In reality, the presence of chemical species in the planetary atmosphere will cause spectral features that deviate from the blackbody spectrum, especially for non-isothermal atmospheres, allowing for constraints on the atmospheric composition to be placed. Early examples of this were carried out for hot Jupiters (e.g. Barman, 2008; Charbonneau et al., 2008; Grillmair et al., 2008; Kreidberg et al., 2014b), and recently has been shown to be possible for terrestrial planets with JWST (e.g. Xue et al., 2024). Additionally, emission spectroscopy is an important tool for determining the temperature structure in the atmosphere (e.g. Haynes et al., 2015; Evans et al., 2017).

Phase Curve Observations

A phase curve observation entails measuring the radiation emitted from a planet throughout its orbit (e.g. Harrington et al., 2006; Knutson et al., 2007; Snellen et al., 2009; Crossfield et al., 2010). The planet does not have to transit to be observed via this method, however this technique is often used for transiting planets in tandem with emission and transmission spectroscopy. Phase curve observations can be photometric (e.g. Snellen et al., 2009), or, more informatively, spectroscopic (e.g. Stevenson et al., 2014). Phase curve spectroscopy permits longitudinal mapping of the temperature structure, composition and cloud/hazes in the planetary atmosphere. With JWST, phase curve observations have been made for a range of exoplanets, from hot Jupiters (e.g. Bell et al., 2024) to sub-Neptunes (e.g. Kempton et al., 2023).

High Resolution Ground-Based Spectroscopy

High resolution spectroscopy can be conducted for both transiting and non-transiting exoplanets, using ground-based telescopes (e.g. Snellen et al., 2010; Birkby et al., 2013; Brogi et al., 2018). This method involves observing the star/planet system throughout the orbit, allowing planetary spectral features to be identified due to the Doppler shift between the star and planet. Typically the analysis is conducted using a cross-correlation technique (e.g. Brogi et al., 2018). Historically, ground-based high-resolution spectroscopy was limited to large planets, of around Jupiter's mass (e.g. Snellen et al., 2010; Birkby et al., 2013; Brogi et al., 2018; Pelletier et al., 2023; Nortmann et al., 2025). However, recently it was shown that these techniques can be successfully applied to smaller mass planets, of Neptune mass (Dash et al., 2024; Grasser et al., 2024) down to sub-Neptune mass (Cabot et al., 2024; Parker et al., 2025).

1.4.2 Atmospheric Processes and Modelling

Energy Transport

For an irradiated planet, the sources of energy in the atmosphere are the radiation from the host star and the internal energy from the deep planetary interior – the latter was discussed in Section 1.3. Energy is also lost to space through escaping radiation.

Within the atmosphere, the transport of energy predominantly takes place by radiative or convective transport. Which of these mechanisms dominates depends on a key property, the optical depth τ_v. This describes how much the radiation will be affected by the atmospheric composition, and is defined as

$$\tau_v(z_0) = -\int_{z_0}^{\infty} (\kappa_v + \sigma_v)\rho \, dz \tag{1.24}$$

where κ_v is the absorption cross-section per unit mass, σ_v is the scattering cross-section per unit mass, and z is the altitude. τ_v is low in the upper regions of the planetary atmosphere, where the density is lower. Radiative energy transport will typically occur in these regions. In contrast, τ_v is high in the deeper regions of the atmosphere, where the density is higher. These optically-thick regions have inefficient radiative energy transport, hence convection tends to dominate. The conditions for convection are described in terms of the Schwartzchild criterion:

$$\left|\frac{d\ln T}{d\ln P}\right| \geq \frac{\gamma - 1}{\gamma} \tag{1.25}$$

where here $\gamma = c_\mathrm{p}/c_\mathrm{v}$ for c_p and c_v the specific heat capacities at constant pressure and volume. The radiative-convective boundary is the region of the atmosphere where the dominant energy transport mechanism changes from radiative to convective.

However, there are conditions where convection is prevented from occurring. This can occur when there's a compositional gradient due to, for instance, condensation in the atmosphere. In the case of hydrogen-dominated atmospheres, the presence of sufficient water vapour in the atmosphere can inhibit convection, forming a super-adiabatic layer near the surface (Guillot, 1995; Leconte et al., 2017; Markham et al., 2022; Leconte et al., 2024). This occurs because condensing water increases the mean molecular weight of a warm, rising air parcel, reducing the buoyancy of the parcel, and stopping it rising. Such cases of convective inhibition have been suggested to be relevant for hycean worlds, depending on the planetary albedo (e.g. Innes et al., 2023; Leconte et al., 2024). The albedo is significantly driven by clouds and hazes, which can have a substantial impact on the atmospheric temperature structure.

Self-consistent one-dimensional atmospheric models can be used to calculate the pressure-temperature structure in a planetary atmosphere, based on the energy sources and atmospheric composition (e.g. Malik et al., 2017; Gandhi and Madhusudhan, 2017; Piette and Madhusudhan, 2020). These models typically solve the equations for radiative transfer under radiative-convective, thermochemical, and hydrostatic equilibrium. Three-dimensional general circulation models (GCMs), which solve fundamental fluid dynamics and thermodynamics equations, are also used to study atmospheric dynamics and convection (e.g., for sub-Neptunes, Christie et al., 2022; Innes et al., 2023; Barrier and Madhusudhan, 2025).

Atmospheric Chemistry

The most simplistic treatment of atmospheric chemistry is under the assumption of thermochemical equilibrium. In this scenario, the chemical abundances are determined by the minimisation of the Gibbs free energy, and hence depend on the temperature structure and the elemental abundance ratios. However, this is only a reasonable approximation for the hottest exoplanets, such as hot Jupiters, or in the deeper, hotter regions of thick envelopes (e.g. Venot et al., 2012; Madhusudhan et al., 2016).

There are a variety of disequilibrium processes in exoplanet atmospheres that shift the composition from thermochemical equilibrium, including photochemistry (e.g. Miller-Ricci Kempton et al., 2012; Hu et al., 2012; Moses, 2014), vertical mixing and quenching (e.g. Visscher and Moses, 2011; Line et al., 2011; Madhusudhan and Seager, 2011), and atmospheric escape (e.g. Moses et al., 2011; Luger and Barnes, 2015). Vertical mixing can take place in planetary atmospheres via molecular diffusion and eddy diffusion; the latter is parameterised by K_{zz}, the eddy diffusion coefficient. This can transport chemical species produced in the deep atmosphere to the upper atmosphere. The process of "quenching" describes where this occurs faster than the thermochemical processes in the cooler, upper atmosphere (e.g. Moses, 2014). Photochemistry, caused by ionising radiation from the planet's host star, can significantly affect the composition of the high-altitude atmosphere, which can result in the breakdown of chemical species, depleting them, and the formation of new species from the reaction products.

Haze particles are often formed through photochemistry (e.g. Trainer et al., 2006; He et al., 2018), while clouds are formed by condensation. For sub-Neptunes, the properties of clouds and hazes can have significant effect on the atmospheric temperature structures (e.g. Morley et al., 2015; Piette and Madhusudhan, 2020), in addition to affecting the observed transmission spectra (e.g. Kreidberg et al., 2014a; Kawashima et al., 2019; Constantinou and Madhusudhan, 2022).

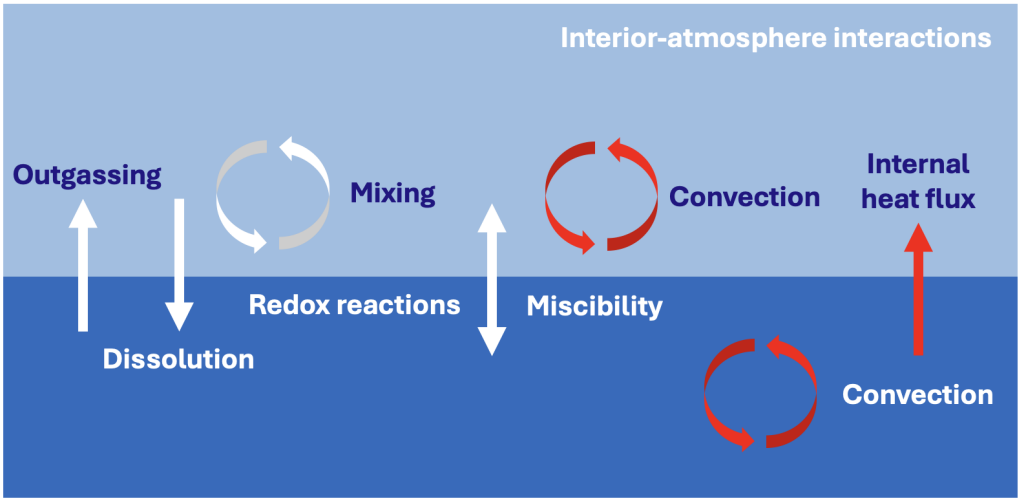

Fig. 1.12 Schematic of possible atmosphere-interior interaction processes relevant to sub-Neptunes.

For exoplanets with a distinct surface, interactions between the surface and atmosphere may have a significant impact on the atmospheric chemistry. Figure 1.12 shows a schematic of some of these processes. Outgassing of volatiles from a planet's interior has been studied extensively in the context of small, rocky planets (e.g. Kite et al., 2016; Schaefer and Fegley, 2017), forming secondary atmospheres. The dissolution of chemical species from the atmosphere into the interior becomes important for non-inert surfaces such as a magma ocean or liquid water ocean. Interactions between a magma ocean and the atmosphere have been considered for terrestrial atmospheres (Schaefer et al., 2016; Schaefer and Fegley, 2017; Daviau and Lee, 2021; Gaillard et al., 2022; Tian and Heng, 2024) and hydrogen-rich atmospheres (Kite et al., 2019, 2020; Schlichting and Young, 2022; Misener et al., 2023; Charnoz et al., 2023; Falco et al., 2024; Shorttle et al., 2024; Tian and Heng, 2024). The exchange of chemical species with a liquid water ocean has not been extensively studied beyond Earth-like scenarios.

In addition to signatures of surface-atmosphere interactions, the presence of a shallow surface can be inferred by the presence or lack of chemical species being recycled in the deep atmosphere (e.g. Yu et al., 2021; Hu et al., 2021; Tsai et al., 2021). Thermochemical equilibrium in the deep atmosphere can recycle photochemical products of, for instance, CH_4 and NH_3 back to these forms. Whereas, in the presence of a shallow surface this replenishment may not be able to take place.

Atmospheric Retrieval

Atmospheric retrievals are a method to infer atmospheric properties from spectroscopic data of a planetary atmosphere (Madhusudhan and Seager, 2009). A parametric forward model is used to describe the atmosphere, which is coupled to a Bayesian parameter estimation algorithm that determines the posterior probability distributions for the parameters of this model. In current retrieval codes, the Bayesian parameter estimation is often carried out using the Nested Sampling algorithm (Feroz et al., 2009). For transmission spectra, the commonly retrieved variables are the abundances of the included chemical species, parameters describing the atmospheric pressure-temperature profile, parameters to model clouds and hazes, and the planetary radius or reference pressure (e.g. MacDonald and Madhusudhan, 2017; Pinhas et al., 2018; Mollière et al., 2019; Al-Refaie et al., 2021; Constantinou and Madhusudhan, 2024). The forward-model component of the retrieval can additionally be used to produce transmission spectra for different atmospheric compositions. This is useful for making predictions for future observations allowing the generation of simulated data on which a retrieval could be performed (e.g. Greene et al., 2016; Mollière et al., 2017; Constantinou and Madhusudhan, 2022).

1.5 Sub-Neptune Exoplanets

In this thesis, we will use the term "sub-Neptune regime" to refer to the whole population of planets between the size of Earth and Neptune, ∼1-4 $R_\oplus$, including super-Earths and sub-Neptunes. There is some inconsistency in the literature, with "sub-Neptune" and "mini-Neptune" sometimes used interchangeably (e.g. as pointed out by Bean et al., 2021). In this thesis, we use "mini-Neptune" to refer to water-rich sub-Neptunes with no distinct surface, with "sub-Neptune" encompassing the broader range of possible volatile-rich interiors.

Planets in the sub-Neptune regime are the most abundant class of exoplanets that have been detected to date (e.g. Fressin et al., 2013; Fulton and Petigura, 2018a). With no analogue in the solar system, sub-Neptune planets provide a unique window into planetary formation and evolution processes. The densities of these planets span a wide range of potential interior compositions, varying in mass fractions of volatiles including water and hydrogen. Sub-Neptunes have gained significant attention in recent years due to being larger and hence typically more conducive to detection and atmospheric observation than Earth-like exoplanets (e.g. Madhusudhan et al., 2020). Hydrogen-rich, low mean molecular weight (MMW) atmospheres in particular are easier

to observe through techniques such as transit spectroscopy. As shown in Section 1.4.1, the atmospheric scale height is larger for these lower MMW atmospheres, which results in greater amplitude spectroscopic features in a planetary transmission spectrum.

1.5.1 Radius Valley

A key feature of the sub-Neptune population is the radius valley: the observed dearth of planets with radii $\sim 1.5 - 2.0$ $R_\oplus$, which was revealed in the Kepler population, after accounting for observational biases (Fulton et al., 2017; Fulton and Petigura, 2018b). The bimodal distribution in radius was found to have a minimum around 1.8 $R_\oplus$ (Fulton et al., 2017), with the location of the radius valley varying with orbital period (e.g. Van Eylen et al., 2018). The radius valley position has also been shown to vary with host star mass, whereby the distribution shifts to smaller radii for lower mass stars (Fulton and Petigura, 2018a; Cloutier and Menou, 2020).

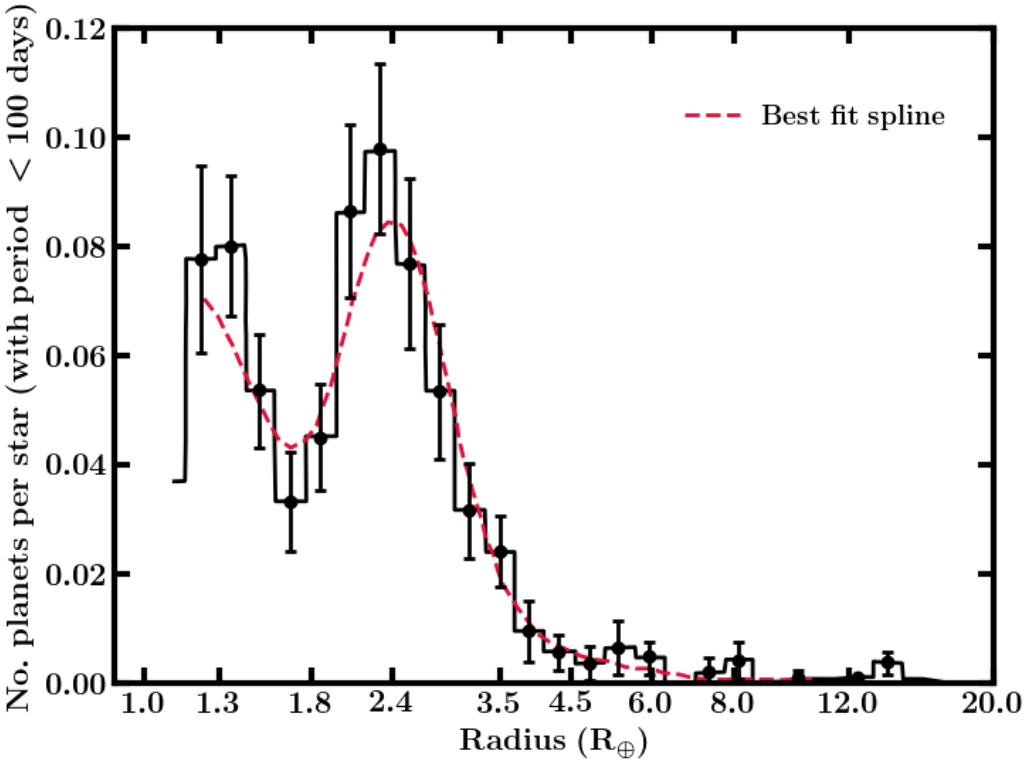

Fig. 1.13 Corrected histogram of planetary radii with orbital periods less than than 100 days. The dashed line show the best-fit spline model. This figure is adapted from Fulton et al. (2017).

The small radius population is widely accepted to be mostly rocky super-Earths with a secondary atmosphere or no atmosphere (e.g. Owen and Wu, 2013; Venturini

et al., 2020). The nature of the sub-Neptune population remains debated, with two broad categories of explanation. The first explanation relies on mechanisms for loss or retention of the primary H/He atmosphere (e.g. Owen and Wu, 2017; Gupta and Schlichting, 2019, 2020; Rogers and Owen, 2021). We will refer to this as the gas dwarf hypothesis. The second explanation suggests an inherent difference in composition, with the larger radius planets possessing significant water mass fractions (e.g. Zeng et al., 2019; Mousis et al., 2020). We will refer to this as the water world hypothesis.

In the gas dwarf hypothesis, the rocky super-Earth population and the larger sub-Neptune population both formed from progenitors that had accreted thick H_2-dominated atmospheres on formation (e.g. Lee et al., 2014; Ginzburg et al., 2016). Atmospheric escape processes then differentially shape the population, with the envelopes of smaller mass planets closer to their stars stripped, producing super-Earths. There are a number of possible contributing mass loss mechanisms: boil-off (Owen and Wu, 2016; Ginzburg et al., 2016), core-powered mass loss (e.g. Ginzburg et al., 2018; Gupta and Schlichting, 2020) and photoevaporation (e.g. Owen and Wu, 2013; Lopez and Fortney, 2013). In earlier works, these mechanisms had been considered in isolation. For instance, photoevaporation was explored in numerous studies (e.g. Owen and Wu, 2013, 2017; Rogers and Owen, 2021). In this mechanism, planets with thick H/He envelopes evolve towards a stability point, and planets with envelopes thinner than this undergo runaway loss via photoevaporative erosion. Studies similarly considered core-powered mass loss, where the planet's retained energy from formation drives atmospheric loss (Ginzburg et al., 2018; Gupta and Schlichting, 2020). Recent work has investigated the combined effect of photoevaporative and core-powered mass loss (Owen and Schlichting, 2024), suggesting that the former dominates for higher gravity planets with lower $T_{\rm eq}$ and the latter dominates for lower gravity and higher $T_{\rm eq}$.

In the water world hypothesis, the super-Earth population and the sub-Neptune population form via distinct pathways: the rocky population forms in the inner protoplanetary disk, while the larger sub-Neptune population forms beyond the water ice line. This population beyond the ice line hence accretes large volumes of ice, before migrating inwards (e.g. Mordasini et al., 2009; Venturini et al., 2016; Zeng et al., 2019; Mousis et al., 2020; Burn et al., 2024). It has been predicted that water worlds may be more prominent around M dwarfs than more massive stars, due to the proximity of the water-ice line to the star, potentially providing more ices for forming sub-Neptunes close to their observed orbital radii. This is, however, yet to be confirmed through observations (Rogers et al., 2023; Ho et al., 2024).

Modelling efforts for the competing hypotheses show that both can reproduce many aspects of the observed population. This includes trends across planetary mass, radius, orbital period, and stellar mass (e.g. Gupta and Schlichting, 2019; Rogers and Owen, 2021; Burn et al., 2024). Studies have also suggested a combination of both mass loss and water-richness may be required to explain the sub-Neptune population (e.g. Venturini et al., 2020). Gaining conclusive observational evidence for either mechanisms is challenging to obtain, given the vast uncertainties in the characterisation of exoplanet interiors. Rogers (2025) suggests the characterisation of young sub-Neptunes as a pathway to distinguishing the gas dwarf and water world hypotheses for this population, through their differing mean molecular weight atmospheres at early ages.

1.5.2 Compositional Degeneracy of Sub-Neptunes

In Section 1.3.4 we introduced the concept of compositional degeneracy, whereby planets of identical mass and radius can have vastly different compositions (e.g. Valencia et al., 2007a; Rogers and Seager, 2010a; Valencia et al., 2013; Otegi et al., 2020). For sub-Neptunes, where the bulk density requires some amount of water and/or hydrogen, there are a wide range of possible compositions with varying fractions of volatiles.

In Figure 1.14 we show the M-R diagram from Madhusudhan et al. (2020) for the temperate sub-Neptune K2-18 b. Prior to this study, it had been established that the atmosphere of K2-18 b was hydrogen-dominated via transmission spectroscopy with the Hubble Space Telescope (HST) (Benneke et al., 2019; Tsiaras et al., 2019). Using this data and their internal structure model, Madhusudhan et al. (2020) established that the atmospheric and bulk properties of K2-18 b were consistent with a wide range of interior compositions and surface conditions. These included a water-poor gas dwarf scenario (Case 1 in Figure 1.14), a mini-Neptune scenario (Case 2), and a water-rich scenario with a thin H_2-rich atmosphere overlying an ocean (Case 3). Case 3 was the impetus for the proposal of the new class of sub-Neptune, hycean worlds, which will be discussed in depth in Section 1.5.3. Figure 1.14 is a useful demonstration of the compositional degeneracy of temperate ($T_{\rm eq} \lesssim 400$ K) sub-Neptunes, with these three demonstrative cases equally able to fit the median mass and radius of K2-18 b. The possible compositions are, of course, even more numerous when considering the uncertainties in the measured mass and radius.

In Figure 1.15 we show cross-sections for some possible sub-Neptune interiors, including mini-Neptune, hycean world, and gas dwarf scenarios. In this thesis we will explore these classes of interior in more detail.

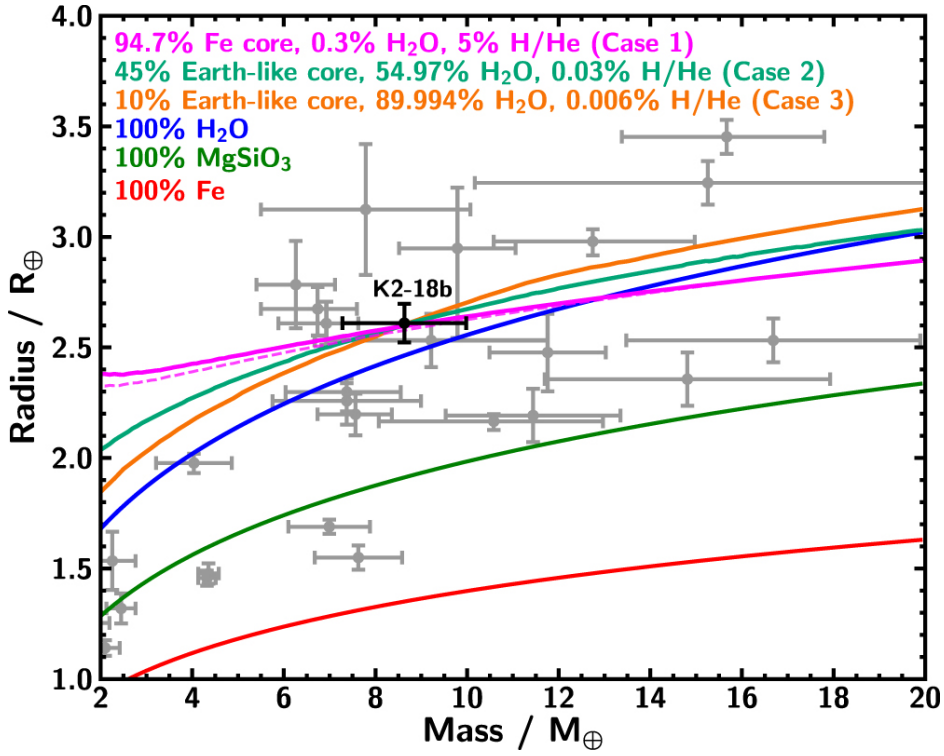

Fig. 1.14 Mass-radius (M-R) relations that match the mass and radius of K2-18 b, shown by the black data point. These are shown alongside some homogeneous M-R relations. Exoplanets with $T_{\rm eq} \leq 1000$ K and masses and radii known to better than 3σ are also shown in grey. This figure is from Madhusudhan et al. (2020).

The work of Madhusudhan et al. (2020), establishing the possible surface conditions for each interior scenario – which were, in this case, the pressure, temperature and phase of water – showed one example of a connection between atmospheric and interior modelling based on observational data. Connecting sub-Neptune atmospheric observations, atmospheric models and interior models will be a consistent theme throughout this thesis, as a crucial mechanism for easing structural degeneracies.

1.5.3 Habitability in the Sub-Neptune Regime

The habitability of a planet refers to the potential for it to host conditions suitable for life. At a minimum, this is generally considered to include the maintenance of liquid water, an energy source, and a source of nutrients. Naturally, our considerations of life's requirements are based on our own planet – we have no other data point. Studies have long considered the habitability of rocky planets, i.e. Earth-like planets or super-Earths (e.g. Kasting et al., 1993; von Bloh et al., 2007; Heller and Armstrong,

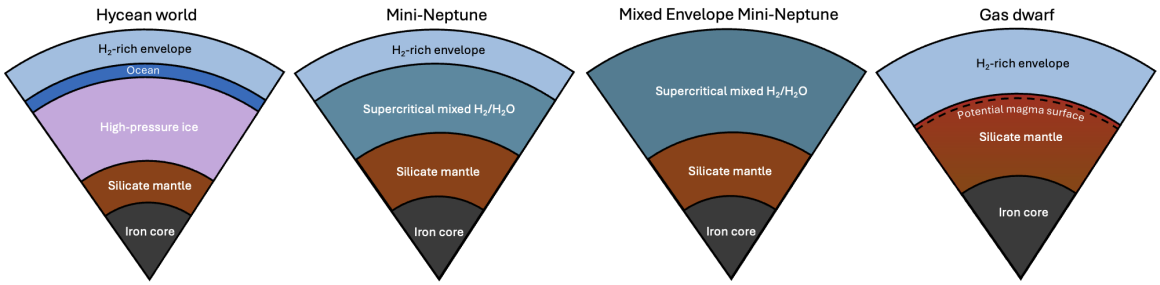

Fig. 1.15 Cross-sections of possible classes of interior for sub-Neptunes. These include hycean worlds, mini-Neptunes, and gas dwarfs. The planetary layers are shown as fully differentiated and not to scale, for visual clarity.

2014; Meadows and Barnes, 2018). Typically, these studies require the planet to possess liquid water in contact with rock, which on Earth is necessary for silicate weathering to maintain the carbonate-silicate cycle, an important process in climate regulation (e.g. Rushby et al., 2018). Considerations of water-rich super-Earths by extension therefore assumed rock/water contact a necessity for habitability (e.g. Alibert, 2014; Noack et al., 2016). In recent years, studies of habitability and the search for biosignatures have broadened to include exoplanets with more varied conditions, including the presence of high-pressure ice layers (e.g. Kalousová and Sotin, 2018; Hernandez et al., 2022; Lebec et al., 2023; Madhusudhan et al., 2023a) and hydrogen-dominated atmospheres (e.g. Pierrehumbert and Gaidos, 2011; Madhusudhan et al., 2021), both of which are highly relevant to the sub-Neptune regime.

Habitable Zones

The habitable zone (HZ) describes the range of orbital distances around a host star where a planet is able to sustain liquid water, and provides a useful first estimate of whether a planet could host habitable conditions. In their seminal work, Kasting et al. (1993) used a one-dimensional climate model to calculate the extent of the HZ as a function of host star spectral type. It was shown that the HZ for M dwarf stars is smaller and closer in than for Sun-like stars (Kasting et al., 1993). This calculation was performed for $N_2/CO_2/H_2O$ atmospheres – i.e. high MMW, Earth-like atmospheres – and the result is known as the classical HZ. The inner edge of the HZ is determined by the runaway greenhouse effect causing ocean evaporation, while the outer edge is determined by CO_2 condensation. The continuous HZ takes into account the evolution of the host star in the extent of the HZ over time, which is an important concept for assessing whether a planet will remain in the HZ for a sufficiently long time to sustain

life. For smaller, cooler stars than our Sun, the HZ is closer to the host star, with a longer-lived continuous HZ (Kasting et al., 1993).

Pierrehumbert and Gaidos (2011) considered an extension to the classical HZ by considering hydrogen-rich atmospheres. In this scenario, collision-induced absorption means that hydrogen acts as an effective greenhouse gas, and can allow the maintenance of surface temperatures that would allow liquid water to exist on a rocky surface at much wider orbits. Below, in Section 1.5.3, we will discuss another development to the classical HZ, which considers a hydrogen-rich atmosphere atop a surface water ocean with a water-rich interior – i.e. a hycean world.

Hycean Worlds

As discussed above, coupling atmospheric and internal structure models for the temperate sub-Neptune K2-18 b showed that this planet could host a liquid water ocean at its surface beneath the H_2-rich atmosphere (Madhusudhan et al., 2020). This prompted the conceptualisation of hycean worlds – a class of sub-Neptune with habitable pressure and temperature liquid water oceans beneath thin hydrogen-rich atmospheres (Madhusudhan et al., 2021).

In their seminal work, Madhusudhan et al. (2021) showed that hycean worlds could broaden the conditions for habitability, in both planetary radius and orbital distance (i.e. the HZ). The M-R plane for hycean worlds was calculated using an internal structure model, through a similar approach to that used for K2-18 b (Madhusudhan et al., 2020). The calculation considered masses in the range $1 - 10$ $M_\oplus$, and H_2O mass fractions (x_{H_2O}) from $10 - 90\%$. 10% was chosen as the minimum to allow for a H_2O reservoir that would have withstood photodissociation and atmospheric escape over Gyr timescales. The planetary surface is defined as the interface between the H_2 atmosphere and the H_2O layer, referred to as the H_2/H_2O boundary or HHB. Habitable HHB conditions were considered to be T_{HHB} between $300 - 400$ K and P_{HHB} from $1 - 1000$ bar, motivated by the range of conditions that host life on Earth (Rothschild and Mancinelli, 2001; Merino et al., 2019). The resulting M-R plane from Madhusudhan et al. (2021) is shown in Figure 1.16. The radii of hycean planets are shown to span from ~ 1 $R_\oplus$ up to 2.6 $R_\oplus$, for masses $1 - 10$ $M_\oplus$. The upper boundary of the hycean M-R corresponds to the largest radius for a given mass – i.e. the largest H_2O mass fraction and the thickest H_2 envelope that allows for habitable surface conditions. In this calculation, this is $x_{H_2O} = 90\%$ with $T_{HHB} = 400$ K and $P_{HHB} = 3$ bar. Meanwhile, the lower boundary corresponds to the smallest radius for a given mass – i.e. the smallest x_{H_2O} and the thinnest H_2 envelope that allows for habitable surface conditions.

In this calculation, this is $x_{H_2O} = 10\%$, $T_{HHB} = 300$ K and $P_{HHB} = 1$ bar. In all cases, the composition of the rocky layers below the water layer was assumed to be Earth-like, with 67% by mass in silicates.

The extent of the hycean HZ was calculated for stellar types ranging from Sun-like to M dwarfs. The inner boundary represents the limiting conditions for a habitable pressure and temperature liquid water ocean to be present at the planetary surface. This was found to correspond to equilibrium temperatures (T_{eq}) up to ∼430 K, with the higher values of T_{eq} possible for cooler stars. The outer boundary was found to be arbitrarily large, due to the effectiveness of hydrogen as a greenhouse gas. We show the hycean HZ from Madhusudhan et al. (2021) in Figure 1.17. This plot shows the HZ for two further potential categories of hycean world, in addition to the standard case as described thus far. The dark hycean case has inefficient day-night redistribution, such that the nightside of higher T_{eq} planets could host habitable conditions. Cold hyceans are those with no stellar irradiation, i.e. with large orbital radii or free-floating planets.

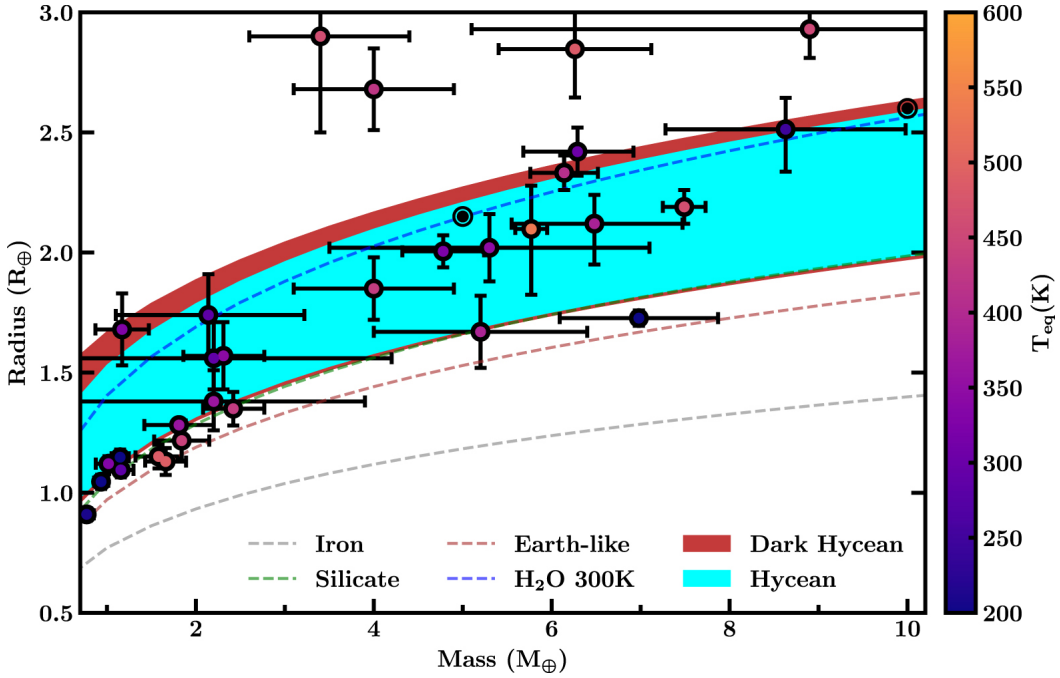

Fig. 1.16 Hycean mass-radius plane from Madhusudhan et al. (2021). The mass-radius relations are from Seager et al. (2007). The data points show planets with equilibrium temperatures <600 K

Madhusudhan et al. (2021) identified 11 hycean candidates, based on their mass, radius and equilibrium temperature. This list has been extended as more sub-Neptunes have been detected (e.g. TOI-1468 c, Chaturvedi et al., 2022). In recent years, the first JWST transmission spectra have been observed for hycean candidates. Atmo-

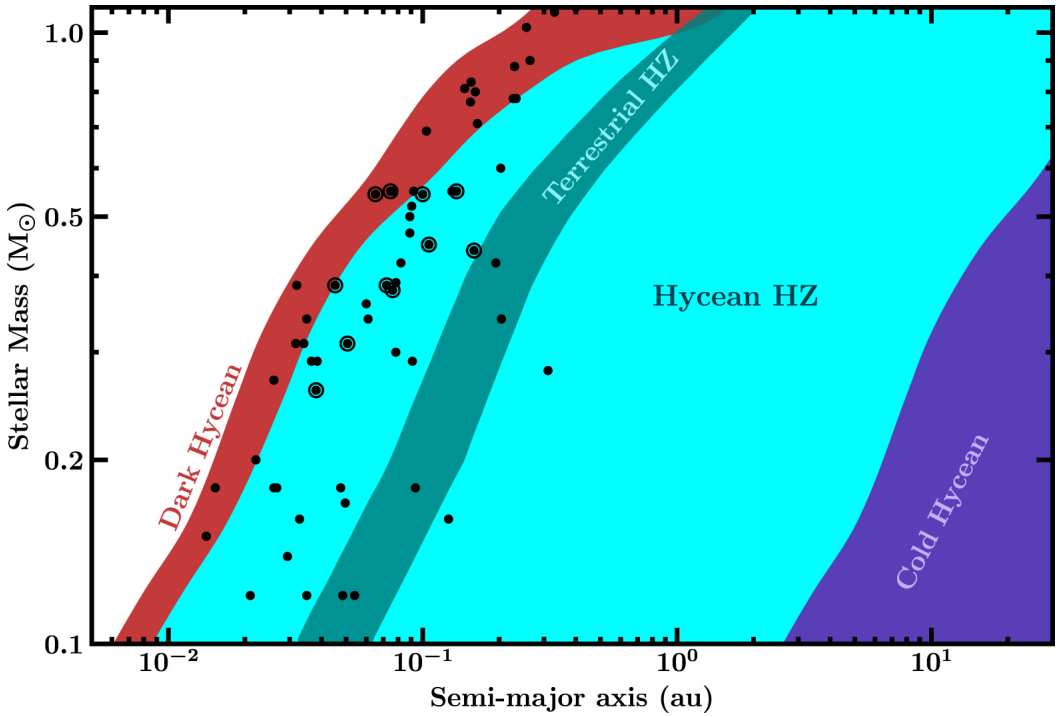

Fig. 1.17 Hycean habitable zone as a function of stellar mass. The turquoise represents the hycean habitable zone. The purple shows the extended habitable zone for cold hyceans, i.e. free-floating planets. The red shows the dark hycean habitable zone, where only the nightside hosts habitable conditions. This figure is from Madhusudhan et al. (2021).

spheric retrievals on these observations have revealed detections of carbon-bearing molecules including CH_4 and CO_2 (e.g. Madhusudhan et al., 2023b; Holmberg and Madhusudhan, 2024; Benneke et al., 2024). The large atmospheric scale height of their hydrogen-rich atmospheres make hycean candidates promising candidates for detailed atmospheric characterisation in this way, including the potential for biosignature detections (Madhusudhan et al., 2021, 2023b, 2025).

1.5.4 JWST Observations of Sub-Neptunes

Multiple sub-Neptunes have so far been observed with JWST. We showed one example of a near-infrared (NIR) JWST transmission spectrum of a temperate sub-Neptune in Section 1.4.1, for K2-18 b from Madhusudhan et al. (2023b). This study reported detections of CH_4 and CO_2, along with non-detections of CO, H_2O and NH_3, which have been confirmed by additional NIR observations (Hu et al., 2025). K2-18 b has also been observed with MIRI (Madhusudhan et al., 2025). Based on both the NIR

and MIR observations, the possible presence of additional absorbing species has also been investigated (Madhusudhan et al., 2023b, 2025; Welbanks et al., 2025; Luque et al., 2025; Pica-Ciamarra et al., 2025). Other temperate sub-Neptunes observed with JWST include TOI-270 d (Benneke et al., 2024; Holmberg and Madhusudhan, 2024), which will be the focus of Chapter 4 of this thesis, and LHS-1140 b (Cadieux et al., 2024a; Damiano et al., 2024).

In addition to temperate sub-Neptunes (Madhusudhan et al., 2023b; Benneke et al., 2024; Holmberg and Madhusudhan, 2024), molecular detections have been made in the atmosphere of the hot sub-Neptune TOI-421 b (Davenport et al., 2025). The cloud and haze free atmosphere of TOI-421 b was shown to be consistent with the prediction that hydrocarbon haze production becomes inefficient for very high temperatures (Davenport et al., 2025). For the intermediate warm sub-Neptunes, it is expected that the clouds and hazes that readily form will mute spectral features. However, at the current precision, and with our current modelling of clouds and hazes, it is hard to distinguish this scenario from a high mean molecular weight atmosphere for a muted or featureless spectrum. Multiple warm sub-Neptunes have now been observed with JWST (Kempton et al., 2023; Wallack et al., 2024; Piaulet-Ghorayeb et al., 2024; Schlawin et al., 2024; Ohno et al., 2025; Teske et al., 2025; Ahrer et al., 2025), revealing often muted or featureless spectra. For example, the archetypal flat-spectrum sub-Neptune GJ 1214 b was observed using phase curve observations (Kempton et al., 2023) and transmission spectroscopy (Schlawin et al., 2024; Ohno et al., 2025). Overall, a high-metallicity atmosphere was suggested to best explain the observations.

We have entered an era where atmospheric observations of sub-Neptunes are now possible with JWST. The findings from these observational efforts are paving the way for the characterisation of sub-Neptune interiors, which will be the focus of this thesis.

1.6 Scope of this Thesis

In this thesis, we investigate the diversity of planetary interiors in the sub-Neptune regime. We focus on this regime for a number of reasons. In the current landscape, sub-Neptunes are proving to be the most promising class of small planet for observational studies. Beyond being conducive to atmospheric characterisation, detection studies have revealed they are the most abundant class of planet (e.g. Borucki et al., 2011). With the advent of JWST and the precise spectroscopic data for sub-Neptunes now available, studying the interiors of these planets is a timely avenue for gaining insight into their diversity, planet formation and evolution mechanisms, and habitability.

Given that there is no sub-Neptune analogue in the solar system, there is a wealth of information that can be gained about the possible diversity of exoplanets through the study of these planets. This can help to develop our understanding of planet formation and evolution mechanisms, through investigating the diversity of their planetary systems and the population-level trends. For instance, answering questions such as why our solar system lacks a sub-Neptune, and shedding light on the radius valley, the cause of which remains debated. The sub-Neptune regime has the potential for a huge diversity of interior compositions, ranging from water-poor to water-rich. The bulk densities of sub-Neptunes require some mass fraction of volatiles, including hydrogen and/or water. Determining the present-day compositions of these planets has important implications for formation and evolution models which suggest differing levels of water-richness among the population (e.g. Owen and Wu, 2017; Rogers and Owen, 2021; Venturini et al., 2020; Izidoro et al., 2022; Burn et al., 2024).

Furthermore, in recent years the possibility of sub-Neptune habitability has been explored, namely for hycean worlds (Madhusudhan et al., 2021). As discussed in the previous section, the larger size and larger atmospheric scale height of hycean worlds compared to rocky planets makes them more conducive to potential biosignature detection. Favourable conditions for observations applies more broadly for temperate sub-Neptunes with hydrogen-rich atmospheres, particularly those orbiting M dwarfs (e.g. Madhusudhan et al., 2023b; Holmberg and Madhusudhan, 2024; Benneke et al., 2024).

This thesis includes theoretical investigations into the interior and surface conditions possible for sub-Neptune exoplanets. We explore the diversity of planets in this regime, considering interior scenarios ranging from water-rich to water-poor, using a self-developed internal structure model specialised for sub-Neptunes. We additionally investigate the constraints that can be placed on the conditions of observed exoplanets through internal structure models coupled to atmospheric observations. In the following, we outline the scope of this thesis by chapter.

1.6.1 Ocean Conditions of Hycean Worlds

We begin with a theoretical exploration of the possible interior compositions and ocean depths for the class of potentially habitable sub-Neptune known as hycean worlds. These planets, characterised by liquid water oceans beneath thin hydrogen-rich atmospheres, have the potential to host habitable conditions across a wide phase space of planetary bulk parameters and orbital distances (Madhusudhan et al., 2021).

We use internal structure modelling to identify the possible interior compositions, surface conditions, and ocean depths for hycean worlds. We first describe our internal structure model, HyRIS. This model numerically solves the planetary structure equations to obtain the planetary radius using a shooting method. It utilises an equation of state for water that takes into account its complex phase behaviour, compiled from multiple sources across pressure-temperature space.

In this chapter, we focus on surface conditions that would permit habitable pressure and temperature conditions at the ocean surface. Beneath such an ocean, the typically large water mass fractions of hycean worlds would result in a transition from liquid to high-pressure ice. We use the internal structure model to calculate the theoretically predicted range of ocean depths for hycean worlds, which depends on the ocean surface temperature and the surface gravity. The model is then applied to five hycean candidates: K2-18 b, TOI-270 d, TOI-732 c, TOI-1468 c, and LHS 1140 b. For each planet, we explore the range of interior compositions that would allow for hycean conditions, and the corresponding pressure-temperature conditions at their surface.

1.6.2 Gas Dwarf Scenarios for Temperate Sub-Neptunes

For temperate sub-Neptunes, compositional degeneracies result in a range of potential interior scenarios, which vary in volatile mass fraction. The recent detections of carbon-bearing molecules in the atmospheres of multiple temperate sub-Neptunes (Madhusudhan et al., 2023b; Holmberg and Madhusudhan, 2024; Benneke et al., 2024) and the varying interpretations of the data (e.g. Shorttle et al., 2024; Wogan et al., 2024; Cooke and Madhusudhan, 2024; Luu et al., 2024) highlights the importance of robust evaluations of each potential interior scenario permitted by the data.

In this chapter we outline an end-to-end framework to evaluate the plausibility of gas dwarf scenarios for temperate sub-Neptunes and investigate their potential atmospheric diagnostics. Gas dwarfs are characterised by a thick hydrogen-rich atmosphere overlying a rocky interior, i.e. lacking significant water content. This framework includes internal structure modelling, atmospheric structure modelling, melt-atmosphere chemistry, photochemical modelling, and spectroscopic predictions. We use the framework to investigate the feasibility of a gas dwarf scenario for K2-18 b.

1.6.3 Interior and Surface Conditions of the Temperate Sub-Neptune TOI-270 d

In this chapter, we apply the internal structure model to the temperate sub-Neptune TOI-270 d, which was recently observed with JWST (Holmberg and Madhusudhan, 2024; Benneke et al., 2024). We use our model to explore the range of interior compositions and surface conditions possible for this planet, using constraints from atmospheric observations. Atmospheric temperature structures are calculated using the observed atmospheric abundances (Holmberg and Madhusudhan, 2024), which are used as inputs to the internal structure model. The planetary bulk properties permit a range of interior compositions, spanning hycean world, gas dwarf and mini-Neptune scenarios. For each of these scenarios, we place constraints on the possible compositions, namely the mass fractions of water, hydrogen, and rock. For mini-Neptune scenarios, we consider mixed hydrogen/water layers, due to the miscibility which has been shown to occur across a wide range of pressures and temperatures relevant to the deep planetary atmosphere (Soubiran and Militzer, 2015; Gupta et al., 2025).

1.6.4 Conclusions and Future Work

Finally, we summarise the preceding chapters of this thesis, and outline the directions for future work. These avenues include incorporating a more complex treatment of planetary materials in the internal structure model, and improving the coupling of the atmosphere and interior.

Chapter 2

Ocean Conditions of Hycean Worlds

Not a Greek God, nor old Latin expression
Simply a portmanteau: hydrogen, ocean

2.1 Introduction

Earth is the only environment in the universe known to host life. Therefore, it is logical that the search for habitable exoplanets and biosignatures began by focusing on Earth-like, rocky exoplanets (e.g. Kasting et al., 1993; Meadows and Barnes, 2018; Ramirez, 2018). However, the rapidly increasing number and diversity of detected exoplanets has prompted wider considerations for habitability studies and candidates for biosignature detections (e.g. Madhusudhan et al., 2021). Another related element is identifying conducive targets for atmospheric characterisation and biosignature detections based on our current and upcoming facilities. As discussed in Chapter 1, the larger sizes of sub-Neptunes compared to small, rocky, Earth-like exoplanets makes these planets more conducive to atmospheric characterisation via transit spectroscopy. Similar interest arises for planets transiting M dwarfs (e.g. Wunderlich et al., 2019; Tremblay et al., 2020), as a smaller host star results in a larger transit depth for a given planetary radius. Numerous sub-Neptunes transiting bright ($J < 10$ mag) M dwarfs have been discovered by recent transit surveys (e.g. Ricker et al., 2015; Günther et al., 2019; Hardegree-Ullman et al., 2020; Cloutier et al., 2020). Spectroscopic observations of these planets with the James Webb Space Telescope (JWST) provide exciting opportunities for detailed atmospheric characterisation and the potential for biosignature searches (e.g. Madhusudhan et al., 2023b).

As introduced in Section 1.5.3, a new class of habitable exoplanet within the sub-Neptune regime was proposed by Madhusudhan et al. (2021), known as hycean

worlds. These temperate planets are characterised by their deep H_2O oceans and H_2-rich atmospheres, and provide a new avenue for habitability studies. The impetus for hycean worlds came from the study of the habitable-zone sub-Neptune K2-18 b (Madhusudhan et al., 2020). By coupling atmosphere and interior models, they placed constraints on the composition and surface conditions of K2-18 b, finding that this planet could host liquid water at its surface beneath an H_2-rich atmosphere. Hycean worlds were shown to broaden the commonly considered limits of habitability, in mass, radius, temperature and orbital distance. Due to their H_2 atmospheres, the hycean habitable zone is significantly wider than the terrestrial habitable zone. Importantly, both the larger size and larger atmospheric scale height of hyceans relative to rocky planets of similar mass make them more promising targets for atmospheric spectroscopy and potential biosignature detections. Recent analysis of JWST transmission spectra of K2-18 b by Madhusudhan et al. (2023b) revealed strong detections of both CH_4 and CO_2, with a lack of key molecules including NH_3, suggesting the presence of a surface ocean, based on chemical arguments (Yu et al., 2021; Hu et al., 2021; Tsai et al., 2021; Madhusudhan et al., 2023a). We are in the exciting position where detailed atmospheric data for multiple temperate sub-Neptunes orbiting M dwarfs is accessible, with observations carried out in Cycles 1 and 2.

Internal structure modelling plays an important role in characterising sub-Neptunes, relating observable properties to possible interior compositions (e.g. Rogers and Seager, 2010b; Valencia et al., 2013; Dorn et al., 2017; Madhusudhan et al., 2020; Nixon and Madhusudhan, 2021; Huang et al., 2022). The sub-Neptune population is thought to contain a diverse range of interior compositions with varying proportions of volatiles including H_2O and H/He, with volatile-rich and volatile-poor populations separated by the radius valley (e.g. Fulton et al., 2017; Fulton and Petigura, 2018a). As we saw in Chapter 1, one of the key challenges in internal structure modelling of sub-Neptunes is compositional degeneracy, with a range of compositions able to explain a planet's observed mass and radius. In the era of JWST, interior constraints can be drastically improved via information revealed about exoplanet atmospheres, allowing us to gain more insight into the nature of these planets than ever before. Atmospheric observations provide the key in breaking the aforementioned degeneracies between possible interior compositions (e.g. Madhusudhan et al., 2020). For example, the presence of a steam atmosphere can be ruled out and an H_2-rich atmosphere can be established through transmission spectroscopy (e.g. Benneke et al., 2019; Tsiaras et al., 2019; Madhusudhan et al., 2020; Mikal-Evans et al., 2023). Even having established the presence of an H_2-rich atmosphere, hycean compositions can be degenerate with

rocky worlds with thick H/He envelopes, and with mini-Neptunes with large fractions of ices. Precise atmospheric data can allow the possible identification of hycean worlds among the sub-Neptune population. Based on photochemical models, Madhusudhan et al. (2023a) outlined a framework for diagnosing a hycean world using retrieved chemical abundances, considering the effect of the surface ocean on the atmospheric composition. Notably in recent work, Madhusudhan et al. (2023b) suggest the presence of a liquid H_2O surface on the hycean candidate K2-18 b.

The interiors of hycean worlds possess substantial fractions of H_2O, order 10s of % by mass (Madhusudhan et al., 2021), compared to $\sim 0.02\%$ for the Earth (Genda, 2016). Accurate internal structure modelling of H_2O-rich planets, including hycean worlds, requires taking into account the thermal behaviour of H_2O across the complex phase diagram (e.g. Thomas and Madhusudhan, 2016; Mousis et al., 2020; Huang et al., 2021; Nixon and Madhusudhan, 2021). As discussed in Section 1.3.3, this is achieved via a pressure and temperature dependent equation of state (EOS), which tends to be compiled from several data sources valid for different phases and/or regions of P-T space (e.g. Thomas and Madhusudhan, 2016; Nixon and Madhusudhan, 2021; Haldemann et al., 2020). At high pressures H_2O forms high-pressure ices, which would occur deep in hycean interiors – specifically, these are ice VI, VII and ice X (Noack et al., 2016; Nixon and Madhusudhan, 2021). The behaviour of high-pressure ices remains uncertain due to a lack of extensive experimental data, which can affect the accuracy of internal structure models for water-rich planets (e.g. Huang et al., 2021).

Several recent studies have investigated the internal structures and ocean depths of temperate water-rich sub-Neptunes. Nixon and Madhusudhan (2021) conducted internal structure modelling to examine the H_2O phase structure across a wide range of masses, compositions and surface conditions of such planets. Other studies have also explored the range of ocean depths on sub-Neptunes, under more specific assumptions (e.g. Léger et al., 2004; Sotin et al., 2007; Alibert, 2014; Noack et al., 2016). For instance, Alibert (2014) investigated cases avoiding high-pressure ice layers, and Sotin et al. (2007) assumed a fixed surface temperature of 300 K. The results of Nixon and Madhusudhan (2021) highlight the wide range of parameter space over which liquid water could exist at the surface of a planet, which suggests a diverse range of planets could host hycean conditions. They also investigated the key factors in determining ocean depth, finding this to be surface gravity and ocean base pressure (and hence surface temperature, due to the adiabatic temperature structure), and constrained the range of ocean depths possible across a wide phase space as functions of these.

In this chapter[1], we focus on the interiors of hycean worlds. For this purpose, we require habitable pressures and temperatures at the interface between the ocean and the H_2-rich atmosphere. Based on previous studies, we expect the depths to reach hundreds of times the depth on Earth. For example, Nixon and Madhusudhan (2021) find that depending on the planet's interior composition and mass, at surface temperatures of 300 K a planet can host oceans between 30-500 km deep. Similarly, depths of ∼100-400 km were found to be possible for the canonical hycean world based on K2-18 b in Madhusudhan et al. (2023a), assuming habitable surface conditions. Given the significant H_2O mass fractions expected in hycean worlds, the ocean base would occur at the transition to high-pressure ice, as opposed to a rocky ocean floor as on Earth, which could have implications for their habitability (Maruyama et al., 2013; Noack et al., 2016; Journaux et al., 2020b; Madhusudhan et al., 2023a). For example, the thick mantle of high-pressure ice on hycean worlds would prevent the weathering of the rocky core below, necessitating alternative methods of nutrient enrichment in the oceans. Madhusudhan et al. (2023a) explored the possible chemical conditions on hycean worlds, identifying feasible pathways to concentrate bioessential elements in hycean oceans. These include atmospheric condensation, external delivery and convective transport from the rocky core across the ice mantle.

The lack of sub-Neptunes in our own solar system and the ubiquity of exoplanets in this regime mean that there is a wealth of information to be gained from their study, on planet formation and evolution, in addition to habitability. As outlined in Section 1.5.1, the radius valley is the observed dearth of planets in the radius range ∼1.5-2 $R_\oplus$, which separates two subpopulations with bimodal peaks at ∼1.4 $R_\oplus$ and ∼2.4 $R_\oplus$ (Fulton et al., 2017; Fulton and Petigura, 2018a; Petigura, 2020). The low radius peak is commonly accepted to be largely rocky super-Earths, while the characteristics of the planets in the second peak remain debated, and link to their formation/evolution mechanism – specifically, the amount of water present. The position of the radius valley is dependent on both orbital period and stellar mass (Fulton and Petigura, 2018a), with the trend with stellar insolation reversing for M dwarfs compared to more massive stars (Cloutier and Menou, 2020). Formation mechanisms for the radius valley remain debated (e.g. Lopez et al., 2012; Owen and Wu, 2013, 2017; Gupta and Schlichting, 2019; Zeng et al., 2019; Mousis et al., 2020; Venturini et al., 2020; Rogers and Owen, 2021; Izidoro et al., 2022). The nature and formation of the sub-Neptune population remains an open question, with the permitted mass fraction for an H_2-rich atmosphere of a sub-Neptune varying by the assumed formation/evolution mechanism. Identifying

[1]The contents of this chapter are adapted from Rigby and Madhusudhan (2024).

the envelope mass fractions of the sub-Neptune population is hence important in testing these mechanisms. Furthermore, constraining the composition requirements of hycean worlds is an important step for investigating the formation/evolution pathway for this class of planet, which has yet to be studied in detail.

In this chapter we present an analysis of the possible conditions on hycean worlds using a selection of hycean candidates with JWST observations: TOI-270 d, TOI-732 c, TOI-1468 c, K2-18 b and LHS 1140 b. We use our internal structure model to estimate the range of possible ocean depths for these planets as hycean worlds, and the maximum mass fraction in H/He to allow habitable conditions. We also consider another end-member scenario, of a rocky planet with a deep H_2-rich atmosphere and no ocean, to constrain the overall upper limit for the H/He mass fraction. This scenario is what will be referred to as a "gas dwarf" in Chapter 3. We discuss the implications of the envelope mass fractions for sub-Neptune formation/evolution, and the effects of hycean conditions on the observable properties of these planets.

2.2 Methods

In this section we present an internal structure model for sub-Neptunes, HyRIS. We first describe the model and the functionality of the code. The specific assumptions made for the purpose of studying candidate hycean worlds are outlined. These include the adopted equation of state (EOS) and temperature profile used to describe each planetary component layer.

2.2.1 Internal Structure Model

Over the past two decades, a number of studies have developed internal structure models to study planetary interiors (e.g. Léger et al., 2004; Fortney et al., 2007; Seager et al., 2007; Sotin et al., 2007; Valencia et al., 2007a; Rogers and Seager, 2010a; Madhusudhan et al., 2012; Zeng and Sasselov, 2013; Thomas and Madhusudhan, 2016; Brugger et al., 2017; Madhusudhan et al., 2020; Nixon and Madhusudhan, 2021; Huang et al., 2022). Here we describe HyRIS, our internal structure model for sub-Neptunes, and how this is customised for the study of hycean worlds in this chapter.

The model solves the planetary structure equations under the assumption of spherical symmetry. The planetary structure equations are the mass continuity equation (Equation 1.6) and the equation for hydrostatic equilibrium (Equation 1.7). The choice of EOS, $\rho = \rho(P, T)$, and temperature profile, $T = T(P)$, for each layer are outlined

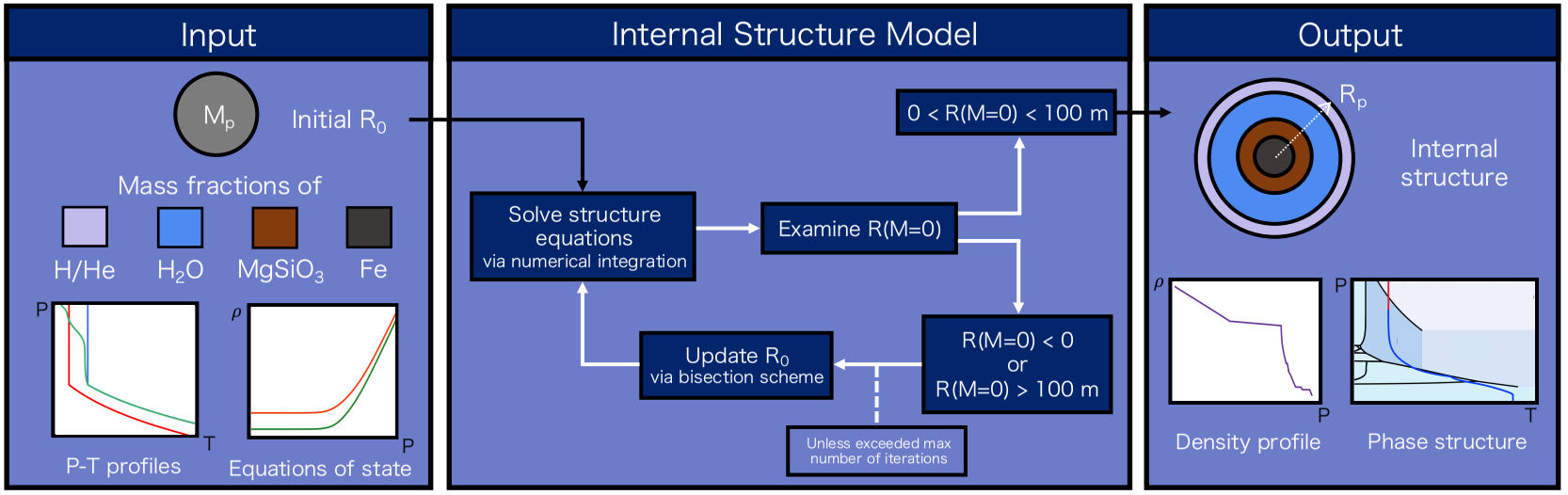

Fig. 2.1 Diagram of the HyRIS internal structure code architecture. The code takes inputs of planetary mass and the mass fractions of the interior layers, and solves the planetary structure equations via numerical integration to output the planetary radius and the internal structure. Equations of state and P-T profiles are adopted for each layer.

in Sections 2.2.2 and 2.2.3. In the default set-up of HyRIS, four differentiated layers are considered – a H/He envelope, a pure H_2O layer, a silicate mantle and an iron core, as are commonly considered for sub-Neptunes (e.g. Rogers and Seager, 2010a; Madhusudhan et al., 2020; Nixon and Madhusudhan, 2021).

In a similar method to Nixon and Madhusudhan (2021), the structure equations are solved using a using a fourth-order Runge-Kutta numerical integration procedure. The boundary conditions are chosen to be at the planet's surface since these are associated with atmospheric observables. The model solves for the planet radius R_p, taking inputs of planet mass M_p, mass fractions of its constituents $x_\mathrm{i} = M_\mathrm{i}/M_\mathrm{p}$, and photospheric pressure P_0 and temperature T_0. If no envelope is included, the boundary P_0 and T_0 will be at the planet's surface. The integration procedure works inwards from the outside of the planet, using some guess of $R_\mathrm{p} = R_0$, stepping through decreasing enclosed mass M, where the size of mass step dM is adjusted according to the current M and ρ, with smaller dM at lower densities. R_p is obtained via a bisection root-finding method with a convergence condition of a radius value of less than 100 m at zero enclosed mass, $0 < R(M = 0) < 100$ m. In this way, the value for R_0 is reduced if $R(M = 0) > 100$ m, or conversely increased if $R(M = 0) < 0$, until convergence. In addition to R_p and the thickness of each planetary layer, the interior density profile and H_2O phase structure can be output if required. The model architecture is summarised in Figure 2.1.

The EOSs adopted for the different materials are described in Section 2.2.2. However HyRIS is flexible, with the nature of each planetary layer and the associated EOS able to be easily modified. For instance, miscibility of the H_2O and H/He layers can be included (e.g. Section 2.4.2). See Section 2.4.3 for further discussion of possible developments and adaptations to the model, which we expand upon in the following chapters.

Exploring Hycean Conditions

For this study, HyRIS has been customised to explore the parameter space for hycean worlds, and facilitate quick extraction of useful quantities. We automate the extraction of 1σ solutions of internal structures for the M_p and R_p measurements for a given planet from a large number of interior model executions across the full parameter space of possible mass fractions. We further automate the determination of hycean solutions from the 1σ solutions. As discussed above, the model can output the density profile and H_2O phase structure, along with R_p and the thickness of each planetary layer. For a given solution, if the surface is found to lie in the liquid phase of H_2O, the ocean depth is calculated. For hyceans, with liquid surfaces with temperatures up to

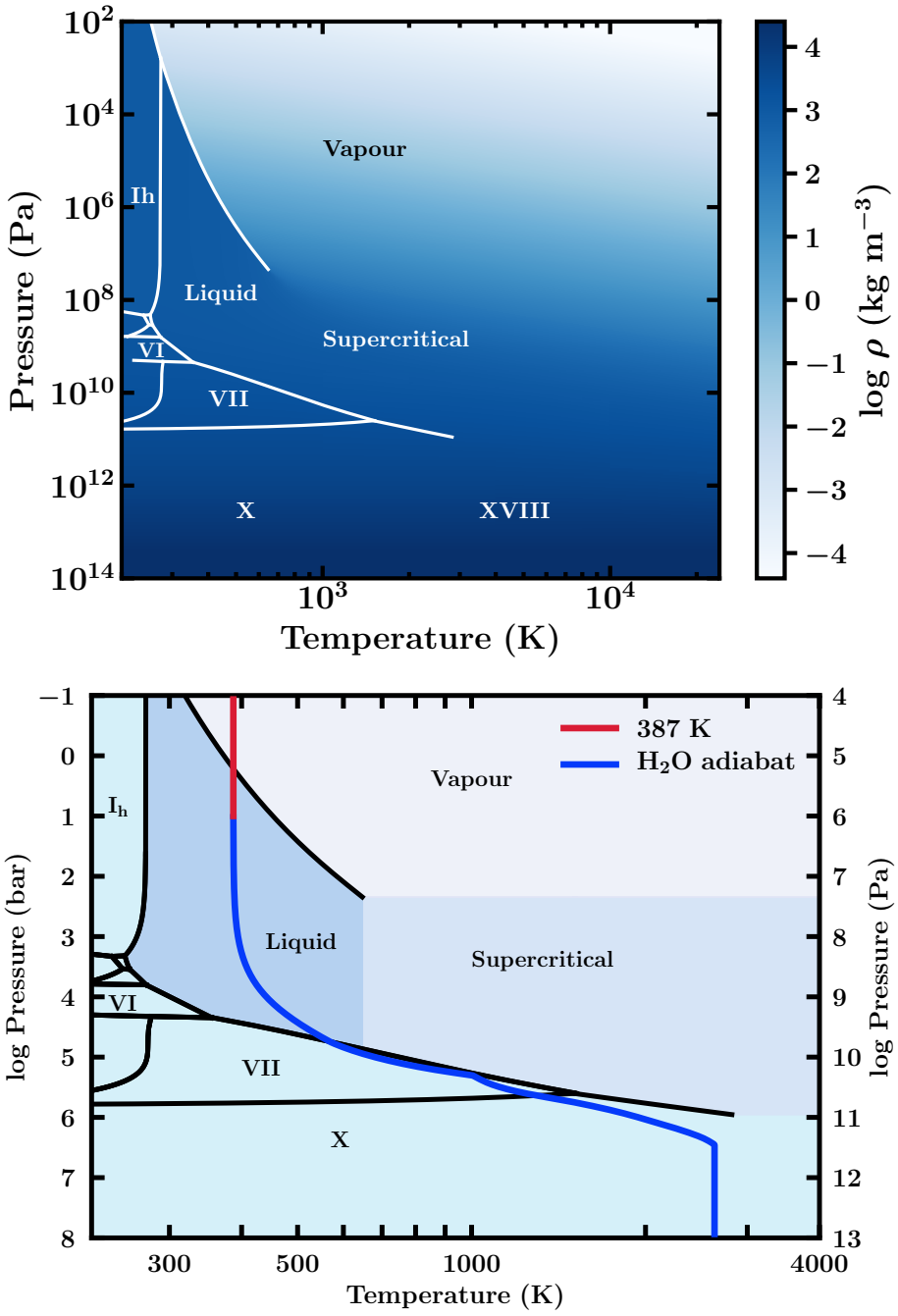

Fig. 2.2 Top: Phase diagram and EOS for H_2O used in our model. The phase diagram is constructed from Dunaeva et al. (2010) and Wagner and Pruß (2002), and the sources for the EOS are outlined in Table 2.1. Bottom: Example H_2O adiabat with HHB at 387 K and $\sim$ 10 bar. This is the profile for the possible interior of TOI-270 d shown in Figure 2.10, with 387 K the equilibrium temperature with $A_B = 0$ for TOI-270 d. The red line shows the atmospheric profile, which follows an isotherm at these pressures.

EOS and Source	**Validity**
IAPWS-1995, (Wagner and Pruß, 2002)	Vapour, liquid, supercritical
French et al. (2009)	Supercritical, ice VII, ice X, ice XVIII, plasma. $1000 - 24000$ K, $1.86 \times 10^9 - 9.87 \times 10^{12}$ Pa
Feistel and Wagner (2006)	Ice Ih. $0 - 273$ K, $0 - 10^8$ Pa
Journaux et al. (2020a)	Ices II, III, V, VI
Fei et al. (1993)	Ice VII
Fei et al. (1993), Klotz et al. (2017)	Ice VIII
Thomas-Fermi-Dirac (TFD), (Salpeter and Zapolsky, 1967)	$P > 7.686 \times 10^{12}$ Pa
Seager et al. (2007)	Remaining high-pressure regions
IAPWS-1995 extrapolation, (Wagner and Pruß, 2002)	Remaining regions, (low-pressure and high-temperature vapour)

Table 2.1 Sources and regions of validity for the components of our H_2O EOS, shown in Figure 2.2.

~ 400 K, the base of the ocean will be high-pressure ice. Hotter surfaces can lead to supercritical oceans, as shown in Nixon and Madhusudhan (2021).

2.2.2 Equations of State

For each planetary layer considered, which are here H/He, H_2O, silicates and iron, we require an EOS to describe the pressure and temperature dependent density variation within each layer. We describe the choice of EOS for each layer and, where relevant, the process to compile them.

H_2O

We use a temperature-dependent EOS for pure H_2O, compiled following a similar approach to Thomas and Madhusudhan (2016) and Nixon and Madhusudhan (2021). Our EOS is valid for temperatures in the range $200 - 24000$ K and pressures $10^2 - 10^{22}$ Pa ($10^{-3} - 10^{17}$ bar). It is comprised of a number of different sources valid for certain phases and/or regions of P-T space. These sources will be described below, and are summarised in Table 2.1. We use phase-boundaries from Dunaeva et al. (2010), in addition to the liquid-vapour boundary from Wagner and Pruß (2002).

For the liquid and vapour phases and some parts of the supercritical phase, we use the EOS from the International Association for the Properties of Water and Steam (IAPWS) (Wagner and Pruß, 2002), referred to as the IAPWS-1995 formulation. This EOS has been well tested experimentally. We use the functional form of the IAPWS-1995 formulation, which is calculated directly from the Helmholtz free energy, to give pressure as a function of density and temperature, $P = P(\rho, T)$. This requires a bounded root-finding procedure to be carried out to obtain $\rho = \rho(P, T)$ for each phase.

We also use the EOS of French et al. (2009), the data for which covers multiple phases, including supercritical, high-pressure ices (ice VII, X and XVIII) and plasma. This EOS is based on quantum molecular dynamics simulations, and has since been experimentally validated by Knudson et al. (2012). The EOS for remaining regions of the supercritical phase is an extrapolation of the IAPWS-1995 EOS.

For the majority of ice VII (the high-temperature region is covered by the French et al. (2009) EOS), we use a functional EOS in the form of a Vinet EOS (Equation 1.13) with a thermal correction from Fei et al. (1993).

The thermal correction is given by

$$\rho\left(P,T\right) = \rho_0\left(P,T_0\right)\left[\exp\left(\int_{T_0}^{T}\alpha\left(P,T\right)dT\right)\right]^{-1} \tag{2.1}$$

where T_0 is the ambient temperature, in this case 300 K (Fei et al., 1993). The thermal expansion coefficient α here is written in the form

$$\alpha\left(P,T\right) = \alpha_0\left(T\right)\left[1+\frac{K_0'}{K_0}P\right]^{-\eta} \tag{2.2}$$

where $\alpha_0\left(T\right)$ is a linear function of T, $\alpha_0\left(T\right) = \alpha_0 + \alpha_1(T)$, and α_0, α_1, and η are constants. These coefficients were experimentally determined via X-ray diffraction, with values $\alpha_0 = -3.9 \times 10^{-4}$, $\alpha_1 = 1.5 \times 10^{-6}$, and $\eta = 0.9$ (Fei et al., 1993). Via an alternative form of $\alpha(P, T)$ from Klotz et al. (2017), we also extrapolate this EOS to cover ice VIII.

For ice Ih we use the functional form of the EOS from Feistel and Wagner (2006), given in a similar format to IAPWS-1995 for liquid and vapour. Ices II, III, V and VI are also covered by experimental data, from Journaux et al. (2020b) via the SeaFreeze package.

At high pressures, above 7.686×10^{12} Pa (7.686×10^{7} bar) we adopt a modified Thomas-Fermi-Dirac (TFD) EOS, as in Salpeter and Zapolsky (1967). This EOS is temperature independent, due to the minimal effect of temperature on the density in

Layer	$\mathbf{K_0}$ **(GPa)**	$\mathbf{K_0'}$	$\mathbf{K_0''}$ **(GPa^{-1})**	ρ **(kg m^{-3})**
Fe	156.2	6.08	N/A	8300
$MgSiO_3$	247	3.97	-0.016	4100

Table 2.2 Values used in the EOSs for the iron and silicate layers, from Anderson et al. (2001) and Karki et al. (2000) respectively.

this regime. There remains an intermediate region in pressure space between ice VII and X not covered by experimental data or the TFD EOS. In this region we use the H_2O EOS from Seager et al. (2007). This is comprised of three regimes – at lower pressures this is a Birch-Murnaghan (BM) EOS (Birch, 1952) with coefficients from Hemley et al. (1987), transitioning to density functional theory results with increasing pressure, and finally to a TFD at high pressures.

Our full H_2O EOS and phase diagram are shown in Figure 2.2. The EOS was constructed based on the regions of validity described above and in Table 2.1. This is either via the phase boundaries, or by the bounds of the data.

We validate our H_2O EOS against the EOS of Nixon and Madhusudhan (2021). We expect these to be almost identical due to the sources used. In Figure 2.5 we show this to be the case, showing the density as a function of pressure for different isotherms.

For c_p, required for the adiabatic gradient (see Section 2.2.3), we use the same sources as the EOS where available (for Wagner and Pruß, 2002; Feistel and Wagner, 2006; Journaux et al., 2020a). For regions where there is no data for c_p, we adopt the c_p value of the nearest available point in P-T space. α is determined directly from the EOS, as in Equation 1.9.

Silicates and Iron

Since thermal effects within the core and mantle have been found to have a minimal effect on the planetary M-R relation (e.g. Grasset et al., 2009), we adopt an isothermal EOS in the silicate mantle and iron core, as is frequently assumed in other internal structure models (e.g. Rogers et al., 2011; Thomas and Madhusudhan, 2016). For this we use the EOS from Seager et al. (2007). These EOSs are shown in Figure 1.7.

The iron core is described by a Vinet EOS (Equation 1.13) (Vinet et al., 1989; Anderson et al., 2001) for hexagonal close-packed Fe, before transitioning to a TFD EOS (Salpeter and Zapolsky, 1967) at higher pressures.

For the silicate layer, assumed to be the perovskite phase of $MgSiO_3$, the EOS is in the form of a fourth-order BM EOS (Birch, 1952; Karki et al., 2000), and, similarly, a

TFD EOS (Salpeter and Zapolsky, 1967) at high pressure. The fourth-order BM EOS is given by Equation 1.12. The coefficients for this are from Karki et al. (2000), and are given in Table 2.2, along with those for the Fe EOS.

Hydrogen/Helium

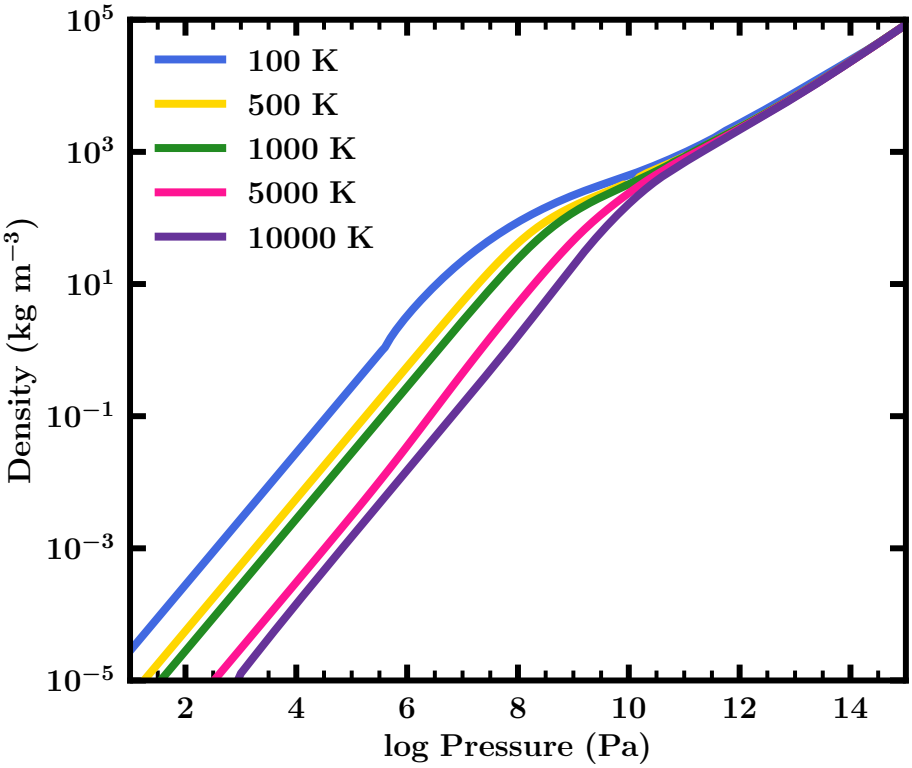

Fig. 2.3 The EOS for H/He used in our model (from Chabrier et al., 2019), shown for different isotherms.

We assume a solar helium fraction for the H/He envelope ($Y = 0.275$). The EOS from Chabrier et al. (2019) is used, which is valid for 1-10^{22} Pa and 100-10^8 K. This EOS is comprised of models applicable at different density and temperature regimes, and the hydrogen and helium EOSs are combined via an additive-volume law. In our temperature range, the models used are from Saumon et al. (1995); Caillabet et al. (2011); Chabrier and Potekhin (1998) – see Chabrier et al. (2019) for a full description of the model. This EOS is shown in Figure 2.3.

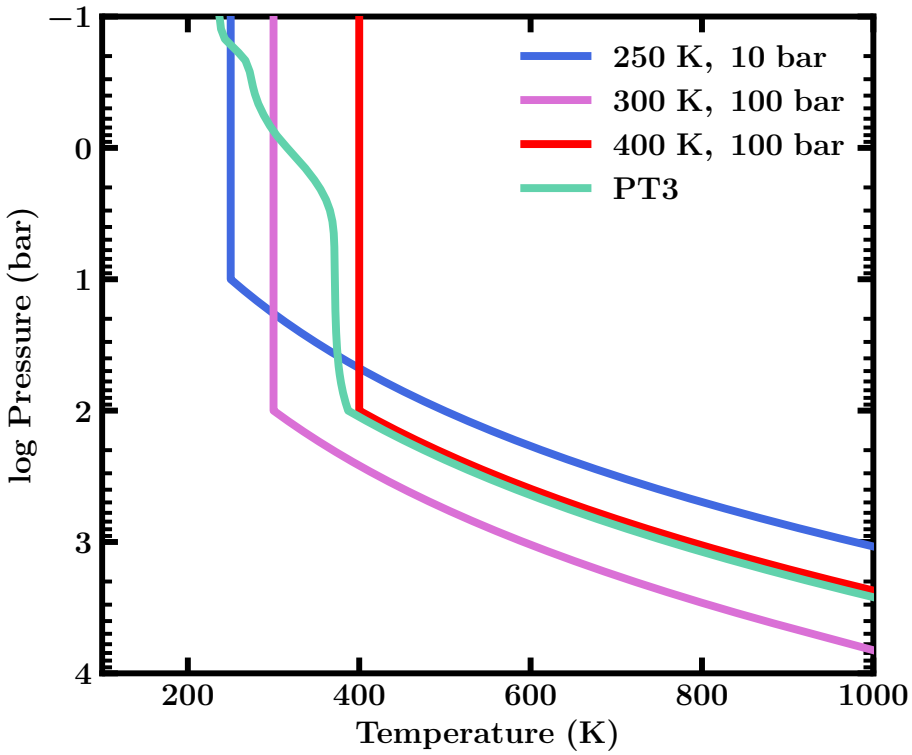

Fig. 2.4 Forms of *P-T* profile used for the H/He envelope. Example isothermal/adiabatic profiles are shown at three different temperatures with $P_{\rm rc}$ between $10 - 100$ bar. PT3 is from Madhusudhan et al. (2023a), generated via self-consistent modelling with GENESIS (Gandhi and Madhusudhan, 2017; Piette and Madhusudhan, 2020) for K2-18 b.

2.2.3 Temperature Profiles

The model considers pressure and temperature dependent EOSs. HyRIS can accommodate user-specified *P-T* profiles for the atmosphere, while in the interior, an adiabatic profile is typically assumed. Madhusudhan et al. (2021) showed that the *P-T* structure expected in the observable H_2-rich atmospheres of hycean worlds around M dwarfs are well approximated by an isothermal profile. We note that the atmospheric compositions of hycean worlds could be rich in CH_4 and CO_2 (e.g. Madhusudhan et al., 2023b), which could further affect the temperature structure. Nixon and Madhusudhan (2021) also showed that *P-T* profiles for sub-Neptunes generated via self-consistent atmospheric modelling with GENESIS (Gandhi and Madhusudhan, 2017; Piette and Madhusudhan, 2020) could be reasonably approximated by isothermal/adiabatic profiles, with the radiative-convective boundary, $P_{\rm rc}$, lying at $\sim$ 1-1000 bar. In the H/He atmosphere, we

hence assume an isotherm down to $P_{\rm rc} = 100$ bar, with the P-T profile then following an adiabat in the deeper atmosphere. Example profiles are shown in Figure 2.4.

Under the assumption of vigorous convection, we similarly assume an adiabatic temperature profile in the H_2O layer, as is commonly assumed in internal structure models (e.g. Sotin et al., 2007; Nixon and Madhusudhan, 2021; Leleu et al., 2021). An example interior adiabat is shown in Figure 2.2. The adiabatic profiles are described by the adiabatic temperature gradient, given by Equation 1.8. The coefficient of volume expansion, required for the adiabatic gradient, is derived from the EOS, as in Equation 1.9.

Alternative temperature profiles can be easily included within HyRIS. For instance, atmospheric temperature profiles generated via self-consistent modelling (e.g. Piette and Madhusudhan, 2020) can be used in the place of the isothermal/adiabatic profiles. An example of this is carried out for K2-18 b in Section 2.3.2, in addition to in Chapters 3 and 4.

2.2.4 Model Validation

We validate our model against the results of previous studies of sub-Neptune internal structures. In Figure 2.5 we reproduce M-R relations from Seager et al. (2007) and Nixon and Madhusudhan (2021). The results of our model are shown in black, with the 100% Fe, 100% silicate and Earth-like curves from Seager et al. (2007), and the M-R curves including H_2O from Nixon and Madhusudhan (2021). The Earth-like composition consists of 67.5% silicates and 32.5% iron. The Seager et al. (2007) cases are taken to be isothermal planets, as the EOSs used are temperature-independent. We expect our results to match those of Seager et al. (2007) due to the use of identical EOSs, which we see. We also see close agreement with the M-R curves from Nixon and Madhusudhan (2021), which represent 30% and 90% H_2O by mass with an Earth-like core. Henceforth, we use "core" to refer to the rocky component of the interior, including both the silicate and iron layers. These cases of 300 K and 1 bar surface were chosen as they are representative of a hycean interior, with the interior P-T profile following an adiabat as described in Section 2.2.3. In Section 2.3.1 we compare our model ocean depth results to those of previous studies.

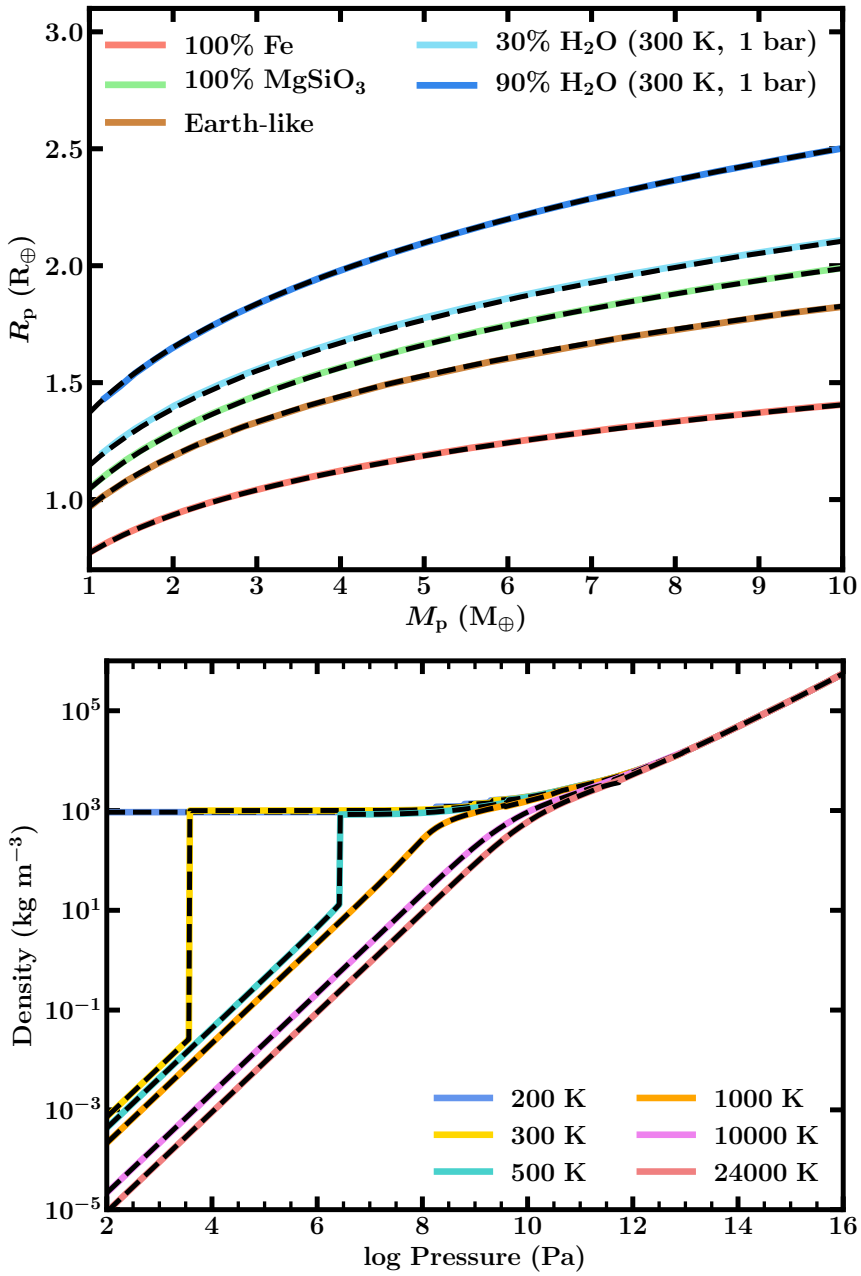

Fig. 2.5 Top: Mass-radius (M-R) relations produced using our model compared to the results of Seager et al. (2007) and Nixon and Madhusudhan (2021). The 100% Fe, 100% $MgSiO_3$ and Earth-like (67.5% $MgSiO_3$, 32.5% Fe) curves are from Seager et al. (2007). The curves with 30% (90%) H_2O and 70% (10%) Earth-like core are from Nixon and Madhusudhan (2021), assuming liquid surfaces at 300 K and 1 bar. The M-R curves produced using our model are shown in black. Bottom: Comparison of our H_2O EOS to the EOS of Nixon and Madhusudhan (2021), for several isotherms. Our results are shown in black. These results are almost identical due to the identical sources used for the EOS and phase boundary data.

2.3 Results

In this section we present our results for the possible oceanic and interior conditions of hycean worlds. Firstly we validate our model ocean depths against the results of previous studies (Léger et al., 2004; Noack et al., 2016; Nixon and Madhusudhan, 2021), before investigating the theoretical range of ocean depths possible on hycean worlds. We then explore in detail five candidate hyceans, placing constraints on their possible ocean depths, interior compositions and envelope mass fractions. The envelope mass fractions are determined for the case of a hycean world and for the case of a rocky world with a thick H/He envelope, the latter representing the overall maximum envelope fraction for these sub-Neptunes.

2.3.1 Ocean Depths on Hycean Worlds

Hycean worlds are defined to have $10 - 90\%$ H_2O by mass (Madhusudhan et al., 2021), therefore in all calculations we impose these limits on the H_2O mass fraction. To allow for the surface ocean, we require the H/He-H_2O boundary (HHB) to lie at pressures and temperatures that support the liquid phase of H_2O. The HHB is what we will refer to as the "surface". We further place the constraint of habitable surface conditions, requiring surface temperatures $T_{\rm HHB}$ of 273-400 K and pressures $P_{\rm HHB}$ of 1-1000 bar, motivated by the range of conditions supporting life on Earth (Rothschild and Mancinelli, 2001; Merino et al., 2019). We note that maintaining a liquid water ocean across this full pressure and temperature range is debated due to the possible onset of a runaway greenhouse effect (e.g. Innes et al., 2023). We consider core compositions between Earth-like (33% Fe) and pure Fe. The internal structure model is then applied across the full hycean phase space, for planets with 1-10 $M_\oplus$, $10\% \leq x_{\rm H_2O} \leq 90\%$, $273 \leq T_{\rm HHB} \leq 400$ K. For each combination we extract $R_{\rm p}$ and the ocean depth.

We first reproduce some previous results in the literature. Noack et al. (2016) found that the maximum ocean depth for a planet varies with the mass, composition and surface temperature of the planet. Similarly, Nixon and Madhusudhan (2021) showed that the ocean depth is affected by the surface gravity and ocean base pressure. The pressure at the ocean base, where the transition from liquid to high-pressure ice occurs, is fixed by the interior adiabat and hence the surface temperature. In Figure 2.6a we reproduce these results using our model, showing the inverse proportionality of ocean depth and surface gravity. The surface pressure is fixed at 100 bar as in Nixon and Madhusudhan (2021) – varying this within a reasonable range ($\sim$ 1-1000 bar)

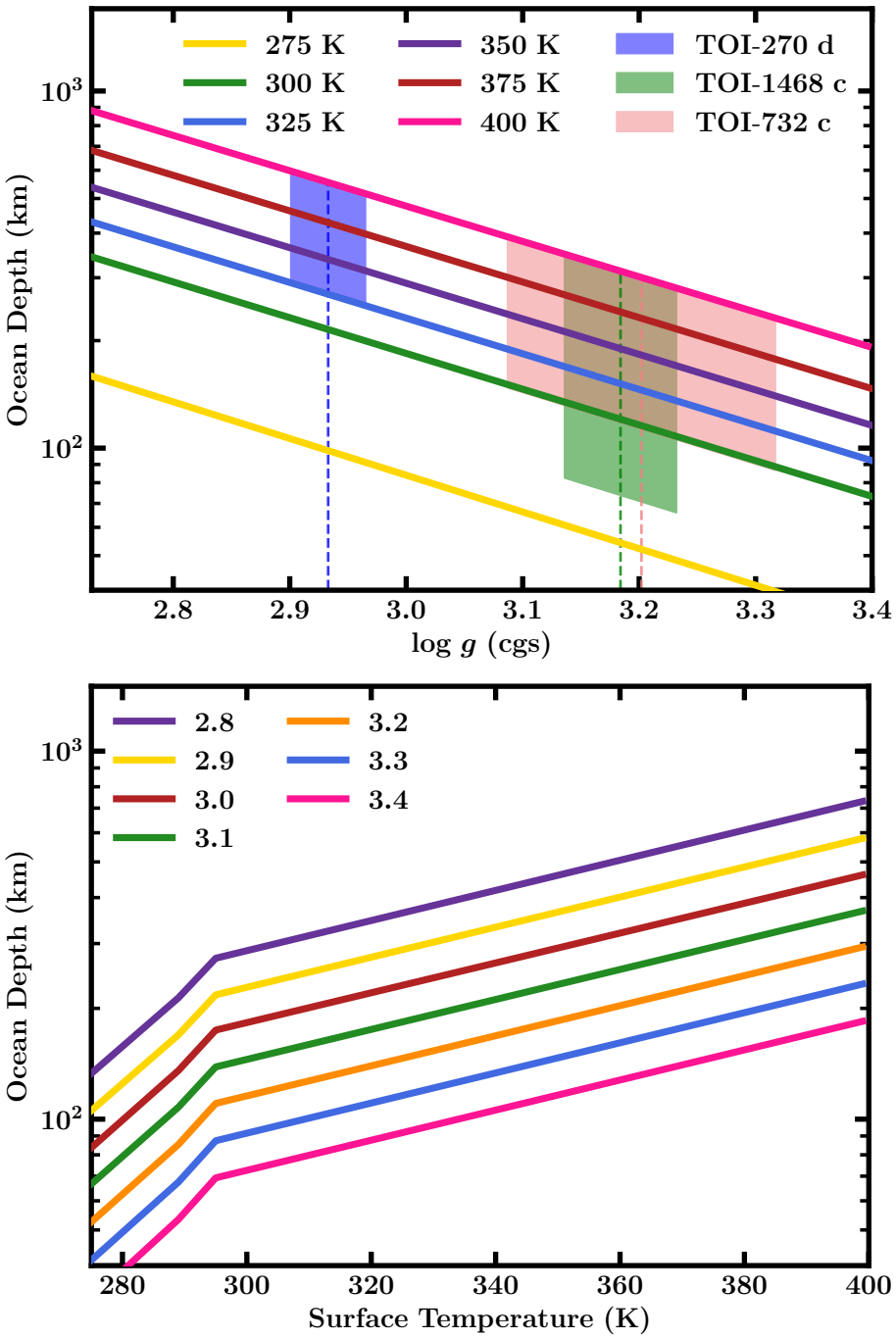

Fig. 2.6 Top (a): Ocean depth against surface gravity for a range of habitable surface temperatures. The shaded regions indicate the estimated range of ocean depths for three hycean candidates, based on the uncertainty in their surface gravity and temperature. The dashed line indicates the median gravity. The mass and radius values adopted for each target are their first entry in Table 2.3. Bottom (b): Ocean depth against surface temperature for a range of surface gravity values.

does not significantly affect the results, in agreement with Nixon and Madhusudhan (2021). In Figure 2.6b we also show the ocean depth against the HHB temperature for a range of surface gravity values. The change in slope at ∼295 K corresponds to the transition between an ocean base of ice VI vs ice VII. Nixon and Madhusudhan (2021) showed that peak depths occur for $T_{\rm HHB} = 413$ K with the trend reversing for $T_{\rm HHB} > 413$ K (up to the critical temperature). Therefore, as seen in Figure 2.6, the trend with temperature is straightforward for our considered temperature range of $273 - 400$ K, with an increase in $T_{\rm HHB}$ causing an increase in ocean depth. We reiterate that in Figure 2.6, this is the gravity and temperature at the ocean surface ($g_{\rm HHB}$, $T_{\rm HHB}$), not with the envelope included (g_0, T_0). As an illustration, for a planet with $M_{\rm p} = 6$ M$_\oplus$, 50% H_2O, 50% Earth-like core and $T_{\rm HHB} = 303$ K, we obtain a depth of 127 km. This is in good agreement with the 125 km found by Nixon and Madhusudhan (2021) and 133 km found by Léger et al. (2004).

We find that ocean depths on hycean worlds can range between 10s of km to ∼1000 km, depending on the planet's mass, composition and surface conditions. For comparison, the average depth of Earth's ocean is 3.7 km (Charette and Smith, 2010), with the deepest part (the Mariana trench) extending to ∼11 km (Gardner et al., 2014). For the theoretical maximum depth of a hycean ocean, we find ∼1000 km – this end-member case is a 1 M$_\oplus$ planet with 90% H_2O and $T_{\rm HHB} = 400$ K, i.e. maximal $T_{\rm HHB}$ and minimal log g. Conversely, the minimum depth is ∼20 km, for a 10 M$_\oplus$ planet with 10% H_2O, 90% Fe and $T_{\rm HHB} = 273$ K.

The calculated ocean depths as a function of surface gravity g and $T_{\rm HHB}$, as shown in Figure 2.6, can be used to estimate the range of ocean depths possible for a given planet. For instance, in Figure 2.6a we show estimates of the ocean depths possible for TOI-270 d, TOI-1468 c and TOI-732 c, shown by the shaded regions. The $T_{\rm HHB}$ range considered is from $T_{\rm eq}$ at $A_{\rm B} = 0.5$, calculated via Equation 2.3, up to the maximum of 400 K. Alternatively, using Figure 2.6b the range of ocean depths can be estimated given a value for the surface gravity. For example, for a surface gravity similar to K2-18 b of log $g = 3.1$, the range of ocean depths would be $\sim 65 - 380$ km, for HHB temperatures $273 - 400$ K. In this method, g is implicitly being assumed as constant throughout the atmosphere. In reality, the gravity for each planet would be higher at the ocean surface than at the photosphere, where $R_{\rm p}$ is measured from. These represent initial estimates, as not all the solutions in these regions will be permissible for a planet when the gravity in the atmosphere is allowed to vary, and an atmospheric P-T profile adopted; these are considered in Section 2.3.2.

We also assess the effect of different mass and radius measurements in the literature for a given planet. For this purpose, we consider the planet TOI-732 c for which such measurements are available from three sources as shown in Table 2.3. In Figure 2.7 we show the range of ocean depths obtained using the mass and radius values from each of the three sources. The Cloutier et al. (2020) (hereafter referred to as "C20") range is the same as in Figure 2.6. If we instead consider the Nowak et al. (2020) values (hereafter referred to as "N20") we find that somewhat deeper oceans are possible. The more precise measurements of N20 compared to C20 result in a smaller log g range at lower values, allowing larger depths. Conversely, the similar maximum log g for Bonfanti et al. (2023) ("B23") and C20 result in a similar upper limit for ocean depth. The improved precision of the B23 measurements again results in a narrower log g range and hence a smaller range of ocean depths. We note that the equilibrium temperature is not varied between the three examples, given the similar estimates between the three studies and the surface temperature being unconstrained. For example, $T_{\rm eq}$ is $305 - 363$ K for N20 compared to $297 - 353$ K for C20, for $0 \leq A_{\rm B} \leq 0.5$.

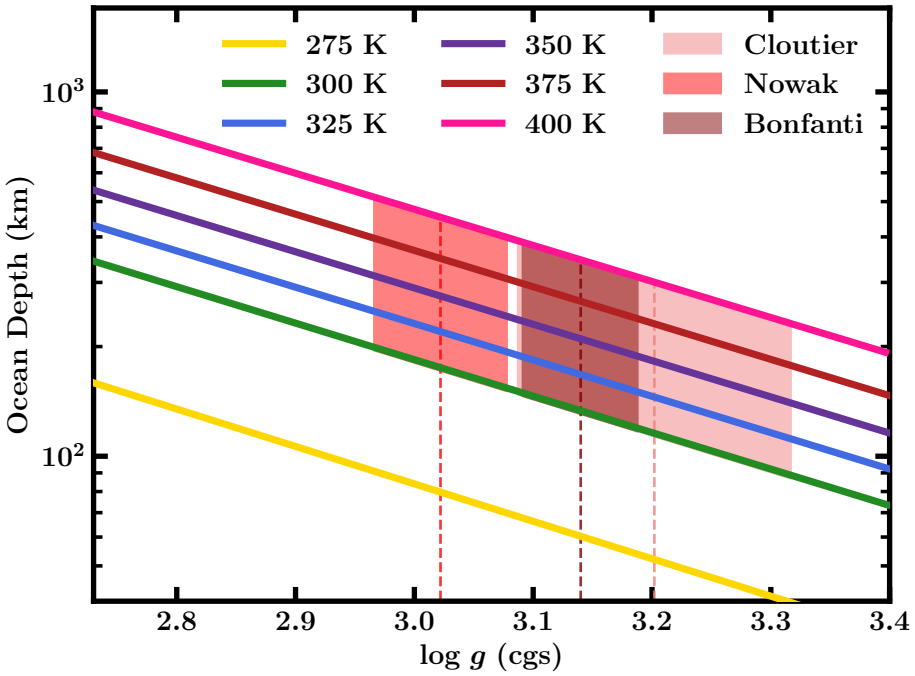

Fig. 2.7 Ocean depth against surface gravity for a range of habitable surface temperatures. The three possible ranges for TOI-732 c for the alternative mass and radius measurements (Cloutier et al., 2020; Nowak et al., 2020; Bonfanti et al., 2023) are shown by the shaded regions.

2.3.2 Case Studies

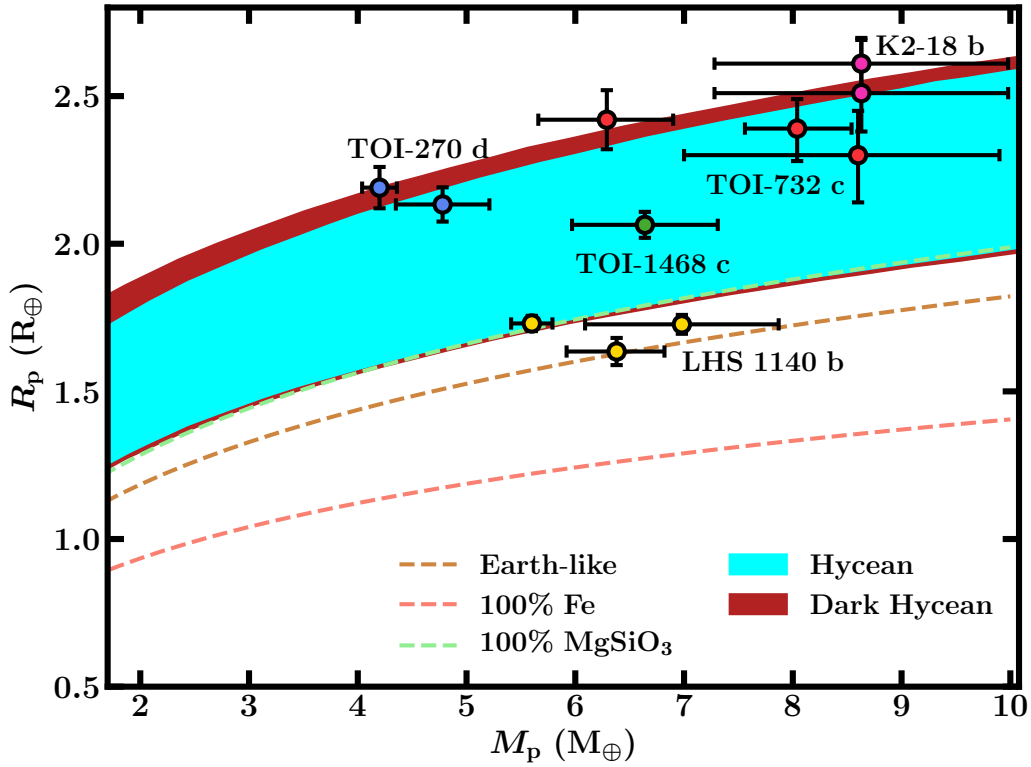

Fig. 2.8 Hycean mass-radius plane from Madhusudhan et al. (2021). The hycean candidates discussed are also shown – different mass/radius measurements for each planet are shown in corresponding colours.

We now explore in detail the possible range of ocean depths and atmospheric mass fractions for five promising hycean candidates with JWST observations. The properties of these planets and their host stars are listed in Table 2.3. The planets include K2-18 b, TOI-270 d, TOI-1468 c, TOI-732 c and LHS 1140 b. These planets are shown against the hycean mass-radius (M-R) plane from Madhusudhan et al. (2021) in Figure 2.8, along with some standard M-R relations. We estimate the maximum mass fraction in the H/He envelope for these planets for two end-member cases – as a hycean world, and as a rocky planet with a deep H_2-rich atmosphere and no H_2O. In the latter case, the maximum density interior of a pure Fe core is assumed in order to obtain the upper limit for H/He mass fraction. We note this is purely an upper limit, as a 100% Fe core is unrealistic by planet formation scenarios. The upper H/He limit has implications for planet formation studies, which is discussed further in Section 2.3.4.

For each planet, we consider equilibrium temperatures assuming Bond albedos in the range $0 \leq A_B \leq 0.5$. This is motivated by the values of Madhusudhan et al.

Planet	$M_p/M_\oplus$	$R_p/R_\oplus$	$T_{eq,0}$ /K	$T_{eq,0.5}$ /K	a/AU	$M_\star/M_\odot$	$R_\star/R_\odot$	T_{eff}/K	V mag	J mag	Refs
K2-18 b	8.63 ± 1.35	2.610 ± 0.087	297	250	0.153	0.45	0.44	3590	13.48	9.76	1,2
		$2.51^{+0.13}_{-0.18}$									3
TOI-732 c	$8.60^{+1.60}_{-1.30}$	$2.30^{+0.16}_{-0.15}$	353	297	0.07673	0.40	0.37	3331	13.14	9.01	4
	$6.29^{+0.63}_{-0.61}$	2.42 ± 0.10									5
	$8.04^{+0.50}_{-0.48}$	$2.39^{+0.10}_{-0.11}$									6
TOI-1468 c	$6.64^{+0.67}_{-0.68}$	2.064 ± 0.044	338	284	0.0859	0.34	0.34	3496	12.50	9.34	7
TOI-270 d	4.78 ± 0.43	2.133 ± 0.058	387	326	0.0733	0.39	0.38	3506	12.60	9.10	8,9
	4.20 ± 0.16	2.19 ± 0.07									10,11
LHS 1140 b	6.98 ± 0.89	1.727 ± 0.032	235	198	0.0936	0.18	0.21	3216	14.15	9.61	12
	$6.38^{+0.46}_{-0.44}$	1.635 ± 0.046									13
	5.60 ± 0.19	1.730 ± 0.025	226								14

Table 2.3 Properties of the hycean candidates considered in this chapter. Equilibrium temperature values are calculated with $A_B = 0$ and $A_B = 0.5$, and assuming uniform day-night redistribution. References: 1: Cloutier et al. (2019), 2: Benneke et al. (2019), 3: Hardegree-Ullman et al. (2020), 4: Cloutier et al. (2020), 5: Nowak et al. (2020), 6: Bonfanti et al. (2023), 7: Chaturvedi et al. (2022), 8: Günther et al. (2019), 9: Van Eylen et al. (2021), 10: Mikal-Evans et al. (2023), 11: Kaye et al. (2022), 12: Ment et al. (2019), 13: Lillo-Box et al. (2020), 14: Cadieux et al. (2024b).

(2021) – the maximum $A_B = 0.5$ is used for their calculation of the inner habitable zone boundary for hycean planets, motivated by Selsis et al. (2007); Yang et al. (2013); de Pater and Lissauer (2010). The equilibrium temperature is calculated by

$$T_{eq} = T_\star \left[\frac{R_\star^2}{2a^2} (1 - A_B) (1 - f_r) \right]^{\frac{1}{4}} \tag{2.3}$$

where a is the orbital semi-major axis, $R_\star$ and $T_\star$ are the stellar radius and effective temperature respectively, and f_r is the fraction of incident radiation that is redistributed to the nightside. In this work we assume that this redistribution is efficient, adopting $f_r = 0.5$ for uniform day-night energy redistribution, giving a uniform equilibrium temperature across the planet. The hycean candidates we consider here are expected to be tidally locked. Depending on the efficiency of day-night redistribution, there could be differences between the temperature of the day and night sides. Future work would be needed to study the effects of inefficient day-night redistribution on their interiors and oceans, including the case of dark hyceans (Madhusudhan et al., 2021). An initial exploration of this scenario is conducted in Chapter 4.

In Section 2.3.1 we assumed constant gravity in the atmosphere, to demonstrate how initial estimates of the possible ocean depths could be obtained via Figure 2.6. As described in Section 2.3.1, the depths in Figure 2.6 were calculated assuming a fixed P_{HHB} of 100 bar. In the subsequent sections, we discuss individual cases with gravity varying in the atmosphere. We evaluate the internal structure model across the full range of possible mass fractions to identify the compositions that satisfy the 1σ range of M_p and R_p, including compositions that allow for hycean conditions. The P_{HHB} and T_{HHB} are not fixed, with the allowed range for hycean solutions spanning $273 \leq T_{HHB} \leq 400$ K and $1 \leq P_{HHB} \leq 1000$ bar. As described in Section 2.2.3, the atmospheric P-T profiles are assumed to be isothermal/adiabatic profiles, typically with $P_{rc} = 100$ bar. T_0 is taken to span the T_{eq} range between $A_B = 0 - 0.5$, as outlined above. P_0 is taken to be the reference pressure for R_p where available, and otherwise we adopt the reference pressure of 0.05 bar, following Madhusudhan et al. (2020). We consider end-member core compositions of Earth-like (33% Fe) and pure Fe.

TOI-270 d

TOI-270 d is a sub-Neptune discovered with TESS (Günther et al., 2019), with RV follow-ups with ESPRESSO (Van Eylen et al., 2021). TOI-270 d orbits at 0.07 au and has $M_p = 4.20 \pm 0.16$ $M_\oplus$ (Kaye et al., 2022) and $R_p = 2.19 \pm 0.07$ $R_\oplus$ (Mikal-Evans et al., 2023). The TOI-270 system contains three transiting planets orbiting an M3V

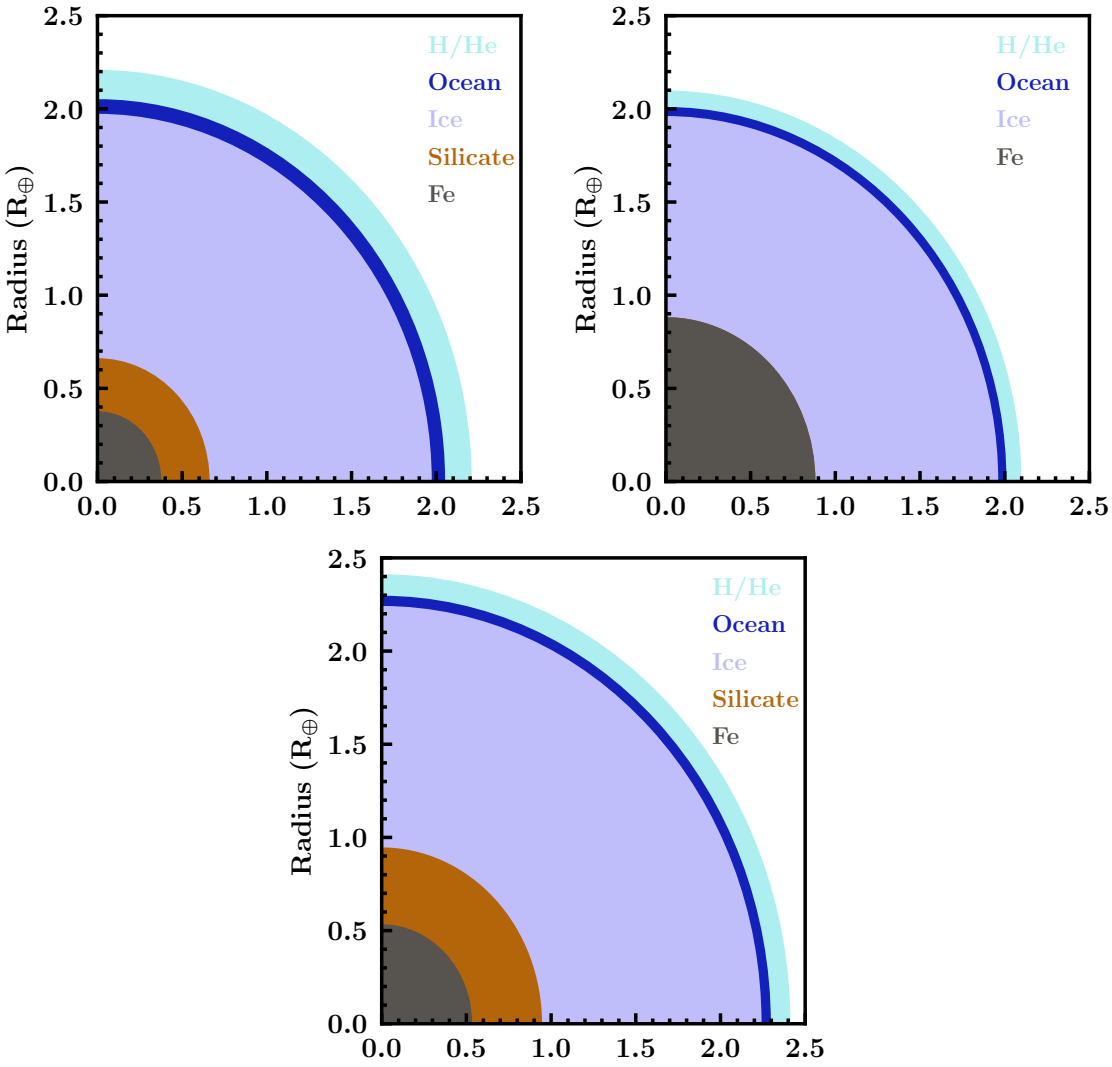

Fig. 2.9 Possible interiors of candidate hycean worlds. a: TOI-270 d, with ocean depth 500 km. b: TOI-1468 c, with ocean depth 309 km. This shows an extreme case with a pure Fe core, which is likely unrealistic based on planet formation mechanisms. c: TOI-732 c, with ocean depth 350 km.

host star with near-mean motion resonance, allowing recent transit-timing variations to be detected (Kaye et al., 2022). Both TOI-270 c and TOI-270 d are hycean candidates (Madhusudhan et al., 2021). TOI-270 d is hottest of the hycean candidates we consider in this chapter, with T_0 taken to be 326-387 K (this is the $T_{\rm eq}$ range for $0 \leq A_{\rm B} \leq 0.5$, as outlined above). This planet was recently the subject of an atmospheric study with HST, which suggested an H_2-rich atmosphere with H_2O absorption (Mikal-Evans et al., 2023). We use a P_0 of 0.0912 bar, which is the reference pressure for this $R_{\rm p}$ (Mikal-Evans et al., 2023).

We find the possible hycean ocean depths for TOI-270 d span $\sim 200 - 500$ km, $\sim 50 - 140$ times the average depth of Earth's ocean at 3.7 km (Charette and Smith, 2010), and $\sim 20 - 50$ times the deepest part at $\sim$11 km (Gardner et al., 2014). As discussed in Section 2.3.1, the maximal ocean depth is achieved with the minimum surface gravity and maximum surface temperature. In Figure 2.9 we show an example interior for TOI-270 d with a maximal ocean depth of 500 km. This case has the lower bound $M_{\rm p} = 4.04$ M$_\oplus$, with $R_{\rm p} = 2.22$ R$_\oplus$. The H_2O mass fraction is at its maximum $x_{\rm H_2O} = 90\%$, with $x_{\rm H/He} = 0.011\%$ and the remaining mass in an Earth-like core. The surface temperature lies at the maximum of 400 K, at pressure 112 bar – more than 100 times the surface pressure on Earth. Conversely, an example interior at the lower end of ocean depths has $x_{\rm H_2O} = 86\%$, $x_{\rm H/He} = 0.0072\%$ and the remainder in an Earth-like core, for $M_{\rm p} = 4.264$ M$_\oplus$ and $R_{\rm p} = 2.13$ R$_\oplus$. The depth in this case is 221 km, with the HHB at the minimum temperature, 326 K, and 90 bar. We note that the interiors able to achieve a given ocean depth are degenerate. The minimum mass fraction of H_2O required for TOI-270 d to be a hycean world is found to be 68%. This occurs for a low density interior, with maximum surface temperature 400 K and an Earth-like core composition. These constraints on the H_2O content of sub-Neptunes can be useful for testing planet formation scenarios (e.g. Bitsch et al., 2021).

We require a H/He mass fraction of $\lesssim 0.0195\%$ for TOI-270 d to be a hycean world. This limit corresponds to the maximal, extreme H_2O mass fraction of 90% and an Earth-like core with mass fraction 9.9815%, with the isothermal temperature in the atmosphere $T_0 = 326$ K. The HHB in this case is 197 bar and at the maximum of 400 K, as an increase in H/He mass fraction would increase the temperature at the surface beyond the habitable range. Conversely, a minimum H/He mass fraction of 1.7×10^{-6} is required for hycean conditions. This limit occurs for the maximum $T_0 = 387$ K and 90% H_2O and an Earth-like core, giving an HHB at 20 bar and 387 K. Lower H/He mass fractions produce an $R_{\rm p}$ below the lower 1σ limit.

If we consider our other end-member case of a rocky planet with an H/He envelope, we find a maximum envelope fraction of 6.1%. This is achieved using the lower T_0 of 326 K and a high density, pure Fe core, with no H_2O. An Earth-like core would reduce the maximum H/He fraction to 3.7%, for the same P-T profile.

We have adopted $P_{\rm rc} = 100$ bar for the H/He envelope. As shown by Nixon and Madhusudhan (2021), the choice of $P_{\rm rc}$ affects the maximum H/He fraction that allows for an HHB within the liquid phase. A lower $P_{\rm rc}$ results in lower permitted H/He fractions, as the atmospheric temperature increases higher in the atmosphere. If we adopt $P_{\rm rc} = 10$ bar and $P_{\rm rc} = 1000$ bar, we find $\sim 0.0017\%$ and $\sim 0.0810\%$ as the maximum H/He fractions for hycean conditions respectively. The overall maximum H/He fraction then varies from $3.4 - 8.3\%$ for $P_{\rm rc}$ from $10 - 1000$ bar. A higher $P_{\rm rc}$ would reduce the range of ocean depths possible, as this restricts the range of $T_{\rm HHB}$ to below the maximum of 400 K. Reducing $P_{\rm rc}$ will not significantly affect the range of ocean depths, as we can already reach the maximum $T_{\rm HHB} = 400$ K with $P_{\rm rc} = 100$ bar.

TOI-1468 c

TOI-1468 c is a recently discovered sub-Neptune (Chaturvedi et al., 2022) orbiting its M3V host star at 0.0859 au, along with the closer-in, rocky TOI-1468 b. TOI-1468 c has $M_{\rm p} = 6.64^{+0.67}_{-0.68}$ $M_\oplus$ and $R_{\rm p} = 2.064 \pm 0.044$ $R_\oplus$ (Chaturvedi et al., 2022), with T_0 ranging from 284-338 K for our $A_{\rm B}$ range. For TOI-1468 c and the remaining planets, we adopt $P_0 = 0.05$ bar, which is the median reference pressure from Madhusudhan et al. (2020) for K2-18 b.

The possible ocean depths for TOI-1468 c are found to span $\sim$ 60-310 km. An example internal structure that facilitates a maximal depth of 309 km is shown in Figure 2.9. This solution has $x_{\rm H/He} = 0.0125\%$, $x_{\rm H_2O} = 63\%$ and a pure Fe core, for lower bound $M_{\rm p} = 5.97$ $M_\oplus$ and upper bound $R_{\rm p} = 2.108$ $R_\oplus$. The surface temperature lies close to the habitable maximum, at 397 K, with an envelope T_0 of 284 K. The surface pressure is ~ 300 times Earth's surface pressure, at 307 bar, while the base of the ocean lies at 6.0×10^4 bar. This case also represents the solution with maximum envelope mass fraction while maintaining hycean conditions. Overall we find a maximum permitted H/He fraction of 4.3% for non-Hycean conditions – this is lower than for TOI-270 d due to the higher bulk density of TOI-1468 c. For an Earth-like core, as opposed to a pure Fe core, the maximum H/He mass fraction is 1.8%.

Unlike TOI-270 d, TOI-1468 c is not permitted to have 90% H_2O by mass, again due to its higher bulk density, with the maximum $x_{\rm H_2O}$ found to be $\sim 75\%$. The

minimum mass fraction of H_2O required for TOI-1468 c to be a hycean world is found to be 24%. Using this minimum mass fraction of H_2O, we find the lower bound for high-pressure ice thickness on TOI-1468 c, while maintaining hycean conditions, to be 0.42 $R_\oplus$, or ∼2700 km. Even in this case, the ocean is still very deep, at 230 km. The thickness of the high-pressure ice layer on hycean worlds could have implications for their habitability, which is discussed further in Section 2.4.1.

TOI-732 c

TOI-732 c, or LTT 3780 c, is a sub-Neptune orbiting an M4V host star discovered by TESS, with independent follow-ups with HARPS & HARPS-N (Cloutier et al., 2019) and CARMENES (Nowak et al., 2020). Most recently, combined analysis of TESS, CHEOPS and ground-based light curves was carried out by Bonfanti et al. (2023), along with RV analysis with MAROON-X. This system also contains a super-Earth, TOI-732 b, making this system an interesting test of radius valley formation around M dwarfs (Cloutier et al., 2019). TOI-732 c orbits its host star at 0.08 au (Cloutier et al., 2019; Nowak et al., 2020), giving equilibrium temperatures in the range 284-353 K for our A_B range. Multiple measurements of mass and radius are reported for TOI-732 c, with the masses varying significantly. Cloutier et al. (2020) find $M_p = 8.60^{+1.60}_{-1.30}$ $M_\oplus$ and $R_p = 2.30^{+0.16}_{-0.15}$ $R_\oplus$ while Nowak et al. (2020) report $M_p = 6.29^{+0.63}_{-0.61}$ $M_\oplus$ and $R_p = 2.42 \pm 0.10$ $R_\oplus$. The most recent mass measurement by Bonfanti et al. (2023) is in best agreement with Cloutier et al. (2020), at $M_p = 8.04^{+0.50}_{-0.48}$ $M_\oplus$, with $R_p = 2.39^{+0.10}_{-0.11}$ $R_\oplus$. These are shown by the blue points in Figure 2.8. In the following calculations and Figure 2.6, we adopt the Cloutier et al. (2020) values (hereafter referred to as "C20").

We find possible hycean ocean depths to range from $\sim 90 - 360$ km. An example internal structure with depth 350 km is shown in Figure 2.9. This case, with $M_p = 7.10$ $M_\oplus$ and $R_p = 2.41$ $R_\oplus$, has $x_{H/He} = 0.0132\%$, $x_{H_2O} = 80\%$ and the remaining mass in an Earth-like core. The surface temperature lies close to the maximum value at 399 K, with a pressure of 270 bar, for $T_0 = 297$ K. We find a maximum H/He fraction of 0.0142% for TOI-732 c under hycean conditions. As for TOI-270 d, this is achieved with a maximal H_2O fraction of 90% with 9.986% in a pure Fe core, and a minimal T_0, which here is 297 K. The overall maximum H/He fraction for non-Hycean conditions is found to be 6.8%, using the lower T_0 of 297 K and a pure Fe core, while a maximum envelope fraction of 3.8% is permitted for an Earth-like core. TOI-732 c has the largest range of permitted H_2O fractions of the planets considered, due to the larger uncertainty in its mass. The minimum mass fraction of H_2O required for

TOI-732 c to be a hycean world is found to be 22%, and the interior in Figure 2.9 demonstrates solutions are possible up to 90% H_2O.

As shown in Section 2.3.1, assuming constant gravity in the atmosphere, different mass measurements for TOI-732 c can affect the possible range of ocean depths. Adopting the Nowak et al. (2020) values ("N20") in our full evaluation of the model (assuming the same range for $T_{\rm eq}$ as used for C20), the maximum depth is found to be 415 km, compared to 350 km for the C20 case. This difference is smaller than Figure 2.7 would suggest, due to the surface conditions permitted by the results of possible compositions. The maximum H/He fraction is found to be higher than for C20, at 8.2%. For hycean conditions, the maximum H/He fraction for N20 values is only slightly higher, at 0.0186%.

K2-18 b

We revisit K2-18 b, a well-studied sub-Neptune (e.g. Benneke et al., 2017; Cloutier et al., 2019; Benneke et al., 2019; Tsiaras et al., 2019; Madhusudhan et al., 2020; Blain et al., 2021; Madhusudhan et al., 2023b) and the first hycean candidate (Madhusudhan et al., 2020, 2021). K2-18 b orbits it M3V host star at 0.15 au, and has $M_{\rm p} = 8.63 \pm 1.35$ $M_\oplus$ (Cloutier et al., 2019) and $R_{\rm p} = 2.610 \pm 0.087$ $R_\oplus$ (Benneke et al., 2019), or $R_{\rm p} = 2.51^{+0.13}_{-0.18}$ $R_\oplus$ (Hardegree-Ullman et al., 2020). We use the former $R_{\rm p}$ value for consistency with previous studies (Madhusudhan et al., 2020). As listed in Table 2.3, $T_{\rm eq}$ varies between $250 - 297$ K for $A_{\rm B} = 0 - 0.5$.

We first adopt PT3 from Madhusudhan et al. (2023a) as the envelope P-T profile, which is shown in Figure 2.4. This profile was generated via self-consistent atmospheric modelling with the GENESIS code (Gandhi and Madhusudhan, 2017; Piette and Madhusudhan, 2020) – see Madhusudhan et al. (2023a) for a full description of the model. This profile was calculated to a pressure of 100 bar at which it has temperature 387 K, and we extend to $P > 100$ bar with an adiabatic profile. We note that this profile is different to those used by Madhusudhan et al. (2020) in their internal structure modelling of K2-18 b. They adopt two atmospheric P-T profiles, also generated with GENESIS, which vary in assumptions, including internal temperature. These have $T_{\rm int} = 25$ K and $T_{\rm int} = 50$ K, while PT3 from Madhusudhan et al. (2023a), used in this work, has $T_{\rm int} = 30$ K; see Madhusudhan et al. (2020) and Madhusudhan et al. (2023a) for full descriptions of the assumptions made.

Using PT3, we find the possible ocean depths to be 140-350 km. The $T_{\rm HHB}$ range possible using PT3 is limited, since at the minimum $P_{\rm HHB}$ of 1 bar, PT3 is at 316 K. For hycean conditions, we find K2-18 b requires a H/He fraction of $\lesssim 0.0052\%$.

Madhusudhan et al. (2020) find permitted envelope fractions of 0.006% for an interior solution with a liquid surface, consistent with our result. Overall we obtain a maximum H/He fraction of 8.1% for non-hycean conditions, with a pure Fe core. In comparison, Madhusudhan et al. (2020) found 6.2% for the maximum H/He mass fraction. For an Earth-like core composition, we find a lower maximum H/He fraction of 4.9%.

If we instead adopt isothermal/adiabatic profiles as we have for the other case studies, we expect the aforementioned importance of the atmospheric P-T profile to affect the results. At pressures $\gtrsim 1$ bar PT3 is at higher temperatures than the isothermal/adiabatic cases with $T_0 = 250$ K and $T_0 = 297$ K. Therefore, we find that a larger H/He fraction is permitted for the isothermal/adiabatic cases. We adopt $T_0 = 250$ K, which is consistent with the isothermal profile found in the photosphere from the atmospheric retrieval carried out by Madhusudhan et al. (2023b). As with our previous case studies, we adopt $P_{\rm rc} = 100$ bar. We find a maximum H/He fraction for hycean conditions of 0.022% for this $T_0 = 250$ K and $T_{\rm HHB} = 400$ K. In this case, the range of ocean depths is also affected as lower values of $T_{\rm HHB}$ are accessible with this P-T profile. For example, an interior with upper bound $M_{\rm p}$, $x_{\rm H/He} = 0.0045\%$, $x_{\rm H_2O} = 86\%$ and the remainder an Earth-like core results in a nearly minimal depth of 54 km, at $T_{\rm HHB} = 277$ K and $P_{\rm HHB} = 139$ bar. The pressure at the base of the ocean in this case is 1.0×10^4 bar, compared to $\sim 6 \times 10^4$ bar for a 400 K surface. The upper depth limit is not significantly affected by a variation in atmospheric P-T profile as the upper limit for $T_{\rm HHB}$ and hence ocean base pressure is unchanged. Reducing T_0 can allow for even larger H/He mass fractions while maintaining hycean conditions. For instance, adopting $T_0 = 200$ K results in a maximum H/He mass fraction of 0.046% for hycean conditions, about twice that for $T_0 = 250$ K. In this case, the HHB lies close to the maximum for habitable conditions, at $\sim$1000 bar.

We note that the depth estimates depend strongly on the HHB conditions, which in turn depend on the temperature structure and atmospheric composition. The non-detection of H_2O in the photosphere of K2-18 b may be consistent with the presence of a tropospheric cold trap, with the temperature and H_2O abundance potentially higher in the lower atmosphere (Madhusudhan et al., 2023b). However, it is difficult to accurately estimate the composition and temperature structure of the dayside atmosphere, and the corresponding surface temperature and pressure, based on observed photospheric properties at the day/night terminator using transmission spectroscopy. We have, therefore, considered a wide range for the $T_{\rm HHB}$ for K2-18 b, similar to the other planets in this chapter, to explore the full range of possibilities.

Across all the *P-T* profiles considered for K2-18 b the ocean depths span $\sim 50 - 350$ km. However, the non-detection of H_2O in K2-18 b (Madhusudhan et al., 2023b) may limit the surface temperatures to well below 400 K. We therefore evaluate the possible ocean depths for a lower maximum $T_{\rm HHB}$ of 340 K. Adopting PT3 as the atmospheric profile for this case, we find a narrow ocean depth range of $140 - 180$ km. Adopting an isothermal/adiabatic profile at $T_0 = 250$ K and $P_{\rm rc} = 100$ bar, we find a range of $\sim 50 - 180$ km. As mentioned previously, given the same maximum $T_{\rm HHB}$, the upper depth limit is not significantly affected by variations in atmospheric *P-T* profile. However, the lower depth limit is affected as a lower $T_{\rm HHB}$, down to 273 K, is possible for the latter *P-T* profile. Similarly, considering an even lower maximum $T_{\rm HHB}$ further decreases the maximum ocean depth possible, e.g. to $\sim 50 - 120$ km for 300 K maximal $T_{\rm HHB}$ for the isothermal/adiabatic profile. Reducing the maximum $T_{\rm HHB}$ also decreases the maximum possible H/He mass fractions for hycean conditions. For instance, using the isothermal/adiabatic profile the maximum H/He fraction is approximately halved for a maximum $T_{\rm HHB}$ of 340 K compared to 400 K, at $\sim$0.011% vs 0.022%.

LHS 1140 b

Finally, we discuss the case of LHS 1140 b (Dittmann et al., 2017; Ment et al., 2019; Lillo-Box et al., 2020; Cadieux et al., 2024b). This planet has a low equilibrium temperature of 235 K for $A_{\rm B} = 0$ (198 K for $A_{\rm B} = 0.5$), orbiting its M4.5V host star at 0.0936 au (Ment et al., 2019). Until recently, LHS 1140 b would only have been considered a hycean candidate for H_2O mass fractions below 10% (Madhusudhan et al., 2021). However, the bulk properties of planet have been revised recently with $M_{\rm p} = 5.60 \pm 0.19$ $M_\oplus$ and $R_{\rm p} = 1.730 \pm 0.025$ $R_\oplus$ (Cadieux et al., 2024b). These latest measurements place LHS 1140 b within the hycean M-R plane, and is close to the upper density limit for hycean candidates, as shown in Figure 2.8 along with the previously reported measurements. For reference, Ment et al. (2019) reported values $M_{\rm p} = 6.98 \pm 0.89$ $M_\oplus$ and $R_{\rm p} = 1.727 \pm 0.032$ $R_\oplus$, placing this planet just outside the upper density limit for hycean candidates. On the other hand, Lillo-Box et al. (2020) reported $M_{\rm p} = 6.38^{+0.46}_{-0.44}$ $M_\oplus$ and $R_{\rm p} = 1.635 \pm 0.046$ $R_\oplus$. Madhusudhan et al. (2021) explain that the lower boundary could be closer to the *M–R* curve for an Earth-like composition if lower H_2O mass fractions were permitted – the minimum was assumed to be 10%, as in this chapter. LHS 1140 b therefore represents an end-member case, in density and temperature, for hycean candidates.

We first use the Ment et al. (2019) values, as the most conservative case. We adopt the equilibrium temperature $T_0 = 235$ K and an envelope *P-T* profile with $P_{\rm rc}$ at 100

bar. Even for this conservative case, large ocean depths are possible. For instance, fractions of $x_{H_2O} = 30\%$, $x_{H/He} = 8.0 \times 10^{-5}$ and remainder pure Fe results in a 145 km ocean. The surface temperature is 360 K in this case. Therefore, LHS 1140 b demonstrates that even planets on the extreme boundaries of being candidate hycean worlds under certain conditions could host 100s of km deep oceans. If we instead use the latest Cadieux et al. (2024b) values for M_p and R_p, giving a lower surface gravity, we find significantly deeper oceans are possible for LHS 1140 b, up to ∼300 km. For example, mass fractions of $x_{H_2O} = 50\%$, $x_{H/He} = 0.021\%$ and remainder in pure Fe can result in a 290 km ocean, for $T_{HHB} = 400$ K. This is calculated adopting the same atmospheric P-T profile as used with the Ment et al. (2019) values. If we instead assume an atmospheric profile with the lower $T_0 = 198$ K and $P_{rc} = 100$ bar, we obtain the maximum H/He fraction for hycean conditions to be 0.036%. Conversely, for non-Hycean conditions, the maximum H/He fraction is found to be 4.2%, using the same P-T profile and the Cadieux et al. (2024b) values, with a pure Fe core. For an Earth-like core, the maximum H/He fraction is reduced to 1.7%.

2.3.3 Envelope Mass Fractions on Hycean Worlds

The requirements of a habitable ocean places limits on the possible mass fraction of the H/He envelope in a given hycean world. The envelope mass fraction depends on the temperature structure and the HHB conditions at the ocean surface. Generally, lower atmospheric temperatures allow for higher envelope mass fractions. For example, higher P_{rc} and lower T_0 allow for higher envelope mass fractions, and vice versa. Across our case studies and the assumptions considered in this work we find the maximum envelope mass fractions admissible for hycean conditions to be $\sim 10^{-3}$. Higher envelope mass fractions correspond to cooler atmospheric temperatures and higher surface pressures. Improved constraints on H/He mass fraction can be obtained via better constraints on the atmospheric temperature structure. Atmospheric observations, for instance with the JWST, are essential for obtaining these improved constraints (e.g. Mikal-Evans et al., 2023; Madhusudhan et al., 2023b). See Section 2.4.4 for further discussion of upcoming observations.

Presently, the formation mechanisms of hycean worlds with such envelope mass fractions have not been investigated in detail. More generally, several mechanisms have been explored for the formation and evolution of sub-Neptune planets, especially with the aim of explaining the radius valley (Fulton et al., 2017; Fulton and Petigura, 2018a). These mechanisms include processes where thick primordial H_2-rich envelopes are depleted via photoevaporative mass loss (e.g. Owen and Wu, 2017) and/or core-

powered mass loss (e.g. Gupta and Schlichting, 2019), as well as processes involving outgassing of H_2 from the interiors (e.g. Elkins-Tanton and Seager, 2008). Other mechanisms suggest the preponderance of sub-Neptunes with water-rich interiors and envelopes of varied compositions (e.g. Zeng et al., 2019; Venturini et al., 2020; Izidoro et al., 2022), which could include hycean worlds. Considering photoevaporative and core-powered stripping of the envelopes of sub-Neptunes with 1:1 silicate-to-ice ratios, Rogers et al. (2023) find envelope mass fractions of $\gtrsim 10^{-3}$ can be retained, at $T_{\rm eq} = 300$ K, after 5 Gyr of photoevaporative evolution. Izidoro et al. (2022) find that water-rich sub-Neptunes with H_2-rich atmospheres, which could include hyceans, can be formed via gas-driven migration models, both with and without the inclusion of photoevaporative mass loss. However, the possible envelope mass fractions were not constrained in this paper – a fixed fraction of 0.3% was assumed, based on Zeng et al. (2019). Such mechanisms could have varying implications for formation of hycean planets.

We note that an H_2-rich envelope mass fraction of $\sim 10^{-4} - 10^{-3}$ is $10^2 - 10^3\times$ larger than that of the Earth, albeit with a lower mean molecular weight. These required mass fractions open a new avenue for investigating the origins of hycean worlds. In principle, these mass fractions are at the limit of what could be retained by mass loss mechanisms in temperate sub-Neptunes based on recent studies (e.g. Owen and Wu, 2017; Gupta and Schlichting, 2019; Rogers et al., 2023). On the other hand, whether outgassing (e.g. Elkins-Tanton and Seager, 2008) or other atmosphere/ocean exchange processes can result in these mass fractions remains to be seen.

2.3.4 Maximum Envelope Mass Fractions

We have additionally placed constraints on the maximum envelope mass fraction for each of the sub-Neptunes we consider. The extreme case assumes a pure Fe interior with no H_2O, with our standard $P_{\rm rc} = 100$ bar in the envelope. We find that the upper envelope fractions are all within $\sim$ 4-8%. This is similar to the $\lesssim 7\%$ found by Valencia et al. (2013) for the well-studied GJ 1214 b. The maximum fraction found by Madhusudhan et al. (2020) for K2-18 b is also similar, at $\sim 6\%$. For an Earth-like core composition, we find the maximum H/He envelope mass fractions to span $\sim$2-5%.

The upper limit for envelope mass fraction has implications for planet formation and evolution scenarios in the sub-Neptune regime. Mechanisms of atmospheric mass loss, including both photoevaporative (e.g. Owen and Wu, 2013, 2017; Rogers and Owen, 2021) and core-powered (e.g. Gupta and Schlichting, 2019, 2020), make predictions for permitted envelope mass fractions for sub-Neptunes. Determining these for a range of

sub-Neptunes including those within and outside of the radius valley can help to test the predictions of these theories. For instance, the photoevaporative scenario (Owen and Wu, 2017) predicts mass fractions of order $\sim$1% are typical for envelope-retaining sub-Neptunes. More recent studies also including core-powered mass loss suggest larger mass fractions up to $\sim$10% are possible, depending on the planet mass and radius (Rogers et al., 2023). Our range of derived H/He mass fractions are consistent with these estimates.

2.4 Summary and Discussion

In this chapter we investigate the range of conditions possible in the interiors of hycean worlds, including their ocean depths, interior compositions and envelope mass fractions. Our results follow previous works on ocean depths in water-rich sub-Neptunes (Noack et al., 2016; Nixon and Madhusudhan, 2021), focusing specifically on hycean conditions and several candidate hycean worlds. Firstly, we find the expected range of ocean depths to extend from 10s of km to $\sim$1000 km for hycean worlds. The depth of a hycean ocean is influenced by the surface conditions, specifically the temperature and gravity, and is hence sensitive to the planet mass, composition, and assumed temperature profile in the envelope. We place constraints on the possible ocean depths and compositions for a sample of five promising hycean candidates with upcoming JWST data: TOI-270 d, TOI-1468 c, TOI-732 c, K2-18 b and LHS 1140 b. Secondly, we investigate the mass fractions of the possible H/He envelopes for all the candidates considered. Across the sample we find the maximum envelope fraction admissible for hycean conditions to be $\sim 10^{-3}$, for the atmospheric temperature structures explored in this work. Finally, we also constrain the maximum H/He envelope mass fraction for non-hycean conditions, i.e. for the limiting case of a rocky core with a thick H/He envelope but no H_2O layer. The corresponding envelope mass fractions are found to span $\sim 4 - 8$% across the sample.

Our results demonstrate the diverse conditions possible among hycean worlds, and reinforce their possibility to host habitable conditions under vastly different circumstances to the Earth. The information we expect to gain on the atmospheric composition of hycean candidates with JWST may provide an indication if these planets could indeed be hycean worlds and allow us to place better constraints on the nature of their interiors and oceans. With JWST, the detection of possible biomarkers in the atmospheres of hycean candidates remains an exciting and potentially imminent

prospect. The study by Madhusudhan et al. (2023b) of K2-18 b is an exciting first look into the capability of JWST to shed light on this regime.

2.4.1 Habitability of Hycean Worlds

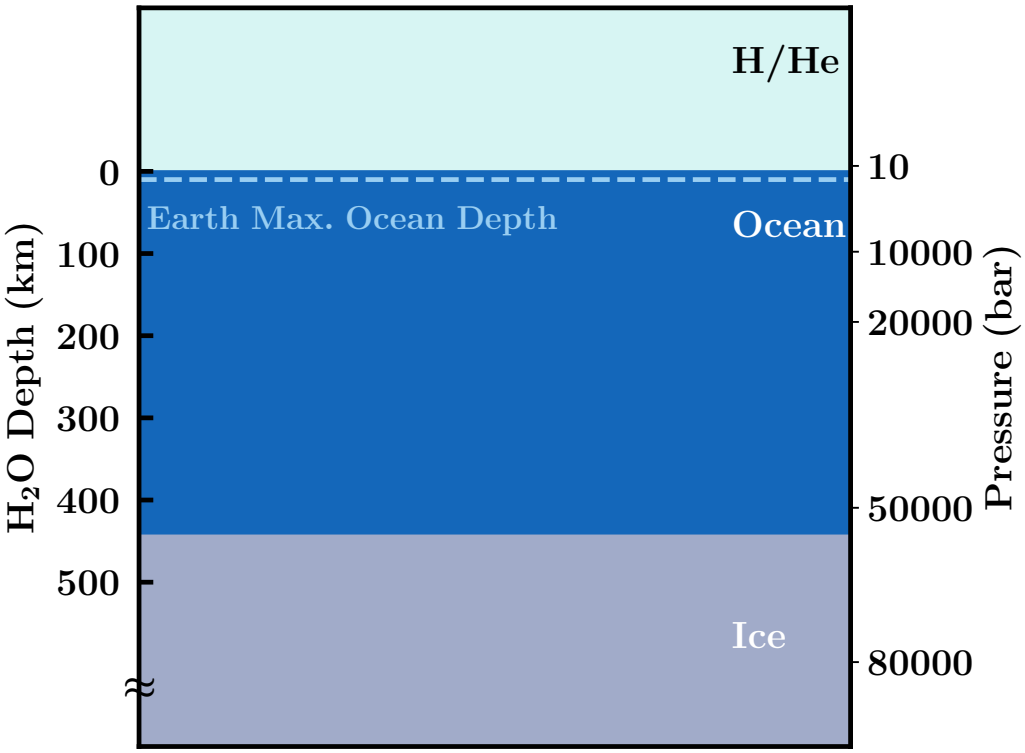

Fig. 2.10 One-dimensional cross-section of a possible ocean of TOI-270 d. This corresponds to a case with an ocean depth of 443 km. The maximum ocean depth on Earth is shown as a dashed line, at 11 km.

The habitability of a hycean world depends on a range of factors. In Figure 2.10 we show an example of a possible ocean cross-section for the planet TOI-270 d. The maximum depth of Earth's ocean is shown by the dashed line, at ∼11 km (Gardner et al., 2014). Life in Earth's oceans spans the entire depth, down to pressures of ∼1000 bar (Rothschild and Mancinelli, 2001; Merino et al., 2019). As we have shown in Section 2.3, the depth of hycean oceans can span hundreds of km down to pressures of $\sim 10^4 - 10^5$ bar ($10^9 - 10^{10}$ Pa) where the transition to ice VI or VII occurs. In this example in Figure 2.10, the ocean base pressure is at 5.5×10^4 bar. Therefore, the majority of the ocean exists at temperatures and pressures greater than those known to host life on the Earth. We define the "habitable depth" as the depth at which we reach $P = 1000$ bar and/or $T = 400$ K. In this example in Figure 2.10, the habitable

depth is 20 km, where we reach 1000 bar (at 394 K), for an HHB at ∼10 bar and 387 K. The habitable depth in this case is approximately double the deepest point of Earth's ocean. Assuming the same surface gravity and temperature, an HHB at lower pressure would result in a larger habitable depth, due to the dependence of depth on the change in pressure. However, changing the HHB pressure within our permitted range makes little difference to the overall ocean depth, which is evident from the rapid increase of pressure with depth shown in Figure 2.10. We should also note that it is unknown whether life could evolve to exist in conditions beyond these Earth-based pressures and temperatures, extending the potentially habitable portion of the ocean.

Hycean planets are generally expected to have high-pressure ice layers beneath their oceans. The presence of an icy mantle separating the ocean from the rocky core may have implications for the habitability of water-rich bodies (Maruyama et al., 2013; Noack et al., 2016; Journaux et al., 2020b; Madhusudhan et al., 2023a). For instance, the prevention of silicate weathering has been suggested to affect geochemical cycling (e.g. Kitzmann et al., 2015). However, alternative mechanisms have already been proposed for ocean worlds with higher mean molecular weight atmospheres which can also possess high-pressure ice layers (Kite and Ford, 2018; Levi et al., 2017; Ramirez and Levi, 2018). The geochemical cycles that would occur in hycean environments are unknown (Madhusudhan et al., 2021) and future work is needed to investigate these possibilities.

The implications of high-pressure ice layers have also been discussed in the context of ocean nutrient enrichment (e.g. Noack et al., 2016; Madhusudhan et al., 2023a). The lack of contact between the ocean and mantle prevents the weathering of the seafloor that can enrich the ocean with nutrients needed for life. Madhusudhan et al. (2023a) suggest alternative ways to meet the chemical requirements for life in hycean oceans, including atmospheric condensation and external delivery from asteroids/comets. However, transport across high-pressure ice layers has also been suggested as a possibility, based on a number of works studying convection in the high-pressure ices that could be present on water-rich exoplanets (Choblet et al., 2017; Kalousová et al., 2018; Kalousová and Sotin, 2018; Hernandez et al., 2022; Lebec et al., 2023; Madhusudhan et al., 2023a), along with work on icy moons (e.g. Lingam and Loeb, 2018; Journaux et al., 2020b). The cases shown in Section 2.3 have high-pressure ice layers that can generally extend for $\gtrsim 1$ $R_\oplus$. As is intuitive, a smaller mass of H_2O results in a thinner high-pressure ice layer. For example, as discussed in Section 2.3.2, for TOI-1468 c we find the ice can be as thin as 0.42 $R_\oplus$ for an interior with the minimum permitted mass fraction of H_2O, while still maintaining an ocean depth

of 189 km. The thinner the ice layer, the smaller the distance required to transport nutrients across. However, the behaviour of high-pressure ices is largely unknown, including potential interactions between high-pressure ice and the underlying rock (e.g. Journaux et al., 2020b), and future investigation is required to address these areas.

Our hycean candidates orbit M dwarfs, which are generally more active than higher mass stars. Effects such as stellar wind and higher UV flux are able to erode a planet's atmosphere, which has the potential to make environments hostile to life (e.g. Shields et al., 2016). However, the level at which a planet will be inhospitable is thought to be significantly dependent on the atmospheric composition and the level of host star activity (e.g. O'Malley-James and Kaltenegger, 2017). As pointed out by Madhusudhan et al. (2021), hycean planets may be more habitable than terrestrial planets around M dwarfs due to their larger gravity and thicker atmospheres. Furthermore, for instance, TOI-270 has been shown by multiple studies (Günther et al., 2019; Van Eylen et al., 2021; Mikal-Evans et al., 2023) to have low stellar activity levels. LTT 3780 (TOI-732) has also been found to be relatively inactive (Nowak et al., 2020; Cloutier et al., 2020), as has TOI-1468 (Chaturvedi et al., 2022). Therefore, these hycean candidates may stand to be among the more promising candidates for life around M dwarfs. Nevertheless, habitability remains a complex topic and a rigorous assessment would need to be made on a planet-by-planet basis.

2.4.2 Mixed Envelopes

In this chapter we have not explicitly included mixed envelopes of H_2O and H/He. The difference in the radius obtained assuming a mixed vs an unmixed envelope is found to be less than the measured uncertainty in R_p of ~ 0.1 $R_\oplus$ for the majority of the hycean candidates. This is in agreement with Nixon and Madhusudhan (2021) finding that 1% H_2O mixed in a H/He atmosphere has a minimal effect on the radius. They adopted a 5% envelope fraction, $T_0 = 500$ K, $P_0 = 0.1$ bar and $P_{rc} = 10$ bar, giving vapour or supercritical H_2O in the envelope to increase the likelihood of miscibility. It should be noted that for hycean cases, the temperatures in the envelope are much less than considered by Nixon and Madhusudhan (2021), with a maximum of 400 K. The envelope mass fractions of hycean worlds are also $\sim 10 - 100\times$ smaller than this. Therefore, the effect of the mixed envelope is expected to be even less. In their study of K2-18 b, Madhusudhan et al. (2020) find the median mixing ratio of H_2O to be 0.7–1.6% across the models considered. With such mixing ratios, they find the radius difference to be less than half the measured uncertainty when a mixed envelope is considered. However, the recent study with JWST found a non-detection of H_2O (Madhusudhan

et al., 2023b), differing from the previous study with HST due to degeneracy with CH_4. The low H_2O mixing ratio implies the presence of a tropospheric cold trap resulting in condensation, with H_2O possibly more abundant below (Madhusudhan et al., 2023a,b).

Therefore, given the current level of uncertainty in radius measurements, incorporating the effect of a mixed envelope into our calculations would introduce an extra source of degeneracy in determining interior compositions, while not significantly affecting results for possible ocean depths. JWST observations of hycean candidates and sub-Neptunes generally can better constrain their H_2O mixing ratios. For instance, for TOI-270 d Mikal-Evans et al. (2023) found with HST a 99% credible upper limit of 30% for the mixing ratio of H_2O, which ruled out a steam atmosphere. Given precise estimates, we can adopt representative mixed envelope EOSs in future studies of these planets. JWST observations will allow more precise H_2O abundance estimates for both TOI-270 d and K2-18 b[2], and observations of other candidate hycean worlds will reveal the diversity in H_2O abundance. We note that as uncertainties in R_p measurements improve with next-generation facilities, it could become important to consider the effect of mixed envelopes.

2.4.3 Future Directions for Internal Structure Modelling

A degenerate set of interior compositions can typically explain the bulk properties of an exoplanet in the sub-Neptune regime. Precise mass and radius measurements are therefore critical for internal structure modelling, as these can reduce the number of plausible solutions. This is evident from Figure 2.7, and from the variation in possible H/He mass fractions for TOI-732 c based on the available sources for M_p and R_p measurements. The other essential avenue is atmospheric observations, which can help to break the degeneracy – this will be discussed further in Section 2.4.4 and in the subsequent chapters of this thesis.

There are a number of assumptions made in our internal structure model, including our adopted EOSs, that may be investigated in the future. We do not consider the effect of hydrated silicate/iron layers, which was recently investigated by Shah et al. (2021). However, the effect on the M-R relation for super-Earths was found to be smaller than the current typical precision of measurements. We also note that Shah et al. (2021) only focused on masses $< 3\ M_\oplus$, and hence the effects for larger mass sub-Neptunes, as considered in this chapter, have not been investigated. Including lighter elements such as sulfur in the iron core would also reduce the density of the rocky layers (Hakim

[2]E.g. see the most recent observational constraints for K2-18 b (Hu et al., 2025).

et al., 2018). Similarly, incorporating the effect of thermal expansion for these layers should be considered in future, beyond the simplistic cold EOS treatment. However, for hycean worlds with large water mass fractions, the water EOS at high-pressures is likely the larger source of uncertainty.

Furthermore, the behaviour of high-pressure ices is largely unknown. This includes potential interactions between the high-pressure ices and underlying rock. Vazan et al. (2022) suggest that for the mass range $5 - 15$ $M_\oplus$, ice and rock can be mixed in the interiors of sub-Neptunes, but whether this occurs is dependent on the conditions at formation. We also note that the phase transitions and EOS of high-pressure ices are still very uncertain and require further study. Our H_2O EOS can be modified as new data becomes available. For instance, recent studies have revealed a new phase of ice VII known as ice VIIt (Grande et al., 2022) which is suggested to have an effect on the M-R relation comparable to observational uncertainties (Huang et al., 2021).

We have adopted an adiabatic profile throughout the H_2O layer, as is commonly assumed in internal structure models for sub-Neptune-sized planets (e.g. Sotin et al., 2007; Nixon and Madhusudhan, 2021; Leleu et al., 2021). However, the presence of thermal boundary layers in the interior would form barriers to convection and could affect the permitted compositions. The effect of these layers has been explored for Uranus and Neptune (e.g. Podolak et al., 2019).

2.4.4 Observational Prospects

As we have shown in this chapter, and has been discussed thoroughly in the literature (e.g. Rogers and Seager, 2010a; Valencia et al., 2013; Leleu et al., 2021; Nixon and Madhusudhan, 2021), the bulk properties of a sub-Neptune are insufficient to place robust constraints on its composition, due to degenerate solutions. Atmospheric data are key for breaking these degeneracies. The first question for these planets will be establishing the presence or lack of an H_2-rich atmosphere. Atmospheric observations with HST and/or JWST have already confirmed H_2-rich atmospheres for K2-18 b (Benneke et al., 2019; Tsiaras et al., 2019; Madhusudhan et al., 2023b) and TOI-270 d (Mikal-Evans et al., 2023). However, even if the presence of an H_2-rich atmosphere is established, hycean worlds can be degenerate with sub-Neptunes with either an H_2-rich envelope and a solid rocky surface, or with a deep H_2-rich atmosphere that causes the surface to be too hot to sustain liquid H_2O. The essential step in diagnosing a hycean world is thus establishing the presence of the surface ocean. This requires precise abundances for a number of different molecules and a comprehensive exploration of the possible chemical pathways on the planet given these abundances. The key molecules

are H_2O, CH_4, NH_3, CO_2 and CO, in addition to any other hydrocarbons present (Yu et al., 2021; Hu et al., 2021; Tsai et al., 2021; Madhusudhan et al., 2023a). Figure 8 in Madhusudhan et al. (2023a) summarises the route to chemically diagnosing a hycean world via these molecules. In the recent study by Madhusudhan et al. (2023b), enhanced CH_4 and CO_2 were detected along with a lack of NH_3 in the observable atmosphere of K2-18 b, suggesting the presence of a surface ocean. This was carried out using JWST transmission spectra for one transit with each of NIRISS SOSS (Single Object Slitless Spectroscopy) and NIRSpec G395H. Additional upcoming JWST observations of K2-18 b, including one transit with MIRI LRS (Low Resolution Spectroscopy) via the same program (GO 2722) and multiple transits with NIRSpec G395H via GO 2372, can verify these detections.[3]

The planets TOI-270 d, TOI-1468 c and TOI-732 c are also scheduled for spectroscopic observations with JWST in Cycle 2. For each planet, at least three transits will be observed, one with each of NIRISS SOSS, NIRSpec G395H and MIRI LRS; for TOI-270 d, additional NIRISS and NIRSpec observations will be obtained[4]. These will be observed in multiple programs (GO 3557, GTO 2759, GO 4098). As discussed above, the same combination of observations is also being carried out for K2-18 b in multiple programs (GO 2722 and GO 2372). The predicted uncertainties and long wavelength coverage are expected to allow robust detections of the key molecules required to diagnose a hycean planet. The observations are hence expected to aid the distinction of a hycean world from scenarios of a rocky planet with a thick H/He envelope, mini-Neptune or water world as outlined above, akin to the initial findings for K2-18 b (Madhusudhan et al., 2023b). LHS 1140 b has also been observed as part of Cycle 1 GO Program 2334, with a transit observed with each of NIRSpec G395H and G235H[5].

Hycean worlds are promising candidates for biomarker detection due to their larger radii and higher temperatures compared to rocky planets. Madhusudhan et al. (2021) investigated the observability of biomarkers in the atmospheres of hycean candidates K2-18 b, TOI-270 d and TOI-732 c, considering DMS, CS_2, CH_3Cl, OCS and N_2O as biomarkers. They predicted that the approved observations of K2-18 b in Cycle 1 would be sufficient to detect biomarkers in its atmosphere if present in the quantities considered. Potential evidence for DMS in the atmosphere of K2-18 b was suggested

[3]These observations have since been published in Madhusudhan et al. (2025) and Hu et al. (2025).

[4]These observations for TOI-270 d have since been published as Holmberg and Madhusudhan (2024) and Benneke et al. (2024).

[5]These observations for LHS 1140 b have since been published as Cadieux et al. (2024a) and Damiano et al. (2024).

by Madhusudhan et al. (2023b), though the abundance is not robustly constrained by the retrieval. They note the need for further theoretical exploration of atmospheric and interior processes when evaluating the viability of any possible biosignature.

The prospect of identifying hycean worlds amongst the exoplanet population and potentially detecting signs of life on them has recently become a tangible possibility. There remains the exciting potential for life's existence on a planet vastly different to our own. Additional theoretical studies in the future could help further develop our understanding of hycean worlds and their potential to support life.

Chapter 3

Towards a Self-Consistent Evaluation of Gas Dwarf Scenarios for Temperate Sub-Neptunes

3.1 Introduction

The nature of the sub-Neptune population remains debated, as their bulk densities can be explained by a number of degenerate interior compositions (e.g. Rogers et al., 2011; Valencia et al., 2013). These include rocky planets with diverse atmospheric compositions, mini-Neptunes with volatile-rich interiors and deep H_2-rich atmospheres, and water worlds with substantial water mass fractions, including hycean worlds (e.g. Rogers et al., 2011; Valencia et al., 2013; Dorn et al., 2017; Zeng et al., 2019; Madhusudhan et al., 2020, 2021; Rigby and Madhusudhan, 2024).

The James Webb Space Telescope (JWST) is revolutionising our understanding of sub-Neptunes through high-precision atmospheric spectroscopy. Such observations have led to confident detections and precise abundance constraints for CH_4 and CO_2 in the atmospheres of the habitable-zone sub-Neptune and candidate hycean world (Madhusudhan et al., 2021) K2-18 b (Madhusudhan et al., 2023b), demonstrating the promise of JWST for detailed atmospheric characterisation. Furthermore, such observations are starting to be available for other temperate sub-Neptunes, including TOI-270 d (Holmberg and Madhusudhan, 2024; Benneke et al., 2024) – where abundance constraints for CH_4 and CO_2 were also retrieved – and LHS 1140 b (Cadieux et al., 2024a; Damiano et al., 2024). These precise abundance measurements pave the way towards understanding the interactions between the planet's atmosphere and interior,

including the presence and nature of an underlying surface, as well as the planetary formation processes that give rise to such planets.

As discussed in previous chapters, one of the most distinct features of the sub-Neptune population is the radius valley, a bimodal distribution of sub-Neptune radii with a minimum around 1.8 $R_\oplus$ (Fulton et al., 2017; Fulton and Petigura, 2018a; Cloutier and Menou, 2020). Two competing hypotheses have been proposed to explain the origin of the radius valley. One explanation suggests that the valley is a consequence of differential atmospheric mass loss between planets of different masses. In this hypothesis, both populations would be composed of planets with predominantly rocky interiors. The more massive planets would retain their primary H_2-rich atmospheres, while the less massive ones would instead largely lose their envelope and hence have a smaller radius. We refer to the larger population, with rocky interiors and a deep H_2-rich atmospheres, as gas dwarfs. The mechanism for the mass loss is debated, with the predictions of two hypotheses – photoevaporation (e.g. Lopez and Fortney, 2013; Jin et al., 2014; Owen and Wu, 2017; Jin and Mordasini, 2018) and core-powered mass loss (e.g. Ginzburg et al., 2016; Ginzburg et al., 2018; Gupta and Schlichting, 2019, 2020) – both proposed to explain the observations (Rogers et al., 2021), potentially in combination (Owen and Schlichting, 2024). The second explanation (e.g. Zeng et al., 2019; Venturini et al., 2020; Izidoro et al., 2021) suggests that the valley could instead be due to planets having different interior compositions. The smaller radius population would be rocky, as in the atmospheric mass-loss scenario, while the larger population would be composed of planets with water-rich interiors due to significant accumulation of icy planetesimals/pebbles during their formation and migration. Atmospheric observations of planets in the sub-Neptune range may be able to distinguish between these two scenarios (e.g. Kite et al., 2019, 2020; Daviau and Lee, 2021; Gaillard et al., 2022; Schlichting and Young, 2022; Charnoz et al., 2023; Misener et al., 2023; Falco et al., 2024).

While the gas dwarf hypothesis has garnered significant attention in the literature (e.g. Lopez and Fortney, 2013; Jin et al., 2014; Ginzburg et al., 2016; Owen and Wu, 2017; Jin and Mordasini, 2018; Ginzburg et al., 2018; Gupta and Schlichting, 2019; Kite et al., 2019; Gupta and Schlichting, 2020; Kite et al., 2020; Bean et al., 2021; Schlichting and Young, 2022; Charnoz et al., 2023), several open questions remain. Firstly, it is unclear whether it is possible for rocky cores to accrete a substantial H_2-rich envelope without significant accretion of other volatiles and ices (Fortney et al., 2013; Venturini et al., 2024). Secondly, it is uncertain whether atmosphere-interior interactions would give rise to distinct atmospheric signatures. This might be expected

if the rocky surface were to be molten, giving rise to a magma ocean scenario (Schaefer et al., 2016; Schaefer and Fegley, 2017; Kite et al., 2019, 2020; Daviau and Lee, 2021; Gaillard et al., 2022; Schlichting and Young, 2022; Misener et al., 2023; Charnoz et al., 2023; Falco et al., 2024; Shorttle et al., 2024; Tian and Heng, 2024). However, it is not fully clear whether this scenario is possible, particularly for planets with a low equilibrium temperature. For these planets, only a subset of atmospheric structures, combining sufficient but not exceedingly high surface pressure and very high surface temperature, could result in magma at the base of the atmosphere.

Several recent studies have explored the implications of a magma ocean on the atmosphere and interior compositions of diverse planets, both with terrestrial-like (Schaefer et al., 2016; Schaefer and Fegley, 2017; Daviau and Lee, 2021; Gaillard et al., 2022; Tian and Heng, 2024) and H_2-rich atmospheres (Kite et al., 2019, 2020; Schlichting and Young, 2022; Misener et al., 2023; Charnoz et al., 2023; Falco et al., 2024; Shorttle et al., 2024; Tian and Heng, 2024). These works identify several key factors, including temperature and oxygen fugacity at the bottom of the atmosphere, that influence the composition of the atmosphere, driven by thermochemical equilibrium at the gas-melt interface. For example, some notable atmospheric signatures of reduced conditions in a rocky interior include potential nitrogen depletion (e.g. Daviau and Lee, 2021; Dasgupta et al., 2022; Suer et al., 2023; Shorttle et al., 2024) and a high CO/CO_2 ratio for H_2-rich atmospheres (Gaillard et al., 2022; Schlichting and Young, 2022). However, the interplay between the atmosphere, interior, and the corresponding surface-atmosphere interactions in sub-Neptunes is only beginning to be explored in a realistic manner (e.g. Kite et al., 2020; Schlichting and Young, 2022).

In this chapter[1], we present an integrated framework to investigate gas dwarf scenarios, including magma oceans, for temperate, H_2-rich sub-Neptunes. This framework, outlined in Section 3.2, includes atmospheric and internal structure modelling, melt-gas interactions, and both equilibrium and disequilibrium processes in the atmosphere, resulting in spectroscopic predictions of atmospheric observables. We consider thermochemical equilibrium at the magma-atmosphere interface, and the solubility of volatile (H, C, N, O, S) bearing species in magma. We explore the extreme case of the habitable-zone sub-Neptune and hycean candidate K2-18 b (Madhusudhan et al., 2020) to investigate the plausibility of a magma ocean (e.g. Kite et al., 2020; Shorttle

[1]The contents of this chapter are adapted from Rigby et al. (2024). This work was carried out with contributions from co-authors, who conducted the atmospheric structure calculations, the melt-atmosphere interface chemistry, and the spectral predictions, and contributed to the photochemical modelling and the writing of the manuscript. This paper was adapted to form part of a chapter in the thesis of co-author Måns Lars Holmberg.

et al., 2024) and, if present, its atmospheric signatures. In doing so, we first use our framework to perform a comparative assessment of previous works in this direction in Section 3.3, both on terrestrial-like atmospheres (Gaillard et al., 2022) and on H_2-rich ones (Kite et al., 2019, 2020; Schlichting and Young, 2022; Charnoz et al., 2023; Misener et al., 2023; Falco et al., 2024; Shorttle et al., 2024; Tian and Heng, 2024), with a focus on the case study of the candidate hycean world K2-18 b. We then present our model predictions in Section 3.4. Finally, we summarise our findings and discuss directions for future work in Section 3.5, highlighting the need for physically consistent models, and new experimental and theoretical work to derive accurate fundamental material properties.

3.2 Methods

We develop an integrated modelling framework to evaluate gas dwarf scenarios for planets in the sub-Neptune regime. A schematic flowchart of the framework is shown in Figure 3.1. We start by considering the constraints that the observed bulk parameters (mass, radius, and hence density) and known atmospheric properties impose on the planet's atmospheric and internal structure. This enables us to infer the possible surface conditions at the interior-atmosphere boundary, and, by considering a relevant mineral phase diagram, assess whether such conditions can in principle lead to a magma ocean scenario. If they can, we proceed by modelling the chemistry at the magma-atmosphere interface, which is determined by equilibrium processes including the solubility of relevant volatiles in the silicate melt, providing us with the elemental abundances in the gas phase at the interface. These are then evolved to the rest of the atmosphere, assuming chemical equilibrium in the lower atmosphere, and non-equilibrium processes (photochemistry and vertical mixing) in the upper atmosphere. This allows us to compute the observable composition of the atmosphere, which can be compared with the molecular abundances retrieved through observations to finally assess the plausibility of a magma ocean scenario for the planet. We now describe in detail each of the steps outlined above.

3.2.1 Atmospheric Structure and Composition

We begin by modelling the atmospheric temperature structure in a self-consistent manner. In order to do so, the atmospheric chemical composition needs to be assumed. This can be done either by assuming the elemental abundances and atmospheric

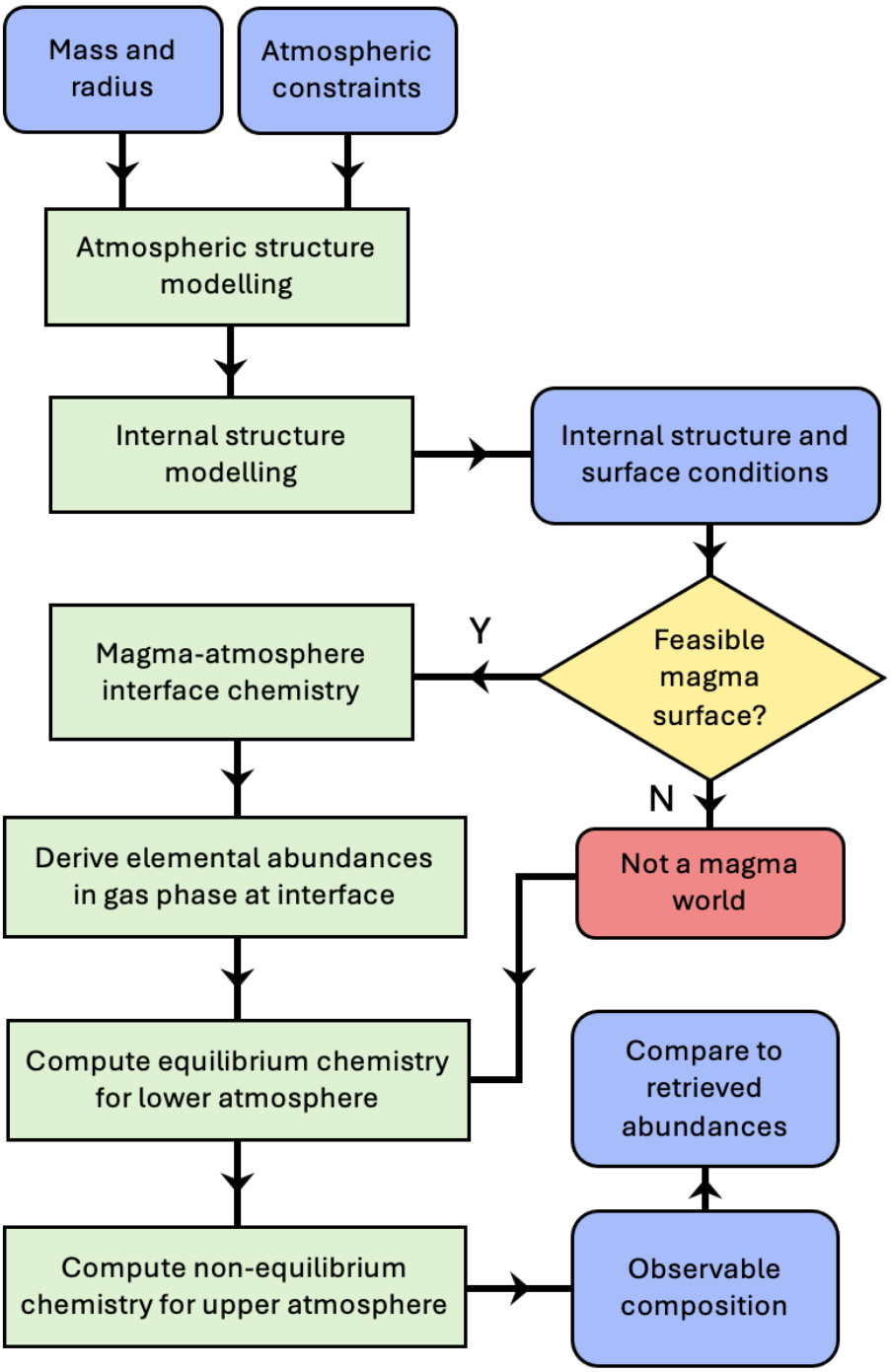

Fig. 3.1 Flowchart showing our integrated modelling framework to assess gas dwarf scenarios for planets in the sub-Neptune regime.

chemistry, or by directly assuming the molecular mixing ratios in the atmosphere. Other parameters that need to be taken into account include the internal temperature $T_{\rm int}$ representing an internal heat flux, the incident irradiation, the stellar properties, the presence and characteristics of clouds/hazes in the planet's atmosphere, and the efficiency of day-night energy redistribution. The self-consistent calculation will yield a pressure-temperature (P-T) profile, which will be coupled to the internal structure model, as discussed in Section 3.2.2.

In order to carry out the self-consistent modelling of the atmospheric structure, we use the GENESIS framework (Gandhi and Madhusudhan, 2017) adapted for sub-Neptunes (Madhusudhan et al., 2020; Piette and Madhusudhan, 2020; Madhusudhan et al., 2021, 2023a). GENESIS solves for radiative-convective equilibrium throughout the atmosphere, which is assumed to be plane-parallel, using the Rybicki scheme. It carries out line-by-line radiative transfer calculations through the Feautrier method (Hubeny, 2017) and the discontinuous finite element method (Castor et al., 1992), while taking into account all of the parameters mentioned earlier in this section.

For the atmospheric composition, we adopt uniform mixing ratios of molecular species based on the retrieved values at the terminator region of K2-18 b (Madhusudhan et al., 2023b). We use the median retrieved abundances for the one-offset case: $\log(X_{\rm CH_4}) = -1.72$ and $\log(X_{\rm CO_2}) = -2.04$. For H_2O, we consider the 95% one-offset upper limit, $\log(X_{\rm H_2O}) = -3.01$. We also assume the incident irradiation and stellar properties of K2-18 b, and uniform day-night energy redistribution. We then explore the remaining parameter space. In particular, we consider two end-member values for $T_{\rm int}$, 25 K and 50 K, following Madhusudhan et al. (2020) and Valencia et al. (2013), and three values for a, the haze Rayleigh enhancement factor: 100, 1500 and 10000. We consider four combinations of these parameters, obtaining a cold case (designated C1, corresponding to $T_{\rm int} = 25$ K, $a = 10000$), two canonical cases (both with $a = 1500$, designated C2 for $T_{\rm int} = 25$ K and C3 for $T_{\rm int} = 50$ K) and a hot case (C4, with $T_{\rm int} = 50$ K and $a = 100$). These profiles are shown in Figure 3.6.

We place the upper boundary of the atmosphere at 10^{-6} bar, and calculate the P-T profile self-consistently down to 10^3 bar, below the radiative-convective boundary. At higher pressures, we extrapolate the profile as an adiabat, using the H_2/He equation of state (EOS), $\rho = \rho(P, T)$, and adiabatic gradient from Chabrier et al. (2019). We note that, in principle, an appropriate P-T profile may be even colder than C1, considering the constraints on clouds/hazes at the terminator from observations of K2-18 b (Madhusudhan et al., 2023b).

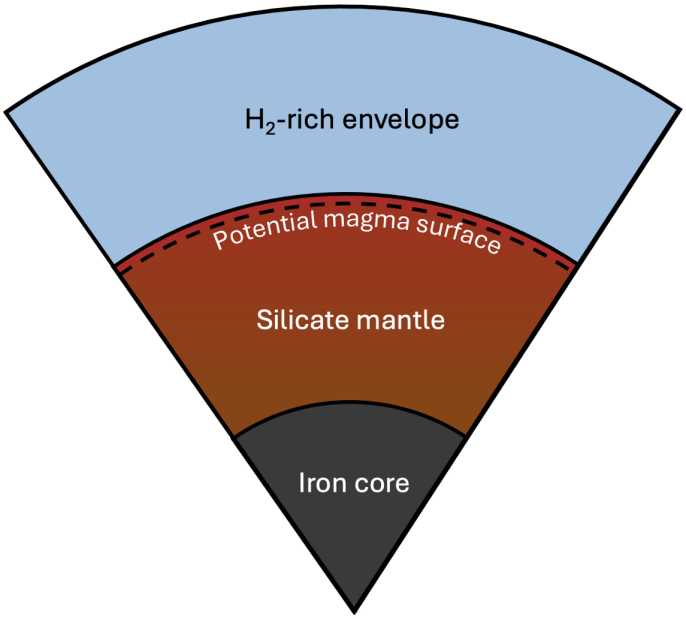

Fig. 3.2 Cross-section of the internal structure of a potential gas dwarf, including the H_2-rich envelope, silicate mantle and iron core.

3.2.2 Internal Structure Modelling

We model planetary internal structures using the HyRIS framework, outlined in Chapter 2. For the purpose of this study investigating gas dwarf scenarios, the internal structure model includes a H_2-rich envelope, a silicate mantle, and an iron core. A schematic of this structure is shown in Figure 3.2.

The silicate mantle is described by EOSs valid for the liquid and solid phases – for simplicity, we adopt a separate EOS prescription on either side of a melting curve. The composition is nominally assumed to be peridotitic. The magma is described by an EOS for peridotitic melt compiled similarly to Monteux et al. (2016), by combining the densities of molten enstatite, forsterite, fayalite, anorthite and diopside, described by third-order Birch-Murnaghan/Mie-Grüneisen EOSs from Thomas and Asimow (2013), weighted by their mass fractions. The resulting EOS for peridotitic melt is shown for different isotherms in Figure 3.3. For the purpose of this initial study, we assume that complete melting occurs at the liquidus, and hence do not include an EOS prescription for the partial melt between the solidus and liquidus curves. We use the peridotite liquidus from Monteux et al. (2016), based on Fiquet et al. (2010) – both the liquidus and solidus are shown in Figure 3.4 (Fiquet et al., 2010; Monteux et al., 2016).

The solid portion of the silicate mantle is described by the EOS of Lee et al. (2004) for the high-pressure peridotite assemblage. This EOS is also in the form

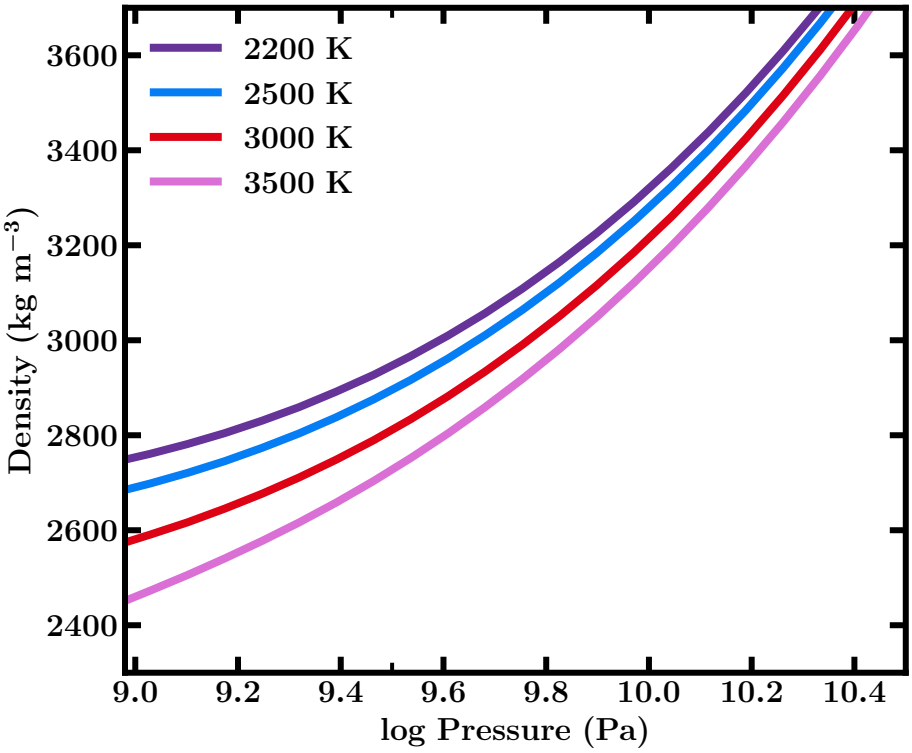

Fig. 3.3 Equation of state for peridotitic melt used in this chapter, shown for different isotherms. The EOS is compiled according to Monteux et al. (2016) using prescriptions from Thomas and Asimow (2013).

of a Birch-Murnaghan EOS with a Mie-Grüneisen thermal correction. At extreme mantle pressures beyond the pressure range of these experiments (107 GPa), we use the temperature-independent EOS of Seager et al. (2007) for $MgSiO_3$ perovskite, originally derived at room temperature. The thermal effects for solid silicates at these high pressures are small (Seager et al., 2007) with negligible effect on the internal structure. The iron core is described by the EOS of Seager et al. (2007) for hexagonal close-packed Fe, as in Chapter 2.

The temperature structure in the melt is assumed to be adiabatic. The adiabatic gradient (Equation 1.8) is calculated using the specific heat for peridotite from Monteux et al. (2016) and the volume expansion coefficient that we calculate from the combined peridotite melt EOS. The adiabatic gradient in the upper portion of the solid mantle is calculated following Lee et al. (2004). Following previous studies (e.g. Rogers et al., 2011; Nixon and Madhusudhan, 2021; Rigby and Madhusudhan, 2024), the

remaining solid portion of the interior is taken to be isothermal, as the EOSs used are temperature-independent (Seager et al., 2007).

The mass of the magma ocean follows from the adiabatic temperature profile in the melt, similarly to the calculation of water ocean depths by Nixon and Madhusudhan (2021) and Rigby and Madhusudhan (2024), as outlined in Chapter 2. The melt adiabat and hence the magma base pressure are defined by the surface pressure and temperature. For a given interior composition and corresponding surface conditions, the mass of the melt can thus be calculated. We adapt HyRIS to automate the extraction of the relevant melt characteristics, similar to the methods for water oceans in Chapter 2 (Rigby and Madhusudhan, 2024). The mass fraction of the melt is an important quantity for considerations of the available volatile reservoir, as discussed below. We note that the moderate increase of the magma ocean mass fraction that may result from partial melting is partly accounted for by our range of considered melt masses in Section 3.4.3.

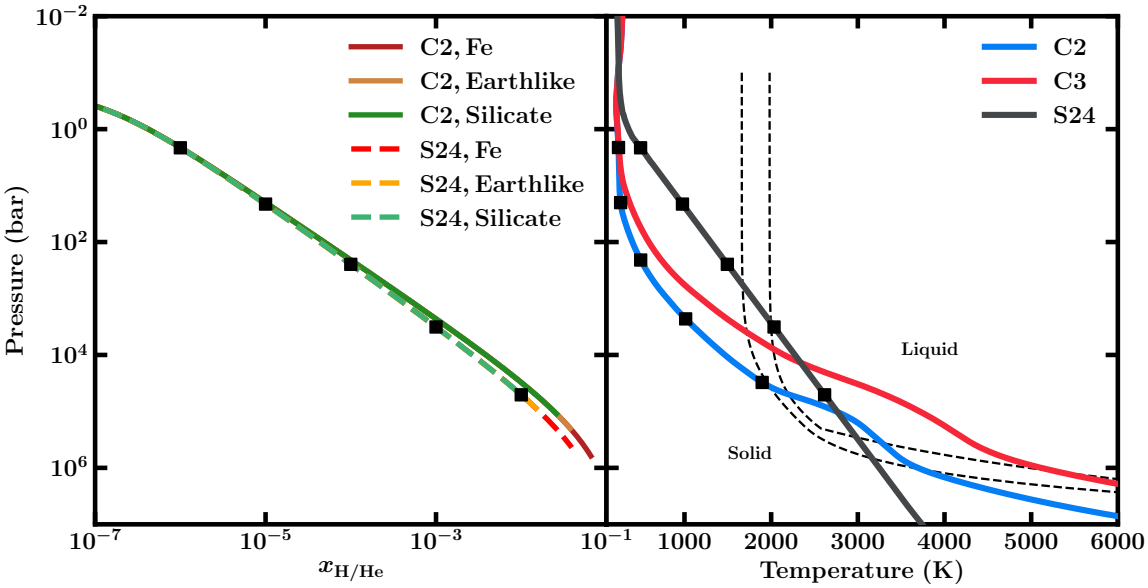

Fig. 3.4 Left: Pressure in the H_2-rich envelope against the envelope mass fraction above this pressure level. Solid and dashed lines show these assuming C2 and the profile used by S24 in the envelope respectively. The black squares indicate expected surface conditions for different envelope mass fractions, independent of satisfying the bulk properties of the planet. Right: The nominal pressure-temperature profiles generated for this work and the *P-T* profile from S24 are shown against the liquidus and solidus for peridotite (Fiquet et al., 2010; Monteux et al., 2016). The solid and liquid phases are shaded. The black squares again show the corresponding surface conditions expected for the different envelope mass fractions.

3.2.3 Melt-atmosphere Interface Chemistry

The atmospheric chemistry is constrained by the elemental composition at the bottom of the atmosphere, which is governed by the interactions at the interface of the magma ocean and atmosphere. At this boundary, we model the reactions and solubility of the gas species in thermochemical equilibrium. We include 82 H-C-N-O-S gas species and He, the set of which we denote X, and their equilibrium reactions, nominally excluding other effects such as condensation and exsolution. Of these volatile species, we consider the solubility in the melt of H_2 (Hirschmann et al., 2012, basalt case), H_2O (Iacono-Marziano et al., 2012), CO (Yoshioka et al., 2019, MORB case), CO_2 (Suer et al., 2023), CH_4 (Ardia et al., 2013), N_2 (Dasgupta et al., 2022), S_2 (Gaillard et al., 2022) and H_2S (Clemente et al., 2004), as further motivated in Appendix A.1. We note that the solubility of H_2S is uncertain at high temperatures/pressures and may be higher if, for example, its solubility approaches that of S_2. Furthermore, we are not considering the possible exsolution of FeS, which may affect the abundance of sulfur in the atmosphere. Likewise, the overall solubility of nitrogen is calculated here through N_2, and may be higher if the solubility of NH_3 is significant. The data on NH_3 solubility in magma is currently limited and it is difficult to make any quantitative estimates of NH_3 solubility. For the explicitly composition-dependent laws, we use the Iacono-Marziano et al. (2012) Etna basalt melt composition. As noted in Appendix A.1, this choice is due to the wide availability of solubility laws for basaltic melt and the association of basalt with peridotite, which we adopt as the mantle composition in the internal structure modelling. We note that basalt is formed from the partial melting of peridotite, meaning that the solubility behaviour may not be realistic for fully molten peridotite. In general, our choice of solubility laws were made by prioritising the validity at high-pressures and how recently the data was obtained – this is explained in detail in Appendix A.1. Similarly to Kite et al. (2020), we assume that the magma is well-stirred such that the equilibration at the surface sets the volatile abundance throughout the melt.

These solubility laws relate the partial pressures in the atmosphere to the concentrations of the volatiles in the melt. The amount of volatiles in the melt thus depends on the equilibrium chemistry, the solubility and the total mass of the melt, $M_{\rm melt}$. For a given mass of the atmosphere and the melt, which are determined by the internal structure model, we have the following mass balance condition for each species i (similar to Gaillard et al., 2022),

$$M_{\rm tot}\, w_i = M_{\rm atm}\, w_{i,\rm atm} + M_{\rm melt}\, w_{i,\rm melt}\,, \tag{3.1}$$

where w_i is the total mass fraction of each species i. The initial volatile budget is set by the mass of the atmosphere, assuming some atmospheric metallicity – in the following sections, we typically adopt 50× solar metallicity.

To determine the chemical composition of the atmosphere and the melt, we solve the element conservation equations

$$\varepsilon_j = \sum_{i \in \mathbf{X}} \nu_{ij} \frac{n_i}{n_{\langle \mathrm{H} \rangle}} \,, \tag{3.2}$$

where n_i is the total amount of moles of species i, $n_{\langle \mathrm{H} \rangle} = n_{\mathrm{H}} + 2n_{\mathrm{H_2}} + 2n_{\mathrm{H_2O}} + \dots$ is the total amount of moles of hydrogen, ν_{ij} are the coefficients of the stoichiometric matrix, and ε_j is the elemental abundance of element j relative to hydrogen. Equation (3.2) is coupled to Equation (3.1) via $n_i \propto w_i/\mu_i$, where μ_i is the molar mass, which in turn is coupled to the law of mass action,

$$\frac{p_i}{p^{\ominus}} = K_i \prod_{j \in E} \left(\frac{p_j}{p^{\ominus}} \right)^{\nu_{ij}} \,, \tag{3.3}$$

and the solubility laws, determining both $w_{i,\mathrm{atm}}$ and $w_{i,\mathrm{melt}}$. Here, E is the set of all elements, p_i is the partial pressure of species i, K_i is the temperature-dependent equilibrium constant, and $p^{\ominus}$ is a standard pressure of 1 bar. For each gas species, we approximate the equilibrium constant as

$$\ln K(T) = \frac{a_0}{T} + a_1 \ln T + b_0 + b_1 T + b_2 T^2 \,, \tag{3.4}$$

using the coefficients provided by FASTCHEM (Stock et al., 2018, 2022), mainly derived using thermochemical data from Chase (1998).

Overall, Equation (3.3) depends on the elemental partial pressures, with 6 unknowns, corresponding to the 6 elements considered. Nominally, we solve for these using the 5 equations in (3.2) for all elements apart from hydrogen, together with

$$P_s = \sum_{i \in \mathbf{X}} p_i \,, \tag{3.5}$$

to fix the total pressure. This treatment of oxygen yields a first-order estimate of the redox state as set by the atmosphere. Alternately, we consider oxygen fugacity (f_{O_2}) as a free parameter, by determining p_{O} in Equation (3.3) via $f_{\mathrm{O_2}} = p_{\mathrm{O_2}} = K_{\mathrm{O_2}}\, p_{\mathrm{O}}^2/p^{\ominus}$, allowing us to consider different redox conditions. In this framework, we assume ideal

gas behaviour such that fugacity and partial pressure are equivalent (e.g. Bower et al., 2022; Schlichting and Young, 2022).

As a cross-check, we validate our new framework against a self-consistent atmosphere composition model (e.g. Schaefer and Fegley, 2017) which uses the Gibbs free energy minimization code IVTANTHERMO (Belov et al., 1999). IVTANTHERMO uses a thermodynamic database based on Gurvich and Veyts (1990), which we modify to include the silicate-melt dissolved volatile species H_2, OH^-, O^{2-}, CO, CO_2, CH_4, N^{3-}, and S^{2-}. We calculate equilibrium between a total possible 366 gas species and 201 condensed species. For the dissolution reactions, we assume no change in isobaric heat capacity, $\Delta C_p = 0$, and that any temperature dependence in the equilibrium constant is due to the heat of the reaction. However, data is available only in limited temperature ranges for most dissolution reactions, so we assume a simple Henry's law solubility relation for all of the dissolved species except S^{2-}, OH^-, H_2, and CH_4. We also neglect non-ideality in both the gas phase and melt. Using IVTANTHERMO, we then compute self-consistent equilibrium between the gas phase and melt species as a function of pressure and temperature.

For this comparison, we use 50×solar bulk elemental abundances (not including He), $P_s = 10^4$ bar, $T_s = 3000$ K, and $M_{melt}/M_{atm} = 0.20$, which is given by the gas-to-melt mass ratio as calculated by IVTANTHERMO. We find that all major H-C-N-O-S gas species agree to within at most 0.35 dex (standard deviation of 0.1 dex), with the largest deviation coming from CO_2. This deviation mostly stems from the oxygen fugacities being somewhat different between the two approaches, with IVTANTHERMO yielding a 0.35 dex lower value. Furthermore, we verify that we recover the atmospheric abundances given by FASTCHEM 2 (Stock et al., 2022) and GGCHEM (Woitke et al., 2018) when setting $M_{melt} = 0$.

3.2.4 Atmospheric Chemistry

We carry out equilibrium and disequilibrium chemistry calculations to determine the atmospheric composition above the magma/rock surface. We use the VULCAN photochemical kinetics framework (Tsai et al., 2021), with the initial atmospheric chemistry obtained using the FASTCHEM equilibrium chemistry code (Stock et al., 2018).

For equilibrium chemistry calculations, we consider thermochemical equilibrium involving H-C-N-O-S species as well as He, along with H_2O condensation. For calculations considering disequilibrium processes, we additionally include the effects of vertical mixing and photochemistry. We follow the K_{zz} parameterisation of Madhusudhan et al.

(2023a):

$$K_{zz}/\mathrm{cm}^2\mathrm{s}^{-1} = \begin{cases} \min(\frac{5.6\times10^4}{(P/\mathrm{bar})^{\frac{1}{2}}}, 10^{10}), & P \leq 0.5 \text{ bar} \\ 10^6, & P > 0.5 \text{ bar}, \end{cases} \tag{3.6}$$

Although we note that the K_{zz} in the troposphere could be higher (e.g. $\sim 10^7 - 10^8$ cm^2 s^{-1}) in the deep convective region of the atmosphere or lower (e.g. $\sim 10^4$ cm^2 s^{-1}) in any radiative regions if moist convection is inhibited by the high molecular weight of water in the H_2-rich atmosphere (see Leconte et al., 2024). Accordingly, we consider a wider range of K_{zz} values than our canonical treatment in Section 3.4.5 and Appendix A.2.

Additionally, we consider photochemical reactions including H-C-N-O-S species, using a nominal stellar spectrum from the HAZMAT spectral library (Peacock et al., 2020) corresponding to a median 5 Gyr star of radius 0.45 $R_\odot$, following previous work (Madhusudhan et al., 2023a). We also specifically consider the condensation of H_2O to liquid and solid droplets, which fall at their terminal velocity, as described in Tsai et al. (2021). We note that while the H-C-N-O chemistry has been extensively explored for sub-Neptunes in various studies (e.g. Yu et al., 2021; Hu et al., 2021; Tsai et al., 2021; Madhusudhan et al., 2023a), the S chemistry has not been explored in significant detail and may be incomplete. Nevertheless, we include S using the VULCAN framework (Tsai et al., 2021) for completeness.

With the above calculations we obtain the vertical mixing ratio profiles for a number of relevant chemical species in the atmosphere. The abundances of key species in the observable part of the atmosphere can then be compared against the constraints retrieved from an atmospheric spectrum.

3.2.5 Spectral Characteristics

We use the results of the chemistry calculation described in Section 3.2.4 to simulate how such an atmosphere would appear in transmission spectroscopy, including the spectral contributions of relevant species. For this, we use the forward model generating component of the VIRA retrieval framework (Constantinou and Madhusudhan, 2024), which treats the planet's terminator as a 1D atmosphere in hydrostatic equilibrium. We consider atmospheric opacity contributions from H_2O (Barber et al., 2006; Rothman et al., 2010), CH_4 (Yurchenko and Tennyson, 2014), NH_3 (Yurchenko et al., 2011), CO (Li et al., 2015), CO_2 (Tashkun et al., 2015), C_2H_2 (Chubb et al., 2020), HCN (Barber et al., 2014), H_2S (Azzam et al., 2016; Chubb et al., 2018) and SO_2 (Underwood et al., 2016). We do not include N_2 in the model, as it has no significant absorption features

in the near-infrared and it is not present in significant enough quantities to affect the atmospheric mean molecular weight. We additionally consider atmospheric extinction arising from H_2-H_2 and H_2-He collision-induced absorption (Borysow et al., 1988; Orton et al., 2007; Abel et al., 2011; Richard et al., 2012), which provide the spectral baseline, as well as H_2 Rayleigh scattering. We simulate transmission spectra using the vertical mixing ratio profiles computed using VULCAN as described above, and the *P-T* profile appropriate to each case considered.

3.3 Results: Comparison with Previous Work

We now apply the framework described in Section 3.2 and compare with previous works on both terrestrial-like and sub-Neptune atmospheres.

3.3.1 Terrestrial-like Atmospheres

Many previous studies have investigated surface-atmosphere interactions for magma oceans underneath terrestrial-like atmospheres (e.g. Matsui and Abe, 1986; Elkins-Tanton and Seager, 2008; Hamano et al., 2013; Lebrun et al., 2013; Wordsworth, 2016; Kite and Schaefer, 2021; Lichtenberg et al., 2021; Bower et al., 2022; Gaillard et al., 2022). Recent studies have explored the implications of diverse interiors of exoplanets for their atmospheric compositions. Daviau and Lee (2021) proposed that, for reduced conditions, nitrogen is expected to be preferentially sequestered in the mantle, providing a valuable way to study the interior composition of such exoplanets. More recently, Gaillard et al. (2022) investigated the primordial distribution of volatiles within the framework of melt-atmosphere interactions and discussed applications for Venus and Earth. For the early Earth, they find that reduced conditions, with oxygen fugacity two dex below the iron-wüstite (IW) buffer, $f_{O_2} \lesssim IW - 2$, result in an atmosphere abundant in H_2, CO and CH_4 but depleted in CO_2 and N_2. On the other hand, for $f_{O_2} \gtrsim IW + 2$, CO_2 becomes the main atmospheric component, with significant levels of SO_2, N_2 and H_2O. In particular, the behaviour of nitrogen is a consequence of the high solubility of N_2 as N^3 in silicate melt at reducing conditions (e.g. Libourel et al., 2003; Dasgupta et al., 2022), via the following reaction

$$\frac{1}{2}\mathrm{N_2\,(gas)} + \frac{3}{2}\mathrm{O^2-_{(melt)}} \rightleftharpoons \mathrm{N^3-_{(melt)}} + \frac{3}{4}\mathrm{O_{2\,(gas)}}\,. \tag{3.7}$$

As a result, the melt concentration of N^{3}- is proportional to $f_{N_2}^{1/2}\ f_{O_2}^{-3/4}$, thus favouring low f_{O_2}. In conclusion, these works predict that the abundance of atmospheric nitrogen may be used as a diagnostic for the redox state of a rocky planet's mantle.

As a benchmark, we compare our melt-atmosphere equilibrium chemistry framework with Gaillard et al. (2022). We use their case with a magma ocean mass of half the bulk silicate mantle at $T = 1773$ K and with volatile contents of 90, 102, 3.3, and 126 ppm-wt for C, H, N, and S, respectively. With this, we reproduce their atmospheric composition as shown in Figure 3.5. Compared to our nominal setup in Section 3.2.3, we added a constraint for the hydrogen abundance and solved for the resulting mass of the atmosphere, coupled to the surface pressure using (Gaillard et al., 2022)

$$P_s = \frac{gM_{\mathrm{atm}}}{4\pi R_{\mathrm{p}}^2}\,, \tag{3.8}$$

where g is the gravitational acceleration at R_{p}. For a like-to-like comparison, we added the condensation of graphite and used the same gas species (excluding Ar) and solubility laws as Gaillard et al. (2022). Overall, we find good agreement between both implementations, with the most deviation coming from N_2 and CH_4. We find that the N_2 discrepancy comes from an inconsistency in the code by Gaillard et al. (2022), whereby they use a molar mass of 14 g/mol for N_2 instead of 28 g/mol. The remaining discrepancy is likely a result of minor differences in the implementations of the different reactions. We find that by accounting for some of these differences we can better match the result by Gaillard et al. (2022), as shown in Figure 3.5. For this purpose, in addition to considering their adopted molar mass, we implemented the reactions $CH_4 + 2\ O_2 \rightleftharpoons 2\ H_2O + CO_2$ and $H_2O \rightleftharpoons 0.5\ O_2 + H_2$ using the equilibrium constants by Gaillard et al. (2022) to obtain the partial pressures of CH_4 and H_2O, instead of deriving these from the elemental partial pressures as described in Section 3.2.3. We also used the oxygen fugacity of the IW buffer from Gaillard et al. (2022) instead of Hirschmann (2021).

3.3.2 Sub-Neptunes with Hydrogen-Rich Atmospheres

Several recent studies have also explored magma-atmosphere interactions in sub-Neptunes with rocky interiors and H_2-rich atmospheres. Kite et al. (2019) considered the impact of H_2 solubility in silicate melts on the radius distribution of sub-Neptunes, addressing the radius cliff, a sharp decline in the abundance of planets with $R_{\mathrm{p}} \gtrsim 3R_{\oplus}$. They find that the high solubility of H_2 in magma, especially at high pressure, limits the maximum radius that can be attained by sub-Neptunes through the accretion of

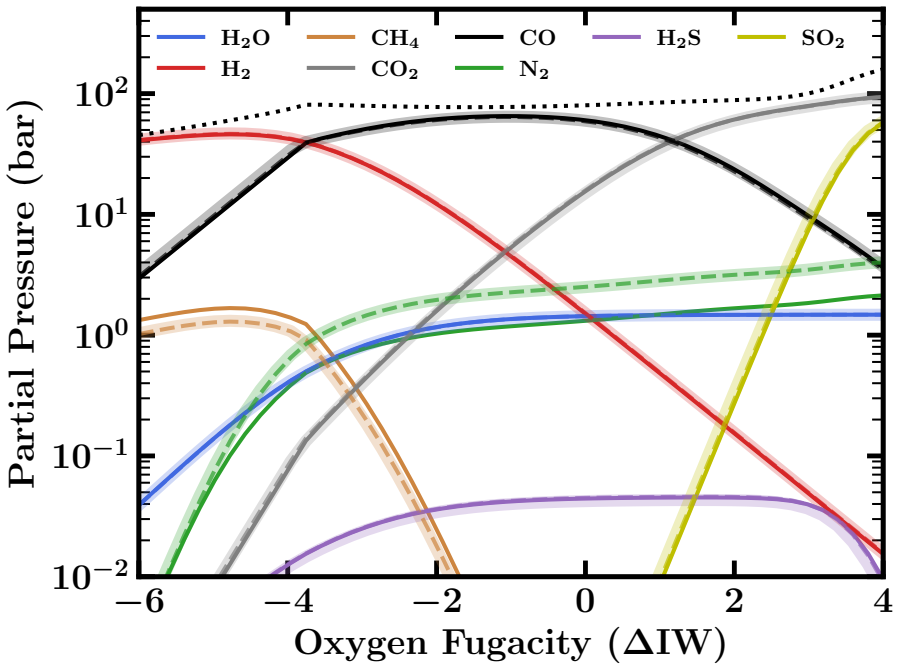

Fig. 3.5 Comparison with Gaillard et al. (2022), showing the atmospheric composition as a function of oxygen fugacity. The solid lines show the partial pressures from our melt-atmosphere framework, described in Section 3.2.3. The transparent lines are computed using the code from Gaillard et al. (2022), and the dashed lines are computed with our framework modified to approximate the results from Gaillard et al. (2022). The dotted line at the top illustrates the total surface pressure.

atmospheric H_2. For a 10 $M_\oplus$ core they find a limiting mass fraction of 1.5 wt% H_2 in the atmosphere – corresponding to $>$ 20 wt% H_2 in the planet – as any additional H_2 would be stored almost exclusively in the interior. Looking at smaller planets (2 $R_\oplus \leq R_p \leq$ 3 $R_\oplus$), Kite et al. (2020) find that magma-atmosphere interactions would significantly affect the atmospheric composition and mass. For example, a key insight is that the H_2O/H_2 ratio in the atmosphere reflects not only external water delivery, but also water production as a result of atmosphere-magma interactions. This would make the H_2O/H_2 ratio a good diagnostic for the atmospheric origin, as well as for the magma composition. In particular, it is found to be proportional to the magma FeO content.

Further investigations were carried out by Schlichting and Young (2022), Charnoz et al. (2023) and, most recently, Falco et al. (2024). Considering a surface temperature $T_s = 4500$ K, 1% to 14% H mass fractions (of overall planet mass) and model parameters resulting in $f_{O_2} \lesssim IW - 2$, Schlichting and Young (2022) find that the atmosphere is

expected to be dominated across the explored parameter space by H_2, SiO, CO, Mg and Na, followed by H_2O, which should exceed CO_2 and CH_4 by two to three orders of magnitude. It should be noted they do not include N in their model. Charnoz et al. (2023) and Falco et al. (2024), instead, consider total hydrogen pressures ranging between 10^{-6} and 10^{6} bar, temperatures between 1800 and 3500 K, and do not include any volatiles in their calculations, but also show that detectable absorption features of H_2O and SiO should be expected. Additionally, the volatile-free investigation by Misener et al. (2023) finds that silane (SiH_4) should also be expected, dominating over SiO at $P \gtrsim 0.1$ bar for an isothermal $T = 1000$ K P-T profile in the upper atmosphere. Most recently, Tian and Heng (2024) also investigated the outgassing mechanism for hybrid atmospheres in sub-Neptunes, but without considering solubilities in magma.

3.3.3 End-member Scenario of K2-18 b

Some of the principles described above were recently applied to the habitable-zone sub-Neptune K2-18 b by Shorttle et al. (2024), hereafter S24. Similarly to Schlichting and Young (2022) and Gaillard et al. (2022), S24 point to a high CO/CO_2 ratio and, like Daviau and Lee (2021) and Gaillard et al. (2022), a depletion in atmospheric N as signatures for the presence of a magma ocean and/or a reduced interior. It should be noted that the case of K2-18 b constitutes an end-member scenario. While most of the work on magma oceans has focused on very hot planets (e.g. Kite et al., 2016; Schaefer et al., 2016; Kite et al., 2020; Gaillard et al., 2022; Charnoz et al., 2023; Misener et al., 2023; Falco et al., 2024), K2-18 b is a temperate sub-Neptune with equilibrium temperature $T_{\rm eq} = 272$ K (assuming an albedo $A_{\rm B} = 0.3$), close to that of the Earth. Here, we assess the findings of S24 using the framework described in Section 3.2 and Figure 3.1.

We briefly note that in addition to gas dwarf and hycean world scenarios, a mini-Neptune scenario with a thick H_2-rich atmosphere has also been proposed for K2-18 b (e.g. Hu et al., 2021; Wogan et al., 2024). Wogan et al. (2024) conduct photochemical modelling of mini-Neptune cases for K2-18 b, suggesting a plausible solution. However, as noted in Glein (2024), the calculated abundances are unable to match the retrieved abundances (Madhusudhan et al., 2023b). In particular, the mixing ratios of CO and NH_3 are too large compared to the retrieved abundances, as is the CO/CO_2 ratio.

Consistency with Bulk Parameters

At the outset, it is important to ensure that any assumption about the internal structure is consistent with the planetary bulk parameters. Previous studies have shown that the bulk parameters of K2-18 b allow a degenerate set of solutions between a mini-Neptune, a hycean world, or a rocky world with a thick H_2-rich atmosphere, i.e. a gas dwarf (Madhusudhan et al., 2020, 2021; Rigby and Madhusudhan, 2024). Considering the present gas dwarf scenario, a purely rocky interior would require a minimum H_2-rich envelope mass fraction of $\sim$1% (Madhusudhan et al., 2020), as discussed below.

The model grid of S24 contains four values of mantle mass fraction relative to the total planet mass (0.001, 0.01, 0.1, and 1) and five values of the hydrogen mass fraction relative to the mantle mass (1, 10, 100, 1000 and 10000 ppm). Firstly, all the cases with a mantle mass fraction of 1 violate mass balance, as the sum of the mantle and atmospheric masses would exceed the total planet mass. Secondly, for the gas dwarf scenario, as noted above, the bulk density of K2-18 b requires an H_2-rich atmosphere with a minimum mass fraction of $\sim$1%. In the S24 model grid, there is only one model which has an atmospheric mass fraction of 1%, and it corresponds to a mantle mass fraction of 1, as noted above. It follows that all the remaining cases, with H_2 mass fraction below 1%, are incompatible with the planet's bulk density.

In order to estimate the allowed atmospheric mass fractions for K2-18 b in the gas dwarf scenario, we consider four possible interior compositions, illustrated in Table 3.1: $f_{\rm silicate} = 100\%$, Earth-like ($f_{\rm silicate} = 67\%$), Mercury-like ($f_{\rm silicate} = 30\%$) and $f_{\rm silicate} = 5\%$, where $f_{\rm silicate}$ is the mass fraction of the interior (i.e. excluding the envelope) in the silicate mantle. We include $f_{\rm silicate} = 5\%$ as a high-density end-member case, close to the upper limit for the allowed envelope mass fraction. Similarly, the extreme pure-silicate interior case is included as an end-member, yielding the lower limit on the allowed envelope mass fraction for a gas dwarf scenario. We adopt the median planetary mass $M_{\rm p} = 8.63$ $M_\oplus$ (Cloutier et al., 2019) and radius $R_{\rm p} = 2.61$ $R_\oplus$ (Benneke et al., 2019) of K2-18 b. The allowed envelope mass also depends on the choice of *P-T* profile, with hotter profiles leading to lower envelope masses for a given interior composition, as shown in Table 3.1.

Considering the four self-consistent *P-T* profiles described in Section 3.2.1, we find that an envelope mass fraction $x_{\rm env} \geq 1.34\%$ is required for consistency with the bulk parameters. This limit corresponds to the extreme case of a 100% silicate interior, adopting C4 for the envelope *P-T* profile. For a like-to-like comparison with the S24 model grid, we also consider their *P-T* profile, which is the profile from Benneke et al. (2019) log-linearly extrapolated to higher pressures. For this profile, we find envelope

mass fractions of $x_{\rm env} \geq 0.90\%$ are required, again corresponding to the extreme 100% silicate interior case. Overall, we find that all the models in the model grid of S24 are incompatible with mass balance and/or the bulk density of the planet considered. We demonstrate a self-consistent approach of accounting for the observed bulk parameters of K2-18 b in such calculations in Section 3.4.

Feasibility of a Magma Ocean

As described in Section 3.2.2 and shown in Figure 3.4, given an interior composition, the choice of P-T profile affects the resulting envelope mass fraction. This, in turn, determines the surface pressure and temperature and the liquid/solid phase of the rocky surface underneath. Therefore, it is important to consider a physically motivated P-T profile in the envelope. As mentioned above, S24 consider the P-T profile from Benneke et al. (2019) at low pressures ($P \leq 4$ bar) and perform a log-linear extrapolation to the deep atmosphere. The resulting temperature gradient can be significantly different from other self-consistent model P-T profiles for the H_2-rich envelope (e.g. Hu, 2021; Madhusudhan et al., 2023a; Leconte et al., 2024); an example is shown in Figure 3.4.

We also note, however, that the actual surface temperature at the magma-atmosphere interface ($T_{\rm s}$) used in S24 appears to be a free parameter rather than self-consistently determined from their P-T profile. The $T_{\rm s}$ ranges between 1500 K and 3000 K, but the corresponding pressure is not clear, considering their assertion that the maximum surface pressure allowed by the model is 10^8 bar. This pressure also appears to be inconsistent with their maximum envelope mass fraction of 1%. Across the range of rocky compositions we consider, the maximum pressure reached is $\sim$5-7$\times10^5$ bar for envelope mass fractions $\sim$5-7% depending on the P-T profile, as shown in Table 3.1 and Figure 3.4.

Nevertheless, in order to establish the feasibility of achieving melt conditions in the S24 model, we consider the five highest envelope mass fractions used in S24. We adopt their mantle mass fraction of 1 and the corresponding five H_2 mass fractions in their model grid, with a maximum of 1%. We then use these envelope mass fractions and the S24 P-T profile to determine the corresponding expected surface pressures and temperatures, independent of satisfying the planetary bulk properties. These model points are shown in Figure 3.4 along with the liquidus and solidus curves for peridotite (Fiquet et al., 2010; Monteux et al., 2016). We find that only two of these five cases result in a magma surface in our framework. Finally, since we considered only the five highest envelope mass fractions of S24, it follows that all of the other models would also be unlikely to result in melt. We further note that for the two cases that result in

a magma surface in S24, the magma mass fraction they consider is equal to the planet mass. However, based on the temperature structures shown in Figure 3.6, we find that the maximum magma mass fraction across the different interior compositions is ∼13%, potentially somewhat higher as a result of partial melting, but not 100%.

Magma-Atmosphere Interactions

If the plausibility of a magma ocean is established, the melt-atmosphere interaction must be considered to determine its effect on the atmospheric composition. As described in Section 3.2.3, the gas phase composition depends on the pressure and temperature at the interface, the elemental abundances, the amount of magma available, the solubilities of the chemical species, and the chemical properties of the melt.

For the case of K2-18 b, S24 consider oxygen fugacity as a free parameter and assess the abundances of several H-C-N-O species in the lower atmosphere following melt-atmosphere interactions. They determine the atmospheric composition by considering three reactions, $CO_2 + 2\ H_2 \rightleftharpoons CH_4 + O_2$, $2CO_2 \rightleftharpoons 2\ CO + O_2$, and $2H_2O \rightleftharpoons 2\ H_2 + O_2$, in thermochemical equilibrium, and solubilities of CH_4, N_2, CO_2, and H_2O in the magma. However, we note that these reactions do not encompass all the prominent H-C-N-O molecules at the considered conditions. In particular, NH_3 is expected to be the dominant N-bearing species at the base of the atmosphere. By not including NH_3 and its equilibrium with N_2 and H_2, S24 may be overestimating the nitrogen depletion in the atmosphere, given that all of the nitrogen is assumed to be in N_2, which is very soluble in magma at reducing conditions, as we show in Figure A.1 in Appendix A.1.

In our framework, described in Section 3.2.3, we find that nitrogen depletion in the atmosphere increases by several orders of magnitude by not including NH_3. Ultimately, this highlights the importance of the completeness of the reactions and solubilities considered. Finally, we note that it is also possible to not have significant N depletion even in the presence of a molten surface depending on the pressure and temperature, as shown in Table 3.1.

Atmospheric Composition and Observables

The properties at the surface determine the composition in the upper layers of the atmosphere, and hence its observable characteristics. These are strongly influenced by model assumptions on elemental abundances. S24 allow the C/H ratio to vary between 0.01× solar and 100× solar, while keeping the N/H ratio fixed to solar, i.e., $N/H = 6.76 \times 10^{-5}$ by number. This itself limits the NH_3 log-mixing ratio to at most $\log(X_{NH_3}) \sim -4$, close to the upper bound of -4.46 found by Madhusudhan et al.

P-T **Profile**	f_{silicate} (% of interior)	x_{interior} (%)	x_{env} (%)	T_{s} (K)	P_{s} (10^5 bar)	x_{melt} (%)	**C/H (log)**	**N/H (log)**	**O/H (log)**	**S/H (log)**
C1	5	93.01	6.99	3278	6.52	0	-1.84	-2.47	-1.61	-3.18
	30	94.35	5.65	3120	3.99	0	-1.84	-2.47	-1.61	-3.18
	67	95.91	4.09	2928	2.15	0.86	-1.84	-4.54	-1.65	-3.21
	100	97.10	2.90	2664	1.23	2.02	-1.84	-3.51	-1.70	-3.25
C2	5	93.40	6.60	3461	6.27	0	-1.84	-2.47	-1.61	-3.18
	30	94.71	5.29	3290	3.79	0	-1.84	-2.47	-1.61	-3.18
	67	96.24	3.76	3084	2.00	1.81	-1.84	-4.36	-1.69	-3.25
	100	97.38	2.62	2819	1.12	3.16	-1.83	-3.34	-1.76	-3.32
C3	5	94.94	5.06	4503	5.05	2.62	-1.83	-6.43	-1.75	-3.33
	30	96.17	3.83	4200	2.83	5.78	-1.83	-4.86	-1.89	-3.56
	67	97.48	2.52	3870	1.36	10.16	-1.83	-3.67	-2.07	-3.94
	100	98.38	1.62	3512	0.70	11.91	-1.82	-3.13	-2.15	-4.18
C4	5	95.43	4.57	4601	4.68	3.65	-1.83	-6.16	-1.81	-3.41
	30	96.61	3.39	4281	2.56	7.43	-1.83	-4.69	-1.98	-3.72
	67	97.84	2.16	3910	1.19	11.67	-1.82	-3.59	-2.15	-4.13
	100	98.66	1.34	3506	0.59	12.53	-1.81	-3.10	-2.21	-4.33

Table 3.1 The H/He envelope mass fraction, resulting surface temperature and pressure, and the melt mass fraction constrained by the median values of the K2-18 b bulk parameters ($R_{\text{p}} = 2.61$ $\text{R}_\oplus$, $M_{\text{p}} = 8.63$ $\text{M}_\oplus$), along with the atmospheric elemental abundances. We use four interior compositions, where 5% and 100% silicate are unrealistic extreme cases included for completeness, and the four self-consistent *P-T* profiles generated for this work. We note that the cases with $x_{\text{melt}} = 0\%$ may include a region of partial melt. The bulk elemental abundances in the melt and atmosphere combined are set to 50×solar.

(2023b), and biases the model by construction to allow for up to 100× more (or down to 100× fewer) C-based molecules than N-based ones. The dependence of the S24 model outcomes on the choice of C/H values is not reported. It should be noted that a 100× enhancement or depletion of C/H without any change in N may be difficult to reconcile with potential formation mechanisms.

We note two further points regarding the abundance of C- and N-bearing species predicted by S24. Firstly, S24 appear to indicate that the total abundances of carbon in their models reach up to 3.8 wt% of the planet mass. It is, however, unclear how this may be compatible with their assumptions of a C/H ratio of at most 100× solar and an H mass fraction $\leq 1\%$, given they adopt the Asplund et al. (2009) value for $(\mathrm{C/H})_\odot$, i.e., 3.2×10^{-3} by mass. Secondly, as argued in Section 3.3.3, only the largest atmospheric mass fractions S24 consider can potentially lead to a magma ocean. At the resulting surface pressures, however, their model predicts a log-mixing ratio for CO_2 of $\log X_{CO_2} \lesssim -3$. This is at the lowest end, if not outside, of the 1σ confidence interval presented in Madhusudhan et al. (2023b). Furthermore, the CO abundance or the CO_2/CO ratio are not reported in S24, making it difficult to assess the validity of the chemical estimates.

Finally, S24 argue that the model spectra from their model ensemble provide a qualitatively reasonable match to the data. Even if the model spectra were taken at face value, the lack of a reported goodness-of-fit metric precludes a reliable assessment of the match to data. More generally, a limited grid of forward models is insufficient to robustly explore the full model space taking into account all the degeneracies involved in an atmospheric spectral model and to obtain a statistically robust fit to the data; that is the purpose of atmospheric retrievals (Madhusudhan, 2018). A more reliable approach in the present context is to compare the model-predicted chemical abundances with the abundance constraints obtained from robust atmospheric retrievals of the observed spectra. As discussed above, the cases of S24 with the highest surface pressure, i.e. those that may allow a magma surface, still predict lower CO_2 abundances than those retrieved for K2-18 b (Madhusudhan et al., 2023b). The CO and H_2O abundances are not reported in S24, which prevents a clear assessment of the agreement between the chemical predictions and the retrieved abundances.

3.4 Results: A Case Study of K2-18 b

After having established the consistency of our results with Gaillard et al. (2022), and having discussed the S24 findings for K2-18 b, we proceed to apply our framework *ex*

novo. We do so for K2-18 b in the present section, starting, as outlined in Figure 3.1, with internal and atmospheric structure modelling that ensures consistency with the known bulk parameters. Through considering magma-atmosphere interactions, equilibrium chemistry in the lower atmosphere and non-equilibrium processes in the upper atmosphere, we make predictions for the observable composition and spectral signatures of a sub-Neptune gas dwarf.

3.4.1 Atmospheric Structure

As discussed in Section 3.2.1, the dayside atmospheric structure is calculated self-consistently from the atmospheric constraints retrieved in the one-offset case of Madhusudhan et al. (2023b): the median $\log(X_{\mathrm{CH_4}}) = -1.74$, $\log(X_{\mathrm{CO_2}}) = -2.04$, and the 2σ upper bound $\log(X_{\mathrm{H_2O}}) = -3.01$. The P-T profile depends on a wide range of parameters, not all of which are observationally well-constrained: these include the internal temperature T_{int}, the properties of clouds/hazes if present, and the efficiency of day-night heat redistribution. A detailed exploration of the temperature profiles in deep H_2-rich sub-Neptune atmospheres has been carried out before, in Piette and Madhusudhan (2020). Here, we assume uniform day-night heat redistribution, and consider four cases for the P-T profiles, varying the internal temperature T_{int} and the Rayleigh enhancement factor (a) for the hazes: C1, corresponding to $T_{\mathrm{int}} = 25$ K, $a = 10000$; C2 and C3, both with $a = 1500$, with $T_{\mathrm{int}} = 25$ K and $T_{\mathrm{int}} = 50$ K, respectively; C4, with $T_{\mathrm{int}} = 50$ K and $a = 100$. We note that, in principle, even colder profiles are plausible, given the clouds/haze properties retrieved from observations (Madhusudhan et al., 2023b). All the P-T profiles are shown in Figure 3.6.

3.4.2 Internal Structure

For each of these profiles, we obtain the permitted H_2-rich envelope mass fraction (x_{env}) and corresponding surface conditions (P_{s}, T_{s}) based on the bulk properties of the planet, as discussed in Sections 3.2.2 and 3.3.3 and shown in Table 3.1. We vary the interior composition from $f_{\mathrm{silicate}} = 5\%$ to $f_{\mathrm{silicate}} = 100\%$, adopting the median $M_{\mathrm{p}} = 8.63$ $\mathrm{M_\oplus}$ (Cloutier et al., 2019) and $R_{\mathrm{p}} = 2.61$ $\mathrm{R_\oplus}$ (Benneke et al., 2019). We note that the pure silicate and 95% iron ($f_{\mathrm{silicate}} = 5\%$) interior cases are unrealistic end-member interior compositions, but we consider them for completeness. We adopt $P_0 = 0.05$ bar as the outer boundary condition for the internal structure modelling, corresponding to the pressure at R_{p}, based on Madhusudhan et al. (2020).

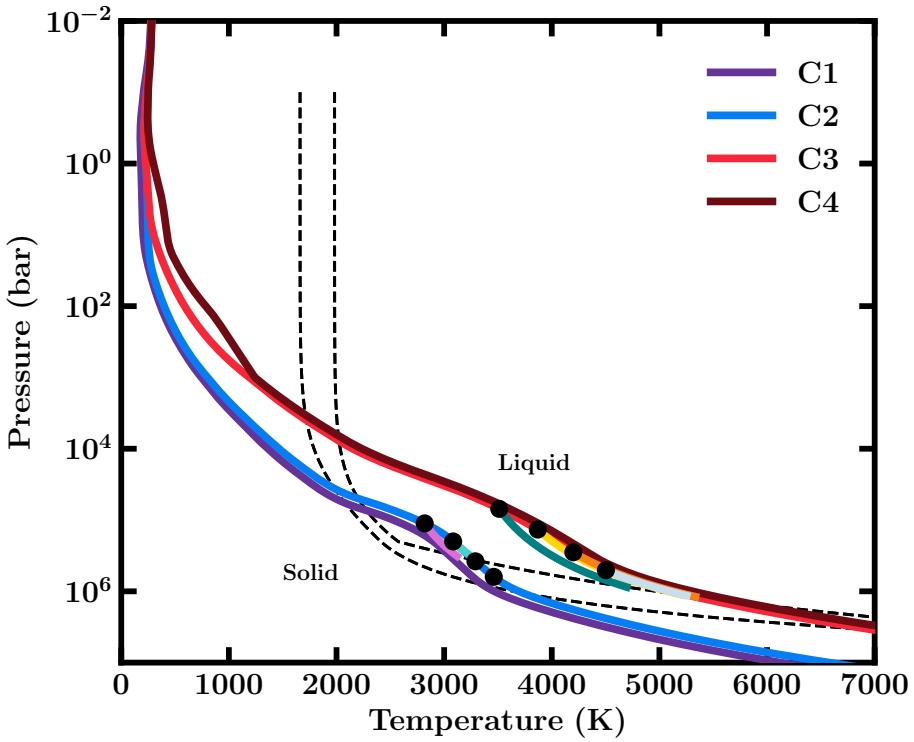

Fig. 3.6 Atmospheric pressure-temperature profiles shown against the adopted phase boundary for the silicate mantle, with the dashed lines corresponding to the Monteux et al. (2016) liquidus and solidus for peridotite. The black circles indicate the surface conditions for the cases discussed and the coloured lines extending from these show the adiabatic temperature structure in the melt, adopting the liquidus as the melt-solid transition.

In Figure 3.6 we show the P-T profiles considered, along with the surface conditions (black circles) and adiabatic profiles in the melt for our nominal C2 and C3 scenarios, which we further discuss below. The results for all P-T profiles are given in Table 3.1.

The presence and amount of magma depend on the adopted P-T profile. We start by considering one of the colder profiles, C2. For an Earth-like interior, we find $x_{\rm env} = 3.76\%$, with surface conditions $P_{\rm s} = 2.00 \times 10^5$ bar and $T_{\rm s} = 3084$ K. The melt mass fraction ($x_{\rm melt}$) in this case is 1.81%. For a Mercury-like interior, i.e. with higher Fe content, we find $x_{\rm env} = 5.29\%$, with surface conditions $P_{\rm s} = 3.79 \times 10^5$ bar and $T_{\rm s} = 3290$ K. Based on our assumption of the liquidus as the melt curve, we class this as having 0% melt in Table 3.1. In reality, these surface conditions lie between the liquidus and solidus, which would lead to partial melting. This is also the case for the $f_{\rm silicate} = 5\%$ interior, with $x_{\rm env} = 6.60\%$, with surface conditions $P_{\rm s} = 6.27 \times 10^5$ bar and $T_{\rm s} = 3461$ K. On the other hand, for the extreme case of a pure silicate interior,

we find a melt mass fraction of 3.16%, for $x_{\rm env} = 2.62\%$, $P_{\rm s} = 1.12 \times 10^5$ bar and $T_{\rm s} = 2819$ K.

We next consider the higher-temperature P-T profile C3, which permits solutions with a magma ocean surface for all the interior compositions considered. For each interior composition, the permitted envelope mass fraction, and hence the surface pressure, is lower for this hotter P-T profile. For an Earth-like interior, we find $x_{\rm env} = 2.52\%$, with surface conditions $P_{\rm s} = 1.36 \times 10^5$ bar and $T_{\rm s} = 3870$ K. The melt mass fraction in this case is 10.16%. For a Mercury-like interior, we find $x_{\rm env} = 3.83\%$, with surface conditions $P_{\rm s} = 2.83 \times 10^5$ bar and $T_{\rm s} = 4200$ K. The corresponding $x_{\rm melt}$ is 5.78%. For the extreme case of a pure silicate interior, we find a lower $x_{\rm env} = 1.62\%$, with $P_{\rm s} = 6.97 \times 10^4$ bar and $T_{\rm s} = 3512$ K. The melt mass fraction in this case is larger, at 11.91%. For the other extreme of $f_{\rm silicate} = 5\%$, we obtain $x_{\rm env} = 5.06\%$, for $P_{\rm s} = 5.05 \times 10^5$ bar and $T_{\rm s} = 4503$ K, with $x_{\rm melt} = 2.62\%$. We note that including modelling of partial melt would somewhat increase the melt mass fraction in all cases.

As shown in Table 1, the envelope mass fractions and surface conditions we find for profiles C1 and C4 are very similar to C2 and C3 respectively. This is despite the differences in envelope temperature structure resulting from differing haze properties; the difference between C2 and C3 is primarily due to the differing $T_{\rm int}$.

3.4.3 Volatile Abundances at the Interface

At the surface-atmosphere interface, the interactions between the gas phase equilibrium reactions and solubility of the gases in the magma, if any is present, drive the elemental abundances in the atmosphere. We consider the four P-T profiles presented in Table 3.1 and assume 50×solar metallicity, using solar abundances by Asplund et al. (2021). The assumed metallicity is approximately based on the median retrieved CH_4 abundance for K2-18 b (Madhusudhan et al., 2023b). Across all considered cases, we find that the dominant H-C-N-O-S gas species at the surface are H_2, H_2O, CH_4, NH_3, and H_2S. The resulting atmospheric elemental abundances from these scenarios are shown in Table 3.1. As expected, the atmosphere is highly reduced, with oxygen fugacities varying between IW-8.8 and IW-4.9 (using the oxygen fugacity of the IW buffer by Hirschmann, 2021) among the 12 cases with magma. We note that although our calculations of the oxygen fugacities agree to within 0.35 dex with the self-consistent IVTANTHERMO code at $P_{\rm s} = 10^4$ bar and $T_{\rm s} = 3000$ K, as described in Section 3.2.3, the redox state at higher pressures/temperatures is not well understood. Future work is needed to better understand the redox state of gas dwarfs at these conditions.

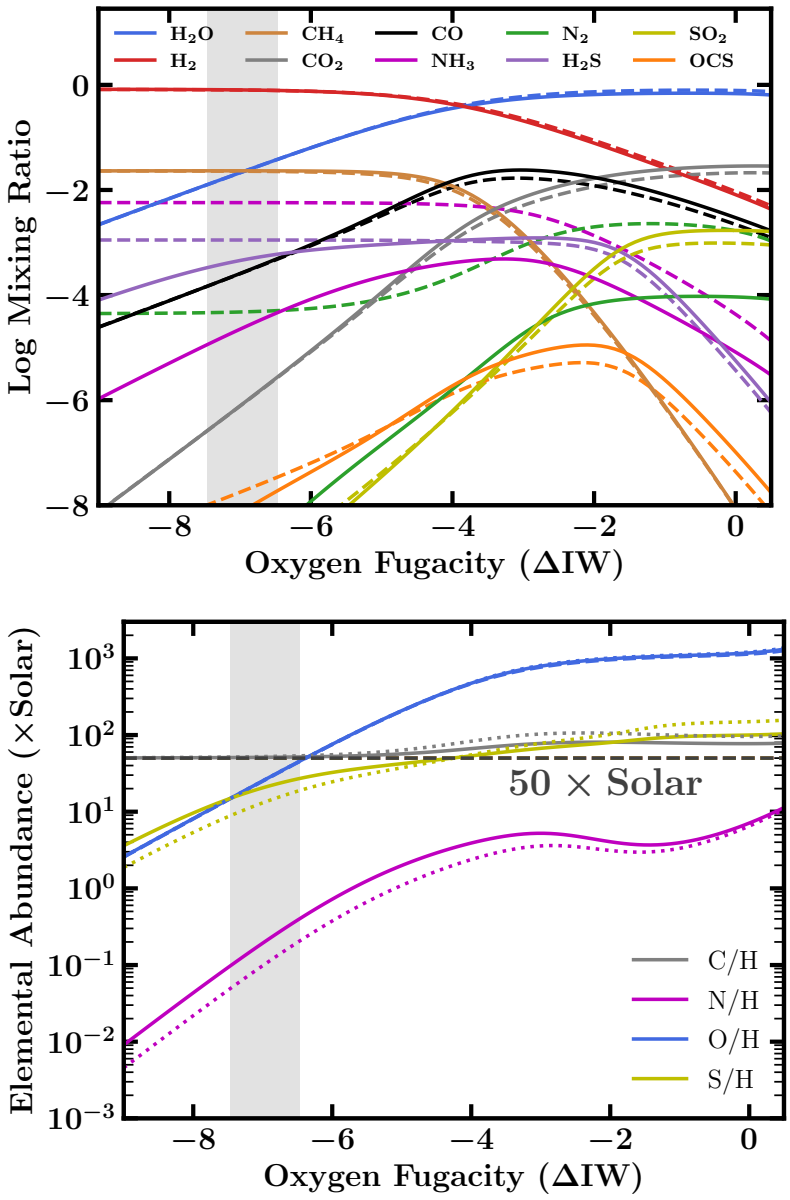

Fig. 3.7 Atmospheric composition at the melt-atmosphere interface as a function of oxygen fugacity, at $T_s = 4200$ K, $P_s = 2.83 \times 10^5$ bar, $M_{melt} = 0.0578\,M_p$, $M_{atm} = 0.0383\,M_p$ and 50×solar metallicity – corresponding to the C3 profile with a Mercury-like interior composition ($f_{silicate} = 30\%$) in Table 3.1. Top: Atmospheric mixing ratios of major H-C-O-N-S species. The solid and dashed lines show the abundances with and without solubility, respectively. Bottom: Atmospheric elemental abundances normalised to hydrogen. The dotted line corresponds to a case with twice the melt mass fraction to highlight the potential effect of partial melt. The dashed horizontal line shows a 50×solar composition. The grey region centred at IW-7 (±0.5), shown in both figures, corresponds to the approximate oxygen fugacity obtained with a total oxygen budget of 50×solar.

Overall, we find that H_2O and molecules containing N and S are the most dominant volatile species in the magma ocean, with high surface pressures strongly favouring the solubility of N_2. As such, for a given interior composition, we find that cooler *P-T* profiles, resulting in higher P_s, act to increase the depletion of nitrogen in the atmosphere - that is, until the temperature is too low to support a molten surface. The dependence of N depletion on P_s is stronger than that on the melt fraction. Therefore, a hotter temperature profile does not necessarily result in higher N depletion. In terms of the internal structure, we find that the interior needs to be more iron-rich than Earth's interior to result in nitrogen depletion larger than ∼2 dex. In our calculations the atmospheric H_2O budget is not significantly depleted by the magma ocean, as indicated in Table 3.1 by the $\lesssim 0.5$ dex change in O/H compared to the solid surface cases. More significant depletion of atmospheric H_2O would result in further preferential formation of CO over CO_2 due to less oxygen being available.

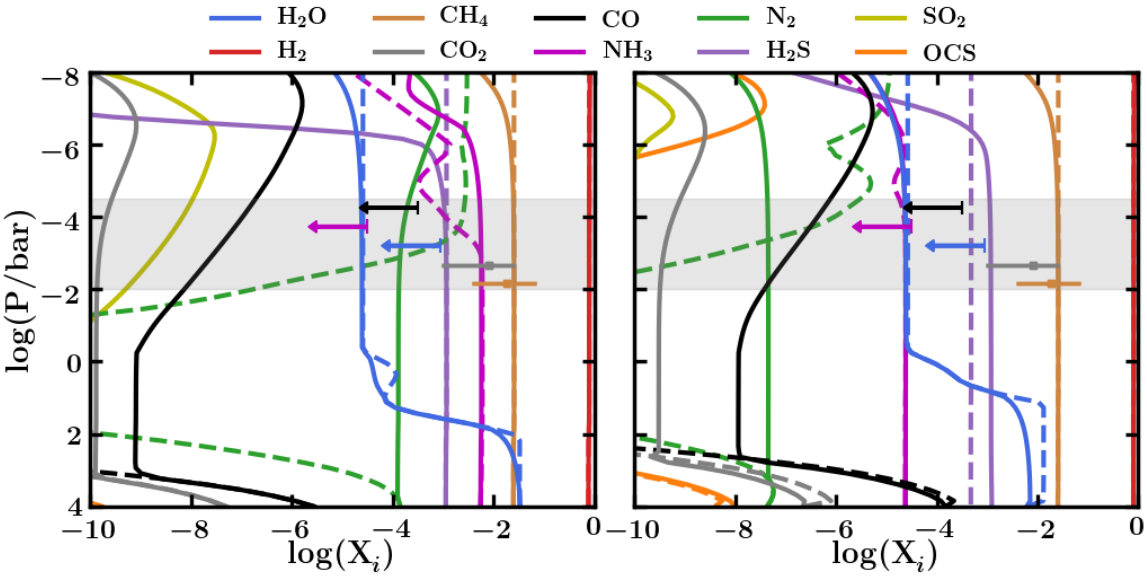

Fig. 3.8 Vertical mixing ratio profiles for several H-C-O-N-S molecular species. X_i denotes the volume mixing ratio of a species i. Solid and dashed lines indicate profiles computed with and without disequilibrium effects. Horizontal data points and arrows denote the mixing ratio constraints and 95% upper limits retrieved by Madhusudhan et al. (2023b). The gray shaded region denotes the pressure range typically probed by transmission spectroscopy (e.g. Constantinou and Madhusudhan, 2024). Left: Mixing ratio profiles corresponding to the C2 *P-T* profile and 30% interior silicate fraction case shown in Table 3.1. This corresponds to 50×solar elemental abundances. Right: Profiles computed for the C3 *P-T* profile and 30% interior silicate fraction case shown in Table 3.1. N is depleted due to dissolution in the magma surface.

Whilst we find that nitrogen can be depleted under certain conditions, in line with previous works investigating the solubility of nitrogen in reduced interiors (Daviau and Lee, 2021; Dasgupta et al., 2022; Suer et al., 2023; Shorttle et al., 2024), we do not reproduce the six orders of magnitude depletion found by S24. Additionally, we also identify sulfur as a potential atmospheric tracer of a magma ocean; however, the depletion is less than that of nitrogen. Finally, we find that the solubility of H_2, CO, CO_2, and CH_4 is less prominent at the considered conditions and does not drive the abundances of these species far from chemical equilibrium expectations without a magma ocean. However, we note that, as further detailed in Appendix A.1, many molecular species lack solubility data at the extreme conditions considered here. Hence, further work is needed to improve our knowledge of the solubility of prominent volatiles in silicate melts.

In Figure 3.7, we show the mixing ratios of the major C-H-O-N-S species in the lower atmosphere and the corresponding elemental abundances for a range of oxygen fugacities using the C3 profile and a Mercury-like interior ($f_{\text{silicate}} = 30\%$). This represents the case with the strongest nitrogen depletion, excluding the extreme 5% silicate interior cases, with atmospheric N/H being ∼2.5 dex lower than the assumed metallicity of 50×solar. We also see the onset of sulfur depletion in the atmosphere due to the solubility of S_2 at very reducing conditions (∼IW-6 in this case). On the other hand, the carbon abundance remains unchanged, as mentioned above. We also highlight the potential effect of partial melt by doubling the melt mass fraction, shown by the dotted line in Figure 3.7, leading to an approximately linear increase in the depletion of nitrogen.

3.4.4 Atmospheric Chemistry

We now use the elemental abundances obtained above to determine the atmospheric composition above the surface, using equilibrium and non-equilibrium calculations. From across all the models shown in Table 3.1, we focus on two realistic cases, one with and one without melt. For the molten case, we consider the C3 profile with 30% silicate fraction, which gives significant N depletion. For the case with no melt we consider the C2 profile with 30% silicates, which has no N depletion. For each case, we set the atmospheric elemental budget to that obtained in Section 3.4.3 and reported in Table 3.1. As expected from the model set-up, the no-melt scenario results in all elemental abundances being identical to those of a 50×solar metallicity gas.

Across all cases considered, the primary O, C, N, and S reservoirs are H_2O, CH_4, NH_3 and H_2S over most of the atmosphere, as indicated by the dashed lines in Figure 3.8.

This is seen for a pressure range spanning over 10 orders of magnitude and a temperature profile ranging between ∼260-2700 K.

The mixing ratio profiles obtained for the no-melt case are shown on the left-hand-side of Figure 3.8. In both the equilibrium and disequilibrium cases, the abundance of H_2O in the upper atmosphere is significantly depleted by a cold trap below the ∼1 bar pressure level. While CO and CO_2 are absent from the photosphere in the equilibrium case, they are present in the disequilibrium case, arising from photochemical processes. However, their abundance is significantly hindered by the limited availability of O, with the main carrier H_2O being depleted by the cold trap. The abundance of CO_2 is lower than that of CO throughout the atmosphere.

Compared to the retrieved atmospheric composition of K2-18 b (Madhusudhan et al., 2023b), shown as errorbars and arrows in Figure 3.8, the computed CH_4 abundance is consistent with the retrieved constraint. However, there is a substantial difference of ∼8 dex between the computed abundance of CO_2 with the measured value across the observable pressure range. Additionally, the retrieved upper limits for H_2O and CO are consistent with the computed amounts. Lastly, the computed value of NH_3 is higher than, and therefore inconsistent with the retrieved upper limit.

The right-hand-side of Figure 3.8 shows the case with a molten surface. This configuration results in very similar abundances for O- and C-carrying molecules as the no-melt case. This includes the significant depletion of H_2O due to a cold trap, the limited production of CO and CO_2, and CO being more abundant than CO_2. The main difference from the no-melt case is the notable depletion of NH_3, due to N dissolving in the magma. Specifically NH_3 and N_2 are at much lower mixing ratios than in the no-melt case, by ∼2 dex. Compared to constraints from observations, CH_4, H_2O, CO and in this case NH_3 as well are consistent with the retrieved constraints and upper limits. However, the resulting CO_2 abundance is still substantially lower than the observed abundance.

In summary, we find that even for the case with significant melt, corresponding to our hotter *P-T* profile with a high $T_{\rm int}$, the NH_3 abundance is close to the observed 95% upper limit, while the CO_2 abundance is still significantly discrepant from the observed value and lower than CO. Therefore, we find that the retrieved atmospheric composition of K2-18 b (Madhusudhan et al., 2023b) is inconsistent with a magma ocean scenario, or more generally with a deep H_2-rich atmosphere with or without melt. In principle, the absence of a cold trap could lead to higher H_2O abundance in the troposphere, which in turn could lead to higher CO_2 abundance. However, such

a scenario would also give rise to a significant amount of H_2O and CO, which are presently not detected.

3.4.5 Sensitivity to Atmospheric Parameters

We also explore other values for the three key atmospheric parameters that may influence the observable composition: the metallicity, the eddy diffusion coefficient K_{zz}, and the internal temperature T_{int}. We consider the two cases shown in Figure 3.8 as the canonical cases corresponding to the two *P-T* profiles (C2 and C3). Both cases assume a median metallicity of 50×solar and K_{zz} of 10^6 cm^2s^{-1} in the deep atmosphere. It may be argued that a higher metallicity could result in higher CO_2 abundances than the canonical cases and better match the observed abundances. Similarly, a broader range of K_{zz} may also influence the abundances. Therefore, for each of the two canonical cases, we investigate models with different values for the metallicity and K_{zz}. We consider metallicities of 100×solar and 300×solar, representing cases with significantly higher metallicities beyond the median retrieved value of ∼50×solar. For K_{zz}, we explore two end-member scenarios of 10^4 cm^2s^{-1} and 10^8 cm^2s^{-1}. Based on Madhusudhan et al. (2020) and Valencia et al. (2013), for our canonical cases we considered values of 25 K and 50 K for T_{int}. We additionally consider the effect of using a *P-T* profile with a higher T_{int} of 60 K, as has been considered by Hu (2021). As found for our canonical cases, we find that the observed CO and CO_2 abundances remain unexplained by these models with different values of metallicity, K_{zz} and T_{int}. These results are discussed in full in Appendix A.2.

3.4.6 Spectral Characteristics

We use the atmospheric compositions computed in Section 3.4.4 to examine the spectral signatures of CH_4, NH_3, CO and CO_2, which have been previously identified as key diagnostics of the presence of a magma surface. Using the VIRA retrieval framework's (Constantinou and Madhusudhan, 2024) capability of considering non-uniform vertical mixing ratios, we directly use the atmospheric composition profiles computed using the VULCAN (Tsai et al., 2021) non-equilibrium code described above and shown in Figure 3.8. We specifically consider the melt case discussed above, to evaluate the spectral implications for the presence of a magma layer. For all cases, we consider parametric grey cloud and Rayleigh-like haze properties corresponding to the median retrieved constraints of Madhusudhan et al. (2023b), to facilitate a qualitative

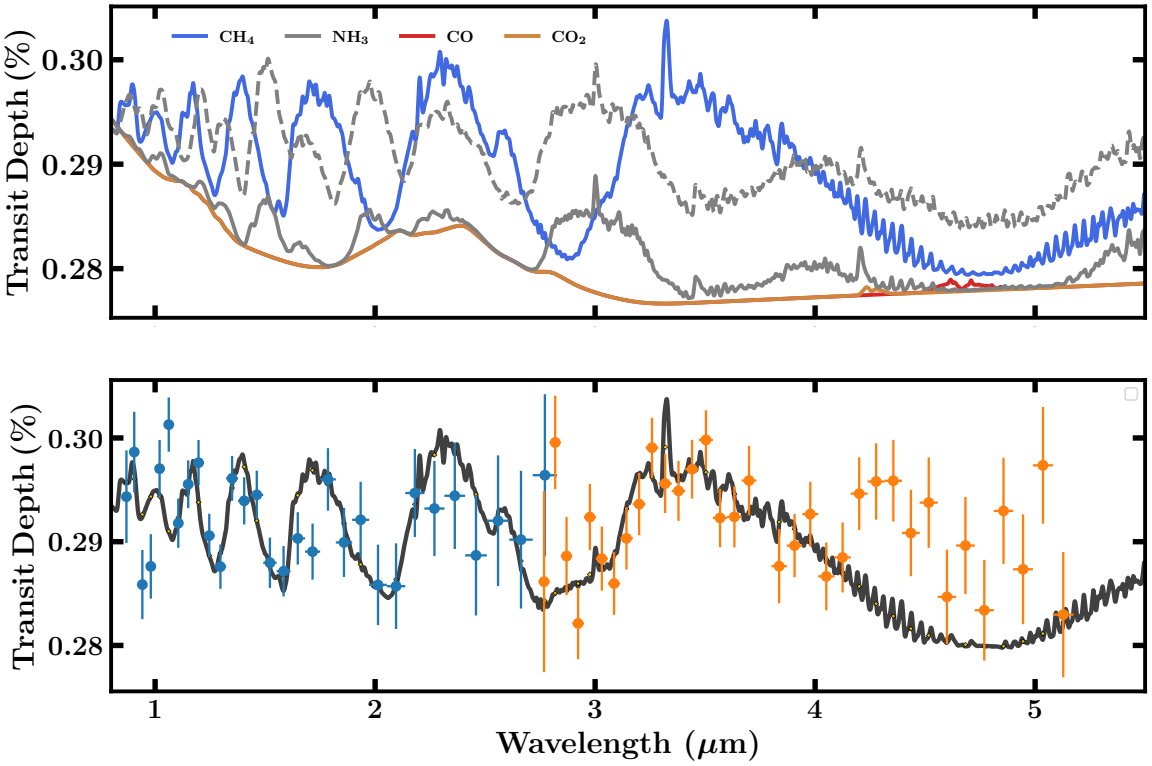

Fig. 3.9 Top: Spectral contributions arising from CH_4, NH_3, CO and CO_2 in the transmission spectrum of K2-18 b. The atmospheric abundance of each molecule corresponds to the right-hand side plot of Figure 3.8, generated with the C3 *P-T* profile, and includes disequilibrium effects. The dashed grey line corresponds to the spectral contribution of NH_3 if it were not depleted by dissolution in the magma. Bottom: The resulting transmission spectrum from all four species' spectral contributions. Blue and orange errorbars are the JWST NIRISS and NIRSpec G395H observations of K2-18 b from Madhusudhan et al. (2023b), which include the reported -41 ppm retrieved offset. It can be seen that the magma ocean scenario does not result in sufficient CO_2 to explain the observations at $\sim$4.3 μm. We emphasise that the present comparison to the data is solely for illustration. A robust comparison necessitates considering the constraints obtained from a detailed retrieval analysis, as done in Figure 3.8.

comparison with the observations. Specifically, we set $\log(a) = 10^{7.31}$, $\gamma = -11.67$, $P_c = 10^{-0.55}$ and $\phi_c = 0.63$.

The resulting spectral contributions and transmission spectrum are shown in Figure 3.9. As can be seen in the top panel, CH_4 has prominent spectral features throughout the 1-5 μm wavelength range, while CO_2 and CO give rise to absorption features at $\sim$4.3 and $\sim$4.7 μm respectively. NH_3 shows a spectral feature at $\sim$3 μm. Due to the depletion of atmospheric nitrogen arising from its dissolution in the magma, the NH_3 spectral contribution is relatively weak and not detected in the present data. Without such a depletion, i.e. with nitrogen at a solar elemental abundance ratio, NH_3 would have prominent spectral features across the wavelength range of comparable strength to CH_4. While CO is more abundant than CO_2 in the observable atmosphere, as described in Section 3.4.4, the low absolute abundances of both molecules give rise to comparably weak spectral features.

The resulting transmission spectrum provides a reasonable match for the NIRISS observations of K2-18 b at shorter wavelengths due to the strong CH_4 features. However, the spectrum does not fit the prominent CO_2 absorption feature seen in the NIRSpec G395H data. Moreover, the spectral contribution of CO is also minimal. Together, the two molecules are present at abundances that do not provide a good fit to the data in the 4-5 μm range.

Overall, we find that the gas dwarf scenario with a thick H_2-rich atmosphere in equilibrium with a magma ocean at depth is not consistent with the existing JWST observations of K2-18 b. In particular, irrespective of the NH_3 depletion, the models predict a low CO_2 abundance and CO > CO_2 which are inconsistent with the retrieved abundances. Future studies need to investigate if other effects may contribute to the observed composition. For example, similar to that discussed in Madhusudhan et al. (2023b), in order for the detected abundance of CO_2 to be compatible with a deep H_2-rich atmosphere, an unphysically low C/O ratio of $\sim$ 0.02–0.06, together with a moderate C/H ratio ($\sim$30-50$\times$ solar) and vertical quenching may be required. However, such an atmosphere could also lead to significant CO abundances that may not be consistent with the observations, and the deep atmosphere would have more H_2O than H_2.

3.5 Summary and Discussion

In this study, we report an integrated framework to investigate the plausibility of gas dwarf scenarios for temperate sub-Neptunes, including the possibility of magma oceans,

and their potential atmospheric signatures. Our framework models the various components of a planet, and their interplay. Specifically, it includes atmospheric and internal structure modelling, magma-atmosphere chemical interactions, and equilibrium as well as disequilibrium (photochemistry and vertical mixing) processes in the atmosphere. Considering all these factors, it predicts the observable abundances of molecular species in the atmosphere and the expected spectral features.

We apply our framework to perform a comparative assessment of previous works, validating our modelling of magma-atmosphere interactions against Gaillard et al. (2022) and assessing the model predictions of Shorttle et al. (2024) for a temperate sub-Neptune. Our findings highlight the importance of considering physically plausible models, set up in a holistic framework. In particular, we note that the use of stand-alone magma-atmosphere interaction models, which do not consider the complex interplay of interior and atmospheric factors, can lead to erroneous results.

3.5.1 Summary

Magma oceans are normally expected for rocky planets with high equilibrium temperatures. In the present work, we have tested the limits of this scenario by exploring whether K2-18 b, a habitable-zone sub-Neptune, can host a magma ocean, as previously suggested by S24, and what the observable signatures could be. In the following, we summarise our key findings.

An integrated framework is essential to obtain physically plausible and self-consistent results for modelling sub-Neptune gas dwarfs. Our framework includes an atmosphere and interior structure model, including phase diagrams and equations of state of appropriate silicates; thermochemical equilibrium calculations for the silicates-atmosphere interface and lower atmosphere; and disequilibrium processes throughout the atmosphere.

The melt fraction admissible in a gas dwarf depends on the atmospheric and interior properties, specifically the interior composition and the atmospheric P-T profile. The P-T profile, in turn, depends strongly on the internal temperature $T_{\rm int}$, as well as on the presence and properties of clouds/hazes and on the molecular absorbers present in the atmosphere. For a gas dwarf scenario assuming the bulk parameters of K2-18 b, we find that maximal melt mass fractions of $\sim$10% are possible with an Earth-like interior composition, and may increase somewhat if partial melting is considered.

A planet's bulk parameters and temperature structure place both upper and lower limits on the envelope mass fraction, assuming a gas dwarf scenario. For the K2-18 b models considered in this work, these limits are $\sim$1% and 7% of the planet mass,

corresponding to a pure silicate and a 95% iron interior, respectively. The envelope mass fraction affects the surface pressure at the rock-atmosphere boundary, which, in turn, affects the potential melt conditions.

We find using our framework that the current chemical constraints for K2-18 b are inconsistent with a magma ocean scenario or any gas dwarf scenario, contrary to S24. Firstly, the high observed abundance of CO_2 along with low H_2O is inconsistent with the chemical expectations for the gas dwarf scenario. Secondly, we find CO to be higher than CO_2 by over 1 dex which is also inconsistent with the observations. We find this to be the case with or without a magma ocean, and relatively independent of the uncertainties in magma-atmosphere interactions at the extremely reduced conditions as described in Appendix A.1. Finally, we find that N depletion in the atmosphere depends on a wide range of atmospheric and interior parameters, and can range between no depletion and $\sim$2.5 dex for a realistic model space, given the available solubility data.

Overall, we find that key atmospheric signatures for identifying a gas dwarf include the CO and CO_2 abundances, and, if melt is present, possible nitrogen depletion, consistent with some previous studies (see Section 3.3). In particular, we expect that $CO/CO_2 > 1$ if no H_2O is observed (as a result of, e.g., condensation), or, in the presence of H_2O, $CO/CO_2 \lesssim 1$, due to photolysis of H_2O making more oxygen available for the formation of CO_2. Furthermore, we find that N depletion is more sensitive to the surface pressure than to the amount of melt present, provided this is non-zero. Thus, the presence of a magma ocean does not ensure a significant N depletion in the atmosphere.

Our models predict significant H_2S for a deep H_2-rich atmosphere scenario. Hence, a lack of H_2S may be indicative of a shallow atmosphere. However, we note that there are significant uncertainties in the behaviour of S-bearing species in silicate melts at such reducing conditions. Therefore, more robust data for these conditions is needed in order for this signature to be used with a higher degree of confidence. We also note that there is uncertainty in the sulfur photochemical network for such planetary conditions.

As discussed below, a number of important unknowns remain. In particular, as discussed in Appendix A.1, the solubility of NH_3 in magma remains poorly understood, especially at extremely reducing conditions, as is also the case for H_2S at high pressures and temperatures.

3.5.2 Future Work

In order to aid accurate modelling of potential gas dwarf magma ocean planets, further developments are needed in three areas: (1) solubility laws for volatiles at extremely high pressures and temperatures and very reducing conditions, (2) equations of state (EOS) of silicates at the conditions relevant to temperate sub-Neptunes, and (3) complete reactions lists for all relevant atmospheric species.

As discussed further in Appendix A.1, there is a pressing need for additional experimental data and/or ab initio simulations on the solubility of volatile species in silicate melt at the physical and chemical conditions that we have shown in this study to be relevant to the magma-atmosphere interface on sub-Neptunes. This includes high pressure and temperature, and low oxygen fugacity conditions. In particular, the availability of NH_3 solubility laws at these conditions would allow more precise prescriptions than assuming its solubility to be negligible, avoiding the resulting likely overestimation of the abundance of N-bearing species in the atmosphere. In general, present laws are expected to give an order-of-magnitude estimate of the solubility at the conditions explored in this study; future work is needed to improve the solubility data.

Furthermore, once more accurate and precise solubility laws become available, the non-ideality of gas behaviour at the high pressures relevant at the interface may become a notable source of error if ignored, and will thus need to be appropriately treated (Kite et al., 2019; Schlichting and Young, 2022). We also note that, as a result of the lack of knowledge on the solubility of volatiles in the melt, the phase of the melt itself is not well-constrained. In particular, it is possible that some of the models considered here fall in a regime where there is no surface, and the atmosphere and magma become a single continuous phase at some lower pressure. This would happen if the volatiles were completely miscible in the melt, as is the case for water above a few GPa (Ni et al., 2017). It is however not known whether this behaviour applies to H_2-dominated atmospheres such as the one considered here. Furthermore, even if complete miscibility is not achieved, it is possible that the presence of volatiles in the magma may lead to a change in its EOS, which has not been accounted for here, where we have instead assumed a volatile-free melt for the internal structure calculations.

There is also scope for future work on the internal structure modelling, including the melt. This includes implementing the partial melting that would occur due to the magma's heterogeneous nature between the solidus and liquidus, as shown in Figures 3.4 and 3.6. This is expected to result in a larger fraction of the mantle being at least partially melted than when considering the fully melted region alone, hence

further depleting the atmosphere of the most soluble species. This effect is, however, in part addressed in this work, by considering the impact of a doubled melt mass fraction, as shown in Figure 3.7. Furthermore, future work will include more detailed prescriptions for the mantle, including alternate mineral compositions, and a fully temperature-dependent EOS for the solid portion.

Overall, JWST provides a promising avenue for atmospheric characterisation of sub-Neptune exoplanets. The high quality of the observations means that concomitant advances need to be made in theoretical models to maximise the scientific return from the data. In this chapter, we have outlined an end-to-end framework for gas dwarf sub-Neptunes to enable an evaluation of this scenario given high precision JWST data, and highlight the need for more accurate inputs for these models. Such advancements in both observations and theory promise a new era in the characterisation of low-mass exoplanets with JWST.

Chapter 4

The Interior and Surface Conditions of the Temperate Sub-Neptune TOI-270 d

4.1 Introduction

A central challenge in exoplanet characterisation is the degeneracy of interior compositions permitted by a planet's bulk properties, a problem that is particularly evident within the sub-Neptune regime. Characterising sub-Neptunes is important for revealing the nature and diversity of planets in this regime which can be related to their formation and evolution, including the shaping of the radius valley, in addition to their potential habitability. Sub-Neptunes orbiting nearby M dwarfs have gained significant attention in the field, as they are both abundant and conducive to atmospheric characterisation with JWST, with observations having been made for multiple such targets (e.g. Madhusudhan et al., 2023b; Kempton et al., 2023; Cadieux et al., 2024b; Holmberg and Madhusudhan, 2024; Benneke et al., 2024; Wallack et al., 2024; Madhusudhan et al., 2025). As demonstrated in Chapter 3, the availability of atmospheric data can begin to rule out possible interior compositions through coupling atmosphere and interior models (e.g. Madhusudhan et al., 2020; Guzmán-Mesa et al., 2022; Rigby et al., 2024; Nixon et al., 2024). However, the relationships between the interiors, surfaces and atmospheres of these planets are complex, and remain an active area of study for both water-rich bodies (e.g. Yu et al., 2021; Hu et al., 2021; Tsai et al., 2021; Madhusudhan et al., 2023a) and water-poor bodies (e.g. Kite et al., 2019, 2020; Rigby et al., 2024; Young et al., 2024).

In the previous chapters of this thesis we have explored two possible interior scenarios for temperate sub-Neptunes: hycean worlds in Chapter 2 and gas dwarfs in Chapter 3. In this chapter[1], we use the techniques developed in the preceding chapters to explore the possible internal structures of a temperate sub-Neptune recently observed with JWST, TOI-270 d, based on its atmospheric constraints and bulk properties.

TOI-270 d (L231-32 d) is a temperate sub-Neptune orbiting an M3 host star (Günther et al., 2019; Van Eylen et al., 2021; Kaye et al., 2022), with planetary mass $M_{\rm p} = 4.78 \pm 0.43$ $M_\oplus$ (Van Eylen et al., 2021) or 4.20 ± 0.16 $M_\oplus$ (Kaye et al., 2022) and radius $R_{\rm p} = 2.133 \pm 0.058$ $R_\oplus$ (Van Eylen et al., 2021), as given in Table 4.1. Orbiting at ∼0.07 au (Van Eylen et al., 2021), TOI-270 d lies just closer to its host star than the inner edge of the classical habitable zone (HZ), with equilibrium temperature 387 K (326 K) for Bond albedo $A_{\rm B} = 0$ ($A_{\rm B} = 0.5$). The bulk density of TOI-270 d is consistent with the presence of an H_2-rich atmosphere, evidence of which was reported by Mikal-Evans et al. (2023), using transmission spectroscopy with the Hubble Space Telescope Wide Field Camera 3 (HST WFC3). Based on its bulk properties and equilibrium temperature, Madhusudhan et al. (2021) proposed TOI-270 d as a hycean candidate, a class of potentially habitable planet with H_2O oceans underlying H_2-rich atmospheres, for which the HZ is considerably wider than the classical HZ.

Recently, TOI-270 d was observed with JWST (Holmberg and Madhusudhan, 2024; Benneke et al., 2024). Two studies, Holmberg and Madhusudhan (2024) and Benneke et al. (2024), used NIRSpec G395H observations in addition to shorter wavelength coverage with HST and JWST NIRISS respectively, to place constraints on the photospheric composition at the terminator via atmospheric retrievals. Holmberg and Madhusudhan (2024) report strong evidence for CH_4 and CO_2, with mixing ratios $\sim 0.1 - 1\%$, and a non-detection of NH_3. This is similar to the reported pattern of detections for the cooler hycean candidate K2-18 b (Madhusudhan et al., 2023b). Holmberg and Madhusudhan (2024) also report moderate evidence for CS_2, and tentative evidence for H_2O. They suggest that TOI-270 d could be a dark hycean world, with only a habitable nightside, due to its relatively high temperature for a hycean candidate. The presence of clouds or hazes in the photosphere could not be constrained by the observations, similar to the findings of Mikal-Evans et al. (2023). Benneke et al. (2024) also find a lack of NH_3 in addition to strong CH_4 and CO_2 detections, albeit at higher abundances than Holmberg and Madhusudhan (2024). They also report a tentative H_2O detection, in addition to potential evidence for SO_2 and CS_2.

[1]This chapter is adapted from a lead-author paper (Rigby & Madhusudhan) submitted to *MNRAS*. Nikku Madhusudhan conducted the atmospheric structure modelling for this study.

In contrast to Holmberg and Madhusudhan (2024) and Mikal-Evans et al. (2023), their analysis suggests that the atmosphere is metal-rich, with a mean molecular weight (MMW) of $5.47^{+1.25}_{-1.14}$ amu. The retrieved photospheric temperatures for the terminator differ between Holmberg and Madhusudhan (2024) and Benneke et al. (2024). For the Holmberg and Madhusudhan (2024) one-offset dual-transit (DT) case, the T_0 is 289^{+80}_{-75} K at 10 mbar, while Benneke et al. (2024) find a hotter T_0 of $385.3^{+44.2}_{-41.8}$ K for their free-chemistry retrieval at the lower pressure of 0.1–1 mbar.

The NIRSpec and NIRISS data were recently re-analysed by Felix et al. (2025). In addition to a fiducial model with the same set of chemical species as Benneke et al. (2024), they consider models including an expanded set of molecules, including CH_3F, CH_3Cl, and/or sulfur chemistry with H_2CS, CS, and $(CH_3)_2S$ (dimethyl sulfide, DMS), all of which were found to be preferred over their fiducial model, but could not be distinguished. They also report detections of CH_4 and CO_2, while the inclusion of H_2O is not preferred by the retrieval. Similarly to Benneke et al. (2024), they find a high mean molecular weight atmosphere. The chemical species with retrieved abundances most significantly different between all three studies is CH_4, with Benneke et al. (2024) finding a high mixing ratio of $\log(X_{CH_4}) = -1.64^{+0.38}_{-0.36}$. Holmberg and Madhusudhan (2024) find a significantly lower abundance, at $\log(X_{CH_4}) = -2.72^{+0.41}_{-0.50}$ for the one-offset DT case. Two of the seven retrieval cases of Felix et al. (2025) give a CH_4 abundance consistent with Benneke et al. (2024) to within 1σ, while six of the seven cases have CH_4 abundance consistent with Holmberg and Madhusudhan (2024) – the exception is the fiducial model, which is disfavoured.

Recently, Glein et al. (2025) conducted thermochemical equilibrium calculations to investigate the quenching of C-H-O-N species in the atmosphere of TOI-270 d. This study adopted the atmospheric abundances of Benneke et al. (2024). The methods outlined in this work for the CO_2-CH_4 speciation are reported to be applicable only for a lack of water clouds. They suggest that a lack of detected CO can be explained by equilibrium chemistry of hot gas, negating the need to invoke a hycean scenario for TOI-270 d. This would be potentially the case for an H_2O-rich and CO_2-poor atmosphere. This argument hinges on the high mean molecular weight (MMW) found by Benneke et al. (2024), and subsequently Felix et al. (2025).

The interpretation of precise chemical abundances in sub-Neptune atmospheres from JWST requires further studies into the complex relationship between sub-Neptune atmospheres, surfaces and interiors. This is evident from the case of habitable zone sub-Neptune K2-18 b, which was recently observed with JWST (Madhusudhan et al., 2023b). The abundance of CH_4 and CO_2 in addition to the non-detection of NH_3

Source	$M_p/M_\oplus$	$R_p/R_\oplus$	$T_{eq,0}$ /K	$T_{eq,0.5}$ /K	a/AU	Period /days
Günther et al. (2019)		2.13±0.12	372	313	0.073	11.4
Van Eylen et al. (2021)	4.78±0.43	2.133±0.058	387	326	0.072	11.4
Kaye et al. (2022)	4.20±0.16					
Mikal-Evans et al. (2023)		2.19 ± 0.07				

Table 4.1 Reported properties of TOI-270 d. Equilibrium temperature values are calculated with $A_B = 0$ and $A_B = 0.5$, and assuming uniform day-night redistribution.

was suggested to indicate the presence of a surface ocean (i.e. hycean conditions) on K2-18 b (Madhusudhan et al., 2023b), based on chemical models (Yu et al., 2021; Hu et al., 2021; Tsai et al., 2021; Madhusudhan et al., 2023a). The other interior solutions permitted by the bulk properties were shown to span a rocky world with thick H_2-rich envelope and a mini-Neptune scenario (Madhusudhan et al., 2020), as is the case for similar density sub-Neptunes like TOI-270 d.

Additional photochemical modelling by Cooke and Madhusudhan (2024) found that a mini-Neptune scenario is incompatible with the retrieved atmospheric abundances for K2-18 b, in contrast to previous studies (Wogan et al., 2024). An uninhabited hycean scenario was found to explain the abundance constraints with the exception of CH_4 (Cooke and Madhusudhan, 2024). The equivalent inhabited hycean case was found to better match observations, with CH_4 produced by methanogenic life satisfying the high observed CH_4 abundance. Recent work explored the possibility of a gas dwarf scenario for K2-18 b. In Chapter 3, we reported a framework including internal structure modelling, atmospheric structure modelling, melt-atmosphere interactions, photochemical modelling and spectral predictions. We found that the CO/CO_2 ratio for K2-18 b and the lack of nitrogen are incompatible with predictions for a gas dwarf scenario. However, the relationship between planetary surfaces and observable atmospheres requires the use of models that rely on incomplete data (e.g. Shorttle et al., 2024; Glein et al., 2025) – for instance, for the solubility of chemical species in a magma ocean at the relevant high pressures and temperatures, and the uncertain phase behaviour of planetary materials. Atmospheric data remains a key factor in breaking degeneracies between possible interior compositions. However, we have not yet reached a position where robust constraints can be made on the nature of a sub-Neptune's surface via atmospheric observations.

In this chapter we present an exploration of the range of possible interior compositions and surface conditions for the temperate sub-Neptune TOI-270 d based on the available atmospheric constraints from JWST observations. We use atmospheric

pressure-temperature profiles generated through self-consistent atmospheric modelling, based on retrieved atmospheric abundances (Holmberg and Madhusudhan, 2024) to place constraints on the possible interior compositions that satisfy the bulk properties of the planet. These span a wide range of possible water mass fractions and surface conditions, including gas dwarf, mini-Neptune and hycean world scenarios. We explore the solutions that permit liquid water at the planet surface, including habitable hycean conditions, and place constraints on the possible ocean depths. We perform initial modelling of dark hycean scenarios for TOI-270 d, where inefficient day-night redistribution could lead to a habitable nightside for a dayside that is too hot for habitable conditions. We also investigate mini-Neptune scenarios, including mixed H_2O/H_2 envelopes, both with and without a cold trap, the presence of which could result in an H_2-rich layer above the mixed portion of the envelope. We explore gas dwarf scenarios, placing constraints on the permitted H_2-rich envelope mass fractions and surface conditions at the envelope/rock interface. Finally, we discuss the future prospects for the characterisation of TOI-270 d via atmospheric observations coupled to atmosphere and interior models, and the avenues for future research required to robustly identify the nature of this and similar planets.

4.2 Methods

We first outline our procedure for calculating the possible interior compositions and surface conditions of TOI-270 d. We use the planetary bulk properties and self-consistently generated atmospheric pressure-temperature (P-T) profiles informed by JWST observations (Holmberg and Madhusudhan, 2024) to place constraints on the interior composition of the planet. In this section we describe how the internal structure model HyRIS, outlined in full in Chapter 2, is used for this purpose.

4.2.1 Internal Structure Model

In Chapter 2 we used HyRIS configured with four differentiated planetary layers: H_2-rich envelope, H_2O layer, silicate ($MgSiO_3$ perovskite) mantle and iron (Fe) core, similar to previous studies of sub-Neptune interiors (e.g. Rogers and Seager, 2010a; Nixon and Madhusudhan, 2021). While, in Chapter 3 we used differentiated layers of H_2-rich envelope, silicate mantle and iron core, with a more complex treatment of silicates to allow the modelling of a magma ocean. In this chapter, we additionally consider mixed envelopes containing H_2O in addition to H_2 and He.

In Section 4.3.2, the internal structure model is evaluated for a grid of models across the full phase space of mass fraction combinations, for different assumptions of core composition and atmospheric P-T profile. (We use "core" to refer to the silicate and iron layers collectively, such that $x_{\rm core} = x_{\rm silicate} + x_{\rm Fe}$.) The inputted $M_{\rm p}$ is also varied within its 1σ uncertainty. We then extract the interior solutions that satisfy the measured $R_{\rm p}$ to within the 1σ uncertainty, defined via an ellipse centred on $M_{\rm p}$ and $R_{\rm p}$. In addition to $R_{\rm p}$, the model outputs the internal structure and phase structure. This facilitates analysis of the surface conditions and values including the ocean or magma ocean depth where relevant, as described in Chapter 2 (Rigby and Madhusudhan, 2024) and Chapter 3 (Rigby et al., 2024).

4.2.2 Temperature Profiles

Under the assumption of vigorous convection, we assume an adiabatic temperature profile in the interior below the envelope, as in previous chapters. The adiabatic profiles are described by the adiabatic temperature gradient (Equation 1.8).

For the H_2-rich envelope, we use pressure-temperature (P-T) profiles generated via self-consistent atmospheric modelling. This modelling is informed by the retrieved atmospheric parameters for TOI-270 d from JWST data (Holmberg and Madhusudhan, 2024). We use the GENESIS framework (Gandhi and Madhusudhan, 2017; Madhusudhan et al., 2020; Piette and Madhusudhan, 2020; Madhusudhan et al., 2021, 2023a), which assumes a plane parallel atmosphere and conducts line-by-line radiative transfer via the Feautrier method, and solves for radiative-convective equilibrium via the Rybicki linearization scheme – see the references above for a more detailed description of the method. For the chemical composition we assume values according to the median retrieved values from Holmberg and Madhusudhan (2024); we adopt $\log(X_{\rm H_2O}) = -2.0$, $\log(X_{\rm CH_4}) = -2.5$ and $\log(X_{\rm CO_2}) = -2.5$. The other key inputs are the internal temperature $T_{\rm int}$, the properties of the host star, the incident irradiation, day-night energy redistribution, and cloud/haze properties. We consider values of 25 K and 50 K for $T_{\rm int}$, similar to previous studies (Madhusudhan et al., 2020), and values for the Rayleigh enhancement factor a for hazes of 100 and 1500. The Rayleigh enhancement factor allows a parameterisation of hazes as H_2 Rayleigh scattering multiplied by some factor a. These values of a were chosen to explore a wide range of atmospheric temperature structures which could be permitted by current observations, and are similar to those used in previous studies (e.g. Piette and Madhusudhan, 2020; Madhusudhan et al., 2021; Rigby et al., 2024). The resulting P-T profiles are generated to 1000 bar pressures. We extrapolate to higher pressures using an adiabat, calculated using the parameters

from Chabrier et al. (2019) for solar proportion H/He. The resulting profiles are shown in Figure 4.1. Case 1, the coldest profile, has $a = 1500$ and $T_{\rm int} = 25$ K; Case 2 has $a = 1500$ and $T_{\rm int} = 50$ K; Case 3 has $a = 100$ and $T_{\rm int} = 25$ K; and Case 4 has $a = 100$ and $T_{\rm int} = 50$ K. For all cases, excluding the mini-Neptune scenarios considered in Section 4.3.4, the density of the envelope is calculated assuming 10% H_2O by mass, informed by the observed H_2O mixing ratio.

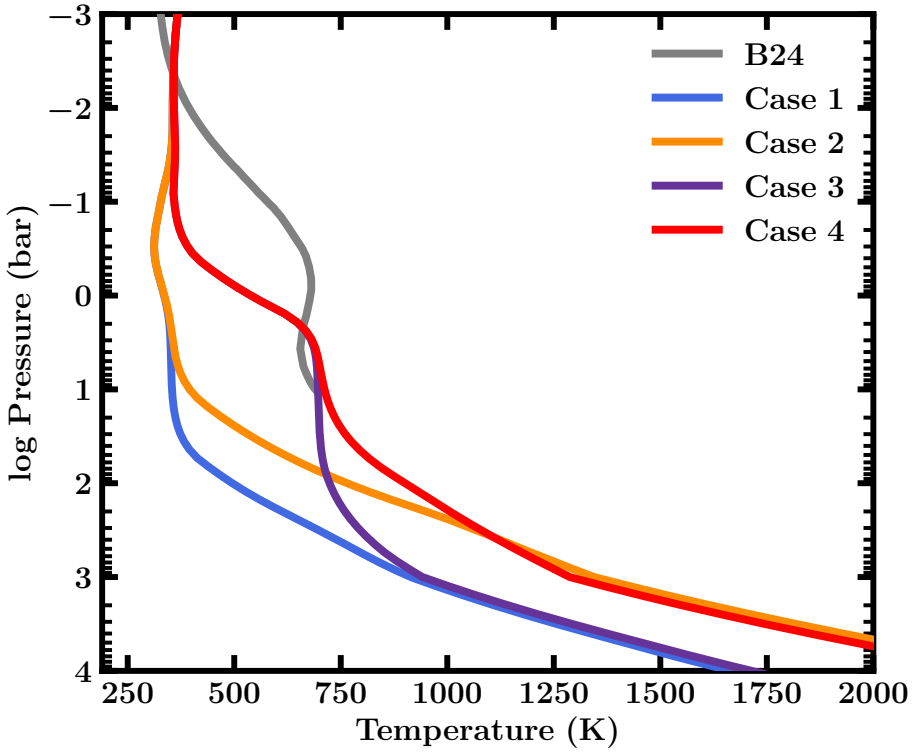

Fig. 4.1 Temperature structures adopted for the H_2-rich envelope, generated with GENESIS using the retrieved abundances of Holmberg and Madhusudhan (2024). These cases correspond to each combination of $T_{\rm int}$ of 25 and 50 K, and Rayleigh enhancement factor a of 100 and 1500. The profiles, generated to 1000 bar, are extended using an adiabat. We also show the "evening" P-T profile from Figure 10 of Benneke et al. (2024).

4.2.3 Equations of State

As in the previous chapters, we use the EOS of Chabrier et al. (2019) to describe the H_2/He portion of the envelope. In this work, as described above, we consider the atmospheric abundances of Holmberg and Madhusudhan (2024) and hence include 10% H_2O by mass in the envelope. Our EOS for H_2O is detailed in Section 2.2.2.

The EOS for a mixed envelope is calculated by combining the densities proportionally to the respective mass fractions ($z_{\rm i}$) for each component,

$$\rho_{\rm mix}(P,T) = \left[\sum \frac{z_i}{\rho_i(P,T)}\right]^{-1} \tag{4.1}$$

and the adiabatic gradient is calculated via

$$\left(\frac{\partial \log T}{\partial \log P}\bigg|_S\right)_{\rm mix} = -\frac{\sum_i z_i S_i \left.\frac{\partial \log S_i}{\partial \log P}\right|_T}{\sum_i z_i S_i \left.\frac{\partial \log S_i}{\partial \log T}\right|_P} \tag{4.2}$$

where S is the specific entropy. As for the density, we use the entropy and entropy derivatives with respect to pressure and temperature from Chabrier et al. (2019).

For H_2O miscible in H_2, we require the entropy and its derivatives with respect to pressure and temperature to calculate the adiabatic gradient for the mixture (Equation 4.2). The specific entropy (only required for the vapour and supercritical phases) is calculated using the IAPWS-1995 formulation (Wagner and Pruß, 2002).

In order to explore gas dwarf scenarios for TOI-270 d we consider the treatment of the silicate mantle from Chapter 3. In water-rich cases (i.e. containing sufficient water to be present as ices), we use the Seager et al. (2007) EOS for $MgSiO_3$ perovskite only, as in Chapter 2. This is because the silicate mantle below a high-pressure ice layer would typically exist at pressures $> 1.07 \times 10^{11}$ Pa, beyond pressures covered by the Lee et al. (2004) EOS for solid peridotite. For all interior scenarios we use the Seager et al. (2007) EOS for iron (Vinet et al., 1989; Anderson et al., 2001), as in previous chapters.

4.3 Results

In this section, we present our results for the possible interior compositions of TOI-270 d based on the planetary bulk properties and constraints from recent transmission spectroscopy with JWST (Holmberg and Madhusudhan, 2024). As described in Section 4.2.2, we adopt self-consistent temperature profiles in the envelope, generated using the atmospheric abundances from Holmberg and Madhusudhan (2024). We investigate the range of interior conditions possible for TOI-270 d with solutions spanning mini-Neptunes, rocky gas dwarfs with thick H_2-rich envelopes, and hycean worlds. In Section 4.3.1, we first describe the observational constraints. In the subsequent sections, we then explore each class of possible interior for TOI-270 d.

4.3.1 Observational Constraints

In Figure 4.2 we show the reported mass (M_p) and radius (R_p) measurements for TOI-270 d alongside some standard mass-radius (M-R) relations (Seager et al., 2007), which include homogeneous compositions of H_2O, silicates and iron, in addition to an Earth-like rocky composition (all isothermal at 300 K). The hycean M-R plane from Madhusudhan et al. (2021) is also shown. TOI-270 d lies towards the lower density region of the hycean M-R plane and within the dark hycean region, depending on the M_p and R_p values adopted. In this study we consider those of Van Eylen et al. (2021) for consistency with Holmberg and Madhusudhan (2024).

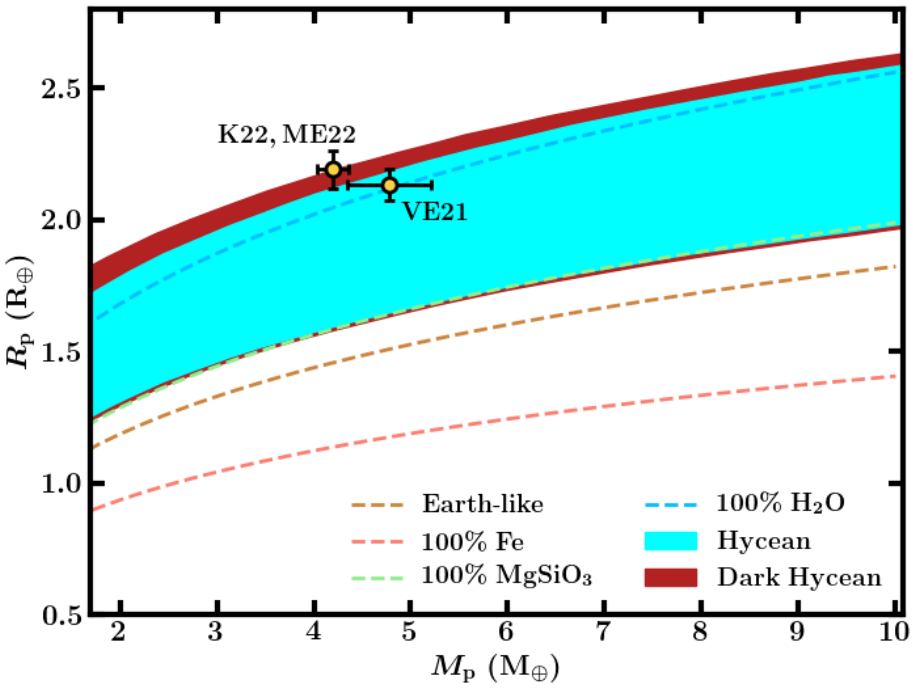

Fig. 4.2 The mass and radius measurements for TOI-270 d, where VE21 is Van Eylen et al. (2021), ME22 is Mikal-Evans et al. (2023) and K22 is Kaye et al. (2022). These are shown against some mass-radius curves for different isothermal compositions, shown by the dashed lines, along with the hycean mass-radius plane from Madhusudhan et al. (2021).

Using the JWST NIRSpec G395H transmission spectrum in addition to HST data (Mikal-Evans et al., 2023), Holmberg and Madhusudhan (2024) report strong evidence for CH_4 and CO_2 and a non-detection of NH_3, in addition to tentative evidence for H_2O and CS_2. For the Holmberg and Madhusudhan (2024) one-offset dual-transit (DT) case, the retrieved T_0 is 289^{+80}_{-75} K at 10 mbar. This study, along with Mikal-Evans et al. (2023), reports a low MMW H_2-dominated atmosphere. In contrast, Benneke et al.

(2024) and Felix et al. (2025) report a high MMW atmosphere, but with Felix et al. (2025) finding a CH_4 abundance broadly consistent with Holmberg and Madhusudhan (2024). In this study, we consider the atmospheric abundances of the published work, Holmberg and Madhusudhan (2024). Additional JWST observations of TOI-270 d may provide the tools to confirm the cause of the discrepancy between these studies, and place more robust constraints on the photospheric abundances for TOI-270 d. We note that the set-up of atmospheric retrievals remains crucial to accurately constrain the atmospheric abundances and photospheric temperature.

In Sections 4.3.2-4.3.5 we consider the *P-T* profiles Cases 1-4, based on the findings of Holmberg and Madhusudhan (2024), to explore the range of possible interior scenarios for TOI-270 d. In Figure 4.1 we show these *P-T* profiles, generated self-consistently with GENESIS, as described in Section 4.2.2, using the retrieved abundances of Holmberg and Madhusudhan (2024). Cases 1 through 4 correspond to values of $T_{\rm int}$ = 25 K, a = 1500; $T_{\rm int}$ = 50 K, a = 100; $T_{\rm int}$ = 25 K, a = 100; $T_{\rm int}$ = 50 K, a = 100 respectively, as described in Section 4.2.2. We also show a *P-T* profile from Benneke et al. (2024), generated via a dual-grey GCM. Specifically, we show the "evening" profile from their Figure 10, however the profiles in this figure are very similar and do not differ much at pressures above ∼1 mbar. This profile is only given to 10 bar.

The envelope *P-T* profiles Cases 1-4 can be used to estimate the potential surface conditions possible, which are particularly informative for H_2O-rich compositions. Our *P-T* profiles are shown against the phase diagram for H_2O in Figure 4.3. Cases 1 & 2 cross the vaporisation curve and therefore have the potential to permit liquid water at the surface, if the corresponding composition producing these surface conditions is compatible with the bulk density. We show that such solutions are possible in Section 4.3.3.

On the other hand, Cases 3 & 4 lack the presence of a cold trap, and do not cross the vaporisation curve. This implies that the H_2/H_2O boundary (HHB) must fall either in the vapour or supercritical region of the H_2O phase diagram. According to studies investigating the miscibility of H_2O and H_2, (e.g. Soubiran and Militzer, 2015; Gupta et al., 2025), this could result in the H_2O being fully mixed with the H_2-rich envelope (Nixon and Madhusudhan, 2021; Benneke et al., 2024). For reference, in Figure 4.3 we show the critical curve from Gupta et al. (2025), representing the transition from two separate phases of H_2 and H_2O to one phase. A mixed envelope would not be compatible with the median observed mixing ratios for H_2O, including for the canonical DT case (Holmberg and Madhusudhan, 2024). We note that with further observation,

a higher observed H_2O mixing ratio, for instance towards the upper limit of the error bar on current estimates, may permit a fully mixed H_2O/H_2 envelope.

4.3.2 Degeneracy in Interior Composition

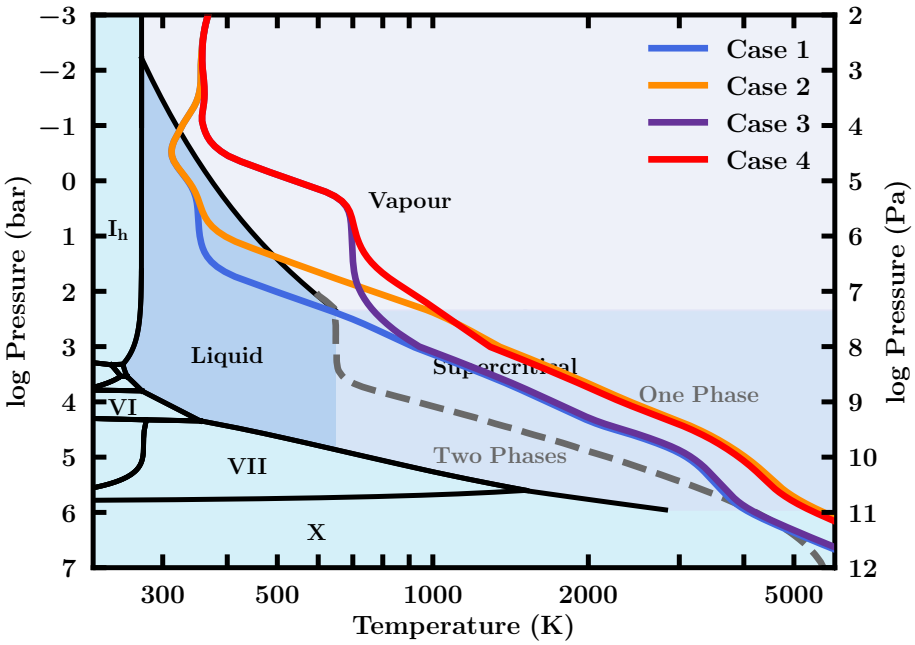

Fig. 4.3 Atmospheric *P-T* profiles against the H_2O phase diagram (Dunaeva et al., 2010) (black) and the critical curve from Gupta et al. (2025) for H_2/H_2O (grey dashed). The profiles shown are generated self-consistently using the atmospheric abundances from Holmberg and Madhusudhan (2024). Above the grey dashed curve, H_2 and H_2O would be expected to exist as one phase.

We first place constraints on the range of possible interior compositions that can reproduce the M_p and R_p of TOI-270 d to within their 1σ uncertainties. For consistency with Holmberg and Madhusudhan (2024), we adopt $M_p = 4.78 \pm 0.43$ $M_\oplus$ and $R_p = 2.133 \pm 0.058$ $R_\oplus$ (Van Eylen et al., 2021). Initially, two end-member core compositions are considered – the extreme case of a high density 100% Fe core ($x_{core} = x_{Fe}$, $f_{silicate} = 0$), and an Earth-like composition core ($f_{silicate} = 67\%$), where we have defined $f_{silicate}$ to be the silicates-to-iron ratio in the interior. We vary the envelope, H_2O and core mass fractions across the full parameter space, adopting an extreme value for the maximum x_{H_2O} of 95%. In this and following sections, we consider the *P-T* profiles informed by the Holmberg and Madhusudhan (2024) results – these are Cases 1-4, generated via self-consistent modelling, as described in Section 4.2.2.

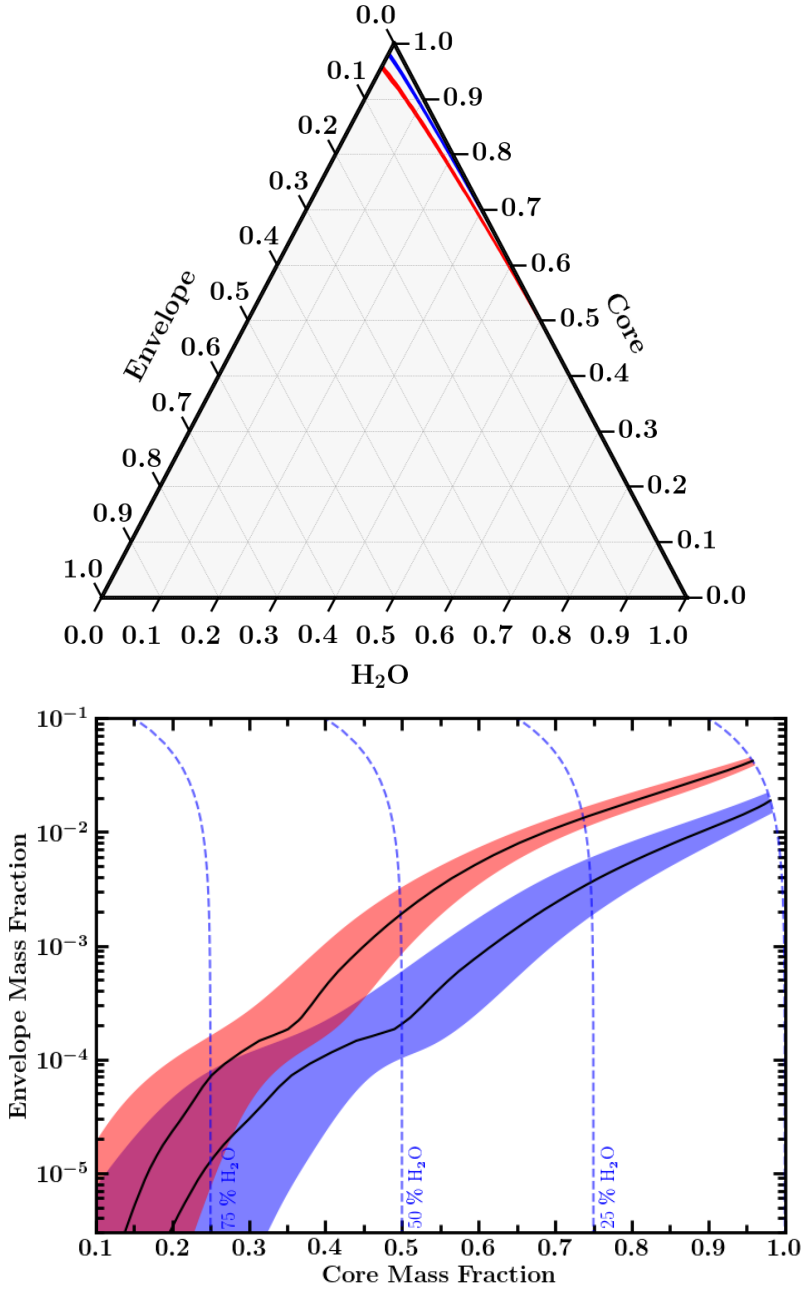

Fig. 4.4 Top: Ternary diagram showing the best-fit compositions for TOI-270 d, for an Earth-like core composition (blue) and a 100% Fe core (red). In both cases we adopt Case 1 as the atmospheric *P-T* profile. Bottom: Mass fractions of the H_2-rich envelope against core mass fraction, for Earth-like (blue) and 100% Fe (red) core compositions. The red and blue regions indicate combinations that reproduce the observed mass and radius to within 1σ. The best fit solutions in each case are shown by the black solid line. The dashed blue lines show constant H_2O mass fractions at 25% intervals.

Case 1 is adopted as our canonical profile, as it permits the full range of possible interior scenarios.

The interior solutions able to reproduce the measured M_p and R_p of TOI-270 d to within 1σ are shown in Figure 4.4, for core compositions of pure Fe and Earth-like, and P-T profile Case 1. In the left-hand plot we represent these solutions on a ternary diagram, with the coloured regions encompassing the 1σ solutions for each of the considered core compositions. Red corresponds to pure Fe while blue corresponds to an Earth-like core composition. In the right-hand side of Figure 4.4 we show the envelope mass fraction against the core mass fraction for the 1σ solutions. The shaded regions show the 1σ solutions as in the ternary diagram, while the black line indicates the best-fit solutions that reproduce the median M_p and R_p. The blue dashed lines indicate a constant H_2O mass fraction. In these initial calculations, we have assumed that the H_2O layer is distinct, i.e. cannot be miscible in the H_2-rich envelope, beyond the standard 10% by mass as informed by observations.

As evident from these figures, the data permit a wide range of envelope, H_2O and hence core mass fractions. These include interior solutions with H_2O mass fractions ($x_{\mathrm{H_2O}}$) across the full range considered ($0 - 95\%$). Within the 1σ solutions, a larger $x_{\mathrm{H_2O}}$ generally corresponds to a smaller envelope mass fraction (x_env), as is evident in Figure 4.4. The upper limit of x_env is constrained to be 4.62%, for an unrealistic high-density 100% Fe core and no distinct H_2O layer. For lower density core compositions, the maximum envelope mass fraction is lower. For an Earth-like core composition, the maximum envelope fraction is found to be 2.27%.

The choice of envelope P-T profile affects the permitted interior solutions and surface conditions. For instance, as is evident from Figure 4.3, only Cases 1 and 2 would permit a liquid ocean. Additionally, as described above, Cases 3 and 4 may not be compatible with the observed atmospheric abundances due to the miscibility of the H_2O in the H_2-rich envelope for a HHB lying in the vapour or supercritical region of the H_2O phase diagram. For interiors lacking a distinct H_2O layer, i.e. gas dwarf solutions, the choice of P-T profile affects the envelope mass fraction required. For instance, with an Earth-like interior, the maximum x_env for Case 1 is 2.27%. For Case 2, which is significantly hotter in the deep atmosphere due to the higher T_int, the maximum x_env reduces to 1.33% for an Earth-like interior. The overall hottest profile, Case 4, has the lowest maximum x_env of 1.06% for an Earth-like composition. Case 3, with the lower $T_\mathrm{int} = 25$ K and low a, has intermediate maximum $x_\mathrm{env} = 1.61\%$ for an Earth-like core. We note that none of our atmospheric P-T profiles permit an immiscible H_2O supercritical ocean, as explored by Luu et al. (2024) for K2-18 b. As

seen in Figure 4.3, our P-T profiles lie above the critical curve from Gupta et al. (2025), indicating that the H_2O and H_2 would likely be miscible at these pressure/temperature HHBs, hence precluding an immiscible supercritical H_2O ocean. Cases with mixed H_2O/H_2 are modelled in Section 4.3.4.

In Figure 4.5 we show the locus of $P_{\rm HHB}$ and $T_{\rm HHB}$ for the possible interior solutions of TOI-270 d, including cases with an Earth-like and a pure Fe core, assuming the Case 1 P-T profile in the envelope, corresponding to the solutions in Figure 4.4. The locus traces the envelope P-T profile between lower and upper limits of $T_{\rm HHB} = 312$ K and $P_{\rm HHB} = 0.3$ bar, and $T_{\rm HHB} = 2922$ K and $P_{\rm HHB} = 7.4 \times 10^4$ bar. The lower pressure and temperature HHBs generally correspond to smaller envelope mass fractions, and hence larger H_2O mass fractions, as in Figure 4.4.

A wide range of compositions for TOI-270 d are permitted, for the P-T profiles Cases 1-4, generated using the abundances of Holmberg and Madhusudhan (2024). Based on these abundances, these interiors generally have hydrogen-dominated envelopes. Broadly, the interior solutions fall into three categories – hycean worlds (with liquid water oceans), mini-Neptunes, and gas dwarfs – as shown in Figure 1.15. These classes of solution will be explored in detail in subsequent Sections 4.3.3-4.3.5. We also show a mixed envelope case, representing the suggested interior of Benneke et al. (2024). In the following, where a distinct boundary occurs between the H_2O and H_2, we refer to the boundary as the H_2O/H_2-envelope boundary, or HHB (Madhusudhan et al., 2020). The equivalent for gas dwarf cases we refer to simply as the surface, or atmosphere-rock/magma interface.

4.3.3 Hycean World Scenarios

We have shown that the pressure and temperature conditions at the surface of TOI-270 d are highly dependent on the assumed temperature structure in the envelope, which in turn defines the phase of water (or silicates, in the gas dwarf scenario) at the surface. The possibility of a liquid H_2O surface is permitted by the P-T profiles Case 1 and Case 2, with the high haze parameter of $a = 1500$ and $T_{\rm int} = 25$ & 50 K respectively. As described above, in Figure 4.5 we show the HHB locus for Case 1 that correspond to the solutions in Figure 4.4.

In this section, we explore the solutions that permit a liquid H_2O surface on TOI-270 d. For cases assuming efficient day-night heat redistribution, we distinguish between liquid water surfaces that host habitable conditions and those that do not, by the terms “hycean worlds” and “hot hycean worlds”. We define a hot hycean world as having a liquid H_2O surface beneath an H_2-rich atmosphere, with surface conditions

beyond the range of commonly considered habitability limits. Habitable conditions are here defined as $273 \leq T_{\mathrm{HHB}} \leq 395$ K and $1 \leq P_{\mathrm{HHB}} \leq 1000$ bar, based on conditions where life is found on Earth (Rothschild and Mancinelli, 2001; Merino et al., 2019). We note that the maintenance of a liquid water ocean beneath a H_2-rich envelope across the full range of pressures and temperatures used here is debated, due to a runaway greenhouse effect (e.g. Leconte et al., 2024) – this will be discussed further in Section 4.4.1.

TOI-270 d is sufficiently close to its host star that it is likely tidally locked. On tidally locked exoplanets, if the day-night heat redistribution is inefficient, this could lead to large temperature differences between the day and night sides. Dark hycean conditions are defined as a hycean world with a nightside that is sufficiently cool to host habitable conditions while the dayside is too hot. In Section 4.3.3 we explore possible dark hycean scenarios for TOI-270 d, which was suggested as a possibility by Holmberg and Madhusudhan (2024).

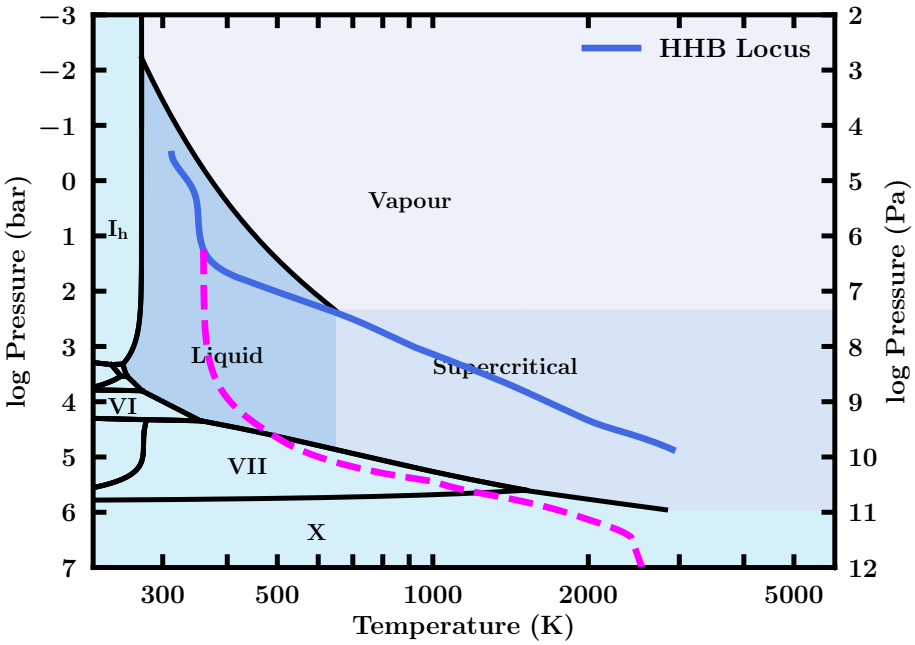

Fig. 4.5 Locus of possible H_2O/H_2-envelope boundary (HHB) conditions for TOI-270 d for the Case 1 envelope P-T profile. An interior adiabat is also shown by the dashed line, corresponding to the hycean case described in Section 4.3.3, with surface conditions at 360 K and 18 bar.

Hycean World

We find compositions permitting a liquid H_2O ocean with habitable surface conditions, i.e. hycean conditions, are permitted by Cases 1 and 2. The range of envelope mass fractions permitting a habitable liquid surface on TOI-270 d are found to be $\lesssim 3.5 \times 10^{-5}$. The limitation defining the maximum envelope mass is the resulting surface temperature rather than pressure; the Case 1 profile reaches 395 K at ~ 100 bar. We find that habitable liquid surfaces require large H_2O mass fractions $\gtrsim 60\%$ in their interiors. As shown in Figure 4.4, the small envelope mass fractions required for low temperature surfaces require a large H_2O mass fraction to satisfy the planet's bulk density.

An example hycean interior with median R_p and M_p consists of $x_{\mathrm{H_2O}} = 75\%$, $x_\mathrm{env} = 0.0012\%$ and the remainder in an Earth-like core. The HHB in this case is at $T_\mathrm{HHB} = 360$ K and $P_\mathrm{HHB} = 18$ bar. The depth of the ocean above the high-pressure ice layer is 284 km, with the high-pressure ice of thickness 1.08 $R_\oplus$ (6861 km). The adiabat throughout the H_2O layer for this case is shown in Figure 4.5.

As seen in Chapter 2, previous studies have investigated the ocean depths of water-rich exoplanets, finding a dependence of depth on the surface gravity and surface temperature (Noack et al., 2016; Nixon and Madhusudhan, 2021; Rigby and Madhusudhan, 2024). For a given surface temperature, a lower surface gravity results in a larger ocean depth. While, for a given surface gravity, a higher surface temperature leads to a deeper ocean for HHB temperatures up to 413 K, where the trend reverses (Nixon and Madhusudhan, 2021) due to the adiabatic temperature structure assumed in the H_2O layer. The difference in pressure from the surface to ocean base affects the ocean depth, and the base pressure is fixed by the surface temperature. Varying the surface pressure within the plausible range for a liquid surface has little effect on the ocean depth. The definition of ocean depth adopted by Nixon and Madhusudhan (2021), which we use in this chapter, is the depth at which the liquid phase ends, either via the transition to high-pressure ice or to supercritical water. For the following, we assume that the HHB pressure is such that the HHB remains in the liquid phase. A surface with $273 \leq T_\mathrm{HHB} \lesssim 295$ K would result in an ice VI ocean base. However, this is not possible for the envelope temperature structure considered for TOI-270 d. $295 \lesssim T_\mathrm{HHB} \leq 413$ K would result in an ice VII base. For $413 < T_\mathrm{HHB} < 647$ K there would be a supercritical portion of the "ocean" between the liquid and high-pressure ice layers – this is discussed in the following section. The contours in the right-hand side of Figure 4.4 show a kink at $x_\mathrm{env} \sim 10^{-4}$ for both core compositions. This corresponds to

the HHB at which the H_2O adiabat will no longer intersect the ice VII phase boundary with increasing HHB temperature.

We find the possible range of hycean ocean depths to be $\sim$ 215-450 km for TOI-270 d. For reference, the average depth of Earth's ocean is 3.7 km (Charette and Smith, 2010) and the deepest point is $\sim$11 km (Gardner et al., 2014). The minimum ocean depth is limited by the surface pressure. The depth of 215 km corresponds to a surface pressure of 1 bar, at a temperature of 337 K. Conversely, the maximum ocean depth occurs for the maximum habitable surface temperature of 395 K. This temperature is the maximum considered for habitability, however the runaway greenhouse limit may be reached at temperatures below this (e.g. Leconte et al., 2024). The thickness of the high-pressure ice layers for TOI-270 d with a hycean surface are found to span up to $\sim 1 R_\oplus$. Thicker high-pressure ice layers correspond to larger H_2O mass fractions and lower HHB temperatures. As discussed in Section 2.4.1, the thickness of high-pressure ice layers may have implications for their habitability (e.g. Madhusudhan et al., 2023a).

Hot Hycean World

In addition to habitable pressure-temperature surface conditions, we find that interior solutions with a liquid H_2O surface at more extreme pressures/temperatures are permitted by both Cases 1 and 2. As shown in Figure 4.5, a liquid surface is permitted by Case 1 up until $T_{\rm HHB} \leq 647$ K, the critical temperature. We note that the runaway greenhouse limit may be reached at temperatures below this (e.g. Leconte et al., 2024), potentially precluding an ocean at these temperatures. For Case 2, a liquid surface is not possible above a HHB temperature of $\sim$500 K where the profile crosses into the vapour region of the water phase diagram, as seen in Figure 4.3. Thicker atmospheres and hence hotter HHBs will result in a supercritical HHB (or vapour, for Case 2). Under these conditions, it may become important to consider H_2O miscible in H_2 – this is considered in Section 4.3.4 for mini-Neptune cases.

Envelope mass fractions permitting a liquid surface on TOI-270 d, not restricted to habitable pressures and temperatures, are found to be $\lesssim 1.5 \times 10^{-4}$ for the envelope P-T profiles considered. The corresponding H_2O mass fractions are found to be $\gtrsim 50\%$. An example interior with a liquid surface with the median $R_{\rm p}$ and $M_{\rm p}$, assuming Case 1 as the envelope P-T profile, consists of $x_{\rm H_2O} = 60\%$, $x_{\rm env} = 0.011\%$ and the remainder in an Earth-like core. The HHB in this case is at $T_{\rm HHB} = 584$ K and $P_{\rm HHB} = 172$ bar. The liquid ocean becomes supercritical beyond a depth of 23 km, down to 1693 km, before a high-pressure ice layer of thickness 4199 km ($0.66 R_\oplus$). An example, also with the median $R_{\rm p}$ and $M_{\rm p}$, instead adopting Case 2 as the envelope P-T profile,

consists of $x_{H_2O} = 72\%$, $x_{env} = 0.00103\%$ and the remainder in an Earth-like core. The HHB in this case is at $T_{HHB} = 436$ K and $P_{HHB} = 15$ bar. The liquid ocean becomes supercritical beyond a depth of 361 km, down to 608 km, and lies atop a high-pressure ice layer of thickness 6331 km ($0.99R_\oplus$). To reproduce the same R_p, the hotter envelope P-T profile requires a smaller value of x_{env} for a given value of x_{H_2O}.

As for the habitable surface cases in Section 4.3.3, we place constraints on the ocean depths permitted for the liquid surface solutions. Overall, we find the possible range of ocean depths for TOI-270 d with a liquid surface to be $\lesssim 480$ km. The peak depth occurs at $T_{HHB} = 413$ K (Nixon and Madhusudhan, 2021), before a supercritical layer beneath the ocean occurs for higher HHB temperatures.

Dark Hycean Conditions

In this section, we explore the possibility of a dark hycean scenario for TOI-270 d, which we note may be infeasible when considering the effects of atmospheric circulation and the runaway greenhouse limit (e.g. Innes et al., 2023; Leconte et al., 2024). It remains difficult to place robust constraints on the day and nightside surface temperatures of tidally-locked sub-Neptunes observed only with transmission spectroscopy, since observations probing the photosphere at the terminator cannot easily constrain the day or night side temperature structure, albedo or atmospheric composition. Therefore, we explore a range of HHB temperatures for the day and night sides of potential dark hyceans. Innes et al. (2023) suggest weak temperature gradients for temperate sub-Neptunes with H_2-rich atmospheres due to the slow rotation rates. Informed by this, we therefore consider day-night temperature contrasts up to a maximum of 100 K. We note that we do not consider the dynamics of the atmosphere or ocean in this initial exploration of the internal structure of dark hycean worlds, which is expected to have a significant effect on the possible day-night contrast. In this highly simplified scenario, we treat the day and night sides independently, adopting an adiabatic profile in the interior on each side for an assumed T_{HHB} and P_{HHB}. For dark hycean conditions, the nightside HHB is at habitable temperatures ($273 \leq T_{HHB} \leq 395$ K) and pressures ($1 - 1000$ bar). On the dayside we allow the temperature to vary within the full possible range while maintaining a liquid surface – at 10 bar this is up to ∼450 K and at 100 bar this is up to ∼585 K. In reality, as discussed above, the day-night contrast would likely be less than this (e.g. Innes et al., 2023). We are also assuming that the hotter day-side surface remains below the runaway greenhouse limit, as potentially possible in the presence of high albedo (e.g. Leconte et al., 2024), as required for a hycean scenario (Madhusudhan et al., 2021).

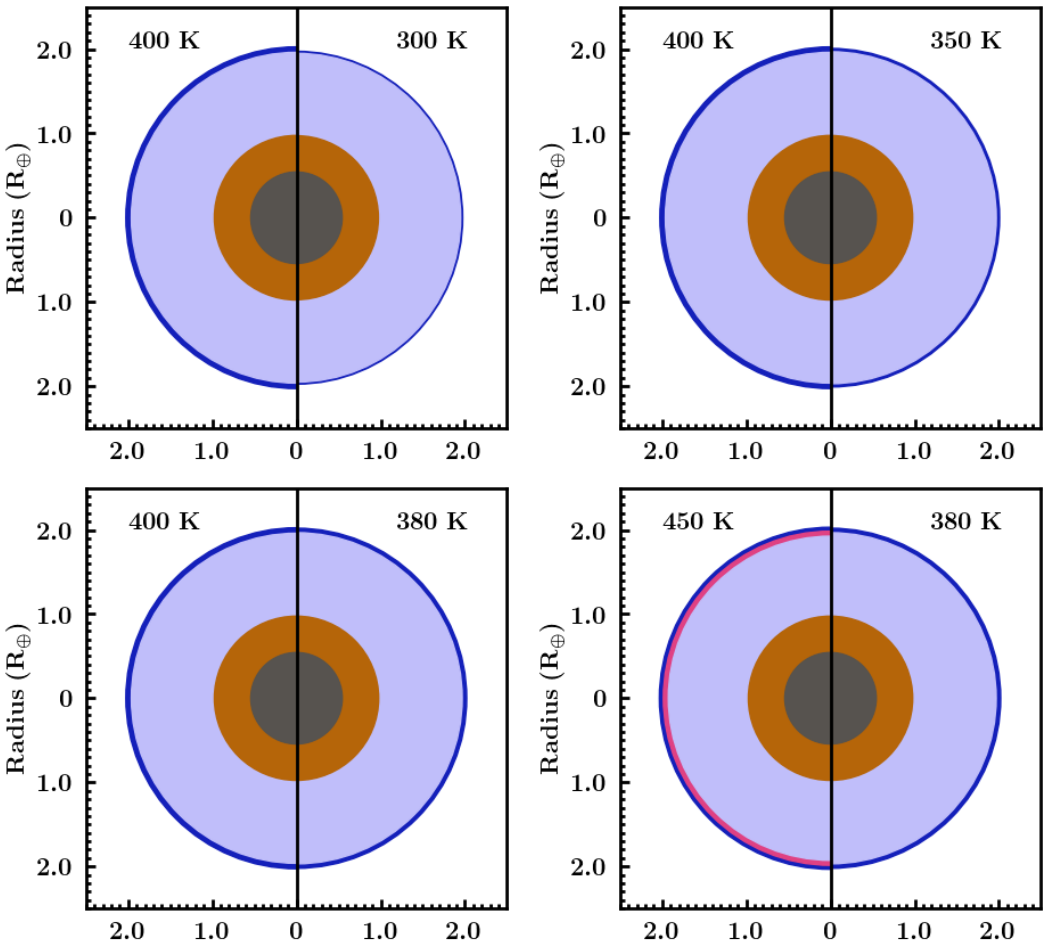

Fig. 4.6 Examples of possible dark hycean interiors of TOI-270 d, excluding the H_2-rich envelope, with varying nightside HHB temperatures. The right-hand-side of each plot shows the nightside with $T_{\rm HHB} = 300$ K, $T_{\rm HHB} = 350$ K and $T_{\rm HHB} = 380$ K, while the left-hand-side of each plot shows the dayside with $T_{\rm HHB} = 400$ K or and $T_{\rm HHB} = 450$ K. All cases except the bottom-right have 70% H_2O by mass, and $P_{\rm HHB} = 50$ bar. The bottom-right case has $P_{\rm HHB} = 75$ bar.

In Figure 4.6 we show examples of dark hycean interiors for TOI-270 d. In these cases, the HHB is fixed at 50 bar for both the day and night sides, i.e. only the HHB temperature is varying between them. The value of 50 bar would be the pressure for a 400 K surface, using the Case 1 *P-T* profile. For these surface conditions, a solution with median $M_{\rm p}$ and $R_{\rm p}$ has $\sim 70\%$ H_2O by mass; therefore we adopt this fraction, with the remaining mass in an Earthlike core. We vary the nightside HHB from 300-380 K, for a 400 K dayside. The corresponding interiors are shown in Figure 4.6. For all of the HHBs shown at 400 K, 380 K, 350 K and 300 K, the resulting H_2O phase structure is liquid to ice VII to ice X. (At this $P_{\rm HHB}$, $T_{\rm HHB} > 413$ K is required for a supercritical portion of the ocean.) We also show an example with the dayside sufficiently hot for a supercritical layer between the ocean and ice, which is shown in pink in Figure 4.6. The dayside HHB here is at 450 K and 75 bar. The effect of ocean dynamics on the existence of supercritical regions is yet to be explored. As is evident from Figure 4.6, this difference in surface temperature makes negligible difference to the internal structure beneath the ocean.

4.3.4 Mini-Neptune

For the *P-T* profiles considered in this work, we find a wide range of H_2O and envelope mass fractions across which the interior of TOI-270 d could host mini-Neptune-like conditions. These interiors correspond to the vapour or supercritical HHBs shown in Figure 4.5. An example of a typical mini-Neptune solution consists of 0.4% H/He envelope, 50% H_2O and 49.6% Earth-like core. The HHB here is supercritical, at 953 K and 5510 bar, with the H_2O transitioning to ice XVIII (superionic ice) deeper in the interior. These calculations assumed that the H_2-rich envelope and H_2O layers remain distinct. However, it has been suggested that supercritical H_2O would become mixed with the H_2-rich envelope (Soubiran and Militzer, 2015; Gupta et al., 2025). Recently, Gupta et al. (2025) performed molecular dynamics simulations based on density functional theory to establish the interactions of hydrogen and water at pressures and temperatures relevant to sub-Neptune planets. They found that the critical curve, marking the transition from single to separate phases, is at lower temperature than previous studies (Soubiran and Militzer, 2015) and can well-match experimental data. Therefore, this underscores the expectation, as suggested by other studies (Nixon and Madhusudhan, 2021; Benneke et al., 2024), that a mixed water/hydrogen envelope may be present for sufficiently warm, water-rich sub-Neptunes. Gupta et al. (2025) suggest this to be the case for TOI-270 d, as found by Benneke et al. (2024), if its temperature at 1 bar exceeds its zero albedo equilibrium temperature of 387 K. This is the case

for our *P-T* profiles Cases 3 & 4, while Cases 1 & 2, with more hazes, are cooler at 1 bar. The median retrieved atmospheric abundances from Holmberg and Madhusudhan (2024) shows an H_2-dominated composition. This would hence correspond to a cold trap, as in Cases 1 & 2.

We calculate the EOS for varying proportions of H_2O by mass in the atmosphere using Equations 4.1 and 4.2, as in Section 4.2.3. We vary the atmospheric H_2O mass proportion (f_{H_2O}) up to 50% (from our canonical 10%), somewhat nominally, informed by the uncertainty in the observed H_2O mixing ratio. We consider a range of envelope *P-T* profiles by varying the radiative-convective boundary pressure, P_{rc}. We modify Case 1 to adopt $P_{rc} = 10$ bar, in addition to the canonical Case 1 profile. Beyond P_{rc} the profile follows an adiabat, which we calculate assuming different values of f_{H_2O}. The envelope composition is considered fully mixed below the cold trap. In all cases, for simplicity, the mass contained in the H_2-rich atmosphere above this cold trap is considered to be negligible, and we treat this as isothermal. We assume there is no phase separation throughout the mixed layer, i.e. no formation of high-pressure ices below the envelope (Gupta et al., 2025). The mass and radius are fixed at their median values for the following calculations.

We first consider the canonical Case 1 profile. For an envelope H_2O to H_2/He fraction (f_{H_2O}) of 50% overlying an Earth-like interior we find an envelope mass fraction of $x_{env} = 5.64\%$ is required to achieve the median R_p for the median M_p. The surface lies at 1.85×10^5 bar and 3186 K. In contrast, from Section 4.3.2, we showed that our canonical envelope composition (f_{H_2O}=10%) has the smaller corresponding $x_{env} = 2.25\%$ for an Earth-like interior. For $f_{H_2O} = 40\%$ and an Earth-like interior we find $x_{env} = 4.12\%$ is required, with the surface at 1.37×10^5 bar and 3125 K.

Next, we consider Case 1 modified to have P_{rc} at 10 bar, which results in a profile hotter than the canonical Case 1. Therefore, for $f_{H_2O} = 40\%$ and an Earth-like interior, a smaller envelope mass fraction of $x_{env} = 3.32\%$ is required to achieve the median radius for the median planetary mass. The equivalent value for f_{H_2O} of 50% is $x_{env} = 5.14\%$.

For the Case 2 profile, we do not vary P_{rc} since this is already ∼10 bar, as seen in Figure 4.1. For $f_{H_2O} = 50\%$ and an Earth-like interior we find $x_{env} = 3.75\%$ is required for median R_p and M_p. The surface lies at 1.29×10^5 bar and 4007 K. In contrast, our canonical $f_{H_2O} = 10\%$ H_2O envelope composition has the smaller corresponding $x_{env} = 1.10\%$ for an Earth-like interior.

As mentioned in Section 4.3.1, Cases 3 and 4 lack a cold trap. This would imply that a mixed H_2O/H_2 envelope would be likely detectable. For the one offset and

simultaneous dual transit case (Holmberg and Madhusudhan, 2024) that we adopt for our canonical mixing ratios in Section 4.2.2, the upper limit may permit f_{H_2O} values of ∼40% by mass in the envelope. However, the observational evidence for H_2O is tentative (Holmberg and Madhusudhan, 2024). Future observations may reveal stronger H_2O detections that will prompt further investigation into the envelope composition and temperature structure, and the corresponding interior composition, similar to that suggested by Benneke et al. (2024).

As a demonstration of a fully mixed envelope, we consider the Case 4 profile. For a $f_{H_2O} = 50\%$ and an Earth-like interior we find $x_{env} = 3.24\%$ is required to achieve the median radius for the median planetary mass. The surface lies at 1.15×10^5 bar and 3821 K. The equivalent for $f_{H_2O} = 40\%$ is $x_{env} = 2.23\%$, with surface at 7.98×10^4 bar and 3668 K. Our canonical $f_{H_2O} = 10\%$ case required $x_{env} = 0.86\%$.

4.3.5 Gas Dwarf

In this section we explore the set of interiors lacking a significant H_2O mass fraction, with H_2-dominated atmospheres overlying rocky interiors, referred to here as gas dwarfs. Gas dwarf scenarios for temperate sub-Neptunes may have solid or molten surfaces beneath the thick H_2-rich envelope. In Chapter 3 we outlined a framework to establish the feasibility of such scenarios for temperate sub-Neptunes. We showed that the feasibility of a solid or magma surface is highly dependent on the atmospheric temperature structure, while remaining consistent with internal structure constraints from the planetary bulk parameters. The possibility and observational implications of a potential rocky or magma surface on TOI-270 d will be discussed in Section 4.4.4.

In Section 4.3.2 we placed initial constraints on the H_2-rich envelope mass fractions permitted by the bulk properties of TOI-270 d. The permitted envelope mass fractions are dependent on the assumed temperature structure in the envelope and the core composition. The maximum envelope mass fraction corresponds to a maximum density pure Fe core with the maximum planet radius, at $x_{env} = 4.70\%$ for the coolest P-T profile (Case 1). With an Earth-like and pure silicate interior, the maximum values of x_{env} are 2.25% and 1.44% respectively. In these initial calculations, we did not include an EOS prescription for silicate melt, instead using the EOS from Seager et al. (2007), as described in Section 4.2.3.

Following from our initial calculations, we now place constraints on the interior compositions allowing a magma or solid rocky surface for our range of P-T profiles, using the EOS treatment for silicates from Chapter 3.

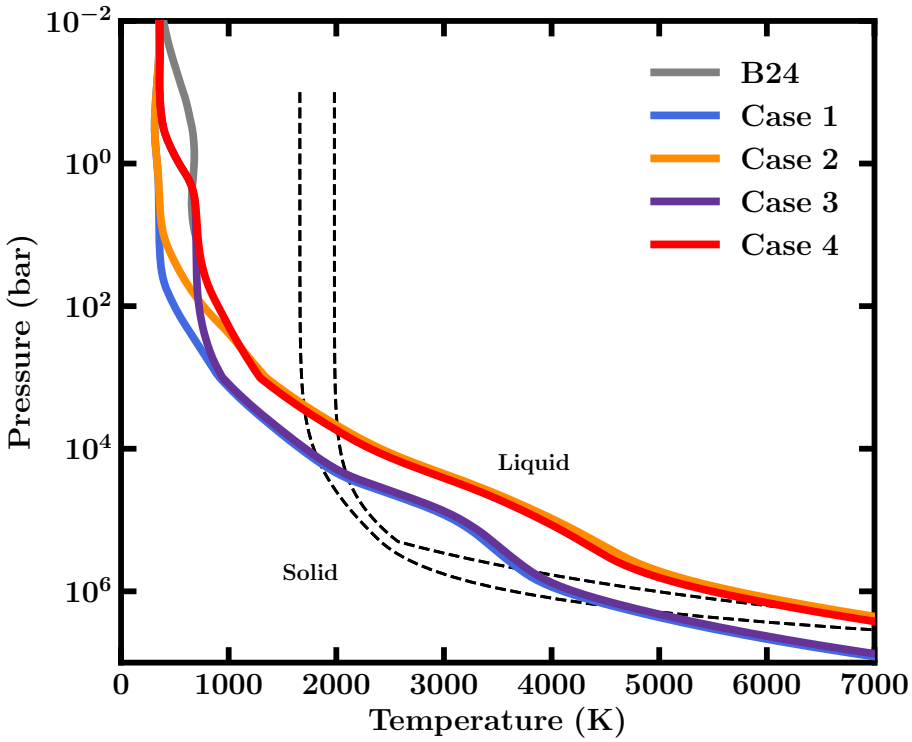

Fig. 4.7 Atmospheric P-T profiles considered in this work, compared to the liquidus and solidus for peridotite (Fiquet et al., 2010; Monteux et al., 2016). Cases 1-4 are the self-consistent profiles generated in this work from the atmospheric abundances of Holmberg and Madhusudhan (2024). We also include the "evening" P-T profile from Benneke et al. (2024) for comparison.

In Figure 4.7 we show the atmospheric P-T profiles Cases 1-4, shown by the solid lines, against the liquidus and solidus for peridotite, shown by the dashed black lines (Fiquet et al., 2010; Monteux et al., 2016). Similar to the process for considering H_2O-rich interiors, the possibility of a magma surface can be initially assessed by the phase of peridotite at the envelope base. As in Chapter 3, the melt-atmosphere interactions and atmospheric chemistry would need to be considered, before establishing the potential feasibility of matching observed atmospheric abundances. We leave an execution of the full framework for TOI-270 d, beyond the internal structure modelling, to future work.

We first adopt our canonical Case 1 P-T profile, the coldest of those considered, and consider interior compositions ranging from the extreme cases of $f_{\rm silicate} = 100\%$ to $f_{\rm silicate} = 5\%$. For the following, the solutions have $M_{\rm p}$ and $R_{\rm p}$ equal to the median measurements. For the extreme case assuming $f_{\rm silicate} = 100\%$, the surface would not be molten. We note that this is assuming the liquidus as the melt-solid transition –

these pressure/temperature surface conditions lie between the solidus and liquidus and would hence be expected to result in partial melt. The corresponding $x_{\rm env}$ is 1.01%, with $P_{\rm s} = 2.66 \times 10^4$ bar and $T_{\rm s} = 2111$ K. With increasing proportion of Fe in the interior, the corresponding surface pressure increases. For an Earth-like interior composition, the surface would be molten, at $P_{\rm s} = 5.25 \times 10^4$ bar and $T_{\rm s} = 2661$ K. The mass fraction contained in the melt ($x_{\rm melt}$) is 16.5%, and the corresponding envelope mass fraction is $x_{\rm env} = 1.65\%$. Increasing the Fe content to a Mercury-like interior ($f_{\rm silicate} = 30\%$) we find $x_{\rm env} = 2.76\%$ and $x_{\rm melt} = 10.13\%$, with surface conditions $P_{\rm s} = 1.18 \times 10^5$ bar and $T_{\rm s} = 3210$ K. For the extreme case of $f_{\rm silicate} = 5\%$, we find a 4.78% melt fraction, with $x_{\rm env} = 3.85\%$, with surface conditions $P_{\rm s} = 2.23 \times 10^5$ bar and $T_{\rm s} = 3472$ K.

We also consider Case 2 for the envelope P-T profile. This profile is calculated assuming high hazes ($a = 1500$) and $T_{\rm int} = 50$ K, compared to $T_{\rm int} = 25$ K for Case 1. The hotter profile at higher pressures results in a molten surface across all $f_{\rm silicate}$ values considered. An example solution for an Earth-like interior composition has envelope mass fraction $x_{\rm env} = 0.94\%$. The corresponding surface conditions are $P_{\rm s} = 3.11 \times 10^4$ bar and $T_{\rm s} = 3241$ K, with $x_{\rm melt}$ is 12.25%. Due to the hotter P-T profile, the surface pressure for the same $f_{\rm silicate}$ in the interior is lower for Case 2 than for Case 1.

4.4 Summary and Discussion

In this study, we have conducted a theoretical exploration of the range of possible interior compositions and surface conditions for TOI-270 d, based on atmospheric constraints. We placed constraints on the possible compositions that satisfy the reported bulk properties of the planet, adopting self-consistent envelope P-T profiles generated using retrieved atmospheric abundances (Holmberg and Madhusudhan, 2024). We presented our results for the possible interior and surface conditions, which span gas dwarfs, mini-Neptunes and water-rich worlds with liquid ocean surfaces, including hycean worlds, hot hycean worlds and dark hycean worlds.

For our assumed envelope temperature structures, we first explored the possible interior compositions that permit liquid H_2O on the surface of TOI-270 d. The H_2-rich envelope mass fractions across these cases span $x_{\rm env} \lesssim 1.5 \times 10^{-4}$, while the H_2O mass fractions are $x_{\rm H_2O} \gtrsim 50\%$. Habitable hycean conditions at the HHB are possible for envelope mass fractions $\lesssim 3.5 \times 10^{-5}$ and H_2O mass fractions $\gtrsim 60\%$, where the surface is defined to be $273 \leq T_{\rm HHB} \leq 395$ K and $1 \leq P_{\rm HHB} \leq 1000$ bar. We note that the

runaway greenhouse limit could be reached for temperatures below the upper limit of our assumed temperature range (e.g. Leconte et al., 2024). Across the hycean cases, the possible ocean depths are found to span $215 - 450$ km, atop icy mantles that can exceed thickness of 1 $R_\oplus$. We additionally explore a simple model of possible dark hycean conditions, where only the nightside has habitable pressures and temperatures at the surface. This was suggested to be a possibility on TOI-270 d due to its relatively high equilibrium temperature for a hycean candidate (Holmberg and Madhusudhan, 2024).

Hycean scenarios are the only shallow-atmosphere interiors compatible with the bulk properties of TOI-270 d. The alternatives are a mini-Neptune and a gas dwarf – a rocky interior beneath a thick H_2 envelope. In Section 4.3.4 we explored the possibility of a mini-Neptune scenario for TOI-270 d. We adopt a mixed H_2O/H_2 envelope up to a cold trap, as permitted by the atmospheric *P-T* profiles Cases 1 and 2, which would remain compatible with the retrieved H_2O abundance of Holmberg and Madhusudhan (2024). For gas dwarf scenarios, considered in Section 4.3.5, we find the possible envelope mass fractions to span $1 - 5\%$, with conditions at the surface $\sim 10^4 - 10^5$ bar. Depending on the atmospheric *P-T* profile, we show that magma oceans may be possible on TOI-270 d for these envelope mass fractions. Further study is required to robustly assess the feasibility of a magma ocean surface given the observed atmospheric composition (e.g. Benneke et al., 2024).

In this section, we explore the possible classification of TOI-270 d and the feasibility of robustly constraining the nature of its surface and interior. We discuss the possibility of TOI-270 d hosting habitable conditions as a hycean or dark hycean world in Section 4.4.1. We then discuss the mini-Neptune scenario for TOI-270 d in Section 4.4.2. In Section 4.4.3, we explore the feasibility of a gas dwarf scenario for TOI-270 d, including its potential to host a magma ocean, in addition to the detectability of this compared to a liquid water ocean. Finally, we outline the future prospects for the characterisation of TOI-270 d in light of the recent and upcoming observations.

4.4.1 Hycean Scenarios

In Section 4.3.3 we investigated interior solutions permitting liquid water on the surface of TOI-270 d. These solutions were explored for our *P-T* profiles Case 1 and Case 2 – the profiles that pass through the liquid region of the H_2O phase diagram. We identified the set of solutions corresponding to habitable hycean scenarios, in addition to liquid surfaces with temperatures $\gtrsim 395$ K, which would preclude habitability. We note that the formation pathway of hycean worlds remains unexplored – for instance,

whether the large mass fraction of water can remain as a distinct layer or is at least partially mixed with the rock (e.g. Vazan et al., 2022; Luo et al., 2024).

Recent studies of hycean climates have suggested that convective inhibition may result in steep temperature gradients in the atmosphere close to the surface, resulting in surfaces too hot to sustain liquid water (e.g. Innes et al., 2023; Leconte et al., 2024). For K2-18 b, which has a lower equilibrium temperature than TOI-270 d, Leconte et al. (2024) found that a high albedo ($A_{\mathrm{B}} > 0.5 - 0.6$) due to clouds and/or hazes would be required to maintain a liquid ocean. This high albedo is consistent with the definition for hycean worlds given by Madhusudhan et al. (2021). The models of Innes et al. (2023) do not incorporate clouds and hazes. For TOI-270 d, from the atmospheric *P-T* profiles, we have established that hazes are required to allow the possibility of a liquid surface on TOI-270 d – Cases 1 & 2 permit liquid oceans at the planetary surface, for a range of internal temperatures, assuming a strong albedo due to hazes. The recent observations did not provide strong constraints on the presence of clouds and/or hazes in the atmosphere of TOI-270 d (Holmberg and Madhusudhan, 2024), which may be refined by future observations.

As suggested by Holmberg and Madhusudhan (2024), even if the dayside of TOI-270 d is too warm to allow for habitable conditions, inefficient day-night redistribution could lead to a habitable nightside. In Section 4.3.3 we explored potential dark hycean scenarios for TOI-270 d. Innes et al. (2023) suggest weak temperature gradients for temperate sub-Neptunes with H_2-rich atmospheres due to the slow rotation rates. These processes and resulting temperature contrasts have yet to be established for a moist hycean atmosphere with clouds and/or hazes, therefore we considered a range of surface temperatures, with day-night temperature contrasts up to a high value of 100 K. The dynamics of hycean atmospheres and oceans have yet to be explored, including the distribution of heat in the oceans in tidally locked hyceans, which will have significant implications for the dark hycean scenario. To maintain a liquid surface, the dayside conditions would further need to remain below the runaway greenhouse limit (e.g. Leconte et al., 2024), requiring a high albedo.

4.4.2 Mini-Neptune Scenarios

In Section 4.3.4 we explored mini-Neptune scenarios for TOI-270 d, which are characterised by a water-rich interior with no distinct surface. We include the possibility of a mixed H_2/H_2O layer, as has suggested to be likely for sufficiently warm conditions on water-rich sub-Neptunes (e.g. Nixon and Madhusudhan, 2021; Benneke et al., 2024; Gupta et al., 2025). This situation can arise with or without a cold trap. In the former

case, H_2O would condense out, resulting in a H_2-dominated upper atmosphere, as consistent with the findings of Holmberg and Madhusudhan (2024). This is represented in the interior solutions from our *P-T* profiles Cases 1 & 2. Meanwhile, the results of Benneke et al. (2024), with high mean molecular weight, are suggested to be consistent with a fully mixed envelope. However, as yet, no strong evidence for H_2O has been found for the atmosphere of TOI-270 d (Holmberg and Madhusudhan, 2024; Benneke et al., 2024; Felix et al., 2025). Future observations are required to strengthen the evidence for H_2O, which will provide further insight into the envelope composition.

Recent work has investigated the conditions for miscibility and phase separation of water and hydrogen at pressures relevant to sub-Neptune interiors (Gupta et al., 2025). Future work, including evolution models, should incorporate a more thorough treatment of this behaviour to assess the possible phase behaviour in such interiors. Whether a sub-Neptune's interior temperature structure crosses the critical curve during its evolution, indicating phase separation of hydrogen and water, may prove crucial to assessing its present interior structure.

The presence of abundant NH_3 and CH_4 have been suggested as characteristics of a mini-Neptune atmosphere, due to the deep atmosphere recycling of photochemically produced nitrogen and carbon species (e.g. Tsai et al., 2021; Hu et al., 2021; Cooke and Madhusudhan, 2024). The atmospheric chemistry of TOI-270 d and similar sub-Neptunes will vary depending on the presence or lack of a cold trap (e.g. Yang and Hu, 2024). Future observations providing improved constraints on the H_2O abundance will be crucial to establish this. Further work is additionally required to strengthen the observational predictions for a mini-Neptune scenario, including accurate and complete cross-section data, and chemical networks for photochemical models. We also note that the chemistry in a supercritical mixed H_2/H_2O envelope has not been explored in detail.

4.4.3 Gas Dwarf Scenarios

The set of compositions permitting a gas dwarf scenario for TOI-270 d, characterised by a rocky interior and a thick H_2-rich envelope, were explored in Section 4.3.5. For our assumed atmospheric temperature profiles, we find the envelope mass fractions required in this scenario to be $\sim 1-5\%$, for interior compositions varying between the extreme cases of pure silicate to pure iron interiors. The corresponding atmospheric base pressures span $\sim 10^4 - 10^5$ bar, depending on the assumed core composition.

In Chapter 3 we outlined a method for evaluating the plausibility of gas dwarf scenarios, including the presence of a magma ocean, for temperate sub-Neptunes. This

end-to-end framework coupled an internal structure model, melt-atmosphere interface chemistry and atmospheric models. Overall, we found that the CO/CO_2 ratio is a key indicator of a deep atmosphere, expected to be $CO/CO_2 > 1$ for a lack of observed H_2O, and $CO/CO_2 \lesssim 1$ in the presence of H_2O. Taking into account the bulk properties of the planet in a holistic modelling framework is hence crucial to establish the feasibility of a gas dwarf scenario and potential presence of a magma ocean. We found using this framework that the observations for K2-18 b could not be explained by a magma ocean. The pattern of detections and non-detections in TOI-270 d is similar to those of K2-18 b (Madhusudhan et al., 2023b), including the depletion of NH_3 (Holmberg and Madhusudhan, 2024; Benneke et al., 2024; Felix et al., 2025). Although, similarly to K2-18 b, JWST observations of TOI-270 d thus far have provided only upper limits on the CO abundance (Holmberg and Madhusudhan, 2024; Benneke et al., 2024). Given these upper limits, a CO/CO_2 ratio > 1 is unlikely for TOI-270 d, which would be difficult to reconcile with the presence of a deep, gas dwarf atmosphere. In Chapter 3 we also tentatively suggest that sulfur depletion could be an indicator, depending on the assumed solubility laws, which could become important for TOI-270 d given the tentative CS_2 detection. Recently, Glein et al. (2025) suggested a lack of CO in the atmosphere of TOI-270 d could be explained by equilibrium chemistry of hot gas in a H_2O-rich and CO_2-poor atmosphere. This study relies on the presence of a high mean molecular weight atmosphere (Benneke et al., 2024; Felix et al., 2025), which is in contrast to the findings of Holmberg and Madhusudhan (2024).

For TOI-270 d, as shown in this work, and K2-18 b as shown in Madhusudhan et al. (2020), large atmospheric mass fractions $\gtrsim 1\%$ are required to satisfy the observed mass and radius in the absence of a H_2O layer. Under these conditions, surface pressures at the lowest are $\sim 10^4$ bar and for many interior solutions for both planets extend to $\gtrsim 10^5$ bar (Madhusudhan et al., 2020; Rigby et al., 2024). The partitioning of volatiles at high pressures ($\gtrsim 10^5$ bar) is not well tested experimentally (Kite et al., 2019; Schlichting and Young, 2022; Shorttle et al., 2024), therefore future studies are needed to further explore the interaction of a magma ocean with a H_2-rich atmosphere at such extreme pressures and temperatures. Modelling gas dwarfs with potential magma oceans also requires an assumption to be made on the nature of the melt composition, which can have significant effects on the density and melt curve. Furthermore, the phase behaviour of hydrogen and rock at such high pressures (e.g. Young et al., 2024) may have implications for the differentiation of these materials, and hence the formation of a distinct surface.

Establishing the nature of planets in the sub-Neptune regime is crucial in understanding planet formation and evolution processes, including the cause of the radius valley (e.g. Fulton et al., 2017; Fulton and Petigura, 2018a; Cloutier and Menou, 2020). Rocky planets with thick H_2-rich envelopes have been suggested to dominate the larger radius peak above the radius valley, with the smaller radius population having lost their H_2-rich atmospheres via photoevaporative (e.g. Lopez and Fortney, 2013; Jin et al., 2014; Owen and Wu, 2017; Jin and Mordasini, 2018) and/or core-powered mass loss (e.g. Ginzburg et al., 2018; Gupta and Schlichting, 2019, 2020). However, this remains debated – for instance, whether water-rich sub-Neptunes also explain this second peak (e.g. Zeng et al., 2019; Rogers, 2025). For individual exoplanets, atmospheric molecular abundances, in addition to improved precision of mass and radius measurements, are crucial for characterising their interiors and surfaces. As discussed above, further theoretical and experimental studies are also necessary to achieve this. Multiple sub-Neptunes have already been observed with JWST (e.g. Madhusudhan et al., 2023b; Kempton et al., 2023; Wallack et al., 2024), however to better understand the nature and diversity of this population, high-precision transmission spectra will need to be obtained for large numbers of these planets.

4.4.4 Prospects for Future Characterisation

TOI-270 d has been observed as part of multiple JWST programs (GTO Program 2759, GO Programs 3557 & 4098), with the NIRISS, NIRSpec and MIRI instruments, spanning 0.9-12 μm. Holmberg and Madhusudhan (2024) analysed recent NIRSpec G395H observations in addition to HST data (Mikal-Evans et al., 2023), reporting strong detections of CH_4 and CO_2 detections and a non-detection of NH_3, along with tentative H_2O and CS_2. As we have shown in this work, the planetary bulk and atmospheric properties allow for a wide range of interior compositions for TOI-270 d, given the current uncertainties.

Constraints on the photospheric metallicity and temperature through transmission spectroscopy can provide useful information on the possible interior compositions. As discussed by Benneke et al. (2024), their high obtained atmospheric metallicity and temperature would likely preclude the presence of a distinct H_2O layer, as this would be supercritical at depth, and hence mixed with H_2. The median retrieved abundances of Holmberg and Madhusudhan (2024) are not compatible with a fully mixed envelope without a cold trap. If future observations were to provide stronger evidence for H_2O at higher abundance, towards the upper limit of the current Holmberg and Madhusudhan (2024) error bars, this may indicate the presence of a mixed H_2O/H_2 envelope. Robust

atmospheric retrievals on precise JWST data are essential to accurately inform these inferences for the interior and surface conditions of sub-Neptunes, including TOI-270 d.

It is difficult to place robust constraints on the day and nightside surface temperatures of tidally-locked sub-Neptunes observed with transmission spectroscopy alone. Atmospheric abundances in the photosphere at the terminator cannot easily constrain the day or night side temperature structure, albedo or composition of the atmosphere. Determining the atmospheric temperature structures of sub-Neptunes is already complex (e.g. Piette and Madhusudhan, 2020; Innes et al., 2023; Leconte et al., 2024), for instance, due to the effects of clouds/hazes. Therefore, to place constraints on the dayside properties of tidally-locked sub-Neptunes, future observations will need to include emission spectroscopy.

The range of explanations for the transmission spectra of the recently observed sub-Neptunes highlights the importance of studies into the complex relationship between sub-Neptune atmospheres and surfaces (e.g. Hu et al., 2021; Rigby et al., 2024; Yang and Hu, 2024; Cooke and Madhusudhan, 2024; Young et al., 2024; Glein et al., 2025). The abundance of high precision spectroscopic data from JWST requires robust theoretical models to best inform interpretation of such results. As discussed earlier in Section 4.4, additional experimental and theoretical work is needed to better establish the observational diagnostics of possible surface layers, including liquid water and magma oceans. Further experimental work is required to improve the solubility data for chemical species in these materials, and to investigate the behaviour of planetary materials at high pressures and temperatures (e.g. Young et al., 2024; Gupta et al., 2025). Atmospheric data remains crucial for helping to break degeneracies in interior composition that are inherent in internal structure modelling. We note that robust data reduction and retrieval frameworks must be employed to accurately determine atmospheric abundances from the high-precision JWST data.

Temperate sub-Neptunes orbiting M dwarfs, including TOI-270 d, remain exciting targets for detailed atmospheric characterisation with JWST. Observations of these planets provide important case studies for understanding the broader nature of the sub-Neptune population and the implications for planet formation/evolution processes. Robustly determining the nature of sub-Neptune atmospheres, surfaces and interiors requires further theoretical and experimental studies, including atmosphere/surface interactions, and equations of state at relevant pressures and temperatures. The high precision JWST transmission spectra of sub-Neptunes, including TOI-270 d, will help to shed light on their individual compositions and overall on this intriguing planetary regime.

Chapter 5

Conclusions and Future Work

In this thesis, we have explored a diverse range of interior scenarios for sub-Neptune exoplanets. These studies have covered both an investigation of theoretically possible interior conditions, as well as efforts to place constraints on the interiors of individual sub-Neptune based on their observable properties. This body of work highlights the importance of coupling internal structure models to atmospheric models and observations to best constrain the nature of these planets. In the following sections, we summarise the conclusions from the preceding chapters of this thesis, and describe potential areas for future research in this area.

5.1 Oceans and Interiors of Hycean Worlds

In this chapter we performed a theoretical exploration of hycean worlds – a recently proposed class of habitable sub-Neptune with surface water oceans beneath thin hydrogen-rich atmospheres (Madhusudhan et al., 2021). We outlined the details of our internal structure model HyRIS, which was used to investigate the range of ocean depths, interior compositions and envelope mass fractions possible for hycean worlds.

We found the expected range of ocean depths for hycean worlds to span 10s of km to ∼1000 km, with the depth influenced by the surface conditions. We confirm the results of Nixon and Madhusudhan (2021), showing the trends of ocean depth with surface temperature and gravity. We then considered five promising hycean candidates with (at the time) upcoming JWST data: TOI-270 d, TOI-1468 c, TOI-732 c, K2-18 b and LHS 1140 b. For each planet, we placed constraints on the interior compositions to allow for hycean conditions and the corresponding ocean depths. We identified the mass fractions of the H_2-rich envelopes across the hycean candidates considered, finding the maximum envelope fraction admissible for hycean conditions to be $\sim 10^{-3}$.

The maximum envelope mass fraction for non-hycean conditions were also calculated, found to span $\sim 4 - 8\%$ across the sample. These cases correspond to a gas dwarf scenario, with a thick H_2-rich envelope overlying a rocky interior.

The results in this chapter demonstrate the diverse range of conditions possible among hycean worlds, and the potential for these planets to host habitable conditions across a wide range of interior compositions, vastly different to the Earth. Identifying hycean conditions on hycean candidates requires establishing the presence of a surface ocean using data on atmospheric composition coupled to models of atmospheric chemistry (e.g. Yu et al., 2021; Hu et al., 2021; Tsai et al., 2021; Madhusudhan et al., 2023a; Cooke and Madhusudhan, 2024).

5.2 Gas Dwarf Scenarios for Temperate Sub-Neptunes

In this chapter we considered one of the degenerate interior scenarios for temperate sub-Neptunes: the gas dwarf scenario, characterised by thick H_2-rich atmospheres overlying a rocky interior. We presented a framework to evaluate the plausibility of this scenario on a case-by-case basis, including modelling the atmospheric structure, internal structure, magma-atmosphere interface chemistry, and atmospheric chemical and disequilibrium processes. The abundances of observable atmospheric species can thus be predicted for a given temperate sub-Neptune which can be compared to observed abundances.

We include the possibility of both solid and magma surfaces, which is determined by the pressure-temperature conditions at the base of the atmosphere. Our findings show that the melt fraction admissible depends on the interior composition and the atmospheric P-T profile, the latter depending on the internal temperature $T_{\rm int}$, the properties of clouds/hazes, and the molecular absorbers present.

The key atmospheric signatures for a gas dwarf are then identified. These include the abundances of CO and CO_2, and the possible nitrogen depletion if melt is present. $CO/CO_2 > 1$ is expected if no H_2O is observed, for instance due to condensation. Alternatively, in the presence of H_2O, $CO/CO_2 \lesssim 1$ is expected due to the additional available oxygen for CO_2 formation from the photolysis of H_2O. We find that the possible nitrogen depletion in the presence of a magma ocean is most strongly dependent on the surface pressure. Therefore, nitrogen depletion alone is not found to be sufficient evidence for a magma ocean.

We present a test-case of the framework, using the habitable-zone sub-Neptune K2-18 b. Our findings indicate that the current chemical constraints (Madhusudhan

et al., 2023b) are inconsistent with a gas dwarf interior for K2-18 b, due to the high observed CO_2 along with the lack of H_2O and the low upper limit of CO compared to predictions. This is the case independent of a magma ocean or solid surface.

This chapter stresses the importance of an integrated framework for obtaining physically plausible results for modelling sub-Neptune gas dwarfs. In addition, we highlight the need for further experimental work to reduce some important unknowns. The solubility of a number of chemical species at high pressures and temperatures and in reducing conditions are not well understood, including NH_3 and H_2S. There are also uncertainties in the sulfur photochemical network that prevents a confident proposal of sulfur species as reliable atmospheric diagnostics.

5.3 Interior and Surface Conditions of the Temperate Sub-Neptune TOI-270 d

In this chapter we presented an exploration of the possible interior and surface conditions for the temperate sub-Neptune TOI-270 d, based on recent atmospheric constraints. TOI-270 d was recently observed with JWST (Holmberg and Madhusudhan, 2024; Benneke et al., 2024). Using the atmospheric abundances from Holmberg and Madhusudhan (2024), we self-consistently generated atmospheric temperature structures for a range of internal temperatures and haze properties. We used these to conduct internal structure modelling for TOI-270 d, exploring the full range of possible interior scenarios. These interiors span gas dwarf, mini-Neptune and hycean world scenarios. For each of these cases, we determine the range of possible interior compositions and, where applicable, surface conditions.

For hycean scenarios, we find that H_2-rich envelope mass fractions $\lesssim 1.5 \times 10^{-4}$ are required, with H_2O mass fractions $\gtrsim 50\%$ for a liquid water surface. For habitable surface conditions, defined to be $273 \leq T_{\rm HHB} \leq 395$ K and $1 \leq P_{\rm HHB} \leq 1000$ bar, we find envelope mass fractions $\lesssim 3.5 \times 10^{-5}$ and H_2O mass fractions $\gtrsim 60\%$ are needed. It is important to note that depending on the surface pressure, the runaway greenhouse limit could be reached at temperatures below our adopted maximum (e.g. Leconte et al., 2024). The possible ocean depths are found to span $215 - 450$ km across all hycean scenarios.

We then explored the mini-Neptune scenarios. In these cases, we incorporated a mixed H_2O/H_2 envelope, since supercritical H_2O is expected to be fully miscible in H_2 across a wide range of pressure and temperature conditions (e.g. Soubiran and Militzer, 2015; Gupta et al., 2025). Mini-Neptune scenarios are shown to be possible for H_2O

mass fractions below those those required for hycean conditions. Finally, we explore gas dwarf scenarios, lacking a significant mass fraction of H_2O. We find the possible envelope mass fractions to be $1 - 5\%$, with surface conditions $\sim 10^4 - 10^5$ bar, across our envelope P-T profiles.

The bulk parameters and atmospheric properties of TOI-270 d allow for a wide range of interior compositions given the current uncertainties. Further observations are required to refine the atmospheric abundances, in addition to future theoretical and experimental work to aid the coupling of the atmosphere and interior of this planet.

5.4 Directions for Future Work

Arguably the largest source of uncertainty in internal structure modelling is the choice of equations of state for the different planetary materials, and their associated phase behaviour. This is particularly acute for high-pressures, for instance the phase boundaries and EOS for different phases of high-pressure ice remain relatively uncertain (e.g. Huang et al., 2022). We have throughout this thesis assumed pure H_2O ices. It may in future be beneficial to consider the effect of more complex compositions on the internal structure of sub-Neptunes, as has been considered in the context of solar system ice giants (e.g. Lee and Scandolo, 2011; Bethkenhagen et al., 2017) and icy moons (e.g. Journaux et al., 2017, 2020b). This could include methane hydrates, which have been studied for the ice giants (e.g. Schaack et al., 2019).

At sufficiently high pressures and temperatures, chemical species may become completely miscible, such that there is no distinct surface. Recently, Gupta et al. (2025) calculated the critical curve for H_2O/H_2 de-mixing in pressure-temperature-composition space, where composition is described through the hydrogen mole fraction. In Chapter 4 we considered the possibility of a mixed H_2O/H_2 layer for TOI-270 d in a mini-Neptune scenario, following previous studies (e.g. Nixon and Madhusudhan, 2021; Benneke et al., 2024). As more sub-Neptunes are observed, internal structure modelling of these planets should include the possibility of mixed H_2O/H_2 layers, depending on the temperature structure. This could be an important effect for inter-comparisons between sub-Neptunes across the 250-400 K equilibrium temperature range (Gupta et al., 2025), and may have significant implications for the inferred compositions of these planets.

The potential for mixed layers is not limited to hydrogen and water. Vazan et al. (2022) investigated ice/rock mixing in planetary interiors based on high-pressure laboratory experiments for peridotite rock (Grove et al., 2006; Melekhova et al., 2007;

Kessel et al., 2015). The degree of mixing depends on the conditions at formation, whether the ice and rock are accreted together or sequentially, with ice accreted after rock. This may result in fully mixed ice/rock layers, a compositional gradient, or fully differentiated layers. Recent DFT simulations by Kovačević et al. (2022) also showed that at high pressures (30-120 GPa) $MgSiO_3$ – one component of peridotite – and water are miscible beyond the melting temperature of $MgSiO_3$. Future work should incorporate the possibility of these scenarios into internal structure models of water-rich sub-Neptunes, which may affect the inferred range of possible compositions. Additional study is required to further investigate the mixing behaviour when Fe is also included (e.g. as recently considered by Young et al., 2025), in addition to the miscibility of hydrogen and molten rock – the latter has been investigated by multiple studies (e.g. Hirschmann et al., 2012; Kite et al., 2019; Young et al., 2024). The miscibility of molten rock and hydrogen will be relevant to consider in future models of gas dwarf scenarios. Including the complex phase behaviour of planetary materials can have substantial effect on the inferred internal structures for these planets, and is important for the interpretation of their nature.

As we have seen throughout this thesis, there is an acute need for further experimental work to better inform modelling efforts in multiple areas. In Chapter 3 we discussed the need for improved data on the solubility of different chemical species in magma at pressures relevant to sub-Neptunes. In particular, the depletion of NH_3 has been suggested to be indicative of a magma ocean on sub-Neptunes (e.g. Shorttle et al., 2024), however the solubility data for NH_3 is lacking. More broadly, considerations of surface-atmosphere interactions is an emerging and complex area, which requires both experimental and theoretical work to improve the interpretation of observations. This includes the atmospheric interactions with a surface water layer. Luu et al. (2024) considered aqueous geochemistry for a supercritical ocean on K2-18 b, however this was not propagated to the observable atmosphere using a full photochemical model. Studies have also considered the solubility of CO_2 in super-Earth oceans (e.g. Levi et al., 2017), which is highly dependent on the pH of the water. Current photochemical modelling of hycean scenarios (Yu et al., 2021; Hu et al., 2021; Tsai et al., 2021; Madhusudhan et al., 2023a; Cooke and Madhusudhan, 2024) typically assume the ocean is a sink, however it may become relevant to consider a surface flux of chemical species to be non-zero and time-varying. This was recently investigated for biologically produced sulfur species by Tsai et al. (2024). Further study into the ocean-atmosphere interactions for liquid, and indeed supercritical, oceans for hydrogen-rich atmospheres is required to ensure the plausibility of these interior scenarios for these planets based on observations. Coupling

such models to an internal structure model, analogously to Chapter 3 for gas dwarfs, may in future be a useful extension to self-consistently assess such scenarios.

Finally, we also note that there remain uncertainties in the atmospheric properties themselves, which are not entirely well-constrained by current JWST observations. In future work, the effect that these different uncertain atmospheric properties have on the inferred interior composition could be explored. For instance, as we saw in Chapter 4, varying the amount of Rayleigh scattering due to hazes has a profound impact on the temperature structure deeper in the atmosphere. This, in turn, affects the phase structure of planetary materials, namely water, in the interior which has significant impact on the overall nature of the planet.

5.5 Concluding Remarks

The lack of a sub-Neptune in our solar system and the wide diversity of compositions and structures possible in this regime means that these planets have the potential to provide a wealth of information about planet formation, evolution and habitability. The fact that sub-Neptunes are more conducive than smaller, rocky planets to atmospheric characterisation with JWST has pushed this exciting planetary regime to the forefront of exoplanet studies. The landscape of the field has changed dramatically over the course of the last few years since the first exoplanet spectra were obtained with JWST. In the first year of operation, JWST observations solved the missing methane problem – the lack of detected methane beyond the solar system – through detections of carbon-bearing molecules including CH_4 in the atmosphere of the temperate sub-Neptune K2-18 b (Madhusudhan et al., 2023b).

The unprecedented precision of JWST data has provided an incredible window into the properties, compositions and diversity of exoplanet atmospheres. Given the now abundant high-precision spectroscopic data, we must now ensure that the inferences we draw from this data are well-informed. Decoding this data to make inferences of the planetary interior requires an understanding of the complex relationship between the observable photosphere, the deeper atmosphere, the surface if present, and the underlying interior. At each of these steps there are many uncertainties, stemming from both inherent degeneracies and from the limited data available to inform modelling efforts. This provides important motivation for future experimental efforts into multiple areas, including high-pressure equations of state; solubility laws; photochemical networks; and cross-sections for a wide range of chemical species at wavelengths relevant to JWST. Atmospheric data provides a promising avenue to

peer into the interiors of these planets, allowing us to eventually break the interior compositional degeneracies of sub-Neptunes. In the era of JWST, we are in the best position yet to understand the nature of this intriguing planetary population.

References

Abel, M., Frommhold, L., Li, X., and Hunt, K. L. C. (2011). Collision-Induced Absorption by H_2 Pairs: From Hundreds to Thousands of Kelvin. *Journal of Physical Chemistry A*, 115(25):6805–6812.

Acuña, L., Deleuil, M., Mousis, O., Marcq, E., Levesque, M., and Aguichine, A. (2021). Characterisation of the hydrospheres of TRAPPIST-1 planets. *A&A*, 647:A53.

Adams, E. R., Seager, S., and Elkins-Tanton, L. (2008). Ocean Planet or Thick Atmosphere: On the Mass-Radius Relationship for Solid Exoplanets with Massive Atmospheres. *ApJ*, 673(2):1160–1164.

Agol, E., Steffen, J., Sari, R., and Clarkson, W. (2005). On detecting terrestrial planets with timing of giant planet transits. *MNRAS*, 359(2):567–579.

Aguichine, A., Mousis, O., Deleuil, M., and Marcq, E. (2021). Mass-Radius Relationships for Irradiated Ocean Planets. *ApJ*, 914(2):84.

Ahrer, E.-M., Radica, M., Piaulet-Ghorayeb, C., Raul, E., Wiser, L., Welbanks, L., Acuña, L., Allart, R., Coulombe, L.-P., Louca, A., MacDonald, R., Saidel, M., Evans-Soma, T. M., Benneke, B., Christie, D., Beatty, T. G., Cadieux, C., Cloutier, R., Doyon, R., Fortney, J. J., Gagnebin, A., Gapp, C., Innes, H., Knutson, H. A., Komacek, T., Krissansen-Totton, J., Miguel, Y., Pierrehumbert, R., Roy, P.-A., and Schlichting, H. E. (2025). Escaping Helium and a Highly Muted Spectrum Suggest a Metal-enriched Atmosphere on Sub-Neptune GJ 3090 b from JWST Transit Spectroscopy. *ApJL*, 985(1):L10.

Al-Refaie, A. F., Changeat, Q., Waldmann, I. P., and Tinetti, G. (2021). TauREx 3: A Fast, Dynamic, and Extendable Framework for Retrievals. *ApJ*, 917(1):37.

Alibert, Y. (2014). On the radius of habitable planets. *A&A*, 561:A41.

Alibert, Y., Mordasini, C., Benz, W., and Winisdoerffer, C. (2005). Models of giant planet formation with migration and disc evolution. *A&A*, 434(1):343–353.

Anderson, O. L. (1984). A universal thermal equation-of-state. *Journal of Geodynamics*, 1(2):185–214.

Anderson, O. L., Dubrovinsky, L., Saxena, S. K., and LeBihan, T. (2001). Experimental vibrational Grüneisen ratio values for ϵ-iron up to 330 GPa at 300 K. *Geophys. Res. Lett.*, 28(2):399–402.

Ardia, P., Hirschmann, M. M., Withers, A. C., and Stanley, B. D. (2013). Solubility of CH_4 in a synthetic basaltic melt, with applications to atmosphere–magma ocean–core partitioning of volatiles and to the evolution of the Martian atmosphere. *Geochimica et Cosmochimica Acta*, 114:52–71.

Armstrong, L. S., Hirschmann, M. M., Stanley, B. D., Falksen, E. G., and Jacobsen, S. D. (2015). Speciation and solubility of reduced C–O–H–N volatiles in mafic melt: Implications for volcanism, atmospheric evolution, and deep volatile cycles in the terrestrial planets. *Geochimica et Cosmochimica Acta*, 171:283–302.

Asplund, M., Amarsi, A. M., and Grevesse, N. (2021). The chemical make-up of the Sun: A 2020 vision. *A&A*, 653:A141.

Asplund, M., Grevesse, N., Sauval, A. J., and Scott, P. (2009). The Chemical Composition of the Sun. *Annual Review of Astronomy and Astrophysics*, 47(1):481–522.

Azzam, A. A. A., Tennyson, J., Yurchenko, S. N., and Naumenko, O. V. (2016). ExoMol molecular line lists - XVI. The rotation-vibration spectrum of hot H_2S. *MNRAS*, 460(4):4063–4074.

Banzatti, A., Pontoppidan, K. M., Carr, J. S., Jellison, E., Pascucci, I., Najita, J. R., Romero-Mirza, C. E., Öberg, K. I., Kalyaan, A., Pinilla, P., Krijt, S., Long, F., Lambrechts, M., Rosotti, G., Herczeg, G. J., Salyk, C., Zhang, K., Bergin, E. A., Ballering, N. P., Meyer, M. R., Bruderer, S., and Jdiscs Collaboration (2023). JWST Reveals Excess Cool Water near the Snow Line in Compact Disks, Consistent with Pebble Drift. *ApJL*, 957(2):L22.

Barber, R. J., Strange, J. K., Hill, C., Polyansky, O. L., Mellau, G. C., Yurchenko, S. N., and Tennyson, J. (2014). ExoMol line lists - III. An improved hot rotation-vibration line list for HCN and HNC. *MNRAS*, 437(2):1828–1835.

Barber, R. J., Tennyson, J., Harris, G. J., and Tolchenov, R. N. (2006). A high-accuracy computed water line list. *MNRAS*, 368(3):1087–1094.

Barman, T. S. (2008). On the Presence of Water and Global Circulation in the Transiting Planet HD 189733b. *ApJL*, 676(1):L61.

Barrier, E. F. L. and Madhusudhan, N. (2025). A new convection scheme for GCMs of temperate sub-Neptunes. *MNRAS*, 538(4):2463–2482.

Baumeister, P., Padovan, S., Tosi, N., Montavon, G., Nettelmann, N., MacKenzie, J., and Godolt, M. (2020). Machine-learning Inference of the Interior Structure of Low-mass Exoplanets. *ApJ*, 889(1):42.

Bean, J. L., Raymond, S. N., and Owen, J. E. (2021). The Nature and Origins of Sub-Neptune Size Planets. *Journal of Geophysical Research: Planets*, 126(1):e2020JE006639. _eprint: https://onlinelibrary.wiley.com/doi/pdf/10.1029/2020JE006639.

Bell, T. J., Crouzet, N., Cubillos, P. E., Kreidberg, L., Piette, A. A. A., Roman, M. T., Barstow, J. K., Blecic, J., Carone, L., Coulombe, L.-P., Ducrot, E., Hammond, M., Mendonça, J. M., Moses, J. I., Parmentier, V., Stevenson, K. B., Teinturier, L., Zhang, M., Batalha, N. M., Bean, J. L., Benneke, B., Charnay, B., Chubb, K. L., Demory, B.-O., Gao, P., Lee, E. K. H., López-Morales, M., Morello, G., Rauscher, E., Sing, D. K., Tan, X., Venot, O., Wakeford, H. R., Aggarwal, K., Ahrer, E.-M., Alam, M. K., Baeyens, R., Barrado, D., Caceres, C., Carter, A. L., Casewell, S. L., Challener, R. C., Crossfield, I. J. M., Decin, L., Désert, J.-M., Dobbs-Dixon, I., Dyrek, A., Espinoza, N., Feinstein, A. D., Gibson, N. P., Harrington, J., Helling, C., Hu, R., Iro, N., Kempton, E. M. R., Kendrew, S., Komacek, T. D., Krick, J., Lagage, P.-O., Leconte, J., Lendl, M., Lewis, N. T., Lothringer, J. D., Malsky, I., Mancini, L., Mansfield, M., Mayne, N. J., Evans-Soma, T. M., Molaverdikhani, K., Nikolov, N. K., Nixon, M. C., Palle, E., Petit dit de la Roche, D. J. M., Piaulet, C., Powell, D., Rackham, B. V., Schneider, A. D., Steinrueck, M. E., Taylor, J., Welbanks, L., Yurchenko, S. N., Zhang, X., and Zieba, S. (2024). Nightside clouds and disequilibrium chemistry on the hot Jupiter WASP-43b. *Nature Astronomy*, 8:879–898.

Belov, G. V., Iorish, V. S., and Yungman, V. S. (1999). Ivtanthermo for windows database on thermodynamic properties and related software. *Calphad*, 23(2):173–180.

Benneke, B., Roy, P.-A., Coulombe, L.-P., Radica, M., Piaulet, C., Ahrer, E.-M., Pierrehumbert, R., Krissansen-Totton, J., Schlichting, H. E., Hu, R., Yang, J., Christie, D., Thorngren, D., Young, E. D., Pelletier, S., Knutson, H. A., Miguel, Y., Evans-Soma, T. M., Dorn, C., Gagnebin, A., Fortney, J. J., Komacek, T., MacDonald, R., Raul, E., Cloutier, R., Acuna, L., Lafrenière, D., Cadieux, C., Doyon, R., Welbanks, L., and Allart, R. (2024). JWST Reveals CH_4, CO_2, and H_2O in a Metal-rich Miscible Atmosphere on a Two-Earth-Radius Exoplanet. *arXiv e-prints*, page arXiv:2403.03325.

Benneke, B., Werner, M., Petigura, E., Knutson, H., Dressing, C., Crossfield, I. J. M., Schlieder, J. E., Livingston, J., Beichman, C., Christiansen, J., Krick, J., Gorjian, V., Howard, A. W., Sinukoff, E., Ciardi, D. R., and Akeson, R. L. (2017). Spitzer Observations Confirm and Rescue the Habitable-zone Super-Earth K2-18b for Future Characterization. *ApJ*, 834(2):187.

Benneke, B., Wong, I., Piaulet, C., Knutson, H. A., Lothringer, J., Morley, C. V., Crossfield, I. J. M., Gao, P., Greene, T. P., Dressing, C., Dragomir, D., Howard, A. W., McCullough, P. R., Kempton, E. M. R., Fortney, J. J., and Fraine, J. (2019). Water Vapor and Clouds on the Habitable-zone Sub-Neptune Exoplanet K2-18b. *ApJL*, 887(1):L14.

Bernadou, F., Gaillard, F., Füri, E., Marrocchi, Y., and Slodczyk, A. (2021). Nitrogen solubility in basaltic silicate melt - Implications for degassing processes. *Chemical Geology*, 573:120192.

Bethkenhagen, M., Meyer, E. R., Hamel, S., Nettelmann, N., French, M., Scheibe, L., Ticknor, C., Collins, L. A., Kress, J. D., Fortney, J. J., and Redmer, R. (2017). Planetary Ices and the Linear Mixing Approximation. *ApJ*, 848(1):67.

Birch, F. (1952). Elasticity and Constitution of the Earth's Interior. *J. Geophys. Res.*, 57(2):227–286.

Birkby, J. L., de Kok, R. J., Brogi, M., de Mooij, E. J. W., Schwarz, H., Albrecht, S., and Snellen, I. A. G. (2013). Detection of water absorption in the day side atmosphere of HD 189733 b using ground-based high-resolution spectroscopy at 3.2μm. *MNRAS*, 436:L35–L39.

Bitsch, B., Lambrechts, M., and Johansen, A. (2015). The growth of planets by pebble accretion in evolving protoplanetary discs. *A&A*, 582:A112.

Bitsch, B., Raymond, S. N., Buchhave, L. A., Bello-Arufe, A., Rathcke, A. D., and Schneider, A. D. (2021). Dry or water world? How the water contents of inner sub-Neptunes constrain giant planet formation and the location of the water ice line. *A&A*, 649:L5.

Blain, D., Charnay, B., and Bézard, B. (2021). 1D atmospheric study of the temperate sub-Neptune K2-18b. *Astron. Astrophys.*, 646:A15.

Bodenheimer, P. and Pollack, J. B. (1986). Calculations of the accretion and evolution of giant planets: The effects of solid cores. *Icarus*, 67(3):391–408.

Boley, A. C., Granados Contreras, A. P., and Gladman, B. (2016). The In Situ Formation of Giant Planets at Short Orbital Periods. *ApJL*, 817(2):L17.

Bond, I. A., Udalski, A., Jaroszyński, M., Rattenbury, N. J., Paczyński, B., Soszyński, I., Wyrzykowski, L., Szymański, M. K., Kubiak, M., Szewczyk, O., Żebruń, K., Pietrzyński, G., Abe, F., Bennett, D. P., Eguchi, S., Furuta, Y., Hearnshaw, J. B., Kamiya, K., Kilmartin, P. M., Kurata, Y., Masuda, K., Matsubara, Y., Muraki, Y., Noda, S., Okajima, K., Sako, T., Sekiguchi, T., Sullivan, D. J., Sumi, T., Tristram, P. J., Yanagisawa, T., Yock, P. C. M., and OGLE Collaboration (2004). OGLE 2003-BLG-235/MOA 2003-BLG-53: A Planetary Microlensing Event. *ApJL*, 606(2):L155–L158.

Bond, J. C., O'Brien, D. P., and Lauretta, D. S. (2010). The Compositional Diversity of Extrasolar Terrestrial Planets. I. In Situ Simulations. *ApJ*, 715(2):1050–1070.

Bonfanti, A., Brady, M., Wilson, T. G., Venturini, J., Egger, J. A., Brandeker, A., Sousa, S. G., Lendl, M., Simon, A. E., Queloz, D., Olofsson, G., Adibekyan, V., Alibert, Y., Fossati, L., Hooton, M. J., Kubyshkina, D., Luque, R., Murgas, F., Mustill, A. J., Santos, N. C., Van Grootel, V., Alonso, R., Asquier, J., Bandy, T., Bárczy, T., Barrado Navascues, D., Barros, S. C. C., Baumjohann, W., Bean, J., Beck, M., Beck, T., Benz, W., Bergomi, M., Billot, N., Borsato, L., Broeg, C., Collier Cameron, A., Csizmadia, S., Cubillos, P. E., Davies, M. B., Deleuil, M., Deline, A., Delrez, L., Demangeon, O. D. S., Demory, B. O., Ehrenreich, D., Erikson, A., Fortier, A., Fridlund, M., Gandolfi, D., Gillon, M., Güdel, M., Günther, M. N., Heitzmann, A., Helling, C., Hoyer, S., Isaak, K. G., Kasper, D., Kiss, L. L., Lam, K. W. F., Laskar, J., Lecavelier des Etangs, A., Magrin, D., Maxted, P. F. L., Mordasini, C., Nascimbeni, V., Ottensamer, R., Pagano, I., Pallé, E., Peter, G., Piotto, G., Pollacco, D., Ragazzoni, R., Rando, N., Rauer, H., Ribas, I., Scandariato, G., Ségransan, D., Seifahrt, A., Smith, A. M. S., Stalport, M., Stefánsson, G., Steinberger, M., Stürmer,

J., Szabó, G. M., Thomas, N., Udry, S., Villaver, E., Walton, N. A., Westerdorff, K., and Zingales, T. (2023). Characterising TOI-732 b and c: new insights on the M-dwarf radius and density valley. *arXiv e-prints*, page arXiv:2311.12577.

Borucki, W. J., Koch, D. G., Basri, G., Batalha, N., Brown, T. M., Bryson, S. T., Caldwell, D., Christensen-Dalsgaard, J., Cochran, W. D., DeVore, E., Dunham, E. W., Gautier, III, T. N., Geary, J. C., Gilliland, R., Gould, A., Howell, S. B., Jenkins, J. M., Latham, D. W., Lissauer, J. J., Marcy, G. W., Rowe, J., Sasselov, D., Boss, A., Charbonneau, D., Ciardi, D., Doyle, L., Dupree, A. K., Ford, E. B., Fortney, J., Holman, M. J., Seager, S., Steffen, J. H., Tarter, J., Welsh, W. F., Allen, C., Buchhave, L. A., Christiansen, J. L., Clarke, B. D., Das, S., Désert, J.-M., Endl, M., Fabrycky, D., Fressin, F., Haas, M., Horch, E., Howard, A., Isaacson, H., Kjeldsen, H., Kolodziejczak, J., Kulesa, C., Li, J., Lucas, P. W., Machalek, P., McCarthy, D., MacQueen, P., Meibom, S., Miquel, T., Prsa, A., Quinn, S. N., Quintana, E. V., Ragozzine, D., Sherry, W., Shporer, A., Tenenbaum, P., Torres, G., Twicken, J. D., Van Cleve, J., Walkowicz, L., Witteborn, F. C., and Still, M. (2011). Characteristics of Planetary Candidates Observed by Kepler. II. Analysis of the First Four Months of Data. *ApJ*, 736(1):19.

Borysow, J., Frommhold, L., and Birnbaum, G. (1988). Collision-induced Rototranslational Absorption Spectra of H 2-He Pairs at Temperatures from 40 to 3000 K. *ApJ*, 326:509.

Boulliung, J., Füri, E., Dalou, C., Tissandier, L., Zimmermann, L., and Marrocchi, Y. (2020). Oxygen fugacity and melt composition controls on nitrogen solubility in silicate melts. *Geochimica et Cosmochimica Acta*, 284:120–133.

Boulliung, J. and Wood, B. J. (2023). Sulfur oxidation state and solubility in silicate melts. *Contributions to Mineralogy and Petrology*, 178(8):56.

Bower, D. J., Hakim, K., Sossi, P. A., and Sanan, P. (2022). Retention of water in terrestrial magma oceans and carbon-rich early atmospheres. *The Planetary Science Journal*, 3(4):93.

Brogi, M., Giacobbe, P., Guilluy, G., de Kok, R. J., Sozzetti, A., Mancini, L., and Bonomo, A. S. (2018). Exoplanet atmospheres with GIANO. I. Water in the transmission spectrum of HD 189 733 b. *A&A*, 615:A16.

Brouwers, M. G. and Ormel, C. W. (2020). How planets grow by pebble accretion. II. Analytical calculations on the evolution of polluted envelopes. *A&A*, 634:A15.

Brugger, B., Mousis, O., Deleuil, M., and Deschamps, F. (2017). Constraints on Super-Earth Interiors from Stellar Abundances. *ApJ*, 850(1):93.

Burn, R., Mordasini, C., Mishra, L., Haldemann, J., Venturini, J., Emsenhuber, A., and Henning, T. (2024). A radius valley between migrated steam worlds and evaporated rocky cores. *Nature Astronomy*, 8:463–471.

Cabot, S. H. C., Madhusudhan, N., Constantinou, S., Valencia, D., Vos, J. M., Masseron, T., and Cheverall, C. J. (2024). High-resolution Spectroscopic Reconnaissance of a Temperate Sub-Neptune. *ApJL*, 966(1):L10.

Cadieux, C., Doyon, R., MacDonald, R. J., Turbet, M., Artigau, É., Lim, O., Radica, M., Fauchez, T. J., Salhi, S., Dang, L., Albert, L., Coulombe, L.-P., Cowan, N. B., Lafrenière, D., L'Heureux, A., Piaulet-Ghorayeb, C., Benneke, B., Cloutier, R., Charnay, B., Cook, N. J., Fournier-Tondreau, M., Plotnykov, M., and Valencia, D. (2024a). Transmission Spectroscopy of the Habitable Zone Exoplanet LHS 1140 b with JWST/NIRISS. *ApJL*, 970(1):L2.

Cadieux, C., Plotnykov, M., Doyon, R., Valencia, D., Jahandar, F., Dang, L., Turbet, M., Fauchez, T. J., Cloutier, R., Cherubim, C., Artigau, É., Cook, N. J., Edwards, B., Hallatt, T., Charnay, B., Bouchy, F., Allart, R., Mignon, L., Baron, F., Barros, S. C. C., Benneke, B., Canto Martins, B. L., Cowan, N. B., De Medeiros, J. R., Delfosse, X., Delgado-Mena, E., Dumusque, X., Ehrenreich, D., Frensch, Y. G. C., González Hernández, J. I., Hara, N. C., Lafrenière, D., Lo Curto, G., Malo, L., Melo, C., Mounzer, D., Passeger, V. M., Pepe, F., Poulin-Girard, A.-S., Santos, N. C., Sosnowska, D., Suárez Mascareño, A., Thibault, S., Vaulato, V., Wade, G. A., and Wildi, F. (2024b). New Mass and Radius Constraints on the LHS 1140 Planets: LHS 1140 b Is either a Temperate Mini-Neptune or a Water World. *ApJL*, 960(1):L3.

Caillabet, L., Mazevet, S., and Loubeyre, P. (2011). Multiphase equation of state of hydrogen from ab initio calculations in the range 0.2 to 5 g/cc up to 10 eV. *Phys. Rev. B*, 83(9):094101.

Castor, J. I., Dykema, P. G., and Klein, R. I. (1992). A New Scheme for Multidimensional Line Transfer. II. ETLA Method in One Dimension with Application to Iron K alpha Lines. *ApJ*, 387:561.

Chabrier, G., Mazevet, S., and Soubiran, F. (2019). A New Equation of State for Dense Hydrogen-Helium Mixtures. *ApJ*, 872(1):51.

Chabrier, G. and Potekhin, A. Y. (1998). Equation of state of fully ionized electron-ion plasmas. *Phys. Rev. E*, 58(4):4941–4949.

Charbonneau, D., Brown, T. M., Noyes, R. W., and Gilliland, R. L. (2002). Detection of an Extrasolar Planet Atmosphere. *ApJ*, 568(1):377–384.

Charbonneau, D., Knutson, H. A., Barman, T., Allen, L. E., Mayor, M., Megeath, S. T., Queloz, D., and Udry, S. (2008). The Broadband Infrared Emission Spectrum of the Exoplanet HD 189733b. *ApJ*, 686(2):1341–1348.

Charette, M. A. and Smith, W. H. (2010). The volume of earth's ocean. *Oceanography*, 23(2):112–114.

Charnoz, S., Falco, A., Tremblin, P., Sossi, P., Caracas, R., and Lagage, P.-O. (2023). The effect of a small amount of hydrogen in the atmosphere of ultrahot magma-ocean planets: Atmospheric composition and escape. *A&A*, 674:A224. Publisher: EDP Sciences.

Chase, M. (1998). *NIST-JANAF Thermochemical Tables, 4th Edition*. American Institute of Physics, -1.

Chaturvedi, P., Bluhm, P., Nagel, E., Hatzes, A. P., Morello, G., Brady, M., Korth, J., Molaverdikhani, K., Kossakowski, D., Caballero, J. A., Guenther, E. W., Pallé , E., Espinoza, N., Seifahrt, A., Lodieu, N., Cifuentes, C., Furlan, E., Amado, P. J., Barclay, T., Bean, J., Béjar, V. J. S., Bergond, G., Boyle, A. W., Ciardi, D., Collins, K. A., Collins, K. I., Esparza-Borges, E., Fukui, A., Gnilka, C. L., Goeke, R., Guerra, P., Henning, T., Herrero, E., Howell, S. B., Jeffers, S. V., Jenkins, J. M., Jensen, E. L. N., Kasper, D., Kodama, T., Latham, D. W., López-González, M. J., Luque, R., Montes, D., Morales, J. C., Mori, M., Murgas, F., Narita, N., Nowak, G., Parviainen, H., Passegger, V. M., Quirrenbach, A., Reffert, S., Reiners, A., Ribas, I., Ricker, G. R., Rodriguez, E., Rodríguez-López, C., Schlecker, M., Schwarz, R. P., Schweitzer, A., Seager, S., Stefánsson, G., Stockdale, C., Tal-Or, L., Twicken, J. D., Vanaverbeke, S., Wang, G., Watanabe, D., Winn, J. N., and Zechmeister, M. (2022). TOI-1468: A system of two transiting planets, a super-earth and a mini-neptune, on opposite sides of the radius valley. *A&A*, 666:A155.

Chauvin, G., Lagrange, A. M., Dumas, C., Zuckerman, B., Mouillet, D., Song, I., Beuzit, J. L., and Lowrance, P. (2004). A giant planet candidate near a young brown dwarf. Direct VLT/NACO observations using IR wavefront sensing. *A&A*, 425:L29–L32.

Choblet, G., Tobie, G., Sotin, C., Kalousová, K., and Grasset, O. (2017). Heat transport in the high-pressure ice mantle of large icy moons. *Icarus*, 285:252–262.

Christie, D. A., Lee, E. K. H., Innes, H., Noti, P. A., Charnay, B., Fauchez, T. J., Mayne, N. J., Deitrick, R., Ding, F., Greco, J. J., Hammond, M., Malsky, I., Mandell, A., Rauscher, E., Roman, M. T., Sergeev, D. E., Sohl, L., Steinrueck, M. E., Turbet, M., Wolf, E. T., Zamyatina, M., and Carone, L. (2022). CAMEMBERT: A Mini-Neptunes General Circulation Model Intercomparison, Protocol Version 1.0.A CUISINES Model Intercomparison Project. *PSJ*, 3(11):261.

Chubb, K. L., Naumenko, O., Keely, S., Bartolotto, S., Macdonald, S., Mukhtar, M., Grachov, A., White, J., Coleman, E., Liu, A., Fazliev, A. Z., Polovtseva, E. R., Horneman, V.-M., Campargue, A., Furtenbacher, T., Császár, A. G., Yurchenko, S. N., and Tennyson, J. (2018). MARVEL analysis of the measured high-resolution rovibrational spectra of H_2 ^{32}S. *J. Quant. Spectrosc. Radiat. Transf.*, 218:178–186.

Chubb, K. L., Tennyson, J., and Yurchenko, S. N. (2020). ExoMol molecular line lists – XXXVII. Spectra of acetylene. *MNRAS*, 493(2):1531–1545.

Clemente, B., Scaillet, B., and Pichavant, M. (2004). The Solubility of Sulphur in Hydrous Rhyolitic Melts. *Journal of Petrology*, 45(11):2171–2196.

Cloutier, R., Astudillo-Defru, N., Doyon, R., Bonfils, X., Almenara, J. M., Bouchy, F., Delfosse, X., Forveille, T., Lovis, C., Mayor, M., Menou, K., Murgas, F., Pepe, F., Santos, N. C., Udry, S., and Wünsche, A. (2019). Confirmation of the radial velocity super-Earth K2-18c with HARPS and CARMENES. *A&A*, 621:A49.

Cloutier, R., Eastman, J. D., Rodriguez, J. E., Astudillo-Defru, N., Bonfils, X., Mortier, A., Watson, C. A., Stalport, M., Pinamonti, M., Lienhard, F., Harutyunyan, A., Damasso, M., Latham, D. W., Collins, K. A., Massey, R., Irwin, J., Winters, J. G.,

Charbonneau, D., Ziegler, C., Matthews, E., Crossfield, I. J. M., Kreidberg, L., Quinn, S. N., Ricker, G., Vanderspek, R., Seager, S., Winn, J., Jenkins, J. M., Vezie, M., Udry, S., Twicken, J. D., Tenenbaum, P., Sozzetti, A., Ségransan, D., Schlieder, J. E., Sasselov, D., Santos, N. C., Rice, K., Rackham, B. V., Poretti, E., Piotto, G., Phillips, D., Pepe, F., Molinari, E., Mignon, L., Micela, G., Melo, C., de Medeiros, J. R., Mayor, M., Matson, R. A., Martinez Fiorenzano, A. F., Mann, A. W., Magazzú, A., Lovis, C., López-Morales, M., Lopez, E., Lissauer, J. J., Lépine, S., Law, N., Kielkopf, J. F., Johnson, J. A., Jensen, E. L. N., Howell, S. B., Gonzales, E., Ghedina, A., Forveille, T., Figueira, P., Dumusque, X., Dressing, C. D., Doyon, R., Díaz, R. F., Fabrizio, L. D., Delfosse, X., Cosentino, R., Conti, D. M., Collins, K. I., Cameron, A. C., Ciardi, D., Caldwell, D. A., Burke, C., Buchhave, L., Briceño, C., Boyd, P., Bouchy, F., Beichman, C., Artigau, É., and Almenara, J. M. (2020). A Pair of TESS Planets Spanning the Radius Valley around the Nearby Mid-M Dwarf LTT 3780. *AJ*, 160(1):3.

Cloutier, R. and Menou, K. (2020). Evolution of the Radius Valley around Low-mass Stars from Kepler and K2. *AJ*, 159(5):211.

Constantinou, S. and Madhusudhan, N. (2022). Characterizing atmospheres of cloudy temperate mini-neptunes with JWST. *MNRAS*, 514(2):2073–2091.

Constantinou, S. and Madhusudhan, N. (2024). VIRA: an exoplanet atmospheric retrieval framework for JWST transmission spectroscopy. *MNRAS*, 530(3):3252–3277.

Cooke, G. J. and Madhusudhan, N. (2024). Considerations for Photochemical Modeling of Possible Hycean Worlds. *ApJ*, 977(2):209.

Cossou, C., Raymond, S. N., Hersant, F., and Pierens, A. (2014). Hot super-Earths and giant planet cores from different migration histories. *A&A*, 569:A56.

Crossfield, I. J. M., Hansen, B. M. S., Harrington, J., Cho, J. Y. K., Deming, D., Menou, K., and Seager, S. (2010). A New 24 μm Phase Curve for υ Andromedae b. *ApJ*, 723(2):1436–1446.

Damiano, M., Bello-Arufe, A., Yang, J., and Hu, R. (2024). LHS 1140 b Is a Potentially Habitable Water World. *ApJL*, 968(2):L22.

Dasgupta, R., Falksen, E., Pal, A., and Sun, C. (2022). The fate of nitrogen during parent body partial melting and accretion of the inner solar system bodies at reducing conditions. *Geochimica et Cosmochimica Acta*, 336:291–307.

Dash, S., Brogi, M., Gandhi, S., Lafarga, M., Meech, A., Bello-Arufe, A., and Wheatley, P. J. (2024). Constraints on atmospheric water abundance and cloud deck pressure in the warm Neptune GJ 3470 b via CARMENES transmission spectroscopy. *MNRAS*, 530(3):3100–3116.

Davenport, B., Kempton, E. M. R., Nixon, M. C., Ih, J., Deming, D., Fu, G., May, E. M., Bean, J. L., Gao, P., Rogers, L., and Malik, M. (2025). TOI-421 b: A Hot Sub-Neptune with a Haze-free, Low Mean Molecular Weight Atmosphere. *ApJL*, 984(2):L44.

Daviau, K. and Lee, K. K. M. (2021). Experimental Constraints on Solid Nitride Phases in Rocky Mantles of Reduced Planets and Implications for Observable Atmosphere Compositions. *Journal of Geophysical Research: Planets*, 126(9):e2020JE006687. _eprint: https://onlinelibrary.wiley.com/doi/pdf/10.1029/2020JE006687.

de Pater, I. and Lissauer, J. J. (2010). *Planetary Sciences*. Cambridge University Press.

Delgado Mena, E., Israelian, G., González Hernández, J. I., Bond, J. C., Santos, N. C., Udry, S., and Mayor, M. (2010). Chemical Clues on the Formation of Planetary Systems: C/O Versus Mg/Si for HARPS GTO Sample. *ApJ*, 725(2):2349–2358.

Demory, B. O., Gillon, M., Deming, D., Valencia, D., Seager, S., Benneke, B., Lovis, C., Cubillos, P., Harrington, J., Stevenson, K. B., Mayor, M., Pepe, F., Queloz, D., Ségransan, D., and Udry, S. (2011). Detection of a transit of the super-Earth 55 Cancri e with warm Spitzer. *A&A*, 533:A114.

Demory, B.-O., Gillon, M., Seager, S., Benneke, B., Deming, D., and Jackson, B. (2012). Detection of Thermal Emission from a Super-Earth. *ApJL*, 751(2):L28.

Dittmann, J. A., Irwin, J. M., Charbonneau, D., Bonfils, X., Astudillo-Defru, N., Haywood, R. D., Berta-Thompson, Z. K., Newton, E. R., Rodriguez, J. E., Winters, J. G., Tan, T.-G., Almenara, J.-M., Bouchy, F., Delfosse, X., Forveille, T., Lovis, C., Murgas, F., Pepe, F., Santos, N. C., Udry, S., Wünsche, A., Esquerdo, G. A., Latham, D. W., and Dressing, C. D. (2017). A temperate rocky super-Earth transiting a nearby cool star. *Nature*, 544(7650):333–336.

Dixon, J. E., Stolper, E. M., and Holloway, J. R. (1995). An Experimental Study of Water and Carbon Dioxide Solubilities in Mid-Ocean Ridge Basaltic Liquids. Part I: Calibration and Solubility Models. *Journal of Petrology*, 36(6):1607–1631.

Dorn, C., Khan, A., Heng, K., Connolly, J. A. D., Alibert, Y., Benz, W., and Tackley, P. (2015). Can we constrain the interior structure of rocky exoplanets from mass and radius measurements? *A&A*, 577:A83.

Dorn, C., Noack, L., and Rozel, A. B. (2018). Outgassing on stagnant-lid super-Earths. *A&A*, 614:A18.

Dorn, C., Venturini, J., Khan, A., Heng, K., Alibert, Y., Helled, R., Rivoldini, A., and Benz, W. (2017). A generalized Bayesian inference method for constraining the interiors of super Earths and sub-Neptunes. *A&A*, 597:A37.

Dunaeva, A. N., Antsyshkin, D. V., and Kuskov, O. L. (2010). Phase diagram of H_2O: Thermodynamic functions of the phase transitions of high-pressure ices. *Solar System Research*, 44(3):202–222.

Elkins-Tanton, L. T. and Seager, S. (2008). Ranges of Atmospheric Mass and Composition of Super-Earth Exoplanets. *ApJ*, 685(2):1237–1246.

Evans, T. M., Sing, D. K., Kataria, T., Goyal, J., Nikolov, N., Wakeford, H. R., Deming, D., Marley, M. S., Amundsen, D. S., Ballester, G. E., Barstow, J. K., Ben-Jaffel, L., Bourrier, V., Buchhave, L. A., Cohen, O., Ehrenreich, D., García Muñoz, A., Henry, G. W., Knutson, H., Lavvas, P., Lecavelier Des Etangs, A., Lewis, N. K., López-Morales, M., Mandell, A. M., Sanz-Forcada, J., Tremblin, P., and Lupu, R. (2017). An ultrahot gas-giant exoplanet with a stratosphere. *Nature*, 548(7665):58–61.

Falco, A., Tremblin, P., Charnoz, S., Ridgway, J. R., and Lagage, P.-O. (2024). Hydrogenated atmospheres of lava planets: Atmospheric structure and emission spectra. *A&A*. Publisher: EDP Sciences.

Fei, Y., Mao, H.-K., and Hemley, R. J. (1993). Thermal expansivity, bulk modulus, and melting curve of H_2O-ice VII to 20 GPa. *J. Chem. Phys.*, 99(7):5369–5373.

Fei, Y., Seagle, C. T., Townsend, J. P., McCoy, C. A., Boujibar, A., Driscoll, P., Shulenburger, L., and Furnish, M. D. (2021). Melting and density of $MgSiO_3$ determined by shock compression of bridgmanite to 1254GPa. *Nature Communications*, 12:876.

Feistel, R. and Wagner, W. (2006). A new equation of state for h_2o ice ih. *Journal of Physical and Chemical Reference Data*, 35(2):1021–1047.

Felix, L., Kitzmann, D., Demory, B.-O., and Mordasini, C. (2025). Evidence for sulfur chemistry in the atmosphere of the warm sub-Neptune TOI-270 d. *arXiv e-prints*, page arXiv:2504.13039.

Feroz, F., Hobson, M. P., and Bridges, M. (2009). MultiNest: an efficient and robust Bayesian inference tool for cosmology and particle physics. *MNRAS*, 398(4):1601–1614.

Fiquet, G., Auzende, A. L., Siebert, J., Corgne, A., Bureau, H., Ozawa, H., and Garbarino, G. (2010). Melting of Peridotite to 140 Gigapascals. *Science*, 329(5998):1516.

Ford, E. B., Fabrycky, D. C., Steffen, J. H., Carter, J. A., Fressin, F., Holman, M. J., Lissauer, J. J., Moorhead, A. V., Morehead, R. C., Ragozzine, D., Rowe, J. F., Welsh, W. F., Allen, C., Batalha, N. M., Borucki, W. J., Bryson, S. T., Buchhave, L. A., Burke, C. J., Caldwell, D. A., Charbonneau, D., Clarke, B. D., Cochran, W. D., Désert, J.-M., Endl, M., Everett, M. E., Fischer, D. A., Gautier, III, T. N., Gilliland, R. L., Jenkins, J. M., Haas, M. R., Horch, E., Howell, S. B., Ibrahim, K. A., Isaacson, H., Koch, D. G., Latham, D. W., Li, J., Lucas, P., MacQueen, P. J., Marcy, G. W., McCauliff, S., Mullally, F. R., Quinn, S. N., Quintana, E., Shporer, A., Still, M., Tenenbaum, P., Thompson, S. E., Torres, G., Twicken, J. D., Wohler, B., and Kepler Science Team (2012). Transit Timing Observations from Kepler. II. Confirmation of Two Multiplanet Systems via a Non-parametric Correlation Analysis. *ApJ*, 750(2):113.

Fortney, J. J., Marley, M. S., and Barnes, J. W. (2007). Planetary Radii across Five Orders of Magnitude in Mass and Stellar Insolation: Application to Transits. *ApJ*, 659(2):1661–1672.

Fortney, J. J., Mordasini, C., Nettelmann, N., Kempton, E. M. R., Greene, T. P., and Zahnle, K. (2013). A Framework for Characterizing the Atmospheres of Low-mass Low-density Transiting Planets. *ApJ*, 775(1):80.

French, M., Mattsson, T. R., Nettelmann, N., and Redmer, R. (2009). Equation of state and phase diagram of water at ultrahigh pressures as in planetary interiors. *Phys. Rev. B*, 79(5):054107.

Fressin, F., Torres, G., Charbonneau, D., Bryson, S. T., Christiansen, J., Dressing, C. D., Jenkins, J. M., Walkowicz, L. M., and Batalha, N. M. (2013). The False Positive Rate of Kepler and the Occurrence of Planets. *ApJ*, 766(2):81.

Fulton, B. J. and Petigura, E. A. (2018a). The California-Kepler Survey. VII. Precise Planet Radii Leveraging Gaia DR2 Reveal the Stellar Mass Dependence of the Planet Radius Gap. *AJ*, 156(6):264.

Fulton, B. J. and Petigura, E. A. (2018b). The California-Kepler Survey. VII. Precise Planet Radii Leveraging Gaia DR2 Reveal the Stellar Mass Dependence of the Planet Radius Gap. *AJ*, 156(6):264.

Fulton, B. J., Petigura, E. A., Howard, A. W., Isaacson, H., Marcy, G. W., Cargile, P. A., Hebb, L., Weiss, L. M., Johnson, J. A., Morton, T. D., Sinukoff, E., Crossfield, I. J. M., and Hirsch, L. A. (2017). The California-Kepler Survey. III. A Gap in the Radius Distribution of Small Planets. *AJ*, 154(3):109.

Gaillard, F., Bernadou, F., Roskosz, M., Bouhifd, M. A., Marrocchi, Y., Iacono-Marziano, G., Moreira, M., Scaillet, B., and Rogerie, G. (2022). Redox controls during magma ocean degassing. *Earth and Planetary Science Letters*, 577:117255.

Gandhi, S. and Madhusudhan, N. (2017). GENESIS: new self-consistent models of exoplanetary spectra. *MNRAS*, 472(2):2334–2355.

Gao, Z., Yang, Y.-N., Yang, S.-Y., and Li, Y. (2022). Experimental determination of N_2 solubility in silicate melts and implications for N_2–Ar–CO_2 fractionation in magmas. *Geochimica et Cosmochimica Acta*, 326:17–40.

Gardner, J. V., Armstrong, A. A., Calder, B. R., and Beaudoin, J. (2014). So, how deep is the mariana trench? *Marine Geodesy*, 37(1):1–13.

Genda, H. (2016). Origin of Earth's oceans: An assessment of the total amount, history and supply of water. *Geochemical Journal*, 50(1):27–42.

Gillon, M., Demory, B. O., Benneke, B., Valencia, D., Deming, D., Seager, S., Lovis, C., Mayor, M., Pepe, F., Queloz, D., Ségransan, D., and Udry, S. (2012). Improved precision on the radius of the nearby super-Earth 55 Cnc e. *A&A*, 539:A28.

Ginzburg, S., Schlichting, H. E., and Sari, R. (2016). Super-Earth Atmospheres: Self-consistent Gas Accretion and Retention. *ApJ*, 825(1):29.

Ginzburg, S., Schlichting, H. E., and Sari, R. (2018). Core-powered mass-loss and the radius distribution of small exoplanets. *MNRAS*, 476(1):759–765.

Glein, C. R. (2024). The Geochemical Potential for Metabolic Processes on the Sub-Neptune Exoplanet K2-18b. *ApJL*, 964(2):L19.

Glein, C. R., Yu, X., and Luu, C. N. (2025). Deciphering Sub-Neptune Atmospheres: New Insights from Geochemical Models of TOI-270 d. *ApJ*, 985(2):187.

Grande, Z. M., Pham, C. H., Smith, D., Boisvert, J. H., Huang, C., Smith, J. S., Goldman, N., Belof, J. L., Tschauner, O., Steffen, J. H., and Salamat, A. (2022). Pressure-driven symmetry transitions in dense H_2O ice. *Phys. Rev. B*, 105(10):104109.

Grasser, N., Snellen, I. A. G., Landman, R., Picos, D. G., and Gandhi, S. (2024). Peering above the clouds of the warm Neptune GJ 436 b with CRIRES+. *A&A*, 688:A191.

Grasset, O., Schneider, J., and Sotin, C. (2009). A Study of the Accuracy of Mass-Radius Relationships for Silicate-Rich and Ice-Rich Planets up to 100 Earth Masses. *ApJ*, 693(1):722–733.

Greene, T. P., Line, M. R., Montero, C., Fortney, J. J., Lustig-Yaeger, J., and Luther, K. (2016). Characterizing Transiting Exoplanet Atmospheres with JWST. *ApJ*, 817(1):17.

Grillmair, C. J., Burrows, A., Charbonneau, D., Armus, L., Stauffer, J., Meadows, V., van Cleve, J., von Braun, K., and Levine, D. (2008). Strong water absorption in the dayside emission spectrum of the planet HD189733b. *Nature*, 456(7223):767–769.

Grove, T. L., Chatterjee, N., Parman, S. W., and Médard, E. (2006). The influence of H_2O on mantle wedge melting. *Earth and Planetary Science Letters*, 249(1-2):74–89.

Guillot, B. and Sator, N. (2011). Carbon dioxide in silicate melts: A molecular dynamics simulation study. *Geochimica et Cosmochimica Acta*, 75(7):1829–1857.

Guillot, T. (1995). Condensation of Methane, Ammonia, and Water and the Inhibition of Convection in Giant Planets. *Science*, 269(5231):1697–1699.

Guillot, T. (2005). The Interiors of Giant Planets: Models and Outstanding Questions. *Annual Review of Earth and Planetary Sciences*, 33:493–530.

Günther, M. N., Pozuelos, F. J., Dittmann, J. A., Dragomir, D., Kane, S. R., Daylan, T., Feinstein, A. D., Huang, C. X., Morton, T. D., Bonfanti, A., Bouma, L. G., Burt, J., Collins, K. A., Lissauer, J. J., Matthews, E., Montet, B. T., Vanderburg, A., Wang, S., Winters, J. G., Ricker, G. R., Vanderspek, R. K., Latham, D. W., Seager, S., Winn, J. N., Jenkins, J. M., Armstrong, J. D., Barkaoui, K., Batalha, N., Bean, J. L., Caldwell, D. A., Ciardi, D. R., Collins, K. I., Crossfield, I., Fausnaugh, M., Furesz, G., Gan, T., Gillon, M., Guerrero, N., Horne, K., Howell, S. B., Ireland, M., Isopi, G., Jehin, E., Kielkopf, J. F., Lepine, S., Mallia, F., Matson, R. A., Myers, G., Palle, E., Quinn, S. N., Relles, H. M., Rojas-Ayala, B., Schlieder, J., Sefako, R., Shporer, A., Suárez, J. C., Tan, T.-G., Ting, E. B., Twicken, J. D., and Waite, I. A. (2019). A super-Earth and two sub-Neptunes transiting the nearby and quiet M dwarf TOI-270. *Nature Astronomy*, 3:1099–1108.

Gupta, A. and Schlichting, H. E. (2019). Sculpting the valley in the radius distribution of small exoplanets as a by-product of planet formation: the core-powered mass-loss mechanism. *MNRAS*, 487(1):24–33.

Gupta, A. and Schlichting, H. E. (2020). Signatures of the core-powered mass-loss mechanism in the exoplanet population: dependence on stellar properties and observational predictions. *MNRAS*, 493(1):792–806.

Gupta, A., Stixrude, L., and Schlichting, H. E. (2025). The Miscibility of Hydrogen and Water in Planetary Atmospheres and Interiors. *ApJL*, 982(2):L35.

Gurvich, L. V. and Veyts, I. (1990). *Thermodynamic properties of individual substances: elements and compounds*, volume 2. CRC press.

Guzmán-Mesa, A., Kitzmann, D., Mordasini, C., and Heng, K. (2022). Chemical diversity of the atmospheres and interiors of sub-Neptunes: a case study of GJ 436 b. *MNRAS*, 513(3):4015–4036.

Hakim, K., Rivoldini, A., Van Hoolst, T., Cottenier, S., Jaeken, J., Chust, T., and Steinle-Neumann, G. (2018). A new ab initio equation of state of hcp-Fe and its implication on the interior structure and mass-radius relations of rocky super-Earths. *Icarus*, 313:61–78.

Haldemann, J., Alibert, Y., Mordasini, C., and Benz, W. (2020). AQUA: a collection of H_2O equations of state for planetary models. *A&A*, 643:A105.

Haldemann, J., Ksoll, V., Walter, D., Alibert, Y., Klessen, R. S., Benz, W., Koethe, U., Ardizzone, L., and Rother, C. (2023). Exoplanet characterization using conditional invertible neural networks. *A&A*, 672:A180.

Hamano, K., Abe, Y., and Genda, H. (2013). Emergence of two types of terrestrial planet on solidification of magma ocean. *Nature*, 497(7451):607–610.

Hardegree-Ullman, K. K., Zink, J. K., Christiansen, J. L., Dressing, C. D., Ciardi, D. R., and Schlieder, J. E. (2020). Scaling K2. I. Revised Parameters for 222,088 K2 Stars and a K2 Planet Radius Valley at 1.9 $R_\oplus$. *ApJS*, 247(1):28.

Hardy, A., Caceres, C., Schreiber, M. R., Cieza, L., Alexander, R. D., Canovas, H., Williams, J. P., Wahhaj, Z., and Menard, F. (2015). Probing the final stages of protoplanetary disk evolution with ALMA. *A&A*, 583:A66.

Harrington, J., Hansen, B. M., Luszcz, S. H., Seager, S., Deming, D., Menou, K., Cho, J. Y. K., and Richardson, L. J. (2006). The Phase-Dependent Infrared Brightness of the Extrasolar Planet υ Andromedae b. *Science*, 314(5799):623–626.

Haynes, K., Mandell, A. M., Madhusudhan, N., Deming, D., and Knutson, H. (2015). Spectroscopic Evidence for a Temperature Inversion in the Dayside Atmosphere of Hot Jupiter WASP-33b. *ApJ*, 806(2):146.

He, C., Hörst, S. M., Lewis, N. K., Yu, X., Moses, J. I., Kempton, E. M. R., Marley, M. S., McGuiggan, P., Morley, C. V., Valenti, J. A., and Vuitton, V. (2018). Photochemical Haze Formation in the Atmospheres of Super-Earths and Mini-Neptunes. *AJ*, 156(1):38.

Helled, R. and Bodenheimer, P. (2014). The Formation of Uranus and Neptune: Challenges and Implications for Intermediate-mass Exoplanets. *ApJ*, 789(1):69.

Helled, R., Bodenheimer, P., Podolak, M., Boley, A., Meru, F., Nayakshin, S., Fortney, J. J., Mayer, L., Alibert, Y., and Boss, A. P. (2014). Giant Planet Formation, Evolution, and Internal Structure. In Beuther, H., Klessen, R. S., Dullemond, C. P., and Henning, T., editors, *Protostars and Planets VI*, pages 643–665.

Helled, R. and Fortney, J. J. (2020). The interiors of Uranus and Neptune: current understanding and open questions. *Philosophical Transactions of the Royal Society of London Series A*, 378(2187):20190474.

Helled, R. and Morbidelli, A. (2021). Planet Formation. In Madhusudhan, N., editor, *ExoFrontiers; Big Questions in Exoplanetary Science*, pages 12–1. IOP Publishing.

Helled, R., Stevenson, D. J., Lunine, J. I., Bolton, S. J., Nettelmann, N., Atreya, S., Guillot, T., Militzer, B., Miguel, Y., and Hubbard, W. B. (2022). Revelations on Jupiter's formation, evolution and interior: Challenges from Juno results. *Icarus*, 378:114937.

Heller, R. and Armstrong, J. (2014). Superhabitable Worlds. *Astrobiology*, 14(1):50–66.

Hemley, R. J., Jephcoat, A. P., Mao, H. K., Zha, C. S., Finger, L. W., and Cox, D. E. (1987). Static compression of H_2O-ice to 128 GPa (1.28 Mbar). *Nature*, 330(6150):737–740.

Hernandez, J.-A., Caracas, R., and Labrosse, S. (2022). Stability of high-temperature salty ice suggests electrolyte permeability in water-rich exoplanet icy mantles. *Nature Communications*, 13:3303.

Hirschmann, M. (2021). Iron-wüstite revisited: A revised calibration accounting for variable stoichiometry and the effects of pressure. *Geochimica et Cosmochimica Acta*, 313:74–84.

Hirschmann, M., Withers, A., Ardia, P., and Foley, N. (2012). Solubility of molecular hydrogen in silicate melts and consequences for volatile evolution of terrestrial planets. *Earth and Planetary Science Letters*, 345-348:38–48.

Hirschmann, M. M. (2000). Mantle solidus: Experimental constraints and the effects of peridotite composition. *Geochemistry, Geophysics, Geosystems*, 1(10):1042–26.

Hirschmann, M. M. (2016). Constraints on the early delivery and fractionation of Earth's major volatiles from C/H, C/N, and C/S ratios. *American Mineralogist*, 101(3):540–553. Publisher: De Gruyter.

Ho, C. S. K., Rogers, J. G., Van Eylen, V., Owen, J. E., and Schlichting, H. E. (2024). Shallower radius valley around low-mass hosts: evidence for icy planets, collisions, or high-energy radiation scatter. *MNRAS*, 531(3):3698–3714.

Holmberg, M. and Madhusudhan, N. (2024). Possible Hycean conditions in the sub-Neptune TOI-270 d. *A&A*, 683:L2.

Howe, A. R., Burrows, A., and Verne, W. (2014). Mass-radius Relations and Core-envelope Decompositions of Super-Earths and Sub-Neptunes. *ApJ*, 787(2):173.

Hu, R. (2021). Photochemistry and Spectral Characterization of Temperate and Gas-rich Exoplanets. *ApJ*, 921(1):27.

Hu, R., Bello-Arufe, A., Tokadjian, A., Yang, J., Damiano, M., Roy, P.-A., Coulombe, L.-P., Madhusudhan, N., Constantinou, S., and Benneke, B. (2025). A water-rich interior in the temperate sub-Neptune K2-18 b revealed by JWST. *arXiv e-prints*, page arXiv:2507.12622.

Hu, R., Damiano, M., Scheucher, M., Kite, E., Seager, S., and Rauer, H. (2021). Unveiling Shrouded Oceans on Temperate sub-Neptunes via Transit Signatures of Solubility Equilibria versus Gas Thermochemistry. *ApJL*, 921(1):L8.

Hu, R., Seager, S., and Bains, W. (2012). Photochemistry in Terrestrial Exoplanet Atmospheres. I. Photochemistry Model and Benchmark Cases. *ApJ*, 761(2):166.

Huang, C., Rice, D. R., Grande, Z. M., Smith, D., Smith, J. S., Boisvert, J. H., Tschauner, O., Salamat, A., and Steffen, J. H. (2021). Implications of an improved water equation of state for water-rich planets. *MNRAS*, 503(2):2825–2832.

Huang, C., Rice, D. R., and Steffen, J. H. (2022). MAGRATHEA: an open-source spherical symmetric planet interior structure code. *MNRAS*, 513(4):5256–5269.

Hubeny, I. (2017). Model atmospheres of sub-stellar mass objects. *MNRAS*, 469(1):841–869.

Iacono-Marziano, G., Morizet, Y., Le Trong, E., and Gaillard, F. (2012). New experimental data and semi-empirical parameterization of H_2O–CO_2 solubility in mafic melts. *Geochimica et Cosmochimica Acta*, 97:1–23.

Innes, H., Tsai, S.-M., and Pierrehumbert, R. T. (2023). The Runaway Greenhouse Effect on Hycean Worlds. *ApJ*, 953(2):168.

Irifune, T. (1994). Absence of an aluminous phase in the upper part of the Earth's lower mantle. *Nature*, 370(6485):131–133.

Izidoro, A., Bitsch, B., Raymond, S. N., Johansen, A., Morbidelli, A., Lambrechts, M., and Jacobson, S. A. (2021). Formation of planetary systems by pebble accretion and migration: Hot super-Earth systems from breaking compact resonant chains. *A&A*, 650:A152.

Izidoro, A., Schlichting, H. E., Isella, A., Dasgupta, R., Zimmermann, C., and Bitsch, B. (2022). The Exoplanet Radius Valley from Gas-driven Planet Migration and Breaking of Resonant Chains. *ApJL*, 939(2):L19.

Jin, S. and Mordasini, C. (2018). Compositional Imprints in Density–Distance–Time: A Rocky Composition for Close-in Low-mass Exoplanets from the Location of the Valley of Evaporation. *ApJ*, 853(2):163.

Jin, S., Mordasini, C., Parmentier, V., Van Boekel, R., Henning, T., and Ji, J. (2014). Planetary population synthesis coupled with atmospheric escape: A statistical view of evaporation. *ApJ*, 795(1):65.

Journaux, B., Brown, J. M., Pakhomova, A., Collings, I. E., Petitgirard, S., Espinoza, P., Boffa Ballaran, T., Vance, S. D., Ott, J., Cova, F., Garbarino, G., and Hanfland, M. (2020a). Holistic Approach for Studying Planetary Hydrospheres: Gibbs Representation of Ices Thermodynamics, Elasticity, and the Water Phase Diagram to 2,300 MPa. *Journal of Geophysical Research (Planets)*, 125(1):e06176.

Journaux, B., Daniel, I., Petitgirard, S., Cardon, H., Perrillat, J.-P., Caracas, R., and Mezouar, M. (2017). Salt partitioning between water and high-pressure ices. Implication for the dynamics and habitability of icy moons and water-rich planetary bodies. *Earth and Planetary Science Letters*, 463:36–47.

Journaux, B., Kalousová, K., Sotin, C., Tobie, G., Vance, S., Saur, J., Bollengier, O., Noack, L., Rückriemen-Bez, T., Van Hoolst, T., Soderlund, K. M., and Brown, J. M. (2020b). Large Ocean Worlds with High-Pressure Ices. *Space Sci. Rev.*, 216(1):7.

Kalousová, K. et al. (2018). Two-phase convection in ganymede's high-pressure ice layer — implications for its geological evolution. *Icarus*, 299:133–147.

Kalousová, K. and Sotin, C. (2018). Melting in high-pressure ice layers of large ocean worlds—implications for volatiles transport. *Geophys. Res. Lett.*, 45:8096–8103.

Karki, B. B., Wentzcovitch, R. M., de Gironcoli, S., and Baroni, S. (2000). Ab initio lattice dynamics of $MgSiO_3$ perovskite at high pressure. *Phys. Rev. B*, 62(22):14750–14756.

Kasting, J. F., Whitmire, D. P., and Reynolds, R. T. (1993). Habitable Zones around Main Sequence Stars. *Icarus*, 101(1):108–128.

Kawashima, Y., Hu, R., and Ikoma, M. (2019). Detectable Molecular Features above Hydrocarbon Haze via Transmission Spectroscopy with JWST: Case Studies of GJ 1214b-, GJ 436b-, HD 97658b-, and Kepler-51b-like Planets. *ApJL*, 876(1):L5.

Kaye, L., Vissapragada, S., Günther, M. N., Aigrain, S., Mikal-Evans, T., Jensen, E. L. N., Parviainen, H., Pozuelos, F. J., Abe, L., Acton, J. S., Agabi, A., Alves, D. R., Anderson, D. R., Armstrong, D. J., Barkaoui, K., Barragán, O., Benneke, B., Boyd, P. T., Brahm, R., Bruni, I., Bryant, E. M., Burleigh, M. R., Casewell, S. L., Ciardi, D., Cloutier, R., Collins, K. A., Collins, K. I., Conti, D. M., Crossfield, I. J. M., Crouzet, N., Daylan, T., Dragomir, D., Dransfield, G., Fabrycky, D., Fausnaugh, M., Fuűrész, G., Gan, T., Gill, S., Gillon, M., Goad, M. R., Gorjian, V., Greklek-McKeon, M., Guerrero, N., Guillot, T., Jehin, E., Jenkins, J. S., Lendl, M., Kamler, J., Kane, S. R., Kielkopf, J. F., Kunimoto, M., Marie-Sainte, W., McCormac, J., Mékarnia, D., Morales, F. Y., Moyano, M., Palle, E., Parmentier, V., Relles, H. M., Schmider, F.-X., Schwarz, R. P., Seager, S., Smith, A. M. S., Tan, T.-G., Taylor, J., Triaud, A. H. M. J., Twicken, J. D., Udry, S., Vines, J. I., Wang, G., Wheatley, P. J., and Winn, J. N. (2022). Transit timings variations in the three-planet system: TOI-270. *MNRAS*, 510(4):5464–5485.

Kempton, E. M. R., Zhang, M., Bean, J. L., Steinrueck, M. E., Piette, A. A. A., Parmentier, V., Malsky, I., Roman, M. T., Rauscher, E., Gao, P., Bell, T. J., Xue, Q., Taylor, J., Savel, A. B., Arnold, K. E., Nixon, M. C., Stevenson, K. B., Mansfield, M., Kendrew, S., Zieba, S., Ducrot, E., Dyrek, A., Lagage, P.-O., Stassun, K. G., Henry, G. W., Barman, T., Lupu, R., Malik, M., Kataria, T., Ih, J., Fu, G., Welbanks, L., and McGill, P. (2023). A reflective, metal-rich atmosphere for GJ 1214b from its JWST phase curve. *Nature*, 620(7972):67–71.

Kessel, R., Fumagalli, P., and Pettke, T. (2015). The behaviour of incompatible elements during hydrous melting of metasomatized peridotite at 4-6 GPa and 1000 °C-1200 °C. *Lithos*, 236:141–155.

Kite, E. S., Bruce Fegley Jr., Schaefer, L., and Gaidos, E. (2016). Atmosphere-Interior Exchange on Hot, Rocky Exoplanets. *ApJ*, 828(2):80.

Kite, E. S., Fegley, Bruce, J., Schaefer, L., and Ford, E. B. (2019). Superabundance of Exoplanet Sub-Neptunes Explained by Fugacity Crisis. *ApJL*, 887(2):L33.

Kite, E. S., Fegley, Bruce, J., Schaefer, L., and Ford, E. B. (2020). Atmosphere Origins for Exoplanet Sub-Neptunes. *ApJ*, 891(2):111.

Kite, E. S. and Ford, E. B. (2018). Habitability of Exoplanet Waterworlds. *ApJ*, 864(1):75.

Kite, E. S. and Schaefer, L. (2021). Water on Hot Rocky Exoplanets. *ApJL*, 909(2):L22. Publisher: The American Astronomical Society.

Kitzmann, D., Alibert, Y., Godolt, M., Grenfell, J. L., Heng, K., Patzer, A. B. C., Rauer, H., Stracke, B., and von Paris, P. (2015). The unstable CO_2 feedback cycle on ocean planets. *MNRAS*, 452(4):3752–3758.

Klotz, S., Komatsu, K., Kagi, H., Kunc, K., Sano-Furukawa, A., Machida, S., and Hattori, T. (2017). Bulk moduli and equations of state of ice VII and ice VIII. *Phys. Rev. B*, 95(17):174111.

Knudson, M. D., Desjarlais, M. P., Lemke, R. W., Mattsson, T. R., French, M., Nettelmann, N., and Redmer, R. (2012). Probing the Interiors of the Ice Giants: Shock Compression of Water to 700 GPa and 3.8g/cm^3. *Phys. Rev. Lett.*, 108(9):091102.

Knutson, H. A., Charbonneau, D., Allen, L. E., Fortney, J. J., Agol, E., Cowan, N. B., Showman, A. P., Cooper, C. S., and Megeath, S. T. (2007). A map of the day-night contrast of the extrasolar planet HD 189733b. *Nature*, 447(7141):183–186.

Kovačević, T., González-Cataldo, F., Stewart, S. T., and Militzer, B. (2022). Miscibility of rock and ice in the interiors of water worlds. *Scientific Reports*, 12:13055.

Kratter, K. and Lodato, G. (2016). Gravitational Instabilities in Circumstellar Disks. *ARA&A*, 54:271–311.

Kreidberg, L., Bean, J. L., Désert, J.-M., Benneke, B., Deming, D., Stevenson, K. B., Seager, S., Berta-Thompson, Z., Seifahrt, A., and Homeier, D. (2014a). Clouds in the atmosphere of the super-Earth exoplanet GJ1214b. *Nature*, 505(7481):69–72.

Kreidberg, L., Bean, J. L., Désert, J.-M., Line, M. R., Fortney, J. J., Madhusudhan, N., Stevenson, K. B., Showman, A. P., Charbonneau, D., McCullough, P. R., Seager, S., Burrows, A., Henry, G. W., Williamson, M., Kataria, T., and Homeier, D. (2014b). A Precise Water Abundance Measurement for the Hot Jupiter WASP-43b. *ApJL*, 793(2):L27.

Kuchner, M. J. (2003). Volatile-rich Earth-Mass Planets in the Habitable Zone. *ApJL*, 596(1):L105–L108.

Kuchner, M. J. and Seager, S. (2005). Extrasolar Carbon Planets. *arXiv e-prints*, pages astro–ph/0504214.

Lebec, L. et al. (2023). Scaling of convection in high-pressure ice layers of large icy moons and implications for habitability. *Icarus*, 396:115494.

Lebrun, T., Massol, H., ChassefièRe, E., Davaille, A., Marcq, E., Sarda, P., Leblanc, F., and Brandeis, G. (2013). Thermal evolution of an early magma ocean in interaction with the atmosphere. *Journal of Geophysical Research (Planets)*, 118(6):1155–1176.

Leconte, J., Selsis, F., Hersant, F., and Guillot, T. (2017). Condensation-inhibited convection in hydrogen-rich atmospheres . Stability against double-diffusive processes and thermal profiles for Jupiter, Saturn, Uranus, and Neptune. *A&A*, 598:A98.

Leconte, J., Spiga, A., Clément, N., Guerlet, S., Selsis, F., Milcareck, G., Cavalié, T., Moreno, R., Lellouch, E., Carrión-González, Ó., Charnay, B., and Lefèvre, M. (2024). A 3D picture of moist-convection inhibition in hydrogen-rich atmospheres: Implications for K2-18 b. *A&A*, 686:A131.

Lee, E. J., Chiang, E., and Ormel, C. W. (2014). Make Super-Earths, Not Jupiters: Accreting Nebular Gas onto Solid Cores at 0.1 AU and Beyond. *ApJ*, 797(2):95.

Lee, K. K. M., O'Neill, B., Panero, W. R., Shim, S.-H., Benedetti, L. R., and Jeanloz, R. (2004). Equations of state of the high-pressure phases of a natural peridotite and implications for the Earth's lower mantle. *Earth and Planetary Science Letters*, 223(3-4):381–393.

Lee, M.-S. and Scandolo, S. (2011). Mixtures of planetary ices at extreme conditions. *Nature Communications*, 2:185.

Léger, A., Grasset, O., Fegley, B., Codron, F., Albarede, A. F., Barge, P., Barnes, R., Cance, P., Carpy, S., Catalano, F., Cavarroc, C., Demangeon, O., Ferraz-Mello, S., Gabor, P., Grießmeier, J. M., Leibacher, J., Libourel, G., Maurin, A. S., Raymond, S. N., Rouan, D., Samuel, B., Schaefer, L., Schneider, J., Schuller, P. A., Selsis, F., and Sotin, C. (2011). The extreme physical properties of the CoRoT-7b super-Earth. *Icarus*, 213(1):1–11.

Léger, A., Selsis, F., Sotin, C., Guillot, T., Despois, D., Mawet, D., Ollivier, M., Labèque, A., Valette, C., Brachet, F., Chazelas, B., and Lammer, H. (2004). A new family of planets? "Ocean-Planets". *Icarus*, 169(2):499–504.

Leleu, A., Alibert, Y., Hara, N. C., Hooton, M. J., Wilson, T. G., Robutel, P., Delisle, J. B., Laskar, J., Hoyer, S., Lovis, C., Bryant, E. M., Ducrot, E., Cabrera, J., Delrez, L., Acton, J. S., Adibekyan, V., Allart, R., Allende Prieto, C., Alonso, R., Alves, D., Anderson, D. R., Angerhausen, D., Anglada Escudé, G., Asquier, J., Barrado, D., Barros, S. C. C., Baumjohann, W., Bayliss, D., Beck, M., Beck, T., Bekkelien, A., Benz, W., Billot, N., Bonfanti, A., Bonfils, X., Bouchy, F., Bourrier, V., Boué, G., Brandeker, A., Broeg, C., Buder, M., Burdanov, A., Burleigh, M. R., Bárczy, T., Cameron, A. C., Chamberlain, S., Charnoz, S., Cooke, B. F., Corral Van Damme, C., Correia, A. C. M., Cristiani, S., Damasso, M., Davies, M. B., Deleuil, M., Demangeon, O. D. S., Demory, B. O., Di Marcantonio, P., Di Persio, G., Dumusque, X., Ehrenreich, D., Erikson, A., Figueira, P., Fortier, A., Fossati, L., Fridlund, M., Futyan, D., Gandolfi, D., García Muñoz, A., Garcia, L. J., Gill, S., Gillen, E., Gillon, M., Goad, M. R., González Hernández, J. I., Guedel, M., Günther, M. N., Haldemann, J., Henderson, B., Heng, K., Hogan, A. E., Isaak, K., Jehin, E., Jenkins, J. S., Jordán, A., Kiss, L., Kristiansen, M. H., Lam, K., Lavie, B., Lecavelier des Etangs, A., Lendl, M., Lillo-Box, J., Lo Curto, G., Magrin, D., Martins, C. J. A. P., Maxted, P. F. L., McCormac, J., Mehner, A., Micela, G., Molaro, P., Moyano, M., Murray, C. A., Nascimbeni, V., Nunes, N. J., Olofsson, G., Osborn, H. P., Oshagh, M., Ottensamer, R., Pagano, I., Pallé, E., Pedersen, P. P., Pepe, F. A., Persson, C. M., Peter, G., Piotto, G., Polenta, G., Pollacco, D., Poretti, E., Pozuelos, F. J., Queloz, D., Ragazzoni, R., Rando, N., Ratti, F., Rauer, H., Raynard, L., Rebolo, R., Reimers, C., Ribas, I., Santos, N. C., Scandariato, G., Schneider, J., Sebastian, D., Sestovic, M., Simon, A. E., Smith, A. M. S., Sousa, S. G., Sozzetti, A., Steller, M., Suárez Mascareño, A., Szabó, G. M., Ségransan, D., Thomas, N., Thompson, S., Tilbrook, R. H., Triaud, A., Turner, O., Udry, S., Van Grootel, V., Venus, H., Verrecchia, F., Vines, J. I., Walton, N. A., West, R. G., Wheatley, P. J., Wolter, D., and Zapatero Osorio, M. R. (2021). Six transiting planets and a chain of Laplace resonances in TOI-178. *A&A*, 649:A26.

Lesne, P., Scaillet, B., and Pichavant, M. (2015). The solubility of sulfur in hydrous basaltic melts. *Chemical Geology*, 418:104–116.

Levi, A., Sasselov, D., and Podolak, M. (2017). The Abundance of Atmospheric CO_2 in Ocean Exoplanets: a Novel CO_2 Deposition Mechanism. *ApJ*, 838(1):24.

Li, G., Gordon, I. E., Rothman, L. S., Tan, Y., Hu, S.-M., Kassi, S., Campargue, A., and Medvedev, E. S. (2015). Rovibrational Line Lists for Nine Isotopologues of the CO Molecule in the X $^1\Sigma^+$ Ground Electronic State. *ApJS*, 216(1):15.

Libourel, G., Marty, B., and Humbert, F. (2003). Nitrogen solubility in basaltic melt. Part I. Effect of oxygen fugacity. *Geochimica et Cosmochimica Acta*, 67(21):4123–4135.

Lichtenberg, T., Bower, D. J., Hammond, M., Boukrouche, R., Sanan, P., Tsai, S.-M., and Pierrehumbert, R. T. (2021). Vertically Resolved Magma Ocean–Protoatmosphere Evolution: H_2, H_2O, CO_2, CH_4, CO, O_2, and N_2 as Primary Absorbers. *Journal of Geophysical Research: Planets*, 126(2):e2020JE006711. _eprint: https://onlinelibrary.wiley.com/doi/pdf/10.1029/2020JE006711.

Lillo-Box, J., Figueira, P., Leleu, A., Acuña, L., Faria, J. P., Hara, N., Santos, N. C., Correia, A. C. M., Robutel, P., Deleuil, M., Barrado, D., Sousa, S., Bonfils, X., Mousis, O., Almenara, J. M., Astudillo-Defru, N., Marcq, E., Udry, S., Lovis, C., and Pepe, F. (2020). Planetary system LHS 1140 revisited with ESPRESSO and TESS. *A&A*, 642:A121.

Line, M. R., Vasisht, G., Chen, P., Angerhausen, D., and Yung, Y. L. (2011). Thermochemical and Photochemical Kinetics in Cooler Hydrogen-dominated Extrasolar Planets: A Methane-poor GJ436b? *ApJ*, 738(1):32.

Lingam, M. and Loeb, A. (2018). Is Extraterrestrial Life Suppressed on Subsurface Ocean Worlds due to the Paucity of Bioessential Elements? *Astron. J.*, 156(4):151.

Lodders, K. (2004). Jupiter Formed with More Tar than Ice. *ApJ*, 611(1):587–597.

Lopez, E. D. and Fortney, J. J. (2013). The Role of Core Mass in Controlling Evaporation: The Kepler Radius Distribution and the Kepler-36 Density Dichotomy. *ApJ*, 776(1):2.

Lopez, E. D., Fortney, J. J., and Miller, N. (2012). How Thermal Evolution and Mass-loss Sculpt Populations of Super-Earths and Sub-Neptunes: Application to the Kepler-11 System and Beyond. *ApJ*, 761(1):59.

Luger, R. and Barnes, R. (2015). Extreme Water Loss and Abiotic O2Buildup on Planets Throughout the Habitable Zones of M Dwarfs. *Astrobiology*, 15(2):119–143.

Luo, H., Dorn, C., and Deng, J. (2024). The interior as the dominant water reservoir in super-Earths and sub-Neptunes. *Nature Astronomy*, 8:1399–1407.

Luque, R., Piaulet-Ghorayeb, C., Radica, M., Xue, Q., Zhang, M., Bean, J. L., Samra, D., and Steinrueck, M. E. (2025). Insufficient evidence for DMS and DMDS in the atmosphere of K2-18 b. From a joint analysis of JWST NIRISS, NIRSpec, and MIRI observations. *arXiv e-prints*, page arXiv:2505.13407.

Luu, C. N., Yu, X., Glein, C. R., Innes, H., Aguichine, A., Krissansen-Totton, J., Moses, J. I., Tsai, S.-M., Zhang, X., Truong, N., and Fortney, J. J. (2024). Volatile-rich Sub-Neptunes as Hydrothermal Worlds: The Case of K2-18 b. *ApJL*, 977(2):L51.

MacDonald, R. J. and Madhusudhan, N. (2017). HD 209458b in new light: evidence of nitrogen chemistry, patchy clouds and sub-solar water. *MNRAS*, 469(2):1979–1996.

Madhusudhan, N. (2018). Atmospheric Retrieval of Exoplanets. In Deeg, H. J. and Belmonte, J. A., editors, *Handbook of Exoplanets*, page 104. Springer Cham.

Madhusudhan, N. (2019). Exoplanetary Atmospheres: Key Insights, Challenges, and Prospects. *ARA&A*, 57:617–663.

Madhusudhan, N., Agúndez, M., Moses, J. I., and Hu, Y. (2016). Exoplanetary Atmospheres—Chemistry, Formation Conditions, and Habitability. *Space Sci. Rev.*, 205(1-4):285–348.

Madhusudhan, N., Constantinou, S., Holmberg, M., Sarkar, S., Piette, A. A. A., and Moses, J. I. (2025). New Constraints on DMS and DMDS in the Atmosphere of K2-18 b from JWST MIRI. *ApJL*, 983(2):L40.

Madhusudhan, N., Lee, K. K. M., and Mousis, O. (2012). A Possible Carbon-rich Interior in Super-Earth 55 Cancri e. *ApJL*, 759(2):L40.

Madhusudhan, N., Moses, J. I., Rigby, F., and Barrier, E. (2023a). Chemical conditions on Hycean worlds. *Faraday Discussions*, 245:80–111.

Madhusudhan, N., Mousis, O., Johnson, T. V., and Lunine, J. I. (2011). Carbon-rich Giant Planets: Atmospheric Chemistry, Thermal Inversions, Spectra, and Formation Conditions. *ApJ*, 743(2):191.

Madhusudhan, N., Nixon, M. C., Welbanks, L., Piette, A. A. A., and Booth, R. A. (2020). The Interior and Atmosphere of the Habitable-zone Exoplanet K2-18b. *ApJL*, 891(1):L7.

Madhusudhan, N., Piette, A. A. A., and Constantinou, S. (2021). Habitability and Biosignatures of Hycean Worlds. *ApJ*, 918(1):1.

Madhusudhan, N., Sarkar, S., Constantinou, S., Holmberg, M., Piette, A. A. A., and Moses, J. I. (2023b). Carbon-bearing Molecules in a Possible Hycean Atmosphere. *ApJL*, 956(1):L13.

Madhusudhan, N. and Seager, S. (2009). A Temperature and Abundance Retrieval Method for Exoplanet Atmospheres. *ApJ*, 707(1):24–39.

Madhusudhan, N. and Seager, S. (2011). High Metallicity and Non-equilibrium Chemistry in the Dayside Atmosphere of hot-Neptune GJ 436b. *ApJ*, 729(1):41.

Malik, M., Grosheintz, L., Mendonça, J. M., Grimm, S. L., Lavie, B., Kitzmann, D., Tsai, S.-M., Burrows, A., Kreidberg, L., Bedell, M., Bean, J. L., Stevenson, K. B., and Heng, K. (2017). HELIOS: An Open-source, GPU-accelerated Radiative Transfer Code for Self-consistent Exoplanetary Atmospheres. *AJ*, 153(2):56.

Mallik, A., Li, Y., and Wiedenbeck, M. (2018). Nitrogen evolution within the Earth's atmosphere–mantle system assessed by recycling in subduction zones. *Earth and Planetary Science Letters*, 482:556–566.

Markham, S., Guillot, T., and Stevenson, D. (2022). Convective inhibition with an ocean. I. Supercritical cores on sub-Neptunes/super-Earths. *A&A*, 665:A12.

Marois, C., Macintosh, B., Barman, T., Zuckerman, B., Song, I., Patience, J., Lafrenière, D., and Doyon, R. (2008). Direct Imaging of Multiple Planets Orbiting the Star HR 8799. *Science*, 322(5906):1348.

Maruyama, S. et al. (2013). The naked planet earth: Most essential pre-requisite for the origin and evolution of life. *Geosci. Front.*, 4:141–165.

Matsui, T. and Abe, Y. (1986). Evolution of an impact-induced atmosphere and magma ocean on the accreting Earth. *Nature*, 319(6051):303–305.

Mayor, M. and Queloz, D. (1995). A Jupiter-mass companion to a solar-type star. *Nature*, 378(6555):355–359.

Mazevet, S., Licari, A., Chabrier, G., and Potekhin, A. Y. (2019). Ab initio based equation of state of dense water for planetary and exoplanetary modeling. *A&A*, 621:A128.

Meadows, V. S. and Barnes, R. K. (2018). Factors Affecting Exoplanet Habitability. In Deeg, H. J. and Belmonte, J. A., editors, *Handbook of Exoplanets*, page 57. Springer International Publishing.

Melekhova, E., Schmidt, M. W., Ulmer, P., and Pettke, T. (2007). The composition of liquids coexisting with dense hydrous magnesium silicates at 11-13.5 GPa and the endpoints of the solidi in the MgO-SiO $_2$-H $_2$O system. *Geochimica et Cosmochimica Acta*, 71(13):3348–3360.

Ment, K., Dittmann, J. A., Astudillo-Defru, N., Charbonneau, D., Irwin, J., Bonfils, X., Murgas, F., Almenara, J.-M., Forveille, T., Agol, E., Ballard, S., Berta-Thompson, Z. K., Bouchy, F., Cloutier, R., Delfosse, X., Doyon, R., Dressing, C. D., Esquerdo, G. A., Haywood, R. D., Kipping, D. M., Latham, D. W., Lovis, C., Newton, E. R., Pepe, F., Rodriguez, J. E., Santos, N. C., Tan, T.-G., Udry, S., Winters, J. G., and Wünsche, A. (2019). A Second Terrestrial Planet Orbiting the Nearby M Dwarf LHS 1140. *AJ*, 157(1):32.

Merino, N., Aronson, H. S., Bojanova, D. P., Feyhl-Buska, J., Wong, M. L., Zhang, S., and Giovannelli, D. (2019). Living at the extremes: extremophiles and the limits of life in a planetary context. *Frontiers in microbiology*, 10:780.

Mikal-Evans, T., Madhusudhan, N., Dittmann, J., Günther, M. N., Welbanks, L., Van Eylen, V., Crossfield, I. J. M., Daylan, T., and Kreidberg, L. (2023). Hubble Space Telescope Transmission Spectroscopy for the Temperate Sub-Neptune TOI-270 d: A Possible Hydrogen-rich Atmosphere Containing Water Vapor. *AJ*, 165(3):84.

Miller-Ricci Kempton, E., Zahnle, K., and Fortney, J. J. (2012). The Atmospheric Chemistry of GJ 1214b: Photochemistry and Clouds. *ApJ*, 745(1):3.

Mills, S. M., Fabrycky, D. C., Migaszewski, C., Ford, E. B., Petigura, E., and Isaacson, H. (2016). A resonant chain of four transiting, sub-Neptune planets. *Nature*, 533(7604):509–512.

Misener, W., Schlichting, H. E., and Young, E. D. (2023). Atmospheres as windows into sub-Neptune interiors: coupled chemistry and structure of hydrogen–silane–water envelopes. *MNRAS*, 524(1):981–992.

Miyazaki, A., Hiyagon, H., Sugiura, N., Hirose, K., and Takahashi, E. (2004). Solubilities of nitrogen and noble gases in silicate melts under various oxygen fugacities: implications for the origin and degassing history of nitrogen and noble gases in the earth. *Geochimica et Cosmochimica Acta*, 68(2):387–401.

Mollière, P., van Boekel, R., Bouwman, J., Henning, T., Lagage, P. O., and Min, M. (2017). Observing transiting planets with JWST. Prime targets and their synthetic spectral observations. *A&A*, 600:A10.

Mollière, P., Wardenier, J. P., van Boekel, R., Henning, T., Molaverdikhani, K., and Snellen, I. A. G. (2019). petitRADTRANS. A Python radiative transfer package for exoplanet characterization and retrieval. *A&A*, 627:A67.

Monteux, J., Andrault, D., and Samuel, H. (2016). On the cooling of a deep terrestrial magma ocean. *Earth and Planetary Science Letters*, 448:140–149.

Mookherjee, M., Stixrude, L., and Karki, B. (2008). Hydrous silicate melt at high pressure. *Nature*, 452(7190):983–986.

Moore, G., Vennemann, T., and Carmichael, I. S. E. (1995). Solubility of water in magmas to 2 kbar. *Geology*, 23(12):1099–1102.

Mordasini, C., Alibert, Y., and Benz, W. (2009). Extrasolar planet population synthesis. I. Method, formation tracks, and mass-distance distribution. *A&A*, 501(3):1139–1160.

Morley, C. V., Fortney, J. J., Marley, M. S., Zahnle, K., Line, M., Kempton, E., Lewis, N., and Cahoy, K. (2015). Thermal Emission and Reflected Light Spectra of Super Earths with Flat Transmission Spectra. *ApJ*, 815(2):110.

Moses, J. I. (2014). Chemical kinetics on extrasolar planets. *Philosophical Transactions of the Royal Society of London Series A*, 372(2014):20130073–20130073.

Moses, J. I., Visscher, C., Fortney, J. J., Showman, A. P., Lewis, N. K., Griffith, C. A., Klippenstein, S. J., Shabram, M., Friedson, A. J., Marley, M. S., and Freedman, R. S. (2011). Disequilibrium Carbon, Oxygen, and Nitrogen Chemistry in the Atmospheres of HD 189733b and HD 209458b. *ApJ*, 737(1):15.

Mousis, O., Deleuil, M., Aguichine, A., Marcq, E., Naar, J., Aguirre, L. A., Brugger, B., and Gonçalves, T. (2020). Irradiated Ocean Planets Bridge Super-Earth and Sub-Neptune Populations. *ApJL*, 896(2):L22.

Murakami, M., Hirose, K., Kawamura, K., Sata, N., and Ohishi, Y. (2004). Post-Perovskite Phase Transition in $MgSiO_3$. *Science*, 304(5672):855–858.

Nesvorný, D. and Morbidelli, A. (2008). Mass and Orbit Determination from Transit Timing Variations of Exoplanets. *ApJ*, 688(1):636–646.

Nettelmann, N., Fortney, J. J., Kramm, U., and Redmer, R. (2011). Thermal Evolution and Structure Models of the Transiting Super-Earth GJ 1214b. *ApJ*, 733(1):2.

Ni, H., Zhang, L., Xiong, X., Mao, Z., and Wang, J. (2017). Supercritical fluids at subduction zones: Evidence, formation condition, and physicochemical properties. *Earth-Science Reviews*, 167:62–71.

Nixon, M. C. and Madhusudhan, N. (2021). How deep is the ocean? Exploring the phase structure of water-rich sub-Neptunes. *MNRAS*, 505(3):3414–3432.

Nixon, M. C., Piette, A. A. A., Kempton, E. M. R., Gao, P., Bean, J. L., Steinrueck, M. E., Mahajan, A. S., Eastman, J. D., Zhang, M., and Rogers, L. A. (2024). New Insights into the Internal Structure of GJ 1214 b Informed by JWST. *ApJL*, 970(2):L28.

Noack, L., Höning, D., Rivoldini, A., Heistracher, C., Zimov, N., Journaux, B., Lammer, H., Van Hoolst, T., and Bredehöft, J. H. (2016). Water-rich planets: How habitable is a water layer deeper than on Earth? *Icarus*, 277:215–236.

Nortmann, L., Lesjak, F., Yan, F., Cont, D., Czesla, S., Lavail, A., Rains, A. D., Nagel, E., Boldt-Christmas, L., Hatzes, A., Reiners, A., Piskunov, N., Kochukhov, O., Heiter, U., Shulyak, D., Rengel, M., and Seemann, U. (2025). CRIRES$^+$ transmission spectroscopy of WASP-127 b: Detection of the resolved signatures of a supersonic equatorial jet and cool poles in a hot planet. *A&A*, 693:A213.

Nowak, G., Luque, R., Parviainen, H., Pallé, E., Molaverdikhani, K., Béjar, V. J. S., Lillo-Box, J., Rodríguez-López, C., Caballero, J. A., Zechmeister, M., Passegger, V. M., Cifuentes, C., Schweitzer, A., Narita, N., Cale, B., Espinoza, N., Murgas, F., Hidalgo, D., Zapatero Osorio, M. R., Pozuelos, F. J., Aceituno, F. J., Amado, P. J., Barkaoui, K., Barrado, D., Bauer, F. F., Benkhaldoun, Z., Caldwell, D. A., Casasayas Barris, N., Chaturvedi, P., Chen, G., Collins, K. A., Collins, K. I., Cortés-Contreras, M., Crossfield, I. J. M., de León, J. P., Díez Alonso, E., Dreizler, S., El Mufti, M., Esparza-Borges, E., Essack, Z., Fukui, A., Gaidos, E., Gillon, M., Gonzales, E. J., Guerra, P., Hatzes, A., Henning, T., Herrero, E., Hesse, K., Hirano, T., Howell, S. B., Jeffers, S. V., Jehin, E., Jenkins, J. M., Kaminski, A., Kemmer, J., Kielkopf, J. F., Kossakowski, D., Kotani, T., Kürster, M., Lafarga, M., Latham, D. W., Law, N., Lissauer, J. J., Lodieu, N., Madrigal-Aguado, A., Mann, A. W., Massey, B., Matson, R. A., Matthews, E., Montañés-Rodríguez, P., Montes, D., Morales, J. C., Mori, M., Nagel, E., Oshagh, M., Pedraz, S., Plavchan, P., Pollacco, D., Quirrenbach, A., Reffert, S., Reiners, A., Ribas, I., Ricker, G. R., Rose, M. E., Schlecker, M., Schlieder, J. E., Seager, S., Stangret, M., Stock, S., Tamura, M., Tanner, A., Teske, J., Trifonov, T., Twicken, J. D., Vanderspek, R., Watanabe, D., Wittrock, J., Ziegler, C., and Zohrabi, F. (2020). The CARMENES search for exoplanets around M dwarfs. Two planets on opposite sides of the radius gap transiting the nearby M dwarf LTT 3780. *A&A*, 642:A173.

Öberg, K. I., Murray-Clay, R., and Bergin, E. A. (2011). The Effects of Snowlines on C/O in Planetary Atmospheres. *ApJL*, 743(1):L16.

Ohno, K., Schlawin, E., Bell, T. J., Murphy, M. M., Beatty, T. G., Welbanks, L., Greene, T. P., Fortney, J. J., Parmentier, V., Edelman, I. R., Mehta, N., and Rieke, M. J. (2025). A Possible Metal-dominated Atmosphere below the Thick Aerosols of GJ 1214 b Suggested by Its JWST Panchromatic Transmission Spectrum. *ApJL*, 979(1):L7.

O'Malley-James, J. T. and Kaltenegger, L. (2017). UV surface habitability of the TRAPPIST-1 system. *MNRAS*, 469(1):L26–L30.

O'Neill, H. and Mavrogenes, J. (2002). The sulfide capacity and the sulfur content at sulfide saturation of silicate melts at 1400°C and 1 bar. *Journal of Petrology*, 43(6):1049–1087.

Orton, G. S., Gustafsson, M., Burgdorf, M., and Meadows, V. (2007). Revised ab initio models for H_2-H_2 collision-induced absorption at low temperatures. *Icarus*, 189(2):544–549.

Otegi, J. F., Dorn, C., Helled, R., Bouchy, F., Haldemann, J., and Alibert, Y. (2020). Impact of the measured parameters of exoplanets on the inferred internal structure. *A&A*, 640:A135.

Owen, J. E. and Schlichting, H. E. (2024). Mapping out the parameter space for photoevaporation and core-powered mass-loss. *MNRAS*, 528(2):1615–1629.

Owen, J. E. and Wu, Y. (2013). Kepler Planets: A Tale of Evaporation. *ApJ*, 775(2):105.

Owen, J. E. and Wu, Y. (2016). Atmospheres of Low-mass Planets: The "Boil-off". *ApJ*, 817(2):107.

Owen, J. E. and Wu, Y. (2017). The Evaporation Valley in the Kepler Planets. *ApJ*, 847(1):29.

Pan, M., Wang, S., and Ji, J. (2022). The terrestrial planet formation around M dwarfs: insitu, inward migration, or reversed migration. *MNRAS*, 510(3):4134–4145.

Pan, V., Holloway, J. R., and Hervig, R. L. (1991). The pressure and temperature dependence of carbon dioxide solubility in tholeiitic basalt melts. *Geochimica et Cosmochimica Acta*, 55(6):1587–1595.

Papale, P., Moretti, R., and Barbato, D. (2006). The compositional dependence of the saturation surface of h_2o + co_2 fluids in silicate melts. *Chemical Geology*, 229(1):78–95.

Parker, L. T., Mendonça, J. M., Diamond-Lowe, H., Birkby, J. L., Meech, A., Vaughan, S. R., Brogi, M., Fisher, C., Buchhave, L. A., Bello-Arufe, A., Kreidberg, L., and Dittmann, J. (2025). Limits on the atmospheric metallicity and aerosols of the sub-Neptune GJ 3090 b from high-resolution CRIRES+ spectroscopy. *MNRAS*, 538(4):3263–3283.

Peacock, S., Barman, T., Shkolnik, E. L., Loyd, R. O. P., Schneider, A. C., Pagano, I., and Meadows, V. S. (2020). HAZMAT VI: The Evolution of Extreme Ultraviolet Radiation Emitted from Early M Stars. *ApJ*, 895(1):5.

Pelletier, S., Benneke, B., Ali-Dib, M., Prinoth, B., Kasper, D., Seifahrt, A., Bean, J. L., Debras, F., Klein, B., Bazinet, L., Hoeijmakers, H. J., Kesseli, A. Y., Lim, O., Carmona, A., Pino, L., Casasayas-Barris, N., Hood, T., and Stürmer, J. (2023). Vanadium oxide and a sharp onset of cold-trapping on a giant exoplanet. *Nature*, 619(7970):491–494.

Pepe, F., Cristiani, S., Rebolo, R., Santos, N. C., Dekker, H., Cabral, A., Di Marcantonio, P., Figueira, P., Lo Curto, G., Lovis, C., Mayor, M., Mégevand, D., Molaro, P., Riva, M., Zapatero Osorio, M. R., Amate, M., Manescau, A., Pasquini, L., Zerbi, F. M., Adibekyan, V., Abreu, M., Affolter, M., Alibert, Y., Aliverti, M., Allart, R., Allende Prieto, C., Álvarez, D., Alves, D., Avila, G., Baldini, V., Bandy, T., Barros, S. C. C., Benz, W., Bianco, A., Borsa, F., Bourrier, V., Bouchy, F., Broeg, C., Calderone, G., Cirami, R., Coelho, J., Conconi, P., Coretti, I., Cumani, C., Cupani, G., D'Odorico, V., Damasso, M., Deiries, S., Delabre, B., Demangeon, O. D. S., Dumusque, X., Ehrenreich, D., Faria, J. P., Fragoso, A., Genolet, L., Genoni, M.,

Génova Santos, R., González Hernández, J. I., Hughes, I., Iwert, O., Kerber, F., Knudstrup, J., Landoni, M., Lavie, B., Lillo-Box, J., Lizon, J. L., Maire, C., Martins, C. J. A. P., Mehner, A., Micela, G., Modigliani, A., Monteiro, M. A., Monteiro, M. J. P. F. G., Moschetti, M., Murphy, M. T., Nunes, N., Oggioni, L., Oliveira, A., Oshagh, M., Pallé, E., Pariani, G., Poretti, E., Rasilla, J. L., Rebordão, J., Redaelli, E. M., Santana Tschudi, S., Santin, P., Santos, P., Ségransan, D., Schmidt, T. M., Segovia, A., Sosnowska, D., Sozzetti, A., Sousa, S. G., Spanò, P., Suárez Mascareño, A., Tabernero, H., Tenegi, F., Udry, S., and Zanutta, A. (2021). ESPRESSO at VLT. On-sky performance and first results. *A&A*, 645:A96.

Petigura, E. A. (2020). Two Views of the Radius Gap and the Role of Light Curve Fitting. *AJ*, 160(2):89.

Piaulet-Ghorayeb, C., Benneke, B., Radica, M., Raul, E., Coulombe, L.-P., Ahrer, E.-M., Kubyshkina, D., Howard, W. S., Krissansen-Totton, J., MacDonald, R. J., Roy, P.-A., Louca, A., Christie, D., Fournier-Tondreau, M., Allart, R., Miguel, Y., Schlichting, H. E., Welbanks, L., Cadieux, C., Dorn, C., Evans-Soma, T. M., Fortney, J. J., Pierrehumbert, R., Lafrenière, D., Acuña, L., Komacek, T., Innes, H., Beatty, T. G., Cloutier, R., Doyon, R., Gagnebin, A., Gapp, C., and Knutson, H. A. (2024). JWST/NIRISS Reveals the Water-rich "Steam World" Atmosphere of GJ 9827 d. *ApJL*, 974(1):L10.

Pica-Ciamarra, L., Madhusudhan, N., Cooke, G. J., Constantinou, S., and Binet, M. (2025). A Systematic Search for Trace Molecules in Exoplanet K2-18 b. *arXiv e-prints*, page arXiv:2505.10539.

Pierrehumbert, R. and Gaidos, E. (2011). Hydrogen Greenhouse Planets Beyond the Habitable Zone. *ApJL*, 734(1):L13.

Piette, A. A. A. and Madhusudhan, N. (2020). On the Temperature Profiles and Emission Spectra of Mini-Neptune Atmospheres. *ApJ*, 904(2):154.

Pinhas, A., Rackham, B. V., Madhusudhan, N., and Apai, D. (2018). Retrieval of planetary and stellar properties in transmission spectroscopy with AURA. *MNRAS*, 480(4):5314–5331.

Podolak, M. and Helled, R. (2012). What Do We Really Know about Uranus and Neptune? *ApJL*, 759(2):L32.

Podolak, M., Helled, R., and Schubert, G. (2019). Effect of non-adiabatic thermal profiles on the inferred compositions of Uranus and Neptune. *MNRAS*, 487(2):2653–2664.

Poirier, J.-P. (2000). *Introduction to the Physics of the Earth's Interior*. Cambridge University Press, 2 edition.

Pollack, J. B., Hubickyj, O., Bodenheimer, P., Lissauer, J. J., Podolak, M., and Greenzweig, Y. (1996). Formation of the Giant Planets by Concurrent Accretion of Solids and Gas. *Icarus*, 124(1):62–85.

Ramirez, R. M. (2018). A More Comprehensive Habitable Zone for Finding Life on Other Planets. *Geosciences*, 8(8):280.

Ramirez, R. M. and Levi, A. (2018). The ice cap zone: a unique habitable zone for ocean worlds. *MNRAS*, 477(4):4627–4640.

Richard, C., Gordon, I., Rothman, L., Abel, M., Frommhold, L., Gustafsson, M., Hartmann, J.-M., Hermans, C., Lafferty, W., Orton, G., Smith, K., and Tran, H. (2012). New section of the hitran database: Collision-induced absorption (cia). *J. Quant. Spectrosc. Radiat. Transf.*, 113(11):1276 – 1285. Three Leaders in Spectroscopy.

Ricker, G. R., Winn, J. N., Vanderspek, R., Latham, D. W., Bakos, G. Á., Bean, J. L., Berta-Thompson, Z. K., Brown, T. M., Buchhave, L., Butler, N. R., Butler, R. P., Chaplin, W. J., Charbonneau, D., Christensen-Dalsgaard, J., Clampin, M., Deming, D., Doty, J., De Lee, N., Dressing, C., Dunham, E. W., Endl, M., Fressin, F., Ge, J., Henning, T., Holman, M. J., Howard, A. W., Ida, S., Jenkins, J. M., Jernigan, G., Johnson, J. A., Kaltenegger, L., Kawai, N., Kjeldsen, H., Laughlin, G., Levine, A. M., Lin, D., Lissauer, J. J., MacQueen, P., Marcy, G., McCullough, P. R., Morton, T. D., Narita, N., Paegert, M., Palle, E., Pepe, F., Pepper, J., Quirrenbach, A., Rinehart, S. A., Sasselov, D., Sato, B., Seager, S., Sozzetti, A., Stassun, K. G., Sullivan, P., Szentgyorgyi, A., Torres, G., Udry, S., and Villasenor, J. (2015). Transiting Exoplanet Survey Satellite (TESS). *Journal of Astronomical Telescopes, Instruments, and Systems*, 1:014003.

Rigby, F. E. and Madhusudhan, N. (2024). On the ocean conditions of Hycean worlds. *MNRAS*, 529(1):409–424.

Rigby, F. E., Pica-Ciamarra, L., Holmberg, M., Madhusudhan, N., Constantinou, S., Schaefer, L., Deng, J., Lee, K. K., and Moses, J. I. (2024). Toward a self-consistent evaluation of gas dwarf scenarios for temperate sub-neptunes. *ApJ*, 975(1):101.

Rogers, J. G. (2025). On the road to the radius valley: distinguishing between gas dwarfs and water worlds with young transiting exoplanets. *MNRAS*, 539(3):2230–2241.

Rogers, J. G., Gupta, A., Owen, J. E., and Schlichting, H. E. (2021). Photoevaporation versus core-powered mass-loss: model comparison with the 3D radius gap. *MNRAS*, 508(4):5886–5902.

Rogers, J. G. and Owen, J. E. (2021). Unveiling the planet population at birth. *MNRAS*, 503(1):1526–1542.

Rogers, J. G., Schlichting, H. E., and Owen, J. E. (2023). Conclusive Evidence for a Population of Water Worlds around M Dwarfs Remains Elusive. *ApJL*, 947(1):L19.

Rogers, L. A., Bodenheimer, P., Lissauer, J. J., and Seager, S. (2011). Formation and Structure of Low-density exo-Neptunes. *ApJ*, 738(1):59.

Rogers, L. A. and Seager, S. (2010a). A Framework for Quantifying the Degeneracies of Exoplanet Interior Compositions. *ApJ*, 712(2):974–991.

Rogers, L. A. and Seager, S. (2010b). Three Possible Origins for the Gas Layer on GJ 1214b. *ApJ*, 716(2):1208–1216.

Roskosz, M., Bouhifd, M., Jephcoat, A., Marty, B., and Mysen, B. (2013). Nitrogen solubility in molten metal and silicate at high pressure and temperature. *Geochimica et Cosmochimica Acta*, 121:15–28.

Rothman, L., Gordon, I., Barber, R., Dothe, H., Gamache, R., Goldman, A., Perevalov, V., Tashkun, S., and Tennyson, J. (2010). Hitemp, the high-temperature molecular spectroscopic database. *J. Quant. Spectrosc. Radiat. Transf.*, 111(15):2139 – 2150. XVIth Symposium on High Resolution Molecular Spectroscopy (HighRus-2009).

Rothschild, L. J. and Mancinelli, R. L. (2001). Life in extreme environments. *Nature*, 409(6823):1092–1101.

Rushby, A. J., Johnson, M., Mills, B. J. W., Watson, A. J., and Claire, M. W. (2018). Long-Term Planetary Habitability and the Carbonate-Silicate Cycle. *Astrobiology*, 18(5):469–480.

Salpeter, E. E. and Zapolsky, H. S. (1967). Theoretical High-Pressure Equations of State including Correlation Energy. *Physical Review*, 158(3):876–886.

Santra, B., Klimeš, J., Alfe, D., Tkatchenko, A., Slater, B., Michaelides, A., Car, R., and Scheffler, M. (2011). Hydrogen bonds and van der waals forces in ice at ambient and high pressures. *Physical review letters*, 107(18):185701.

Saumon, D., Chabrier, G., and van Horn, H. M. (1995). An Equation of State for Low-Mass Stars and Giant Planets. *ApJS*, 99:713.

Schaack, S., Ranieri, U., Depondt, P., Gaal, R., Kuhs, W. F., Gillet, P., Finocchi, F., and Bove, L. E. (2019). Observation of methane filled hexagonal ice stable up to 150 GPa. *Proceedings of the National Academy of Science*, 116(33):16204–16209.

Schaefer, L. and Fegley, B. (2017). Redox states of initial atmospheres outgassed on rocky planets and planetesimals. *ApJ*, 843(2):120.

Schaefer, L., Wordsworth, R. D., Berta-Thompson, Z., and Sasselov, D. (2016). Predictions of the atmospheric composition of gj 1132b. *ApJ*, 829(2):63.

Scheibe, L., Nettelmann, N., and Redmer, R. (2021). Thermal evolution of Uranus and Neptune. II. Deep thermal boundary layer. *A&A*, 650:A200.

Schlawin, E., Ohno, K., Bell, T. J., Murphy, M. M., Welbanks, L., Beatty, T. G., Greene, T. P., Fortney, J. J., Parmentier, V., Edelman, I. R., Gill, S., Anderson, D. R., Wheatley, P. J., Henry, G. W., Mehta, N., Kreidberg, L., and Rieke, M. J. (2024). Possible Carbon Dioxide above the Thick Aerosols of GJ 1214 b. *ApJL*, 974(2):L33.

Schlichting, H. E. and Young, E. D. (2022). Chemical Equilibrium between Cores, Mantles, and Atmospheres of Super-Earths and Sub-Neptunes and Implications for Their Compositions, Interiors, and Evolution. *The Planetary Science Journal*, 3(5):127. Publisher: IOP Publishing.

Seager, S., Kuchner, M., Hier-Majumder, C. A., and Militzer, B. (2007). Mass-Radius Relationships for Solid Exoplanets. *ApJ*, 669(2):1279–1297.

Selsis, F., Kasting, J. F., Levrard, B., Paillet, J., Ribas, I., and Delfosse, X. (2007). Habitable planets around the star Gliese 581? *A&A*, 476(3):1373–1387.

Shah, O., Alibert, Y., Helled, R., and Mezger, K. (2021). Internal water storage capacity of terrestrial planets and the effect of hydration on the M-R relation. *A&A*, 646:A162.

Shields, A. L., Ballard, S., and Johnson, J. A. (2016). The habitability of planets orbiting M-dwarf stars. *Phys. Rep.*, 663:1.

Shorttle, O., Jordan, S., Nicholls, H., Lichtenberg, T., and Bower, D. J. (2024). Distinguishing Oceans of Water from Magma on Mini-Neptune K2-18b. *ApJL*, 962(1):L8.

Silver, L. A., Ihinger, P. D., and Stolper, E. (1990). The influence of bulk composition on the speciation of water in silicate glasses. *Contributions to Mineralogy and Petrology*, 104(2):142–162.

Snellen, I. A. G., de Kok, R. J., de Mooij, E. J. W., and Albrecht, S. (2010). The orbital motion, absolute mass and high-altitude winds of exoplanet HD209458b. *Nature*, 465(7301):1049–1051.

Snellen, I. A. G., de Mooij, E. J. W., and Albrecht, S. (2009). The changing phases of extrasolar planet CoRoT-1b. *Nature*, 459(7246):543–545.

Sossi, P. A., Tollan, P. M. E., Badro, J., and Bower, D. J. (2023). Solubility of water in peridotite liquids and the prevalence of steam atmospheres on rocky planets. *Earth and Planetary Science Letters*, 601:117894.

Sotin, C., Grasset, O., and Mocquet, A. (2007). Mass radius curve for extrasolar Earth-like planets and ocean planets. *Icarus*, 191(1):337–351.

Soubiran, F. and Militzer, B. (2015). Miscibility Calculations for Water and Hydrogen in Giant Planets. *ApJ*, 806(2):228.

Stefánsson, G., Mahadevan, S., Winn, J. N., Marcussen, M. L., Kanodia, S., Albrecht, S., Fitzmaurice, E., Mikulskytė, O., Cañas, C. I., Espinoza-Retamal, J. I., Zwart, Y., Krolikowski, D. M., Hotnisky, A., Robertson, P., Alvarado-Montes, J. A., Bender, C. F., Blake, C. H., Callingham, J. R., Cochran, W. D., Delamer, M., Diddams, S. A., Dong, J., Fernandes, R. B., Giovinazzi, M. R., Halverson, S., Libby-Roberts, J., Logsdon, S. E., McElwain, M. W., Ninan, J. P., Rajagopal, J., Reji, V., Roy, A., Schwab, C., and Wright, J. T. (2025). Gaia-4b and 5b: Radial Velocity Confirmation of Gaia Astrometric Orbital Solutions Reveal a Massive Planet and a Brown Dwarf Orbiting Low-mass Stars. *AJ*, 169(2):107.

Stevenson, K. B., Désert, J.-M., Line, M. R., Bean, J. L., Fortney, J. J., Showman, A. P., Kataria, T., Kreidberg, L., McCullough, P. R., Henry, G. W., Charbonneau, D., Burrows, A., Seager, S., Madhusudhan, N., Williamson, M. H., and Homeier, D. (2014). Thermal structure of an exoplanet atmosphere from phase-resolved emission spectroscopy. *Science*, 346(6211):838–841.

Stixrude, L. and Lithgow-Bertelloni, C. (2011). Thermodynamics of mantle minerals - II. Phase equilibria. *Geophysical Journal International*, 184(3):1180–1213.

Stock, J. W., Kitzmann, D., and Patzer, A. B. C. (2022). FASTCHEM 2 : an improved computer program to determine the gas-phase chemical equilibrium composition for arbitrary element distributions. *MNRAS*, 517(3):4070–4080.

Stock, J. W., Kitzmann, D., Patzer, A. B. C., and Sedlmayr, E. (2018). FastChem: A computer program for efficient complex chemical equilibrium calculations in the neutral/ionized gas phase with applications to stellar and planetary atmospheres. *MNRAS*, 479(1):865–874.

Stolper, E. (1982). The speciation of water in silicate melts. *Geochimica et Cosmochimica Acta*, 46(12):2609–2620.

Suer, T.-A., Jackson, C., Grewal, D. S., Dalou, C., and Lichtenberg, T. (2023). The distribution of volatile elements during rocky planet formation. *Frontiers in Earth Science*, 11:1159412.

Tamayo, D., Rein, H., Petrovich, C., and Murray, N. (2017). Convergent Migration Renders TRAPPIST-1 Long-lived. *ApJL*, 840(2):L19.

Tashkun, S. A., Perevalov, V. I., Gamache, R. R., and Lamouroux, J. (2015). CDSD-296, high resolution carbon dioxide spectroscopic databank: Version for atmospheric applications. *J. Quant. Spectrosc. Radiat. Transf.*, 152:45–73.

Terquem, C. and Papaloizou, J. C. B. (2007). Migration and the Formation of Systems of Hot Super-Earths and Neptunes. *ApJ*, 654(2):1110–1120.

Teske, J., Batalha, N. E., Wallack, N. L., Kirk, J., Wogan, N. F., Gordon, T. A., Alam, M. K., Aguichine, A., Wolfgang, A., Wakeford, H. R., Scarsdale, N., Adams Redai, J., Moran, S. E., López-Morales, M., Meech, A., Gao, P., Batalha, N. M., Alderson, L., and Gagnebin, A. (2025). JWST COMPASS: NIRSpec/G395H Transmission Observations of TOI-776 c, a 2 $R_\oplus$ M Dwarf Planet. *AJ*, 169(5):249.

Thomas, C. W. and Asimow, P. D. (2013). Direct shock compression experiments on premolten forsterite and progress toward a consistent high-pressure equation of state for CaO-MgO-Al_2O_3-SiO_2-FeO liquids. *Journal of Geophysical Research (Solid Earth)*, 118(11):5738–5752.

Thomas, S. W. and Madhusudhan, N. (2016). In hot water: effects of temperature-dependent interiors on the radii of water-rich super-Earths. *MNRAS*, 458(2):1330–1344.

Tian, M. and Heng, K. (2024). Atmospheric Chemistry of Secondary and Hybrid Atmospheres of Super Earths and Sub-Neptunes. *ApJ*, 963(2):157.

Trainer, M. G., Pavlov, A. A., Dewitt, H. L., Jimenez, J. L., McKay, C. P., Toon, O. B., and Tolbert, M. A. (2006). Inaugural Article: Organic haze on Titan and the early Earth. *Proceedings of the National Academy of Science*, 103(48):18035–18042.

Tremblay, L., Line, M. R., Stevenson, K., Kataria, T., Zellem, R. T., Fortney, J. J., and Morley, C. (2020). The Detectability and Constraints of Biosignature Gases in the Near- and Mid-infrared from Transit Transmission Spectroscopy. *AJ*, 159(3):117.

Tsai, S.-M., Innes, H., Lichtenberg, T., Taylor, J., Malik, M., Chubb, K., and Pierrehumbert, R. (2021). Inferring Shallow Surfaces on Sub-Neptune Exoplanets with JWST. *ApJL*, 922(2):L27.

Tsai, S.-M., Innes, H., Wogan, N. F., and Schwieterman, E. W. (2024). Biogenic sulfur gases as biosignatures on temperate sub-Neptune waterworlds. *arXiv e-prints*, page arXiv:2403.14805.

Tsiaras, A., Waldmann, I. P., Tinetti, G., Tennyson, J., and Yurchenko, S. N. (2019). Water vapour in the atmosphere of the habitable-zone eight-Earth-mass planet K2-18 b. *Nature Astronomy*, 3:1086–1091.

Underwood, D. S., Tennyson, J., Yurchenko, S. N., Huang, X., Schwenke, D. W., Lee, T. J., Clausen, S., and Fateev, A. (2016). ExoMol molecular line lists - XIV. The rotation-vibration spectrum of hot SO_2. *MNRAS*, 459(4):3890–3899.

Valencia, D., Guillot, T., Parmentier, V., and Freedman, R. S. (2013). Bulk Composition of GJ 1214b and Other Sub-Neptune Exoplanets. *ApJ*, 775(1):10.

Valencia, D., O'Connell, R. J., and Sasselov, D. (2006). Internal structure of massive terrestrial planets. *Icarus*, 181(2):545–554.

Valencia, D., Sasselov, D. D., and O'Connell, R. J. (2007a). Detailed Models of Super-Earths: How Well Can We Infer Bulk Properties? *ApJ*, 665(2):1413–1420.

Valencia, D., Sasselov, D. D., and O'Connell, R. J. (2007b). Radius and Structure Models of the First Super-Earth Planet. *ApJ*, 656(1):545–551.

Valenti, J. A. and Fischer, D. A. (2005). Spectroscopic Properties of Cool Stars (SPOCS). I. 1040 F, G, and K Dwarfs from Keck, Lick, and AAT Planet Search Programs. *ApJS*, 159(1):141–166.

Van Eylen, V., Agentoft, C., Lundkvist, M. S., Kjeldsen, H., Owen, J. E., Fulton, B. J., Petigura, E., and Snellen, I. (2018). An asteroseismic view of the radius valley: stripped cores, not born rocky. *MNRAS*, 479(4):4786–4795.

Van Eylen, V., Astudillo-Defru, N., Bonfils, X., Livingston, J., Hirano, T., Luque, R., Lam, K. W. F., Justesen, A. B., Winn, J. N., Gandolfi, D., Nowak, G., Palle, E., Albrecht, S., Dai, F., Campos Estrada, B., Owen, J. E., Foreman-Mackey, D., Fridlund, M., Korth, J., Mathur, S., Forveille, T., Mikal-Evans, T., Osborne, H. L. M., Ho, C. S. K., Almenara, J. M., Artigau, E., Barragán, O., Barros, S. C. C., Bouchy, F., Cabrera, J., Caldwell, D. A., Charbonneau, D., Chaturvedi, P., Cochran, W. D., Csizmadia, S., Damasso, M., Delfosse, X., De Medeiros, J. R., Díaz, R. F., Doyon, R., Esposito, M., Fűrész, G., Figueira, P., Georgieva, I., Goffo, E., Grziwa, S., Guenther, E., Hatzes, A. P., Jenkins, J. M., Kabath, P., Knudstrup, E., Latham, D. W., Lavie, B., Lovis, C., Mennickent, R. E., Mullally, S. E., Murgas, F., Narita, N., Pepe, F. A., Persson, C. M., Redfield, S., Ricker, G. R., Santos, N. C., Seager,

S., Serrano, L. M., Smith, A. M. S., Suárez Mascareño, A., Subjak, J., Twicken, J. D., Udry, S., Vanderspek, R., and Zapatero Osorio, M. R. (2021). Masses and compositions of three small planets orbiting the nearby M dwarf L231-32 (TOI-270) and the M dwarf radius valley. *MNRAS*, 507(2):2154–2173.

Vazan, A., Sari, R., and Kessel, R. (2022). A New Perspective on the Interiors of Ice-rich Planets: Ice-Rock Mixture Instead of Ice on Top of Rock. *ApJ*, 926(2):150.

Venot, O., Hébrard, E., Agúndez, M., Dobrijevic, M., Selsis, F., Hersant, F., Iro, N., and Bounaceur, R. (2012). A chemical model for the atmosphere of hot Jupiters. *A&A*, 546:A43.

Venturini, J., Alibert, Y., and Benz, W. (2016). Planet formation with envelope enrichment: new insights on planetary diversity. *A&A*, 596:A90.

Venturini, J., Guilera, O. M., Haldemann, J., Ronco, M. P., and Mordasini, C. (2020). The nature of the radius valley. Hints from formation and evolution models. *A&A*, 643:L1.

Venturini, J. and Helled, R. (2017). The Formation of Mini-Neptunes. *ApJ*, 848(2):95.

Venturini, J., Ronco, M. P., Guilera, O. M., Haldemann, J., Mordasini, C., and Miller Bertolami, M. (2024). A fading radius valley towards M dwarfs, a persistent density valley across stellar types. *A&A*, 686:L9.

Vinet, P., Rose, J. H., Ferrante, J., and Smith, J. R. (1989). Universal features of the equation of state of solids. *Journal of Physics Condensed Matter*, 1(11):1941–1963.

Visscher, C. and Moses, J. I. (2011). Quenching of Carbon Monoxide and Methane in the Atmospheres of Cool Brown Dwarfs and Hot Jupiters. *ApJ*, 738(1):72.

von Bloh, W., Bounama, C., Cuntz, M., and Franck, S. (2007). The habitability of super-Earths in Gliese 581. *A&A*, 476(3):1365–1371.

Wagner, F. W., Tosi, N., Sohl, F., Rauer, H., and Spohn, T. (2012). Rocky super-Earth interiors. Structure and internal dynamics of CoRoT-7b and Kepler-10b. *A&A*, 541:A103.

Wagner, W. and Pruß, A. (2002). The IAPWS Formulation 1995 for the Thermodynamic Properties of Ordinary Water Substance for General and Scientific Use. *Journal of Physical and Chemical Reference Data*, 31(2):387–535.

Wahl, S. M., Hubbard, W. B., Militzer, B., Guillot, T., Miguel, Y., Movshovitz, N., Kaspi, Y., Helled, R., Reese, D., Galanti, E., Levin, S., Connerney, J. E., and Bolton, S. J. (2017). Comparing Jupiter interior structure models to Juno gravity measurements and the role of a dilute core. *Geophys. Res. Lett.*, 44(10):4649–4659.

Wallack, N. L., Batalha, N. E., Alderson, L., Scarsdale, N., Adams Redai, J. I., Aguichine, A., Alam, M. K., Gao, P., Wolfgang, A., Batalha, N. M., Kirk, J., López-Morales, M., Moran, S. E., Teske, J., Wakeford, H. R., and Wogan, N. F. (2024). Jwst compass: A nirspec/g395h transmission spectrum of the sub-neptune toi-836c. *AJ*, 168(2):77.

Welbanks, L., Nixon, M. C., McGill, P., Tilke, L. J., Wiser, L. S., Rotman, Y., Mukherjee, S., Feinstein, A., Line, M. R., Seager, S., Beatty, T. G., Seligman, D. Z., Parmentier, V., and Sing, D. (2025). The Challenges of Detecting Gases in Exoplanet Atmospheres. *arXiv e-prints*, page arXiv:2504.21788.

Winn, J. N., Matthews, J. M., Dawson, R. I., Fabrycky, D., Holman, M. J., Kallinger, T., Kuschnig, R., Sasselov, D., Dragomir, D., Guenther, D. B., Moffat, A. F. J., Rowe, J. F., Rucinski, S., and Weiss, W. W. (2011). A Super-Earth Transiting a Naked-eye Star. *ApJL*, 737(1):L18.

Wogan, N. F., Batalha, N. E., Zahnle, K. J., Krissansen-Totton, J., Tsai, S.-M., and Hu, R. (2024). JWST Observations of K2-18b Can Be Explained by a Gas-rich Mini-Neptune with No Habitable Surface. *ApJL*, 963(1):L7.

Woitke, P., Helling, C., Hunter, G. H., Millard, J. D., Turner, G. E., Worters, M., Blecic, J., and Stock, J. W. (2018). Equilibrium chemistry down to 100 K. Impact of silicates and phyllosilicates on the carbon to oxygen ratio. *A&A*, 614:A1.

Wolszczan, A. and Frail, D. A. (1992). A planetary system around the millisecond pulsar PSR1257 + 12. *Nature*, 355(6356):145–147.

Woodland, A. B., Girnis, A. V., Bulatov, V. K., Brey, G. P., and Höfer, H. E. (2019). Experimental study of sulfur solubility in silicate–carbonate melts at 5–10.5 GPa. *Chemical Geology*, 505:12–22.

Wordsworth, R. D. (2016). Atmospheric nitrogen evolution on Earth and Venus. *Earth and Planetary Science Letters*, 447:103–111.

Wunderlich, F., Godolt, M., Grenfell, J. L., Städt, S., Smith, A. M. S., Gebauer, S., Schreier, F., Hedelt, P., and Rauer, H. (2019). Detectability of atmospheric features of Earth-like planets in the habitable zone around M dwarfs. *A&A*, 624:A49.

Xue, Q., Bean, J. L., Zhang, M., Mahajan, A., Ih, J., Eastman, J. D., Lunine, J., Mansfield, M. W., Coy, B. P., Kempton, E. M. R., Koll, D., and Kite, E. (2024). JWST Thermal Emission of the Terrestrial Exoplanet GJ 1132b. *ApJL*, 973(1):L8.

Yang, J., Cowan, N. B., and Abbot, D. S. (2013). Stabilizing Cloud Feedback Dramatically Expands the Habitable Zone of Tidally Locked Planets. *ApJL*, 771(2):L45.

Yang, J. and Hu, R. (2024). Chemical mapping of temperate sub-neptune atmospheres: Constraining the deep interior h_2o/h_2 ratio from the atmospheric co_2/ch_4 ratio. *ApJL*, 971(2):L48.

Yoshioka, T., Nakashima, D., Nakamura, T., Shcheka, S., and Keppler, H. (2019). Carbon solubility in silicate melts in equilibrium with a CO-CO_2 gas phase and graphite. *Geochimica et Cosmochimica Acta*, 259:129–143.

Young, E. D., Stixrude, L., Rogers, J. G., Schlichting, H. E., and Marcum, S. P. (2024). Phase Equilibria of Sub-Neptunes and Super-Earths. *Planetary Science Journal*, 5(12):268.

Young, E. D., Werlen, A., Marcum, S. P., and Dullemond, C. P. (2025). Differentiation, the exception not the rule – Evidence for full miscibility in sub-Neptune interiors. *arXiv e-prints*, page arXiv:2507.00947.

Yu, X., Moses, J. I., Fortney, J. J., and Zhang, X. (2021). How to Identify Exoplanet Surfaces Using Atmospheric Trace Species in Hydrogen-dominated Atmospheres. *ApJ*, 914(1):38.

Yurchenko, S. N., Barber, R. J., and Tennyson, J. (2011). A variationally computed line list for hot NH_3. *MNRAS*, 413(3):1828–1834.

Yurchenko, S. N. and Tennyson, J. (2014). ExoMol line lists – IV. The rotation–vibration spectrum of methane up to 1500 K. *MNRAS*, 440(2):1649–1661.

Zajacz, Z., Candela, P. A., Piccoli, P. M., Sanchez-Valle, C., and Wälle, M. (2013). Solubility and partitioning behavior of Au, Cu, Ag and reduced S in magmas. *Geochimica et Cosmochimica Acta*, 112:288–304.

Zapolsky, H. S. and Salpeter, E. E. (1969). The Mass-Radius Relation for Cold Spheres of Low Mass. *ApJ*, 158:809.

Zeng, L., Jacobsen, S. B., Sasselov, D. D., Petaev, M. I., Vanderburg, A., Lopez-Morales, M., Perez-Mercader, J., Mattsson, T. R., Li, G., Heising, M. Z., Bonomo, A. S., Damasso, M., Berger, T. A., Cao, H., Levi, A., and Wordsworth, R. D. (2019). Growth model interpretation of planet size distribution. *Proceedings of the National Academy of Science*, 116(20):9723–9728.

Zeng, L. and Sasselov, D. (2013). A Detailed Model Grid for Solid Planets from 0.1 through 100 Earth Masses. *PASP*, 125(925):227.

Zhao, Y., Ni, D., and Liu, Z. (2023). Machine-learning Inferences of the Interior Structure of Rocky Exoplanets from Bulk Observational Constraints. *ApJS*, 269(1):1.

Appendix A

Supplementary Information for Chapter 3

A.1 Availability of Solubility Laws

We first discuss the availability of silicate melt solubility laws for the volatile species of interest, at the chemical and physical conditions relevant for magma oceans on temperate sub-Neptunes in the gas dwarf scenario. These findings motivate our choices for the solubility laws adopted in Chapter 3[1]. We compile a bibliography of the solubility laws consulted for the preparation of this chapter in Table A.1, and show a selection of them in Figure A.1. For most composition-dependent laws, we adopt a basalt composition for the melt – specifically, when a law explicitly depends on melt composition parameters, we set these to the values corresponding to the Mt Etna basalt from Iacono-Marziano et al. (2012). This choice is due to the wide availability of solubility laws for basaltic melt, and the association of basalt with peridotite, which we adopt as the mantle composition in the internal structure modelling.

A.1.1 Nitrogen Species

The solubility of N_2 has been explored for a wide range of parameters (e.g., Libourel et al., 2003; Miyazaki et al., 2004; Roskosz et al., 2013; Mallik et al., 2018; Boulliung et al., 2020; Bernadou et al., 2021; Gao et al., 2022), at pressures up to 14.8 GPa and temperatures up to 2800 K (Roskosz et al., 2013). By compiling the available data at $P \leq 8.2$ GPa and adding their own measurements, Dasgupta et al. (2022) proposed the solubility law which we use in our calculations. However, this law does

[1]This chapter and these relevant appendices are adapted from Rigby et al. (2024).

not appear to extrapolate well at higher pressures and moderately reduced conditions ($f_{O_2} \sim \mathrm{IW} - 2$). As warned by Dasgupta et al. (2022), experimental data indicate the solubility seems to reach a plateau, while the law predicts solubility to monotonically increase with pressure. A direct comparison with the data points of Roskosz et al. (2013) at 10 GPa and 14.8 GPa reveals a true solubility ∼1 order of magnitude lower than predicted using the Dasgupta et al. (2022) law for pure nitrogen vapour. At the extremely reduced conditions explored in Chapter 3, the plateau effect is expected to already be significant at lower pressures (Dasgupta et al., 2022).

It is also noteworthy that Gao et al. (2022) – whose data was included in the Dasgupta et al. (2022) dataset – find some indication of a decrease in the physical solubility of N_2 already at 8 GPa. Physical solubility is expected to be the dominant solubility mechanism at the oxidized conditions explored by Gao et al. (2022), as opposed to the chemical solubility relevant at reduced conditions (Libourel et al., 2003). Nevertheless, as the relevant quantity is not the total pressure but rather the nitrogen partial pressure, we believe that the Dasgupta et al. (2022) law remains a reasonably good approximation even at the reducing, high-pressure conditions at the magma-atmosphere interface, given that the expected N_2 mixing ratio in the atmosphere is $\lesssim 10^{-4}$ in the present models.

The lack of data or simulations for the solubility of NH_3 in silicate melt leads us to neglect it, with the caveat that this will lead to our calculations setting only an upper limit on the abundance of N-bearing species in the atmosphere.

A.1.2 Carbon Species

Of the three prominent carbon species (CO_2, CO, CH_4), CO_2 is by far the one for which the most complete experimental data on solubility in magma is available (e.g. Pan et al., 1991; Dixon et al., 1995; Papale et al., 2006; Iacono-Marziano et al., 2012). Considering this wide dataset, for the case of $T = 2273$ K and a bulk silicate Earth (BSE) melt composition, Suer et al. (2023) find that the solubility of CO_2 is well-approximated by Henry's Law, which they fit to the data. The law of Suer et al. (2023) is in excellent agreement with high pressure ($P \geq 8$ GPa) molecular dynamics simulations by Guillot and Sator (2011) for the $T = 2273$ K and rhyolite case, and is in good agreement with the corresponding mid-ocean ridge basalt (MORB) case. Interestingly, the agreement is slightly worse with the kimberlite melt case, where instead the melt is closest to the BSE composition.

At lower pressures, the agreement with the simulations is worse, but still within a factor of order unity. In any case, the agreement between Suer et al. (2023)'s law

and Guillot and Sator (2011)'s simulations is always satisfactory, which also highlights the weak dependence of the solubility of CO_2 on the melt composition, particularly at $P \leq 8$ GPa (Guillot and Sator, 2011). Despite the fact that the Suer et al. (2023) law is intended for lower temperatures than those relevant in this chapter, due to the lack of more appropriate alternatives we adopt it in our calculations.

For CO, there is a lack of solubility data at high pressure and temperature. Solubility laws are provided by, e.g., Armstrong et al. (2015) and Yoshioka et al. (2019) (for both MORB and rhyolite melts), both of which carried out experiments at $P \sim 1$ GPa and $T \sim 1500$°C. The lack of data may be explained by the fact that exploring the solubility of CO at high pressures is especially complicated because the $2CO = C + CO_2$ reaction gets skewed to the right as pressure grows, making an initially pure CO vapour spontaneously become mostly CO_2 at $P \gtrsim 1$ GPa (Yoshioka et al., 2019).

An alternative prescription, as used by Schlichting and Young (2022), informed by Hirschmann (2016), is to set the solubility of CO to be one third of that of CO_2. This method, taking the Suer et al. (2023) BSE law for the CO_2 solubility, yields a CO solubility significantly higher than any of the other laws mentioned so far. This might be due to Suer et al. (2023)'s law being tested for different temperatures and melt compositions. However, this seems unlikely: the solubility of CO is only weakly dependent on temperature (Yoshioka et al., 2019), although Yoshioka et al. (2019)'s two laws for MORB and rhyolite yield results less than an order of magnitude apart. This indicates a comparatively weak dependence of solubility on melt composition, while Schlichting and Young (2022)'s prescription applied to Suer et al. (2023)'s law results in a solubility between 1 and 2 orders of magnitude higher, depending on the pressure.

Ultimately, we use the Yoshioka et al. (2019) MORB law in our calculations, due to it being more recent and calibrated at higher pressures than Armstrong et al. (2015).

The data on CH_4 seems to be even sparser: we encountered only one in the literature from Ardia et al. (2013), which we use in this work. This solubility law results from experiments at $0.7 \leq P \leq 3$ GPa and $1400 \leq T \leq 1450$°C, and the Henry's Law fit to their data by Lichtenberg et al. (2021) – indeed, the law by Ardia et al. (2013) follows Henry's law for total pressures $P \lesssim 10^4$ bar (at $T = 3000$ K, regardless of the CH_4 partial pressure).

A.1.3 Other Volatiles

The other major volatiles of note are expected to be sulfur species, water, and H_2. Helium is also expected, however as a noble gas it has no impact on the atmospheric chemistry.

Chemical equilibrium calculations indicate that, at conditions relevant to the magma-atmosphere interface, sulfur will be mostly in H_2S, with little S_2. For S_2 we use the law by Gaillard et al. (2022). It should be noted that this law is calibrated only with data collected at atmospheric pressure, relatively low temperature ($T \leq 1673$ K), and not very reducing conditions ($\Delta\text{IW} \geq -1$). As such, its extrapolation to the extreme conditions explored in this paper should be considered only as a zeroth-order estimate of the true solubility. No significant high-pressure/high-temperature data to compare with the Gaillard et al. (2022) predictions were found, the Woodland et al. (2019) high-pressure data being for a carbonate-silicate melt.

For H_2S, we found two laws in the literature, by Clemente et al. (2004) for rhyolite and by Lesne et al. (2015) for basaltic melts. The former is calibrated for $1073 \leq T \leq 1273$ K and $P = 2 \times 10^3$ bar, while the latter for $1323 \leq T \leq 1473$ K and $250 \leq P \leq 2 \times 10^3$ bar. The two laws differ significantly in their temperature dependence: Clemente et al. (2004) find that the solubility of H_2S moderately increases with increasing temperature, while the law by Lesne et al. (2015) indicates an extremely strong and negative temperature dependence. Furthermore, Lesne et al. (2015) include a dependence on the mole fraction of FeO in the magma, while the law by Clemente et al. (2004) only depends on thermodynamic parameters. However, when extrapolated to high temperature ($T \sim 3000$ K) and pressure ($P \sim 10^5$ bar), both laws predict negligibly small solubility for H_2S at the expected mixing ratios (shown in Figure 3.7). Hence, we do not expect the results of our investigation to be noticeably impacted by the choice of one law over the other. In this work, we use the law by Clemente et al. (2004).

For H_2, the law most used in the literature is by Hirschmann et al. (2012), who carry out experiments at $0.7 \leq P \leq 3$ GPa and $1400 \leq T \leq 1500$°C, and give two expressions, for basaltic and andesitic melt. Their law for basaltic melt is in excellent agreement with that given by Suer et al. (2023) for BSE melt up to $P \sim 1$ GPa, and so is, to a slightly lesser extent, their andesitic melt law. However, they diverge at higher pressures, with Suer et al. (2023) predicting Henrian behaviour to arbitrary pressure, while Hirschmann et al. (2012) predict a decline in solubility as pressure increases, consistently with their experimental results. As the laws given in Hirschmann et al.

(2012) have a robust high-pressure experimental background, we use their basaltic melt case.

For H_2O, there is a great deal of experimental data on the solubility in silicate melts (e.g., Stolper, 1982; Silver et al., 1990; Moore et al., 1995; Dixon et al., 1995; Papale et al., 2006; Iacono-Marziano et al., 2012; Sossi et al., 2023), a complete review of which is beyond the scope of this work. We focus here on two solubility laws: Sossi et al. (2023), the most recent law available, and Iacono-Marziano et al. (2012), which is the one we choose to implement in our study. Sossi et al. (2023) provide two slightly different estimates depending on the value of the molar absorption coefficient ϵ_{3550}, each depending linearly on the square roots of the atmospheric fugacities of both water and molecular hydrogen. These are the result of experiments carried out at very low pressure ($P = 1$ atm) and high temperature ($T = 2173$ K).

Higher-pressure experiments are carried out in Iacono-Marziano et al. (2012), who also propose a solubility law. This is calibrated using a vast but low-temperature experimental database ($10^2 \leq P \leq 10^4$ bar, $1100 \leq T \leq 1400$°C), which is in rough agreement with that of Sossi et al. (2023) for an H_2-rich envelope. However, the fact that the Sossi et al. (2023) law depends on a linear combination of the square roots of the fugacities of both H_2 and H_2O risks breaking element conservation for oxygen. It would predict some dissolved O in the magma even if no O is present – in any species – in the initial atmospheric composition. This effect is expected to be particularly relevant at the very reduced conditions explored here, where the abundance of O is expected to be low.

We thus consider extrapolating the law of Iacono-Marziano et al. (2012) to higher temperatures to be a more accurate prescription than extrapolating that by Sossi et al. (2023) to high pressures. We do so assuming an Etna basalt composition for the melt. This choice is also consistent with that in Gaillard et al. (2022).

A.1.4 Summary

Data on solubility in silicate melt are available at some conditions for several species of interest, with the one exception being NH_3, for which we were unable to find any solubility laws. We list the bibliography on solubility laws and/or data points we have explored for this study in Table A.1, and we show a selection of them in Figure A.1. The scenario explored in Chapter 3, for magma oceans on temperate gas dwarf sub-Neptunes, is extreme in three ways: it leads to high temperatures ($T \gtrsim 2500$ K), high pressures ($P \gtrsim 10^5$ bar), and very reduced melts compared to Earth ($\Delta\text{IW} \lesssim -5$). There is no data for any species at such conditions in all three ways. Only for N_2 does

Species	Reference	Temperature (K)	Pressure (bar)
N_2	Dasgupta et al. (2022)	$1323 \leq T \leq 2700$	$1 \leq P \leq 8.2 \times 10^4$
	Gao et al. (2022)	$1473 \leq T \leq 1873$	$3 \times 10^3 \leq P \leq 8 \times 10^4$
	Bernadou et al. (2021)	$1473 \leq T \leq 1573$	$8 \times 10^2 \leq P \leq 10^4$
	Boulliung et al. (2020)	$T = 1698$	$P = 1$
	Mallik et al. (2018)	$1323 \leq T \leq 1573$	$2 \times 10^4 \leq P \leq 4 \times 10^4$
	Roskosz et al. (2013)	$2500 \leq T \leq 2800$	$1.8 \times 10^4 \leq P \leq 1.48 \times 10^5$
	Miyazaki et al. (2004)	$1573 \leq T \leq 1823$	$1 \leq P \leq 2 \times 10^3$
	Libourel et al. (2003)	$1673 \leq T \leq 1698$	$P = 1$
CO_2	Suer et al. (2023)	$T = 2273$	$1 \leq P \leq 10^2$
	Guillot and Sator (2011)[a]	$1473 \leq T \leq 2273$	$10^3 \leq P \leq 1.5 \times 10^5$
	Pan et al. (1991)	$1443 \leq T \leq 1873$	$10^3 \leq P \leq 1.5 \times 10^4$
CO_2 & H_2O	Iacono-Marziano et al. (2012)	$1373 \leq T \leq 1673$	$10^2 \leq P \leq 10^4$
	Papale et al. (2006)	$1073 \leq T \leq 1973$	$191 \leq P \leq 3.5 \times 10^4$
	Dixon et al. (1995)	$T = 1473$	$2.01 \times 10^2 \leq P \leq 9.8 \times 10^2$
H_2O	Sossi et al. (2023)	$T = 2173$	$P = 1$
	Moore et al. (1995)	$973 \leq T \leq 1473$	$1 \leq P \leq 2 \times 10^3$
	Silver et al. (1990)	$1123 \leq T \leq 1723$	$49 \leq P \leq 2 \times 10^4$
CO	Yoshioka et al. (2019)	$1473 \leq T \leq 1873$	$2.08 \times 10^3 \leq P \leq 3 \times 10^4$
	Armstrong et al. (2015)	$T = 1673$	$P = 1.2 \times 10^4$
CH_4	Ardia et al. (2013)	$1673 \leq T \leq 1723$	$7 \times 10^3 \leq P \leq 3 \times 10^4$
S_2	Boulliung and Wood (2023)	$1473 \leq T \leq 1773$	$P = 1$
	Gaillard et al. (2022)[b]	$1073 \leq T \leq 1673$	$P = 1$
	Woodland et al. (2019)[c]	$1673 \leq T \leq 1873$	$5 \times 10^4 \leq P \leq 1.05 \times 10^5$
	O'Neill and Mavrogenes (2002)	$T = 1673$	$P = 1$
H_2S	Lesne et al. (2015)	$1323 \leq T \leq 1473$	$250 \leq P \leq 2 \times 10^3$
H_2S & SO_2	Clemente et al. (2004)	$1073 \leq T \leq 1273$	$P = 2 \times 10^3$
H_2	Hirschmann et al. (2012)	$1673 \leq T \leq 1773$	$7 \times 10^3 \leq P \leq 3 \times 10^4$

Table A.1 Sources of solubility data and laws considered in Chapter 3. The (total) pressure and temperature ranges indicated are those corresponding to the experiments carried out in the respective studies, or, if the studies calibrate a solubility law based on data from previous works, the range spanned by those.

[a]: Molecular dynamics simulation.

[b]: Gaillard et al. (2022) state that their law is calibrated against data obtained with gas at a pressure of one atmosphere. However, they refer to Zajacz et al. (2013), whose experiments were carried out at 200 MPa.

[c]: For carbonate-silicate melt.

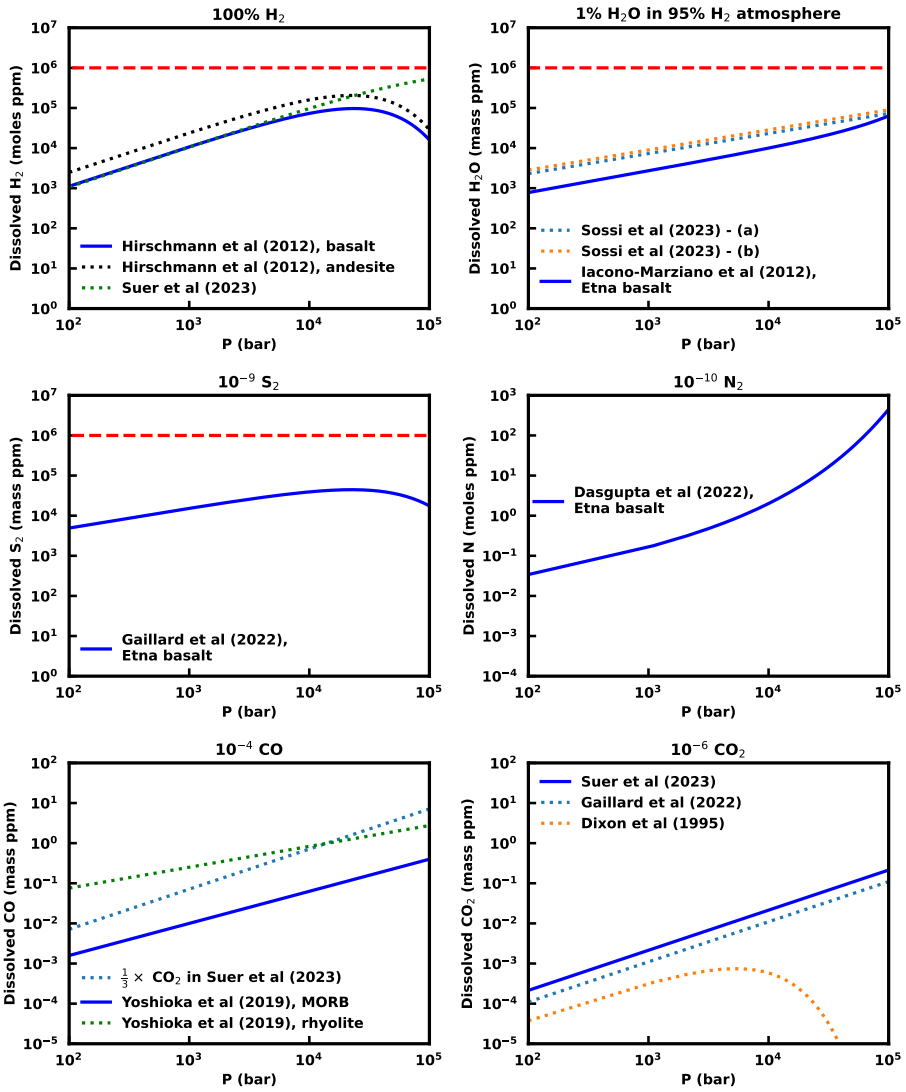

Fig. A.1 Behaviour of selected solubility laws in silicate melt for some prominent molecules. Solid blue lines indicate the laws used in this study. All temperature-dependent laws are shown here for $T = 3000$ K; the ΔIW-dependent N_2 and S_2 laws are shown for $\Delta\text{IW} = -6.4$; all laws with free composition-dependent parameters are shown for the Mt. Etna basalt composition (Iacono-Marziano et al., 2012). For H_2O, we label as (a) the law given in Sossi et al. (2023) for $\epsilon_{3550} = 6.3$ m^2/mol, and as (b) that for $\epsilon_{3550} = 5.1$ m^2/mol. The mixing ratio of each species, informed by Section 3.4.3, is indicated in the title of the respective subplot; the x-axis indicates total pressure. The gases are treated ideally, i.e. we take the fugacity of each species' to be equal to its partial pressure. We do not plot the CH_4 solubility, for which Ardia et al. (2013) – whose law we use – predicts a much lower value than the other carbon-bearing species, nor the solubility of H_2S, for which both Clemente et al. (2004) and Lesne et al. (2015) predict much lower solubility than for S_2

data at both very high temperature and pressure exists, but for relatively oxidised conditions (Roskosz et al., 2013). High-pressure ($P \geq 10^5$ bar) simulations exist for CO_2, but only at $T \leq 2273$ K. For S_2, for a co-existing fluid phase, high-pressure data only exists at low temperature, and only for carbonate-silicate melt (Woodland et al., 2019). All other species seem to lack high-pressure data.

Exploring this region of the parameter space, either experimentally or through simulations, will be crucial for improving our understanding of potential magma oceans in sub-Neptunes, and our ability to lift observational degeneracies with other possible internal structures.

A.2 Sensitivity to Atmospheric Parameters

As described in Section 3.4.5, we explore a range of values for three key atmospheric parameters that could influence the observable composition: the metallicity, the eddy diffusion coefficient K_{zz}, and the internal temperature T_{int}. Our canonical cases, shown in Figure 3.8, correspond to P-T profiles C2 and C3 with median metallicity of 50× solar, with and without elemental depletion respectively, and K_{zz} of 10^6 cm^{2}s^{-1} in the deep atmosphere. We investigate if a higher metallicity, a broader range of K_{zz} values and/or a higher T_{int} could better match the observed abundances than our canonical cases, for example with higher CO_2 abundance. We therefore consider models with higher metallicities of 100× solar and 300× solar, and two end-member scenarios of 10^4 cm^{2}s^{-1} and 10^8 cm^{2}s^{-1} for K_{zz} in the deep, convective region. We also consider the effect of using a higher value of T_{int} of 60 K, as previously considered by Hu (2021). Disequilibrium effects due to photochemistry and vertical mixing are included in all cases discussed here.

We start with investigating departures from the canonical C2 case, as shown in Figure 3.8. We first fix the K_{zz} profile to that used in the canonical case and vary the metallicity as described above. The resulting vertical mixing ratio profiles are shown in Figure A.2, along with those for 50× metallicity from Figure 3.8 for comparison. For both the 100× and 300× solar cases, the abundance of CO_2 remains lower than that of CO throughout the atmosphere, as for the 50× solar case. Similarly, the CO_2 and NH_3 abundances are inconsistent with the retrieved values in the photosphere, between ∼0.01-10 mbar, in all cases. Additionally, the CH_4 abundance for 300× solar metallicity is higher than the retrieved abundance.

Next we consider a range of K_{zz} values in the deep atmosphere, using the C2 P-T profile. We vary K_{zz} at $P > 0.5$ bar from 10^4 to 10^8 cm^{2}s^{-1}, with our canonical

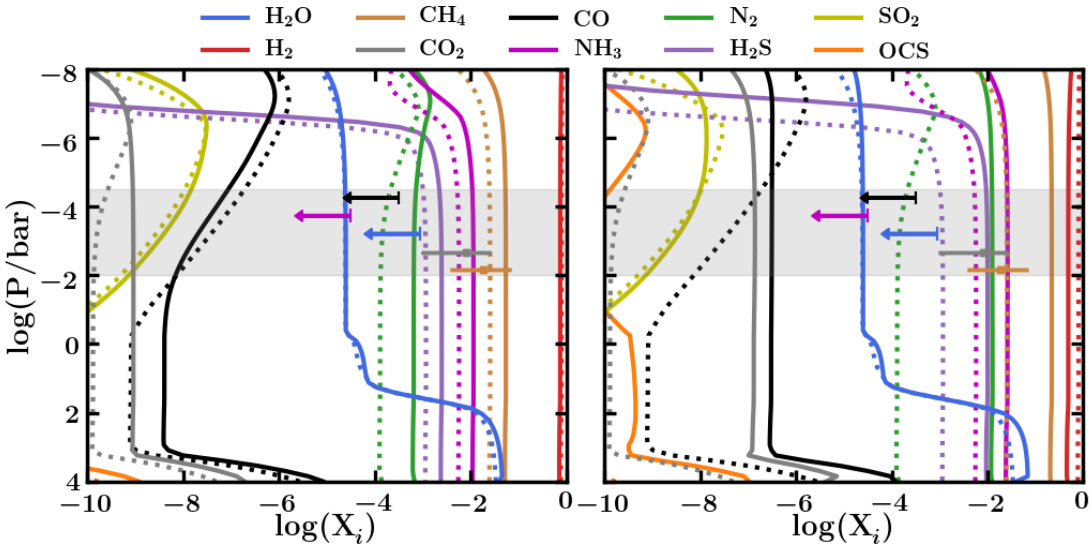

Fig. A.2 Effect of enhanced metallicity on the vertical mixing ratio profiles for several H-C-O-N-S molecular species with the C2 *P-T* profile. Dotted lines show the profile from the left-hand side of Figure 3.8, for C2 with 30% silicates, equivalent to 50× solar elemental abundances. Left: solid lines indicate the corresponding profiles for 100× solar metallicity. Right: solid lines indicate the corresponding profiles for 300× solar metallicity.

value at 10^6 cm^{2}s^{-1}. The metallicity remains fixed at the canonical value of 50× solar. As shown in Figure A.3, both the higher and lower K_{zz} values negligibly affect the computed mixing ratios at observable pressures. Increasing K_{zz} shifts the quench point to higher (deeper) pressures, as shown by the mixing ratio profile for CO_2 in the right-hand panel of Figure A.3.

We now consider the hotter *P-T* profile case with NH_3 depletion due to magma; this is the C3 profile with 30% silicates, as discussed above. The higher metallicities of 100× and 300× solar are implemented by proportionately enhancing the canonical elemental abundances for this case. These originally corresponded to 50× solar, hence we increase the relevant elemental abundances in Table 3.1 by factors of 2 and 6, respectively. The results are shown in Figure A.4. As for the C2 profile, the predicted CO_2 abundance remains significantly below the retrieved value in both cases, with the CO mixing ratio exceeding that of CO_2 throughout the atmosphere. The CH_4 abundance for 300× solar metallicity is additionally too high compared to the retrieved abundance.

As an end-member case, we consider each of the C2 and C3 profiles discussed above and adopt our extreme values of 300×solar metallicity and $K_{zz} = 10^8$ cm^{2}s^{-1} in the

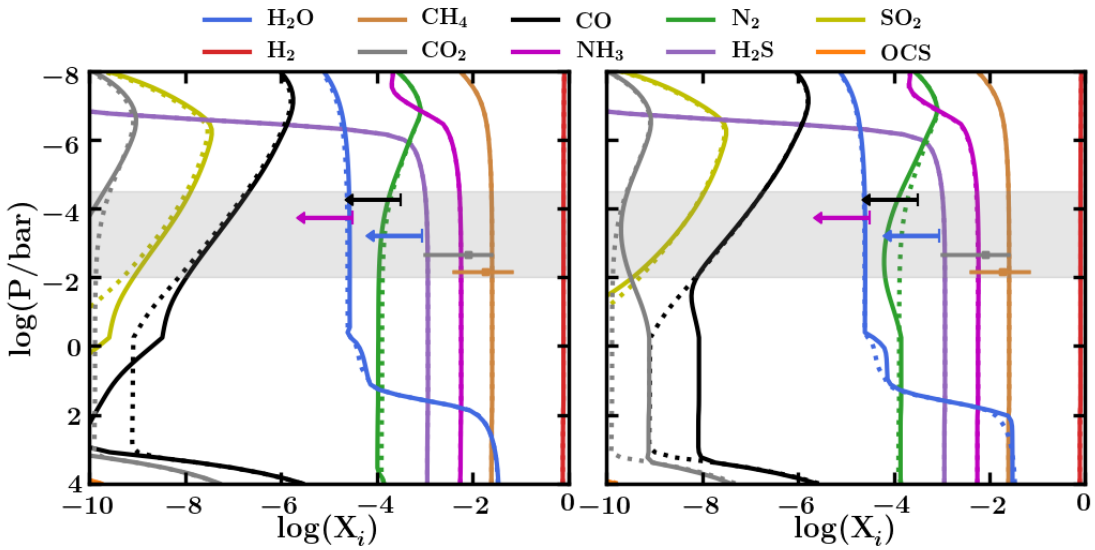

Fig. A.3 Effect of varying K_{zz} on the vertical mixing ratio profiles for several H-C-O-N-S molecular species for the C2 *P-T* profile. Dotted lines show the profile from the left-hand side of Figure 3.8, for C2 with 30% silicates, equivalent to 50× solar elemental abundances with our canonical treatment of K_{zz}, with a value of 10^6 cm^{2}s^{-1} in the deep atmosphere. Left: solid lines indicate the corresponding profiles with a lower $K_{zz} = 10^4$ cm^{2}s^{-1} in the deep atmosphere. Right: solid lines indicate the corresponding profiles with a higher $K_{zz} = 10^8$ cm^{2}s^{-1} in the deep atmosphere.

deep atmosphere. The resulting vertical mixing ratio profiles are shown in Figure A.5 along with the canonical cases. These end-member cases are similarly unable to match the retrieved CO_2 abundance constraints. A higher K_{zz} would further increase the abundances of both CO and CO_2, however CO remains more abundant than CO_2.

Thus far we have considered values of 25 K and 50 K for T_{int}, corresponding the C2 and C3 profiles, respectively. Lastly, we explore the effect of increasing T_{int} to a higher value of 60 K for completeness, as has been considered by other works for K2-18 b (e.g. Hu, 2021). We adopt the *P-T* profile of Hu (2021) with 100× solar metallicity, extrapolated to higher pressures (1000 bar) using an adiabat. We consider two cases: 1) 100× solar metallicity with depletion (i.e. twice the C3 30% silicates abundances from Table 3.1) and our canonical K_{zz} treatment, and 2) a high $K_{zz} = 10^8$ cm^{2}s^{-1} and a high metallicity of 300× solar (i.e. 6× the C3 30% silicates abundances). With the canonical K_{zz}, we find that the computed CO abundance exceeds the retrieved upper limit, while the computed CO_2 abundance remains significantly lower than the retrieved abundance. The retrieved CH_4 abundance and NH_3 upper limits can be explained by this model. For the high K_{zz} and high metallicity case, the computed CO abundance similarly

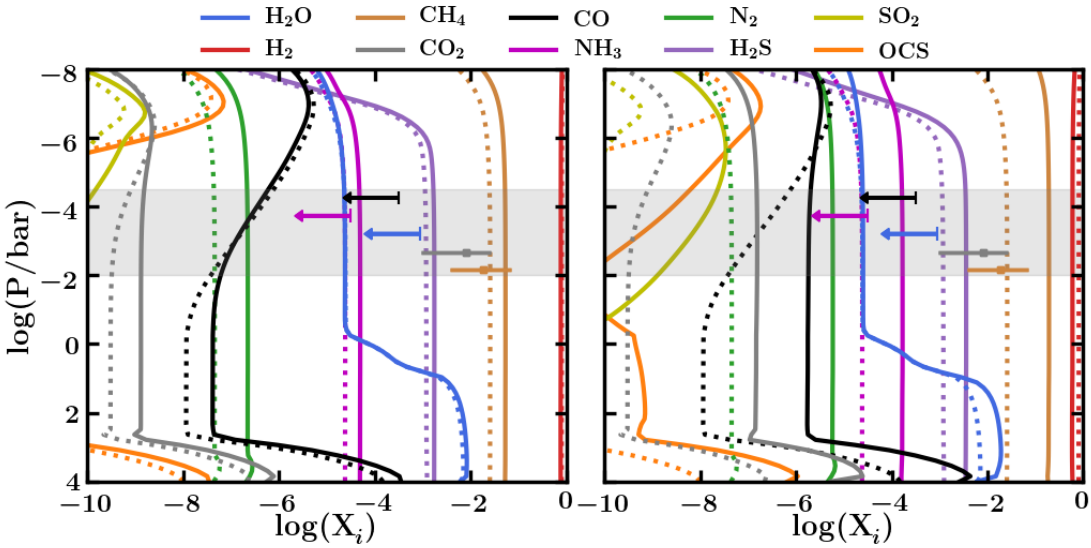

Fig. A.4 Effect of enhanced metallicity on the vertical mixing ratio profiles for several H-C-O-N-S molecular species with the C3 *P-T* profile. Dotted lines show the profile from the right-hand side of Figure 3.8, for C3 with 30% silicates, with N depletion due to the presence of magma. Left: solid lines indicate the corresponding profiles for 100× solar metallicity, i.e. 2× the respective elemental abundances given in Table 3.1. Right: solid lines indicate the corresponding profiles for 300× solar metallicity, i.e. 6× the respective elemental abundances in Table 3.1.

exceeds the retrieved abundance. In this case the retrieved CO_2 abundance can be explained by the model. However, the computed CH_4 abundance exceeds the retrieved value. Due to the higher temperatures in this *P-T* profile, the H_2O abundance exceeds the retrieved value for both cases of metallicity and K_{zz} considered.

Overall, we have explored a wide parameter space for the atmospheric chemistry, considering a range of values for K_{zz}, metallicity and T_{int}. In this exploration, we do not find a case resulting in $CO_2 > CO$ that would satisfy the retrieved atmospheric abundance constraints for K2-18 b (Madhusudhan et al., 2023b).

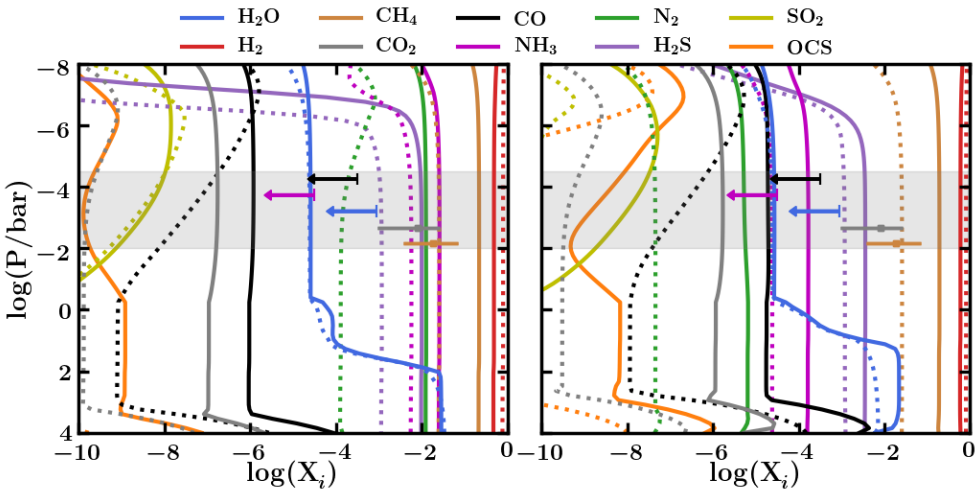

Fig. A.5 Effect of high metallicity and high K_{zz} on the vertical mixing ratio profiles for several H-C-O-N-S molecular species. Dotted lines show the canonical profiles from Figure 3.8. Left: solid lines indicate the profiles with the C2 *P-T* profile with 300× solar abundance and $K_{zz} = 10^8$ cm^{2}s^{-1} in the deep atmosphere. Right: solid lines indicate the profiles with the C3 *P-T* profile with 6× the elemental abundances from Table 3.1, i.e. equivalent to 300× solar abundance, and $K_{zz} = 10^8$ cm^{2}s^{-1} in the deep atmosphere.

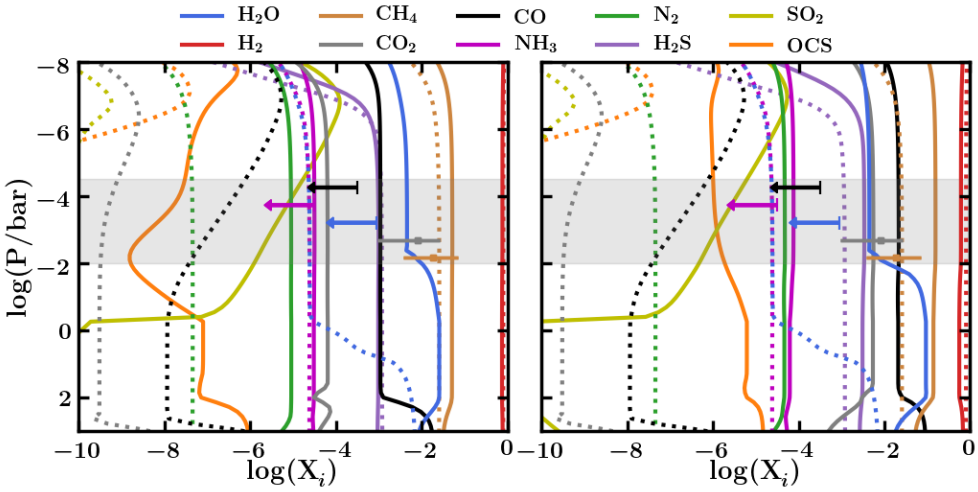

Fig. A.6 Effect of higher T_{int} on the vertical mixing ratio profiles for several H-C-O-N-S molecular species. We adopt the *P-T* profile from Hu (2021) with T_{int} of 60 K and 100× solar metallicity, extrapolated to 1000 bar. Dotted lines show the canonical profiles using the hotter C3 profile from Figure 3.8. Left: solid lines indicate profiles assuming 100× solar metallicity including N depletion, adopting $K_{zz} = 10^6$ cm^{2}s^{-1} in the deep atmosphere, for the Hu (2021) *P-T* profile. Right: solid lines indicate profiles assuming 300× solar metallicity including N depletion, adopting $K_{zz} = 10^8$ cm^{2}s^{-1} in the deep atmosphere, for the Hu (2021) *P-T* profile.